

# An Analytical Model to Determine the Bearing Capacity of Existing Steel-Concrete-Composite Bridges Without Mechanical Connectors

Anders Jørgensen

2023

MSc Thesis in Structural  
Engineering





# An Analytical Model to Determine the Bearing Capacity of Existing Steel-Concrete-Composite Bridges Without Mechanical Connectors

Thesis by:

Anders Jørgensen

To be defended on 4th of July 2023

Student name: Anders Jørgensen  
Student number: 5379504  
Place: Delft University of Technology  
Institution: Faculty of Civil Engineering and Geosciences  
Thesis committee: Dr. Ir. Y. Yang, TU Delft, Chairman  
Dr. M. Poliotti, TU Delft, Daily Supervisor  
Dr. F. Kavoura, TU Delft, 1st Member  
Dr. Ir. A. de Boer, Ingenieursbureau Gemeente Amsterdam,  
2nd Member

# Acknowledgements

This thesis marks the end of my Master's studies and my time at TU Delft, a period I will define as life-changing and one I will hardly forget. Therefore, I would like to thank several people for participating in this.

Firstly, I would like to thank my girlfriend Deniz for her unconditional support, everything from reading bits of my report and helping with all the practical stuff that is not directly related to this thesis. Your help has been invaluable for me to achieve my goals, and I feel truly fortunate to have you by my side.

Moreover, I would like to express my gratitude for the unwavering support from my parents. Their constant encouragement and willingness to lend an ear whenever I need to talk have been invaluable. Likewise, I would like to thank Mia and Rohat for being great inspirations and role models, inspiring me to follow my goals and study abroad to achieve my Master's degree. Thanks for everything. A special thanks to my fellow students and friends who have a significant part in this thesis with their support and ideas on this subject.

I want to thank Ingenieursbureau Gemeente Amsterdam for allowing me to use data and literature from previous tests of the Amsterdam bridges. Finally, I would like to thank each of my thesis committee members for their help and expertise on this subject.

## Abstract

In Amsterdam, more than 30 steel-concrete composite bridges were constructed from 1880-1960 without mechanical connectors and transverse reinforcement. Currently, there are no simplified analytical methods to determine the bearing capacity of these bridges. Thus, the bearing capacity is verified using NLFEM or oversimplified analytical calculations. This research proposes an analytical method to determine the bearing capacity of historic steel-concrete-composite bridges without mechanical connectors to avoid time-consuming FEM calculations and offers reasonable results.

An experimental and numerical study is performed on data from in situ and laboratory testing of samples from two different bridge decks from these Amsterdam bridges. The tests are accompanied by a numerical model that has been studied and adjusted to a more generalized loading case. This study determined that the exterior composite girders are critical due to their lower lateral stiffness.

An analytical model is proposed to examine the behaviour of the exterior composite girder. The model considers a 3-point bending load at midspan between the exterior composite and adjacent girder. The force distribution is described through a compatibility-based strut and tie model (C-STM). The concrete in compression is considered elastic compression struts, only limited by the ultimate load of the model. The concrete in tension is interpreted as a tensile tie, which fails when it exceeds the concrete tensile resistance. Following the failure of the tensile tie, it is assumed that a longitudinal crack propagates between the exterior composite girder and the adjacent girder. Additionally, vertical and lateral stiffness components are included in the model. These account for the flexural stiffness of the exterior and interior composite girder. The vertical stiffness is accounted for as elastic springs, and the lateral stiffness as spring beams. The interior lateral spring beam summarises all the interior composite girders' stiffness, whereas the exterior lateral spring beam only considers the exterior composite girder. Therefore, the configuration assumes that the interior spring beam is significantly stiffer than the exterior. Moreover, the stiffness of the exterior spring beam reduces when the longitudinal cracking occurs, assuming a part of the concrete fails. The C-STM is linked to the cross-section verification of longitudinal shear, biaxial bending and vertical shear resistance in two stages. Stage 1, at the load at longitudinal cracking, determines if the specimen fails at this moment, indicating that there possibly is a brittle failure. Stage 2 is after longitudinal cracking, where the steel-concrete contact perimeters have reduced, and the corresponding resistances accordingly reduce.

The failure modes obtained by the analytical model are comparable to the ones observed during the experimental testing. The analytical model showed that the bridges failed due to biaxial bending limited by partial shear interaction. One of the specimens from the testing yielded due to bending but with limited ductility. The other specimen also yielded due to bending with concrete crushing at the top concrete fibre. Further, the bearing capacities obtained from the analytical model are comparable to the failure loads from the experimental and numerical results.

The model predicts the failure modes and the bearing capacity and can therefore contribute to the assessment of the historic Amsterdam bridges, helping to reduce the assessment time of the bridges and understand their load-bearing behaviour better. Future work should focus on verifying the method by examining more bridges using FEM.



# Contents

<b>1</b>	<b>Introduction</b>	<b>15</b>
1.1	Context . . . . .	15
1.2	Research Objective and Questions . . . . .	17
1.3	Methodology . . . . .	17
<b>2</b>	<b>Literature Review</b>	<b>19</b>
2.1	Early 20th Century Composite Bridge Design . . . . .	19
2.1.1	Load Models - VOSB1933 . . . . .	19
2.1.2	Design Methods . . . . .	20
2.2	Eurocode Recommendations . . . . .	21
2.2.1	Load Models - Eurocode NEN-EN 1991-2:2005 . . . . .	21
2.2.2	Design Verification - Eurocode NEN-EN 1994:2004 . . . . .	22
2.2.3	Bending Resistance - Eurocode NEN-EN 1993-1-1:2005 . . . . .	24
2.2.4	Vertical Shear Resistance - Eurocode NEN-EN 1993-1-1:2005 . . . . .	25
2.2.5	Vertical Shear Resistance - Eurocode NEN-EN 1992-1-1:2004 . . . . .	25
2.3	Longitudinal Shear Resistance . . . . .	27
2.4	Strut and Tie Method . . . . .	31
2.4.1	STM for Analysis of Reinforcement-free Decks . . . . .	32
2.4.2	Compatibility-based Strut and Tie Method . . . . .	34
2.4.3	Design Requirements - Eurocode NEN-EN 1992-1-1:2004 . . . . .	34
2.5	Transverse Load Distribution Models . . . . .	35
2.5.1	Guyon Massonnet Method . . . . .	35
2.5.2	Transfer Matrix Method . . . . .	38
2.6	Summary . . . . .	41
<b>3</b>	<b>Experimental and Numerical Study</b>	<b>43</b>
3.1	Experimental Setup . . . . .	43
3.1.1	In Situ Testing . . . . .	43
3.1.2	Laboratory Testing . . . . .	46
3.2	Numerical Model . . . . .	54
3.2.1	Material Properties . . . . .	55
3.2.2	Boundary and Loading Conditions . . . . .	55
3.2.3	Results . . . . .	56
3.3	Summary of Experimental and Numerical Study . . . . .	62
<b>4</b>	<b>Analytical Design Using the Strut and Tie Method</b>	<b>64</b>
4.1	Compatibility-based Strut and Tie Method . . . . .	64
4.1.1	Compression Strut . . . . .	67
4.1.2	Tensile Tie . . . . .	68
4.1.3	Vertical Springs . . . . .	69
4.1.4	Lateral Spring Beams . . . . .	70
4.1.5	Stage 1 - Cross-section Verification . . . . .	75
4.1.5.1	Compression Resistance of Struts . . . . .	76
4.1.5.2	Longitudinal Shear Resistance . . . . .	76

4.1.5.3	Biaxial Bending Resistance . . . . .	77
4.1.5.4	Vertical Shear Resistance . . . . .	81
4.1.6	Stage 2 - Cross-section Verification . . . . .	84
4.1.6.1	Longitudinal Shear Resistance . . . . .	84
<b>5</b>	<b>Verification of the Analytical Model with Experimental and Numerical Results</b>	<b>89</b>
5.1	Results of Analytical Calculations . . . . .	89
5.2	Verification using Experimental and Numerical Results . . . . .	92
5.3	Extended Comparison of Results . . . . .	97
<b>6</b>	<b>Discussion</b>	<b>100</b>
6.1	Differences Between the FEM and the Analytical Model . . . . .	100
6.2	Other Loading Cases . . . . .	103
6.3	Sensitivity Analysis of Stiffness Parameters . . . . .	106
6.3.1	Compression Struts . . . . .	106
6.3.2	Tensile Tie . . . . .	107
6.3.3	Interior Spring Beam . . . . .	109
6.4	Limitations . . . . .	111
<b>7</b>	<b>Conclusions and Recommendations</b>	<b>113</b>
7.1	Conclusions . . . . .	113
7.2	Recommendations . . . . .	114
<b>A</b>	<b>Calculation Example</b>	<b>118</b>
A.1	Example - Establish the C-STM . . . . .	118
A.1.1	Stage 1 Cross-section Verification . . . . .	123
A.1.1.1	Resistance Compression Struts . . . . .	124
A.1.1.2	Longitudinal Shear Resistance . . . . .	124
A.1.1.3	Biaxial Bending Resistance . . . . .	125
A.1.1.4	Vertical Shear Resistance . . . . .	127
A.1.2	Stage 2 Cross-section Verification . . . . .	128
A.1.2.1	Resistance of Compression Struts . . . . .	128
A.1.2.2	Longitudinal Shear Resistance . . . . .	129
A.1.2.3	Biaxial Bending Resistance . . . . .	131
A.1.2.4	Vertical Shear Resistance . . . . .	134
<b>B</b>	<b>Solution Strategy to Determine Displacements of the C-STM</b>	<b>135</b>
B.1	Equilibrium Conditions . . . . .	135
B.2	Compatibility Conditions . . . . .	136
B.3	Kinematic and Constitutive Relations . . . . .	138
B.4	MATLAB Compatibility-based Strut and Tie Method . . . . .	139
<b>C</b>	<b>MATLAB Iteration for Biaxial Bending</b>	<b>143</b>
<b>D</b>	<b>Experimental Results - LB1 and LB3</b>	<b>147</b>
D.1	LB1 Reaction Forces . . . . .	147
D.2	LB3 Reaction Forces . . . . .	148
<b>E</b>	<b>Numerical Model Input</b>	<b>150</b>

# List of Figures

1.1	Cross section of a steel-concrete composite bridge in Amsterdam without mechanical connectors. . . . .	15
1.2	Cross-section of a historical steel-concrete bridge without mechanical connectors from Amsterdam. Showing the position of shrinkage reinforcement and steel girders. . . . .	16
1.3	A workflow diagram of the work included in this research. . . . .	18
2.1	Loading scheme according to VOSB1933 [4]. . . . .	20
2.2	Application of load model 1.[8] . . . . .	22
2.3	Example of plastic stress distribution according to NEN-EN 1994-1-1:2004 [2]. . . . .	23
2.4	Plastic stress distribution for partial shear connection from NEN-EN 1994-1-1:2004[2]. . . . .	23
2.5	Relation between plastic moment resistance and degree of shear connection. Simplified theory vs plastic theory from NEN-EN 1994-1-1:2004[2]. . . . .	24
2.6	Test setup and details of the cross sections from the study by Vasedravellis and Uy [13]. . . . .	26
2.7	Development of Mohr-Coulomb failure envelope [20]. . . . .	29
2.8	Examples of disturbed regions and Bernoulli regions [24]. . . . .	31
2.9	Example of different strut and tie models [24]. . . . .	32
2.10	Reinforcement free deck.[29] . . . . .	32
2.11	STM and compression stress trajectory. [29] . . . . .	33
2.12	a) Plan view of deck and girders. b) Components of lateral stiffness. [29] . . . . .	33
2.13	C-STM for a deep beam. [30] . . . . .	34
2.14	Guyon Massonnet Method reference system [31]. . . . .	36
2.15	Distribution coefficient $K_0$ at point 0 [31]. . . . .	37
2.16	Influence lines at reference points between 0 and b [31]. . . . .	38
2.17	TLD influence line peak values for slab 1-5 at L/8. <b>a)</b> slab 1. <b>b)</b> slab 2. Etc. [32]. . . . .	39
2.18	The force diagram of articulated slab bridge. (a) external force, (b) vertical shear of joints, (c) distribution load of each slab, (d) deflection of slabs. [32] . . . . .	40
3.1	Cross section of Amsterdam Bridge 70 side span bridge deck [1]. . . . .	44
3.2	Position of the load before the in situ testing. Internal distribution of stresses from the load. [1] . . . . .	44
3.3	Load and sensor location of the testing at midspan. The red rectangle indicates the wheel print load. The blue rectangles indicate strain sensors on the bottom steel flanges. The orange dots are the lasers measuring the vertical displacement. The green lines show the measurement of the transverse displacement between the bottom steel flanges.[1] . . . . .	45
3.4	Western half of bridge 70. Showing the location of cut-out sections LB1-LB3. [33] . . . . .	46
3.5	Cross-section of LB1 showing the dimensions. . . . .	47
3.6	Cross-section of LB3 showing the dimensions. . . . .	47
3.7	Side view of the test setup of LB1. Showing the position of hydraulic jacks.[34] . . . . .	48
3.8	Top view of the test setup of LB1. Showing the position of loading plates.[34] . . . . .	48
3.9	Bottom view position of 3D DIC at LB1. . . . .	49

3.10	Orientation of the 3D DIC positioned underneath LB1. Showing the DIC when the total load is 1400 kN and 1500 kN at LB1. . . . .	49
3.11	Bottom view of the specimen indicating the location of the LVDTs relative to the loading plates. . . . .	50
3.12	A-A section of the specimen in Figure 3.11 a cross-section with the position of LVDTs underneath the specimen of LB1. . . . .	50
3.13	LB1 - Transverse displacement versus loading measured from underneath. $F_{total}$ is the total load. . . . .	51
3.14	LB3 - Transverse displacement versus loading measured from underneath. $F_{total}$ is the total load. . . . .	51
3.15	LB1 - Vertical displacement versus the total load $F_{total}$ . Vertical displacement was measured from the hydraulic jack. . . . .	52
3.16	At the left: Opening between steel and concrete at one of the exterior girders observed after the failure of LB1. At the right: Longitudinal cracking observed after the failure of LB1.[34] . . . . .	53
3.17	LB3 - Vertical displacement versus the total load $F_{total}$ . Vertical displacement was measured from the hydraulic jack. . . . .	53
3.18	Sideview of LB3 showing concrete crushing at the top concrete fibre following failure [34]. . . . .	54
3.19	3D view of the mesh of LB1. . . . .	55
3.20	3D view of LB1 showing the boundary- and loading conditions. . . . .	56
3.21	Total load versus transverse displacement at midspan of LB1. . . . .	57
3.22	Cross-section showing the measuring point for the transverse displacement profiles of LB1 and LB3. . . . .	57
3.23	Sideview of LB1 at the onset of cracking. a) Crack width at 457 kN. b) Crack width at 488 kN. . . . .	58
3.24	3D view of LB1 showing the start of yielding at 940 kN. . . . .	58
3.25	Bottom view of LB1 showing the longitudinal cracking. a) crack width at 1145 kN. b) crack width at 1169 kN. . . . .	59
3.26	X, distance from support to mid-span, including the length of the cross beams, versus the transverse displacement for LB1. . . . .	60
3.27	Total load versus transverse displacement at midspan of LB3. . . . .	60
3.28	3D view of LB3 showing the start of yielding at 808 kN. . . . .	61
3.29	Bottom view of LB3 showing the longitudinal cracking. a) crack width at 916 kN. b) crack width at 932 kN. . . . .	61
3.30	X, distance from support to mid-span, including the length of the cross beams, versus the transverse displacement for LB3. . . . .	62
4.1	The cracks due to lack of transverse reinforcement. (a) bottom view showing the cracks underneath the exterior and adjacent girder. (b) shows the cross-section of the bridge slab. . . . .	64
4.2	Geometry of C-STM and forces acting on the model. . . . .	65
4.3	Topview of the C-STM, showing the spring components. . . . .	65
4.4	Definition of cross-section properties used to determine the geometry of the C-STM and flexural stiffness. . . . .	66
4.5	Load dispersal according to EN1991-2. . . . .	67
4.6	Linear constitutive relation of the compression struts. . . . .	67
4.7	Nonlinear constitutive relation of the tensile tie. . . . .	68

4.8	Forces acting on the C-STM following the failure of the tensile tie. . . . .	69
4.9	Sideview showing the assumption of the vertical spring. . . . .	69
4.10	Linear constitutive relation for the vertical springs. . . . .	70
4.11	Topview of the C-STM in Figure 4.2. Showing configuration of the spring beams, as Euler-Bernoulli beams. . . . .	71
4.12	Linear elastic constitutive relation for spring 2. . . . .	72
4.13	Constitutive relation for spring 1. $F_u$ is the ultimate load assuming full shear connection . . . . .	72
4.14	Cross section considered for calculating the flexural stiffness of the cross-section, $EI_{1,cr}$ , following longitudinal cracking. . . . .	73
4.15	Example of the load versus displacement depending on failure type. . . . .	74
4.16	Flowchart to establish the C-STM. . . . .	75
4.17	Contact perimeter for the longitudinal shear resistance before longitudinal cracking. . . . .	76
4.18	Vertical and lateral force components acting on the exterior girder. . . . .	77
4.19	Example of plastic bending resistance calculation about the major axis with the plastic neutral axis in the steel flange. . . . .	78
4.20	Example of plastic bending resistance calculation about the minor axis with the plastic neutral axis in the steel flange. . . . .	79
4.21	Example of plastic moment resistance calculation about the major axis with a reduced concrete compression force due to partial shear connection. . . . .	79
4.22	Flowchart of the biaxial bending calculation. . . . .	80
4.23	Cross-section properties considered for calculation of the vertical shear. . . . .	81
4.24	Flowchart of the vertical shear resistance calculation. . . . .	83
4.25	Flowchart for the stage 1 cross-section verification. . . . .	84
4.26	An opening is formed between the concrete and steel of the exterior girder facing the other girder. . . . .	85
4.27	Shear stress flow along steel-concrete interface at the exterior composite girder. The red line indicates the contact perimeter accounted for when considering cohesion. . . . .	86
4.28	Longitudinal shear resistance versus the shear force $V_{Ed}$ . $F_{cr}$ is the load at longitudinal cracking. . . . .	87
4.29	Flowchart of the stage 2 cross-section verification. . . . .	88
5.1	LB1 - Actual and simplified longitudinal shear resistance and shear force versus the single point load, $F$ . . . . .	90
5.2	Moment interaction diagram for LB1 at different full, partial and zero shear connections. . . . .	91
5.3	Assumed loading of the proposed analytical model for comparison with the ex- perimental and numerical results. . . . .	93
5.4	LB1 - comparison of the resistance to longitudinal cracking and failure from the experiments, numerical and analytical results. . . . .	93
5.5	LB3 - comparison of the resistance to longitudinal cracking and failure from the experiments, numerical and analytical results. . . . .	94
5.6	Cross-section showing the measuring point for the transverse displacement pro- files of LB1 and LB3. . . . .	95
5.7	LB1 - Transverse displacement profile at $F = 380$ kN from the experiment, nu- merical and analytical model. $X$ is the distance from the support to the midspan. . . . . .	96

5.8	LB3- Transverse displacement profile at $F = 250$ kN from the experiment, numerical and analytical model. $X$ is the distance from the support to the midspan.	97
5.9	Location and notation of loads for calculating the point load at midspan, giving a maximum bending moment equivalent to 4-point bending.	98
5.10	Comparison of the resistances for LB1 and LB3 from experiments, numerical and analytical results.	99
6.1	Bottom view exterior and adjacent composite girder. (a) numerical model concrete tensile tie as uniformly distributed spring. (b) analytical model concrete tensile tie as single spring.	100
6.2	The lateral displacement profile of LB1 before cracking the C-STM and the numerical model. $X$ is the distance from the support to the midspan.	101
6.3	Longitudinal shear resistance of the exterior composite girder. (a) idealised distribution of the longitudinal shear resistance. (b) Simplification of the distribution of the longitudinal shear resistance in the analytical model.	102
6.4	Longitudinal shear resistance and shear force versus the single point load, $F_{Ed}$ .	102
6.5	The lateral strain along the exterior composite girder of LB1 right after longitudinal cracking. $X$ is the distance from the cross beam to the midspan.	103
6.6	Example of load dispersal in the transverse direction from the two wheel print loads influencing the same area.	104
6.7	Location and notation of loads for calculating the point load equivalent 4-point bending resistance from the 3-point bending ultimate load.	105
6.8	Example showing the load distribution at loading between interior composite girders.	105
6.9	The sensitivity to longitudinal cracking to changes of the axial stiffness of the compression struts relative to the original axial stiffness.	107
6.10	The sensitivity to longitudinal cracking to changes of the cross-section area of the tensile tie relative to the original axial stiffness.	108
6.11	The sensitivity of the exterior lateral displacement at 250 kN to changes of the cross-section area of the tensile tie relative to its original value.	108
6.12	The sensitivity to longitudinal cracking to changes of spring $k_2$ relative to spring $k_1$ .	109
6.13	The sensitivity of the exterior lateral displacement to changes of spring $k_2$ relative to spring $k_1$ at a load at 400 kN.	110
6.14	The sensitivity of the load distribution to changes of spring $k_2$ relative to spring $k_1$ .	111
A.1	Cross-section of LB1 of the exterior and middle girder.	118
A.2	Reference axis for cross-section properties of LB1 and LB3.	121
A.3	Concrete considered following longitudinal cracking.	122
A.4	Internal force components from major axis bending of the exterior composite girder. The red dots indicate the centroid of each force component.	126
A.5	Internal force components from minor axis bending of the exterior composite girder. The red dots indicate the centroid of each force component.	126
A.6	Concrete strain and strain criteria along the length of LB1 at $F_{cr} = 421$ kN.	129
A.7	Reduced cross-section considered following longitudinal cracking	131
A.8	Internal force components from major axis bending of the exterior composite girder. The red dots indicate the centroid of each force component.	132

- A.9 Internal force components from minor axis bending of the exterior composite girder. The red dots indicate the centroid of each force component. . . . . 133
- B.1 Coordinate system for the ordinary differential equations. . . . . 135
- B.2 Forces at the top compression node. . . . . 136
- B.3 Forces considered for at the bottom right joint of the C-STM. . . . . 137
- B.4 Forces considered for at the bottom left joint of the C-STM. . . . . 137
- B.5 Coordinates used to create the MATLAB *polyshape*. . . . . 139
- D.1 Location and notation of the supports used during experimental testing. . . . . 147
- D.2 LB1 - Support reaction forces of support FS01-FS03 positioned at the west end of the specimen . . . . . 147
- D.3 LB1 - Support reaction forces of support FS04-FS06 positioned at the east end of the specimen. . . . . 148
- D.4 LB3 - Support reaction forces of support FS01-FS03 positioned at the west end of the specimen. . . . . 148
- D.5 LB3 - Support reaction forces of support FS04-FS06 positioned at the east end of the specimen. . . . . 149

# List of Symbols

$\alpha$	Torsional stiffness coefficient
$\delta_{v,3}$	Vertical displacement of the exterior composite girder
$\delta_{v,4}$	Vertical displacement of the adjacent composite girder
$\eta$	Degree of shear connection
$\gamma_x$	Effective contact perimeter between the steel and concrete
$\gamma_y$	Effective contact perimeter between the steel and concrete
$\lambda_{sd}$	Slenderness function
$\mu$	Coefficient of friction
$\nu_{min}$	Minimum strength reduction factor concrete
$\rho$	Reduction parameter
$\rho_x$	Flexural rigidity per unit width
$\rho_y$	Moment of inertia of composite section
$\sigma$	Normal stress
$\sigma_{Rd,max}$	Maximum compression design resistance
$\tau_{Rd}$	Longitudinal shear resistance
$\tau_{surf}$	Effective shear stress
$\theta$	Flexural stiffness coefficient
$\theta_1$	Angle between vertical and compression strut
$\theta_2$	Angle between horizontal and compression strut
$\varphi$	Friction angle
$\varphi_i$	Lateral angle rotation of the <i>ith</i> girder
$\varphi_s$	Safety factor recommended to be 0.8
$a$	Half the width of the slab
$A_c$	Concrete area
$A_s$	Steel area
$A_a$	Steel girder cross-section area
$A_{c,eff}$	Effective steel-concrete contact area
$A_{s,i}$	Area of the <i>ith</i> strut
$A_{sl}$	Area of the tensile reinforcement
$A_t$	Area tension tie

$A_v$	Shear area
$b$	Length loading plate
$b_f$	Steel girder flange width
$b_w$	Smallest width of the cross-section in the tensile area
$c$	Cohesion
$C_{Rd,c}$	Country recommended value that can be found in the National Annex
$d$	Height of the concrete section
$d$	Span length
$D_{beam}$	Depth of the steel girder
$D_{slab}$	Depth of the concrete slab
$E_a$	Young's modulus steel girders
$E_c$	Young's modulus concrete
$e_{T0}$	Elastic neutral axis of the composite section
$EI$	Flexural stiffness
$f(\lambda_{sd})$	Slenderness function
$f_b$	Flexural stiffness coefficient
$f_t$	Flexural stiffness coefficient
$F_u$	Ultimate load
$F_{ac,y}$	Steel compression force from major axis bending
$F_{ac,z}$	Steel compression force from minor axis bending
$F_{at,y}$	Steel tension force from major axis bending
$F_{at,z}$	Steel tension force from minor axis bending
$F_{cc,y,red}$	Concrete compression force from major axis bending reduced due to partial shear interaction
$F_{cc,y}$	Concrete compression force from major axis bending
$F_{cc,z,red}$	Concrete compression force from minor axis bending reduced due to partial shear interaction
$F_{cc,z}$	Concrete compression force from minor axis bending
$f_{cd}$	Concrete design compression strength
$f_{ck}$	Characteristic compressive cylinder strength of concrete at 28 days
$F_{cr}$	Load at longitudinal cracking
$F_{eq}$	Single point load giving equivalent bending moment as two forces from 4-point bending
$f_{yd}$	Steel design yield strength

$F_y$	Vertical force component
$F_z$	Horizontal force component
$G$	Shear modulus of concrete
$h_t$	Height tensile tie
$h_{c1}$	Concrete cover
$h_{c2}$	Height from bottom of cut-out section to top concrete fibre
$h_o$	Height of the steel within the concrete cover requirement
$h_{s,i}$	Height of the $i$ th strut
$I_{a,y,3}$	Major axis moment of inertia of the exterior steel girder
$I_{a,y,4}$	Major axis moment of inertia of the adjacent steel girder
$I_{a,z,1}$	Minor axis moment of inertia of the exterior steel girder
$I_{c,y,3}$	Major axis moment of inertia of the concrete of the exterior composite girder
$I_{c,y,4}$	Major axis moment of inertia of the concrete of the adjacent composite girder
$I_{c,z,1}$	Minor axis moment of inertia of the concrete of the exterior composite girder
$J$	Torsional inertia moment
$K$	Distribution coefficient
$K_0$	Distribution coefficient with 0 torsional stiffness
$K_1$	Distribution coefficient with full torsional stiffness
$k_1$	Country recommended value that can be found in the National Annex
$k_3$	Vertical spring stiffness of the exterior composite girder
$k_4$	Vertical spring stiffness of the adjacent composite girder
$L$	Distance from the nearest support
$L$	Span length between supports
$L_d$	Length load dispersal
$L_t$	Length of the tensile tie
$L_1$	Distance from support to nearest point load at 4-point bending
$L_c$	Length cross beams
$L_{eff}$	Span length between cross beams
$L_{emb,s}$	Embedded length of the steel girder
$L_o$	Length where the concrete has formed an opening from the steel
$M_i$	Moment of the $i$ th girder
$M_{y,Ed}$	Design major axis bending moment

$M_{y,pl,Rd}$	Plastic moment design resistance for major axis bending
$M_{y,Rd}$	Major axis bending moment resistance
$M_{z,Ed}$	Design minor axis bending moment
$M_{z,pl,Rd}$	Plastic moment design resistance for minor axis bending
$M_{z,Rd}$	Minor axis bending moment resistance
$n$	Modular ratio
$N_{c,f}$	Concrete compression force from bending with the full shear connection
$N_c$	Concrete compression force due to bending with partial shear connection
$N_{Ed}$	Design normal force
$N_{Rd}$	Normal force resistance
$N_{s,i}$	Normal force of the $i$ th strut
$N_t$	Normal force from tensile tie
$p$	Number of interior composite girders
$P_{cs}$	Effective contact perimeter between the steel and concrete
$r$	Steel girder root radius
$t_f$	Steel girder flange thickness
$t_w$	Steel girder web thickness
$u_{cr}$	Steel-concrete contact perimeter where the concrete has formed an opening
$u_{eff}$	Effective steel-concrete contact area
$u_{s,eff}$	Effective steel-concrete contact perimeter
$u_{s,i}$	Axial displacement of compression strut of the $i$ th strut
$u_t$	Axial displacement of the tensile tie
$V_i$	Shear force of the $i$ th girder
$V_{1,x,Rd}$	Longitudinal shear resistance where the concrete has formed an opening
$V_{2,x,Rd}$	Longitudinal shear resistance where there is full steel-concrete contact
$V_{comp,0}$	Composite vertical shear resistance with no shear interaction
$V_{comp}$	Composite vertical shear resistance
$V_{Ed}$	Design shear force
$V_{pl,Rd}$	Design vertical shear resistance of steel
$V_{Rd,c}$	Vertical shear resistance of the concrete
$V_{slab}$	Vertical shear resistance of concrete slab
$V_{x,Rd}$	Total longitudinal shear resistance

$w_p$	Width of the loading plate
$w_i$	Lateral displacement of the $i$ th girder
$x_{cr}$	Distance from the support to where the concrete starts to form an opening to the steel
$y_1$	Minor axis bending. Distance from the concrete compression force to the steel tension force
$y_2$	Minor axis bending. Distance from the steel compression force to the steel tension force
$z_a$	Distance from top concrete fibre to centroid of the steel girder
$z_c$	Distance from top concrete fibre to centroid of the concrete
$z_1$	Major axis bending. Distance from the concrete compression force to the steel tension force
$z_2$	Major axis bending. Distance from the steel compression force to the steel tension force

# 1 Introduction

## 1.1 Context

From 1880 to 1960, many bridges were constructed in Amsterdam, following the design regulations of that time, and more than 30 were designed as steel-concrete-composite bridges without mechanical connectors. These bridges are under assessment due to their age and the changing loads. Despite this historical development of the design and implementation of composite structures as well as the introduction of European Standards, the Eurocode does not include recommendations for assessing the historical steel-concrete composite bridges. Furthermore, it is stated by law that the Dutch government must ensure that the bearing capacity of these bridges is sufficient [1]. Thus, the municipality of Amsterdam wants to assess the historic bridges to determine if the bearing capacity is sufficient to avoid unneeded replacements or repairs. Replacing the bridges can be costly, time demanding and hinder Amsterdam's infrastructure users. Moreover, the environmental impact related to the possibly-unnecessary replacement of the bridges may be substantial, assuming that the construction and production of a new bridge has an environmentally negative footprint. If the bearing capacity is acceptable, the bridges can remain or be repaired relatively cheaply without impacting the infrastructure and the environment. Figure 1.1 shows an example of one of the historic Amsterdam bridges.

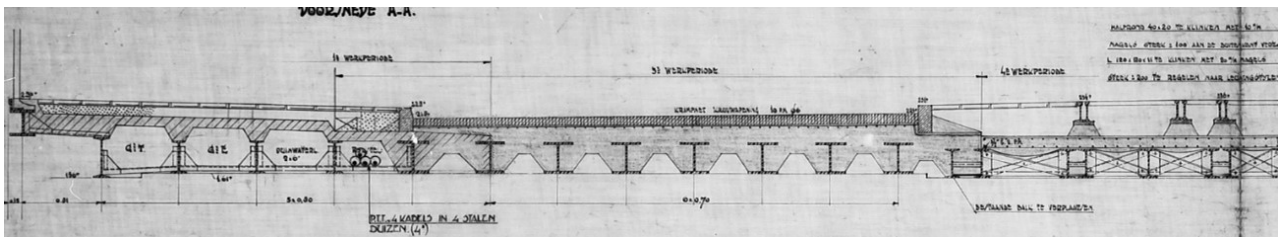


Figure 1.1: Cross section of a steel-concrete composite bridge in Amsterdam without mechanical connectors.

Archive studies were done by de Boer *et al.* [1] looking further into the construction papers of these bridges. To take a closer look at the historic steel-concrete composite bridges without mechanical connectors, a cross-section is shown in Figure 1.2. The bridges consist of several partially encased steel girders spanning in the longitudinal direction, only leaving the bottom flange concrete-free. The transfer of forces between steel and concrete comes merely from cohesion and friction due to the lacking mechanical connectors. In the top concrete layer of the encasement, there is a mesh shrinkage reinforcement, which is the only reinforcement. The reinforcement only has a diameter of 6 mm and 100 mm spacing. The typical historic Amsterdam bridges have three spans, with two side spans and one main span. The bridges have side spans of 5 to 8 m, whereas the main span is 8.5 to 14 m. The spans are usually statically determined. The steel girders are DIN profiles of different types, and the height varies from 260 mm to 700 mm. There is always a cut-out section between the steel girders with a height of 140 mm, whereas the width of the cut-out section depends on the dimension of the steel girders.

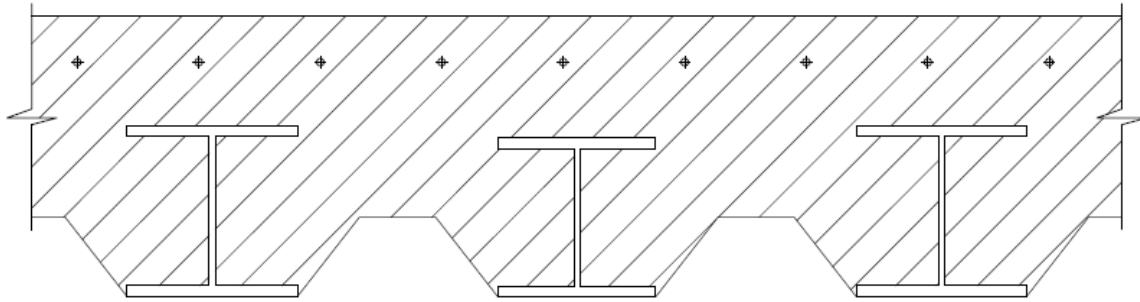


Figure 1.2: Cross-section of a historical steel-concrete bridge without mechanical connectors from Amsterdam. Showing the position of shrinkage reinforcement and steel girders.

The bridges' composite behaviour and lateral load distribution are mainly unknown for the following reasons.

- There are no mechanical connectors; Thus, the transfer of forces at the interface merely comes from the steel-concrete bond.
- There is very little transverse reinforcement; Hence, the lateral load distribution and composite behaviour are uncertain.

Currently, EN1994-1-1:2004 and EN1994-2:2005 are used for the design of composite bridges. Regarding shear connection, the European Standard states, "*Shear connection and transverse reinforcement shall be provided to transmit the longitudinal shear force between the concrete and the structural steel element, ignoring the effect of natural bond*" [2, p. 52], which is not ensured for the historic Amsterdam bridges without mechanical connectors.

The bridges differ from those mentioned in EN1994 for the above reasons. For bridges that differ from the European Standard, it states that the design should, as far as practicable, rely on existing design rules and methods and must be supported by experiments [3]. The only existing methods to determine the bearing capacity of the bridges are oversimplified analytical calculations or NLFEM (Nonlinear Finite Element Method) calculations. These oversimplified calculations are based on conservative guesses, as the actual composite behaviour and load distribution are unknown. Whereas FEM analysis provides more accurate results, modelling the bridges can be time-consuming and requires knowledge of the interface behaviour, which is also unknown.

Due to a larger construction of the inner infrastructure in Amsterdam, one of the steel-concrete composite bridges without mechanical connectors, Amsterdam Bridge 70, had to be replaced. The construction papers of the bridge date back to the early 1930s, and the bridge's lifetime had already passed. Still, it was considered to be in relatively good condition. Therefore, this was an opportunity to perform a series of tests investigating this bridge, first by performing in situ tests before it was demolished. After the in situ tests, three specimens were cut out from the bridge deck and transported to Delft for further laboratory testing. The in situ and laboratory tests were accompanied by numerical models helping to understand the behaviour of the bridges.

Before the testing, the hypothesis was that the bridges would be subject to punching shear failure due to the geometry at the cut-out section where the concrete is thinnest, as shown in Figure 1.2. This was also anticipated due to the small amount of transverse reinforcement. This hypothesis was tested by applying the load between the steel girders. However, the in situ

tests and numerical analysis proved that the bridges had sufficient bearing capacity to resist punching shear, according to existing design standards [1]. It can be expected that the failure of the historic steel-concrete composite bridges will occur as one of the following:

- Yielding due to flexural bending
- Concrete crushing of the top fibre due to flexural bending
- Slip due to longitudinal shear
- Vertical shear failure

Punching shear failure is not regarded, as it was already covered and proved sufficient during the in situ testing. Current methods to verify the resistance to these failure modes rely on existing methods from the European Standards. These are for composite bridges with shear connectors and transverse reinforcement. Thus, there is no straightforward analytical method to assess the steel-concrete composite bridges without mechanical connectors adequately.

## 1.2 Research Objective and Questions

This study aims to provide an analytical model to determine the bearing capacity of historic steel-concrete composite bridges without mechanical connectors. The model will be based on the initial research in the form of experiments and FEM models previously created. The purpose of the analytical model is to avoid time-consuming FEM modelling and oversimplified analytical calculations. To help address the research objectives, the following research question has been stated.

**How can the bearing capacity of existing steel-concrete-composite bridges without mechanical connectors be determined using an analytical model?**

While the main question is meant to help address the problem, the sub-questions guide the process. The sub-questions are given as follows:

1. Which are the failure modes of the composite bridges?
2. How can the load distribution between composite girders be determined?

## 1.3 Methodology

The following part briefly describes the main steps taken in this research project. Figure 1.3 shows an overview of the workflow performed in this study. Initially, the literature is reviewed to get an overview of the relevant analytical models. The chosen compatibility-based strut and tie model (C-STM) is used to analytically determine the bearing capacity of the historic steel-concrete composite bridges without mechanical connectors. The model is configured from geometry, compatibility conditions and material parameters. The C-STM is verified using a comparative study, including the experimental results from the laboratory testing and a FEM model. The FEM model is modified to a generalized case, similar to the analytical model. Then, conclusions are made on the work done and the results achieved. Finally, recommendations are made based on the assessment of the analytical model and the comparative study.

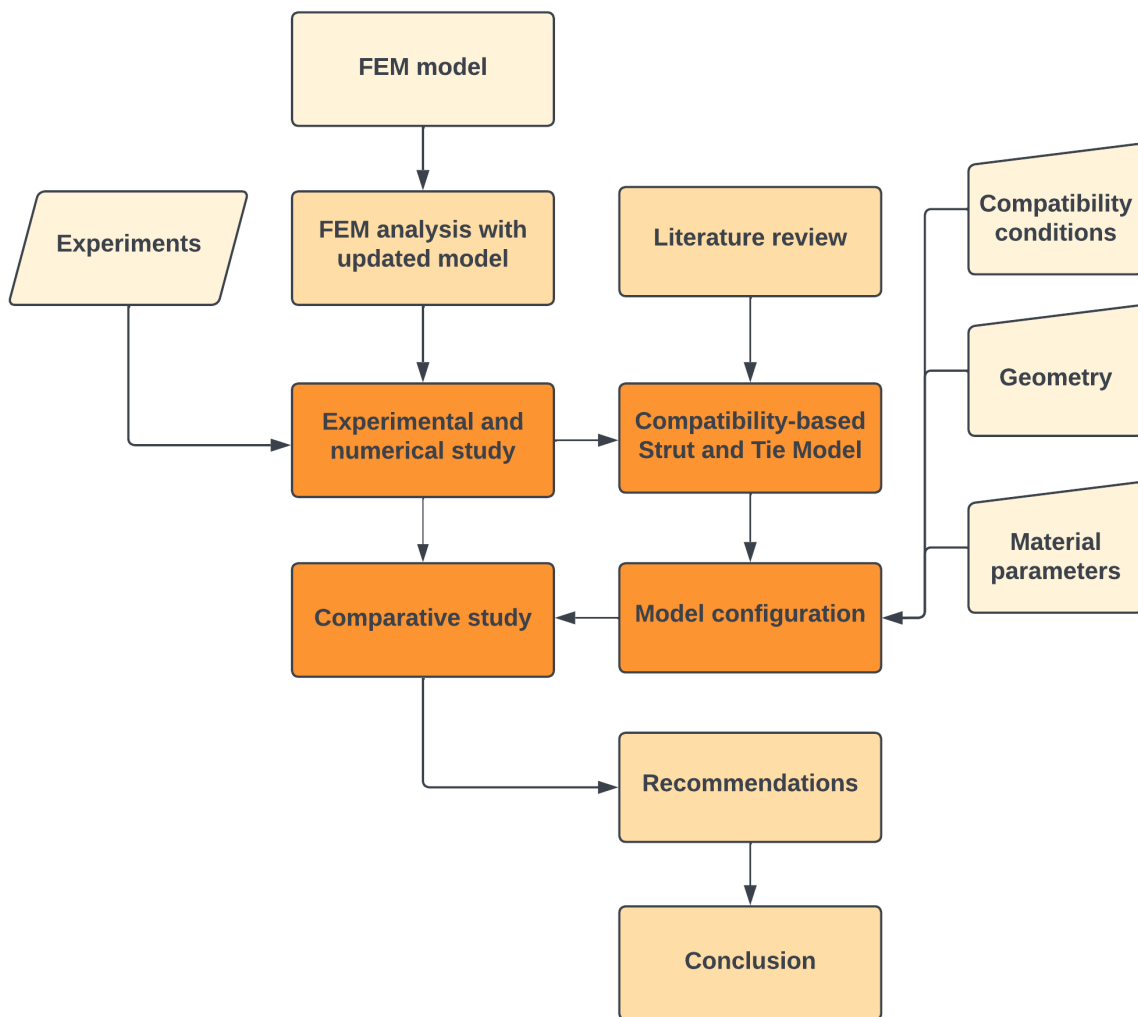


Figure 1.3: A workflow diagram of the work included in this research.

## 2 Literature Review

This literature review covers the methodologies previously and currently used to design steel-concrete composite bridges. This includes the load models and design methods for cross-section verification. Attention is put on cross-section verifications that, according to the European Standards, may apply to this case. In addition, covering what these current methods lack that must be accounted for to determine the bearing capacity of the steel-concrete composite bridges in Amsterdam. Finally, alternative methods for analysing steel-concrete composite bridges are considered; this includes the strut and tie method and two analytical methods to determine the transverse load distribution of concrete bridges.

### 2.1 Early 20th Century Composite Bridge Design

The following sections include an overview of previously used concrete and steel-concrete composite bridge design methods. This includes loads used during the early 20th century and the design approach.

#### 2.1.1 Load Models - VOSB1933

The VOSB1933 [4] was the first Dutch code for the design of steel bridges, including design traffic loads. Although this code was for steel bridges, concrete bridges are assumed to be designed for similar loads. The code proposes loading similar to the current code for traffic loads EN 1991-2:2005. However, the VOSB1933 does not differentiate between traffic lanes, as is the case for the current European Standard. The design loads are applied as concentrated and uniformly distributed loads. The code has four different load classes that depend on the use of the road bridge, e.g. if it allows heavy vehicles. The load classes are A/60 (60 ton), B/45 (45 ton), C/30 (30 ton) and D. Load class D is only for light traffic such as pedestrians and is therefore not considered in the following. The remaining loads are shown in Table 2.1. For the steel-concrete composite bridges in Amsterdam, it is assumed that they belonged to load class B/45, as they are located in Amsterdam. Hence, not an industrialised area, although heavy vehicles are expected.

Table 2.1: Traffic load classes from VOSB1933 [4].

Load Class	a [kN]	b [kN]	c [kN/m <sup>2</sup> ]
A/60	200	200	4
B/45	100	200	4
C/30	100	0	3.5

The loads from Table 2.1 must be applied according to Figure 2.1.

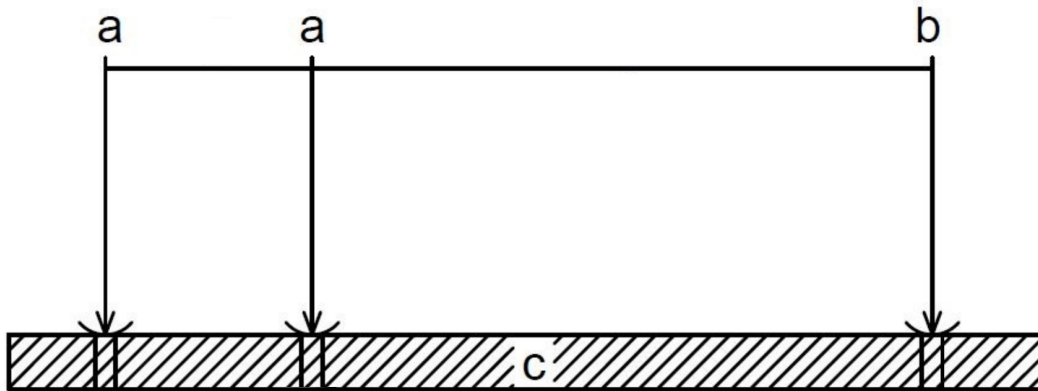


Figure 2.1: Loading scheme according to VOSB1933 [4].

In addition, more examples of traffic loads from different European countries are given, assuming that similar tendencies were present in the Netherlands. Assuming traffic loads used for design in Great Britain in the early 20th century were similar to those in the Netherlands in the same period, the bridges were designed to carry two fully loaded trams weighing about 12 tons per tram. In more industrialised areas, the bridges were designed to carry 15-ton machines pulling a 40-ton trolley[5]. Another design specification from the time is the one devised by the Austrian engineer Joseph Melan, who designed a bridge in Lausanne in 1901 using the design load of a 20-ton two-axle truck and a surface load of about  $4.4\text{ kN/m}^2$  [6]. The loads from the two previous cases are assumed to be similar to those applied in Amsterdam in the same period.

### 2.1.2 Design Methods

As previously, assuming that the design standards in the Netherlands followed the same trends as the rest of Europe, very little understanding of the application of shear connectors was present in the early 1900s. The standards for designing composite structures have similarly changed through time as the knowledge, and use of composite structures has increased. One of the most recognised design protocols from the beginning of the 1900s century is the Melan system invented by previously mentioned Austrian engineer Joseph Melan, who patented this method in 1890. Following this, the approach became standard practice in the united states, many European countries and Japan [6]. Using this method, the strain behaviour in composite beams could be determined, accounting for the steel and concrete[1]. However, following World War II, the use of composite structures with mechanical shear connectors in Germany rose, similar to the implementation of composite elements in road bridges around the beginning of the 1950s. This surge of composite structures in Germany led to the two first German design standards for composite structures being published, DIN 4239 *Composite beams in building construction* (1956) and DIN 1078 *Composite road bridges* (1955).

These first publications were simplified; they just considered elastic-static analysis for the composite elements and the shear connectors design. However, this simplified approach is expected since it can be assumed that there was generally limited research on composite structures with mechanical shear connectors before the publication of the first German standards [7]. The focus was primarily on steel elements with concrete encasements and no mechanical connectors.

Thus, composite elements without shear connectors designed before World War II do not seem uncommon, as with some of the historic bridges in Amsterdam.

## 2.2 Eurocode Recommendations

The following includes an overview of design recommendations from the European Standards that generally apply to the design of steel-concrete composite bridges. For the cross-section verifications, the focus is mainly put on EN 1994:2004. However, certain parts also consider EN 1993:2005 and EN 1992:2005 as the Standard refers to these for guidelines regarding the material they concern.

### 2.2.1 Load Models - Eurocode NEN-EN 1991-2:2005

According to NEN-EN 1991-2:2005 [8], four load models are currently applied for road bridges, from load model 1 to 4, where load model 1 is the most commonly used. For load model 1, the load decreases on increasing traffic lane numbers. For the first traffic lane, which is the heaviest loaded traffic lane, the applied load is 300 kN, which equates to 30.6 tons. Thus, for the first traffic lane, the applied load already exceeds most of the loads suggested in the cases of load models in the early 1900s, described in the previous section. The loads from load model 1 are given in Table 2.2, and the application of the loads are shown in Figure 2.2.

Table 2.2: Load model 1 from EN 1991-2:2005.[8]

Location	Tandem system TS Axle Loads $Q_k$ (kN)	UDL system $q_{ik}$ (kN/m <sup>2</sup> )
Lane number 1	300	9
Lane number 2	200	2,5
Lane number 3	100	2,5
Other lanes	0	2,5

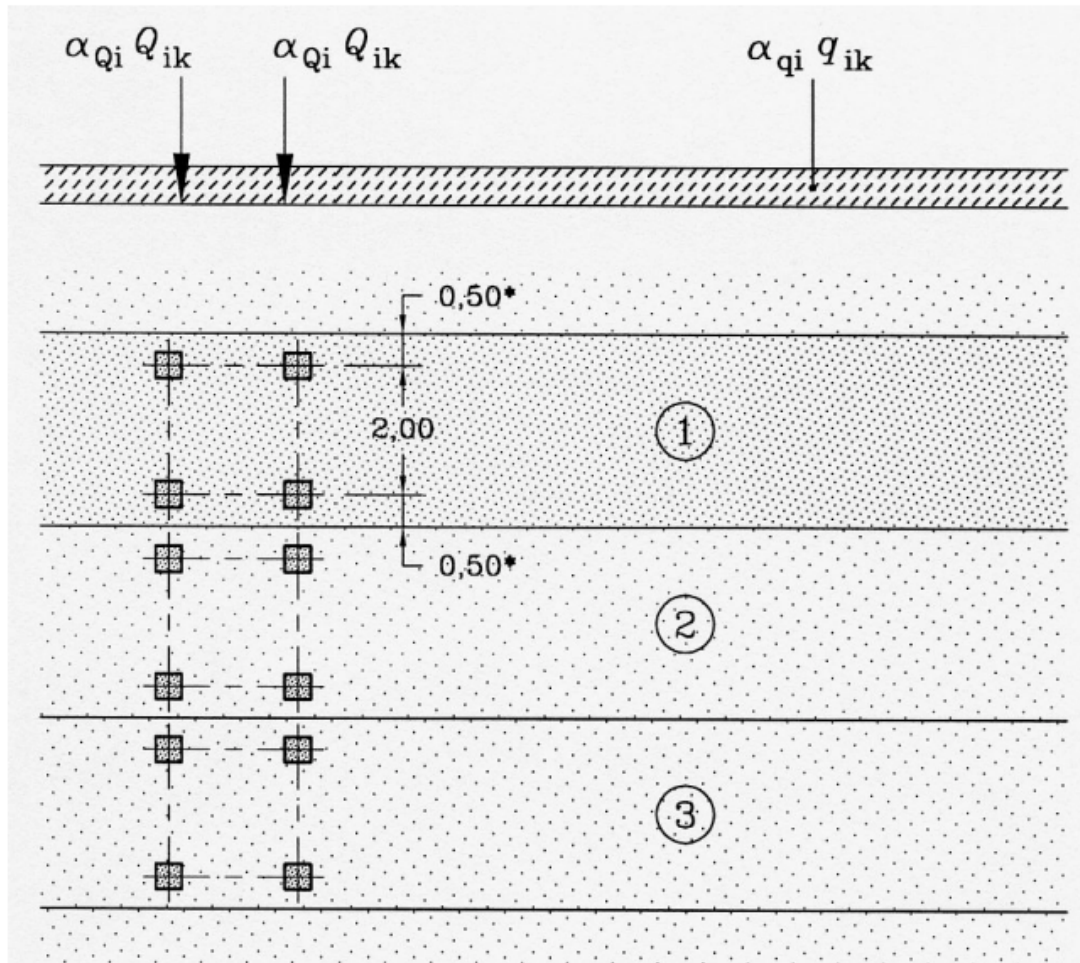


Figure 2.2: Application of load model 1.[8]

### 2.2.2 Design Verification - Eurocode NEN-EN 1994:2004

The following covers cross-section verification in agreement with the European Standards for composite bridges. For composite bridges different from those described in EN 1994-1-1:2004 [2] and EN 1994-2:2005 [3], as far as practicable, the design should rely on existing design rules and methods, which experiments must also support. Hence, for steel-concrete composite bridge slabs without mechanical connectors, the design approach should strive to follow that of steel-concrete composite bridges with mechanical connectors. The most similar design situation would be the design of a composite slab with a partial shear connection, assuming that the natural steel-concrete bond gives a lower shear connection than a full shear connection.

For composite beams with a partial encasement, EN 1994-1-1:2004 [2] describes two cross-section verifications that must be made: *bending and vertical shear resistance*. These verifications are briefly described in the following. Moreover, as the historic steel-concrete composite bridges do not ensure shear connection following the European Standard, it must also be verified that there is sufficient longitudinal shear resistance. Lateral torsional buckling is not considered as the European Standard describes that a steel flange that is attached to a concrete slab by shear connection according to the standard can be assumed to be laterally stable [2]. For the case of steel-concrete composite bridges without mechanical connectors, as this research

concerns, the steel girders are partially encased. Thus, it is assumed that lateral stability is provided.

## Bending Resistance

Conforming to EN1994-1-1:2004 [2], plastic theory may be applied to determine the bending resistance. However, reinforcement in compression can be neglected, and concrete is assumed to be cracked. Hence it has no tension strength. Figure 2.3 shows an example of the plastic stress distribution to determine the bending moment resistance. Where the concrete compression stress block is reduced by a factor of 0.85 according to the European Standard [2].

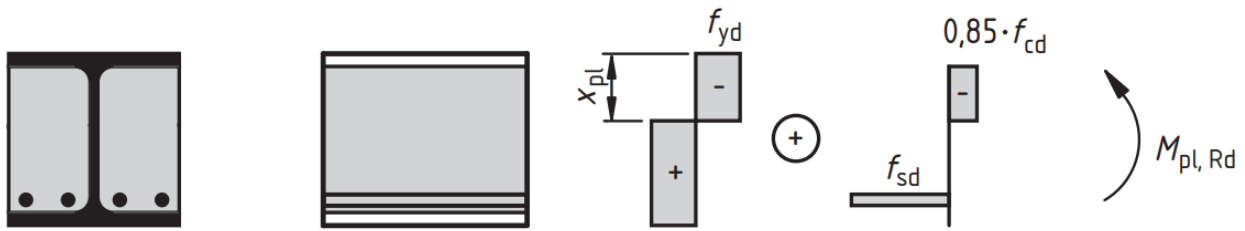


Figure 2.3: Example of plastic stress distribution according to NEN-EN 1994-1-1:2004 [2].

Additionally, the degree of shear connection must be considered. This is defined as the longitudinal shear resistance denoted as  $V_{x,Rd}$ , which must be equal or larger to the compression force in the concrete to ensure full shear connection. If there is a partial shear connection, the stress distribution for the plastic bending resistance must be considered, as shown in Figure 2.4. Here the concrete compression stress block is reduced due to the degree of shear connection,  $\eta$ . The degree of shear connection is defined from Eq.2.1.

$$\eta = \frac{N_c}{N_{c,f}} \quad (2.1)$$

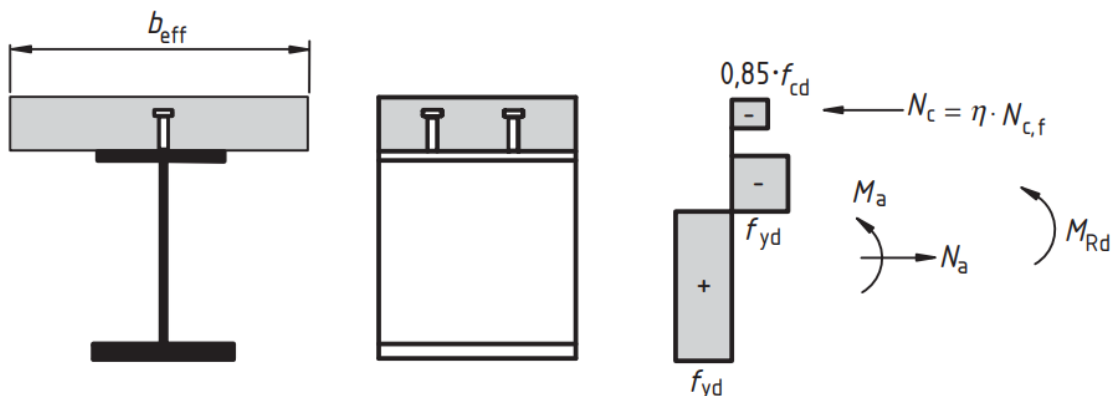


Figure 2.4: Plastic stress distribution for partial shear connection from NEN-EN 1994-1-1:2004[2].

Decreasing the shear connection will reduce the plastic bending resistance. Simplifying this, it can be interpreted as a linear relationship between the degree of shear connection and the

moment resistance, as the dotted line in Figure 2.5 shows. However, the ideal behaviour is nonlinear, as the figure also illustrates.

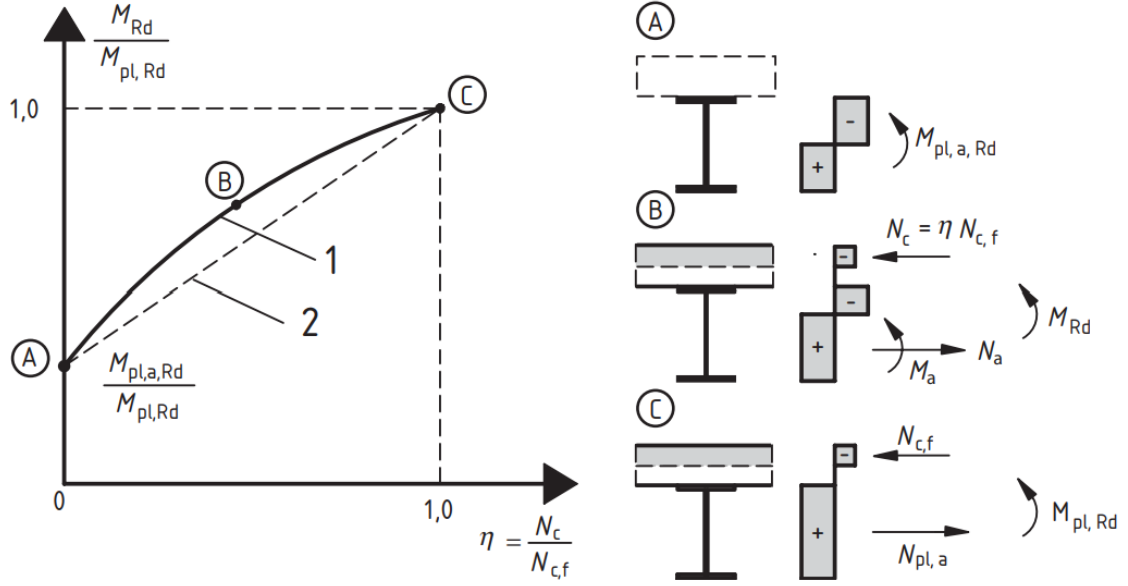


Figure 2.5: Relation between plastic moment resistance and degree of shear connection. Simplified theory vs plastic theory from NEN-EN 1994-1-1:2004[2].

To verify the resistance to biaxial bending, which is relevant for this case, EN 1994-2:2005 refers to the methods described in EN 1993-1-1:2005 [9].

### 2.2.3 Bending Resistance - Eurocode NEN-EN 1993-1-1:2005

EN 1994-2:2005 states that composite beams subject to biaxial bending or combined bending and torsion account should be taken of EN 1993-1-1:2005, 6.2.1(5) [3]. The Standard refers to the yield criterion in Eq. 2.2 from EN 1993-1-1:2005 [9]. The yield criterion can be used for elastic verification of cross-sections subject to biaxial bending.

$$\left(\frac{\sigma_{x,Ed}}{f_y/\gamma_{M0}}\right)^2 + \left(\frac{\sigma_{z,Ed}}{f_y/\gamma_{M0}}\right)^2 - \left(\frac{\sigma_{x,Ed}}{f_y/\gamma_{M0}}\right)\left(\frac{\sigma_{z,Ed}}{f_y/\gamma_{M0}}\right) + 3\left(\frac{\tau_{Ed}}{f_y/\gamma_{M0}}\right)^2 \leq 1,0 \quad (2.2)$$

Another method is a linear summarization of the utilization ratios for each stress component from Eq. 2.3.

$$\frac{N_{Ed}}{N_{Rd}} + \frac{M_{y,Ed}}{M_{y,Rd}} + \frac{M_{z,Ed}}{M_{z,Rd}} \leq 1,0 \quad (2.3)$$

However, a linear summarization of the utilization ratios is relatively conservative in the case of no normal force. Therefore, the expression in Eq.2.3 may be expressed as Eq.2.4

$$\sqrt{\left(\frac{M_{y,Ed}}{M_{y,Rd}}\right)^2 + \left(\frac{M_{z,Ed}}{M_{z,Rd}}\right)^2} \leq 1,0 \quad (2.4)$$

## 2.2.4 Vertical Shear Resistance - Eurocode NEN-EN 1993-1-1:2005

Conforming to EN 1994-1-1:2004, [2], the design vertical shear resistance of the structural steel must be determined by EN1993-1-1:2005 [9]. Generally, the concrete encasement is neglected. However, for composite slabs, EN 1994-1-1:2004 states that the vertical shear resistance of the concrete encasement may be accounted for following the guidelines of EN1992-1-1:2004, 6.2.2. Several studies have experimentally proved that the vertical shear strength of a partially encased girder has improved shear resistance compared to the strength of a steel girder alone [10] [11]. Therefore, it would be a conservative assumption neglecting the encasement of the steel-concrete composite bridges in Amsterdam, where the concrete volume is a great part of the total volume. Thus, the vertical shear resistance of the composite bridges is covered in two stages, first for the steel part, followed by the concrete encasement from EN 1992-1-1:2004. Finally, the feasibility of summarizing the two shear resistance components into a total shear resistance is concluded based on the literature examined. When only the steel is considered, the vertical shear resistance is determined from Eq.2.5 [9].

$$V_{pl,Rd} = \frac{A_v f_{yd}}{\sqrt{3}} \quad (2.5)$$

For a hot rolled section, the area subject to the shear force is determined from Eq.2.6.

$$A_v = A - 2bt_f + (t_w + 2r)t_f \quad (2.6)$$

If  $V_{Ed} \leq 0.5V_{pl,Rd}$  is valid, there is no need to reduce the bending moment resistance. However, if  $V_{Ed} > 0.5V_{pl,Rd}$ , a reduction is needed by reducing the web yield strength to  $(1 - \rho)f_{yd}$ . The reduction parameter,  $\rho$ , is obtained from Eq. 2.7.

$$\rho = \left( \frac{2V_{Ed}}{V_{pl,Rd}} - 1 \right)^2 \quad (2.7)$$

However, the requirement in Eq. 2.7 may be disregarded as the shear resistance is assumed to be increased significantly by accounting for the encasement.

## 2.2.5 Vertical Shear Resistance - Eurocode NEN-EN 1992-1-1:2004

This section merely focuses on the shear resistance of concrete, as a significant part of the cross-section area of the steel-concrete composite bridges consists of concrete. Hence, it would be very conservative to neglect this part. The vertical shear resistance of structural concrete members can be determined according to EN 1992-1-1:2004 [12]. For concrete structural members not requiring design shear reinforcement, the shear resistance of the concrete is determined from Eq. 2.8.

$$V_{Rd,c} = \left[ C_{Rd,c} k (100\rho_l f_{ck}^{1/3} + k_1 \sigma_{cp}) \right] b_w d \quad (2.8)$$

With a minimum given from Eq. 2.9.

$$V_{Rd,c} = (\nu_{min} + k_1 \sigma_{cp}) b_w d \quad (2.9)$$

Where:

$$k = 1 + \sqrt{\frac{200}{d}} \leq 2, 0.$$

$$\rho_l = \frac{A_{sl}}{b_w d} \leq 0, 02 .$$

$k_1$ : Country recommended value found in the National Annex.

$$\sigma_{cp} = N_{Ed}/A_c < 0, 2f_{cd}.$$

The minimum value in Eq. 2.9 can be determined from Eq. 2.10.

$$\nu_{min} = 0, 035k^{3/2} \cdot f_{ck}^{1/2} \quad (2.10)$$

However, Eq.2.9 does not apply to the case of the steel-concrete composite bridges in Amsterdam, as these do not have any reinforcement. Furthermore, none of these equations previously presented account for the interaction and the case of partial shear connection. Therefore, using Eq. 2.8 is deemed impossible.

### Vertical Shear Resistance - Composite Slabs

In a study by Vasdravellis and Uy [13], the shear strength and moment-shear interaction of steel-concrete composite beams were investigated. The motivation for the research was that steel-concrete composite beams are designed neglecting the concrete slab. Therefore, Vasdravellis and Uy proposed an analytical design procedure to account for the shear resistance of the concrete in the composite beam. The analytical model was based on the results of testing. Figure 2.6 shows the test setup used for the experimental program, 14 specimens were tested, and the clear span varied from 0.8 m to 5.5 m. The degree of shear interaction also varied, so it was possible to determine the vertical shear resistance accounting for this.

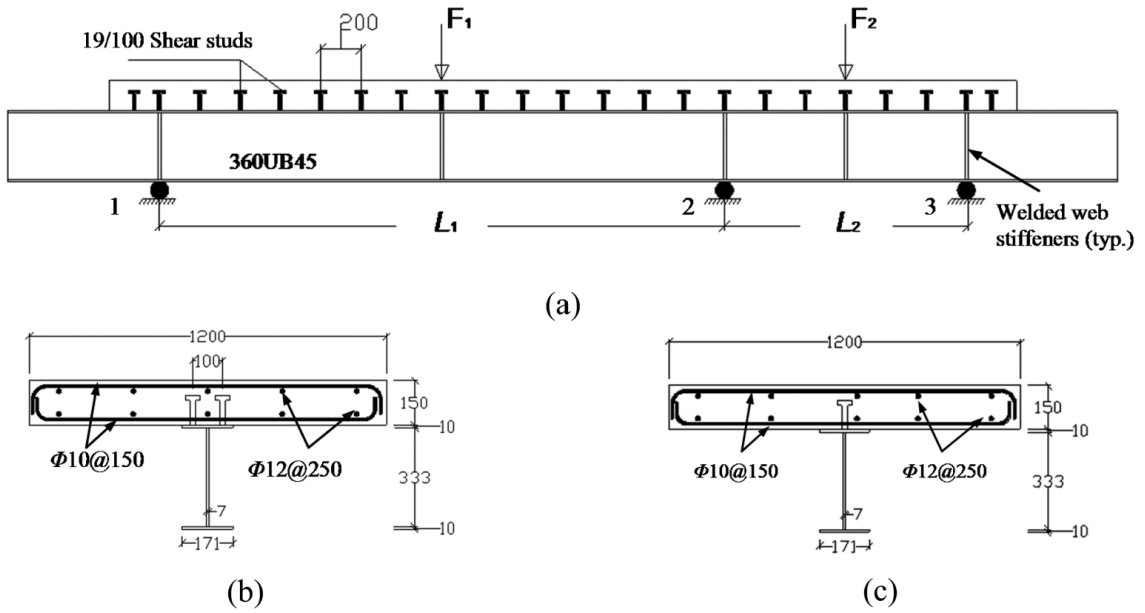


Figure 2.6: Test setup and details of the cross sections from the study by Vasedravellis and Uy [13].

The vertical shear resistance assuming full shear connection and accounting for the individual

contribution from steel and concrete is obtained from Eq.2.11.

$$V_{comp} = V_{pl,Rd} + V_{slab} \quad (2.11)$$

The shear resistance of the steel girder is obtained from Eq.2.5, which was previously described. The contribution from the concrete slab is determined from Eq.2.12.

$$V_{slab} = \varphi_s f(\lambda_{sd}) (b_f D_{slab})^{0.7} \sqrt{f_c} \quad (2.12)$$

$f(\lambda_{sd})$ , which is a function of the slab slenderness is obtained from Eq.2.13

$$f(\lambda_{sd}) = 110\lambda_{sd} + 13 \quad (2.13)$$

For partial shear connection, the vertical shear resistance is determined through a number of steps. First, the slenderness ratio,  $\lambda_{sd}$  and the vertical shear resistance of a composite beam with the full shear connection are determined. Following Eq.2.14 is used to obtain the shear resistance with no shear connection,  $V_{comp,0}$ .

$$V_{comp} = V_{comp,0}(0.76\lambda_{sd} + 0.92) \quad (2.14)$$

Finally, the vertical shear resistance with the degree of shear connection,  $\eta$ , can be obtained from linear interpolation between the full and no shear connection values.

It is assumed that the analytical equations proposed by Vasdravellis and Uy give a more accurate estimation of the vertical shear resistance. Moreover, these make it possible to account for the degree of shear connection, which was impossible using the European Standards' recommendations.

## 2.3 Longitudinal Shear Resistance

The following covers the relevant literature regarding the longitudinal shear resistance of concrete-encased steel girders. The steel-concrete bond strength of concrete-encased steel profiles without mechanical connectors is complex to determine. This depends on several factors: time, geometry, concrete cover, and surface treatment, are some of them.

FIB Model Code 2010 [14] generally provides recommendations and guidance for the Eurocode. According to the Model Code, specific recommended values exist for a steel-to-concrete bond. The Model Code distinguishes between bond types, such as chemical adhesion and active friction. The typical bond strength for chemical adhesion is around 0.1 MPa, whereas the Model Code does not include any recommendations for physical adhesion. Moreover, the recommended values for active friction are between 0 and 0.6. Nevertheless, it can be challenging to determine the exact value. Despite the Model Code providing guidelines for the European Standards, the Standard recommends neglecting the effect of natural bonds for steel-concrete composite beams [2]. Several studies have investigated the steel-concrete bond.

A recent study by Chrzanowski *et al.* [15] investigated the natural steel-concrete bond to determine its contribution to the longitudinal shear resistance when shear connectors also are

present. This was done as the contribution of shear connectors is commonly determined by applying grease on the steel-concrete interface, so only the connectors contribute to shear connection. However, tests have shown that the natural bond still provides bond strength regardless of the grease applied. Thus, the isolated contribution from the shear connection can be determined by determining the natural steel-concrete bond. This study used two test types to evaluate the natural steel-concrete bond: small-scale cube push-out tests (SSCPOT) and large-scale column-type push-out tests (CoPOT). The SSCPOTs were performed on steel profiles with three different kinds of surface treatment to see how the bond strength varies. THE CoPOTs were performed on HEB120 profiles, similar to DIN profiles, as the steel girders in the historic Amsterdam bridges, although the ones from the tests had smaller dimensions.

As a result of the research Chrzanowski *et al.* stated that ” *The contribution of the steel-concrete bond is significant in the force transfer mechanism of shear connectors in push-out tests with embedded steel profiles (even for greased surfaces) and cannot be disregarded*” [15, p. 50]. Hence, according to this study, the effect of the steel-concrete bond should be accounted for, regardless of the surface treatment. The experimental results by Chrzanowski *et al.* are given in table 2.3. The table also includes the results of several other studies investigating the steel-concrete bond on HEB profiles.

Table 2.3: Data from literature review on steel-concrete bond strength from push-out tests with HEB-profiles.

No.	Test Specimen	Surface treatment	Concrete cover	Encased length	Bond strength
Chrzanowski <i>et al.</i> [15]					
1.	2xHEB120	Anti adhesive relase agent	440 mm and 110 mm. Stir-rups Ø12/117	350 mm	0.87 MPa
Roik [16]					
2.	9xHEB200 encased steel profiles	Cleaned with paint thin-ners.	65 mm	440 mm	0.7-1.40 MPa
Wium [17]					
3.	29xHEB200	Sandblasted Sa2.5	50 mm and 100 mm. Stir-rups Ø8/100	440 mm	0.54-1.20 MPa
SmartCoCo [18]					
4.	One HEB120 encased steel profile	Painted sur-face	440 mm and 110 mm. Stir-rups Ø12/150	900 mm	1.34 MPa
5.	One HEB120 encased steel profile	Rust surface	440 mm and 110 mm. Stir-rups Ø12/150	900 mm	2.91 MPa

Table 2.3 shows that even for untreated and cleaned surfaces, there is a significant steel-concrete bond. Therefore, steel-concrete bond strength can be assumed based on the values from Table 2.3. However, as previously mentioned, these should be chosen conservatively as they vary depending on multiple parameters. From Table 2.3, a conservative estimate on the steel-concrete

bond strength of the steel-concrete composite bridges in Amsterdam could be 0.54 MPa, taking the lowest value in the range of the experiments.

One of the factors that the bond strength is greatly sensitive to is the concrete cover. The 1970 AISC Specification [19] suggests that the natural bond between steel and concrete can be accounted for when a concrete cover of 38 mm at the top and 51 mm at the sides and bottom is provided. Thus, the effective concrete contact area may be determined using this assumption. Furthermore, time effects can reduce the bond strength due to creep and shrinkage. In the study by Wium [17], two identical specimens were investigated roughly six months apart with a 15% loss of bond strength. This was not investigated further, yet a conservative assumption of the bond strength from Table 2.3 is still considered safe.

## Mohr-Coulomb Mechanism

The longitudinal shear resistance increases when two surfaces are subject to a normal compression stress. This effect is known as the Mohr-Coulomb mechanism. The Mohr-Coulomb shear resistance can be determined from Eq. 2.15.

$$\tau_{Rd} = c + \sigma \cdot \tan \varphi = c + \sigma \mu \quad (2.15)$$

Figure 2.7 shows how the shear resistance linearly increases with increasing normal stress.

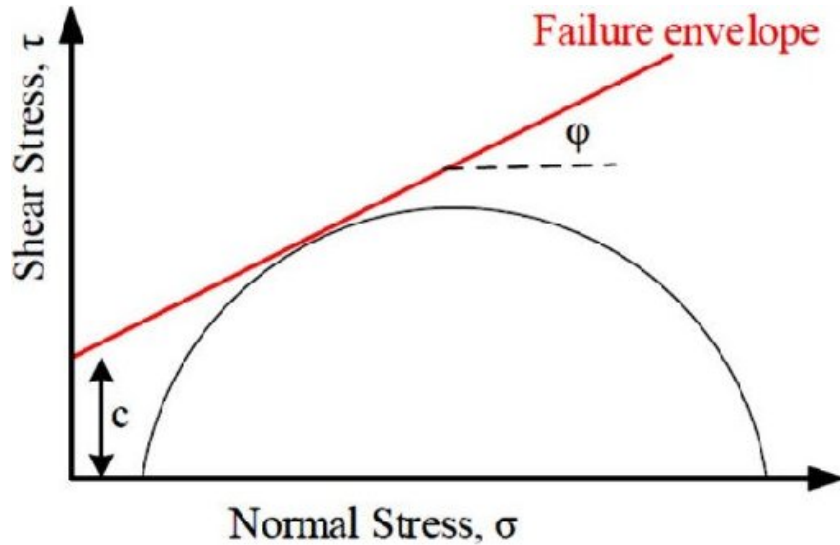


Figure 2.7: Development of Mohr-Coulomb failure envelope [20].

The friction coefficient depends on the surface roughness. Thus, for a frictionless surface, this is 0, whereas, for concrete-to-concrete surfaces, this value could typically be around 0.6 [14].

A study performed by Rabbat *et al.* [21] strived to determine the static friction coefficient of steel on concrete or grout. The test parameters included in the study were wet/dry interface and level of normal compressive stress. In total, 15 tests were conducted and resulted in static friction coefficients varying between 0.57 and 0.70. For a dry interface, Rabbat *et al.* recommends using a friction coefficient at 0.57, whereas, for a wet interface, the recommended value is 0.65.

In another study by Baltay and Gjelsvik [22], the coefficient of friction for steel on concrete was investigated. The research showed that the coefficient of friction for a mild steel surface varied depending on the nominal stress. For values between 1 and 470 MPa the coefficient of friction linearly increased from 0.3 to 0.57. Furthermore, for a machined surface, the coefficient of friction was on average 0.47 regardless of the nominal normal stress. Table 2.4 summarizes the coefficient of friction from a few studies. However, the values vary greatly depending on the surface roughness and the material.

Table 2.4: Coefficient of friction according to different references.

Reference	Coefficient of friction
FIB Model Code 2010 [14]	0.00-0.60
Rabbat and Russel [21]	0.57-0.65
Baltay and Gjelsvik [22]	0.30-0.57

From Table 2.4, it can be concluded that the coefficient of friction should be accounted for, as experiments have proved that the coefficient of friction should be at least 0.3. However, the value is also related to a lot of uncertainty, as the coefficient of friction increases at increasing normal stresses due to the concrete crushing that forms small grains. At these higher values, the steel-concrete interface is assumed to fail due to the concrete crushing. Thus, a higher coefficient of friction can not coexist with nonzero cohesion values. Therefore, it is assumed to be safe, accounting for cohesion and a lower coefficient of friction value.

## Longitudinal Shear Strees

The study by Chrzanowski *et al.* [15], evaluates the shear stresses from the effective steel-concrete contact area that is determined from Eq. 2.16.

$$A_{c,eff} = L_{emb,s} \cdot u_{s,eff} \quad (2.16)$$

The shear stresses on the surface are determined from Eq. 2.17.

$$\tau_{surf} = \frac{F}{A_{c,eff}} \quad (2.17)$$

The previous equations are derived from push-out tests, where the loading is in the same direction as the effective shear stresses. Hence, in this case, the shear stress must be evaluated differently, as the loads on the Amsterdam bridges are perpendicular to the surface. The shear stress in the case of a load perpendicular to the surface can be obtained from Eq. 2.18 [19].

$$\tau_{surf} = \frac{VS}{IP_{cs}} \quad (2.18)$$

## 2.4 Strut and Tie Method

The Strut and Tie Method (STM) is a force equilibrium method used to perform detailed analysis and design of concrete structures. The method is used to rationally design concrete structures using struts and ties connected at nodal points. The STM originates from the truss analogy introduced by Ritter (1889) and Morsch (1902). After introducing the truss analogy, it was further developed and adapted. Following the initial introduction of the strut-and-tie models, more research was done to implement this method to design various concrete structures. In the early 1990s, Schlaich and Schäfer [23] proposed using strut and tie models for designing concrete structures. Previously, this was limited to only deep beams and corbels. This proposal by Schlaich and Schäfer suggested using STM for both reinforced and prestressed concrete structures. The design of these structures using STM became possible with the introduction of disturbed regions (D regions) and Bernoulli regions (B regions). The D regions exist at discontinuities, where a nonlinear stress pattern is present, whereas the B regions, opposite of D regions, are where the stress patterns are linear. Figure 2.8 shows two examples of the B and D regions [24].

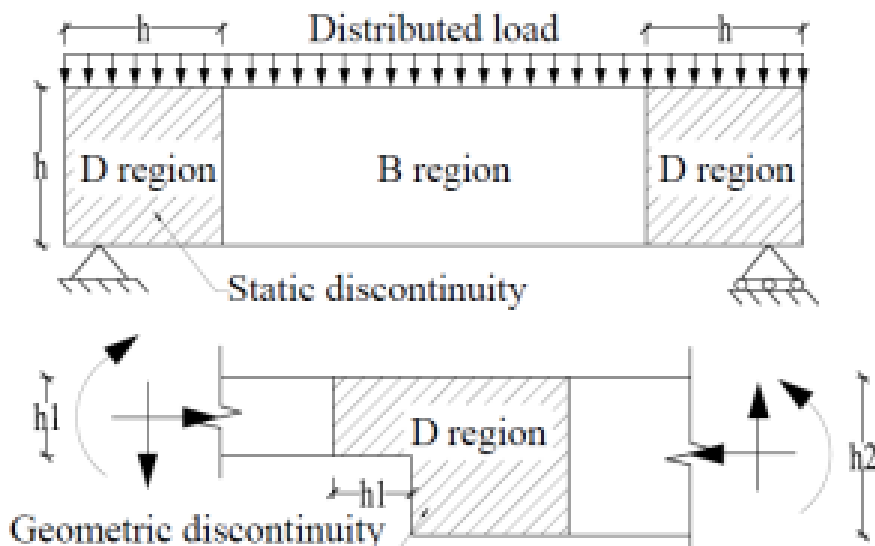


Figure 2.8: Examples of disturbed regions and Bernoulli regions [24].

Nowadays, strut and tie models are described in various literature, including several design standards, both European and American [12][25][26]. The method mainly applies to the disturbed region of concrete elements, simplifying stress patterns into compression struts and tensile ties connected by node regions. For instance, the STM can determine the transverse prestressing reinforcement's size and position [27]. One significant advantage of using the STM is that it allows engineers to customise the model as long as it meets equilibrium requirements. Ensuring that the yield and equilibrium criteria are satisfied makes it possible to accurately calculate the stresses present in the model [28]. Figure 2.9 shows an example of different configurations of strut and tie models applied to the same structure.

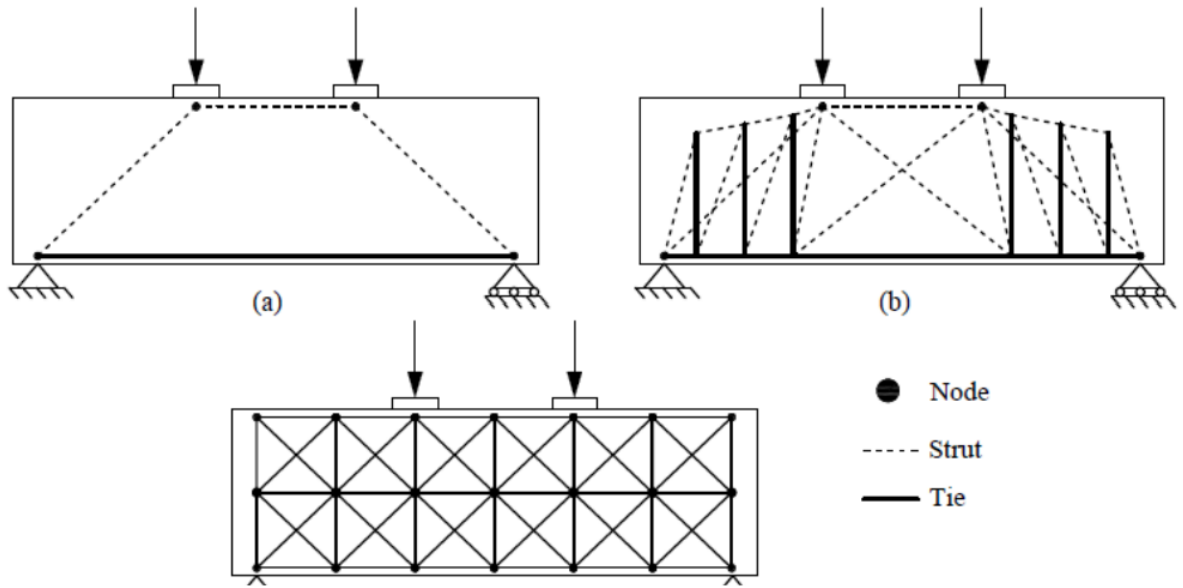


Figure 2.9: Example of different strut and tie models [24].

STM is used for a wide range of design problems, and the complexity of the technique varies from simple hand calculations to detailed numerical analysis. The following predominantly focuses on the STM for analytical calculations, as this research investigates analytical methods.

### 2.4.1 STM for Analysis of Reinforcement-free Decks

A study by Ug Bae *et al.* [29] describes the application of an STM to determine the punching shear resistance of reinforcement-free decks. The purpose of the study, was similar to this research, to determine an analytical method that can replace time-demanding FEM calculations. The reinforcement-free decks consist of I-girders and a deck on top; both elements are fibre-reinforced concrete. Moreover, the I-girders are connected by lateral steel ties, as illustrated in Figure 2.10. The STM is applicable for short-span bridge decks on girders.

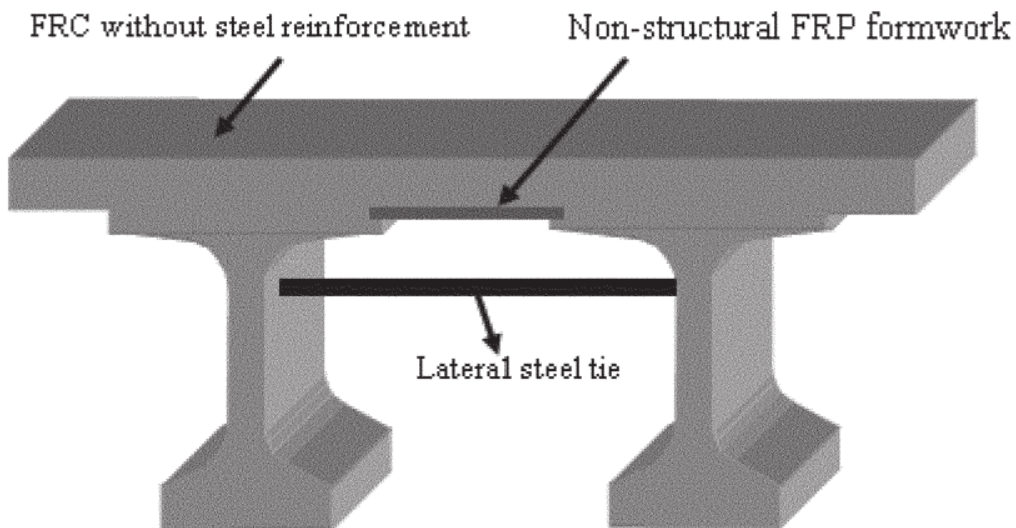


Figure 2.10: Reinforcement free deck.[29]

The STM is shown in Figure 2.11, also illustrating the compression stress trajectory, which explains the position of the struts.

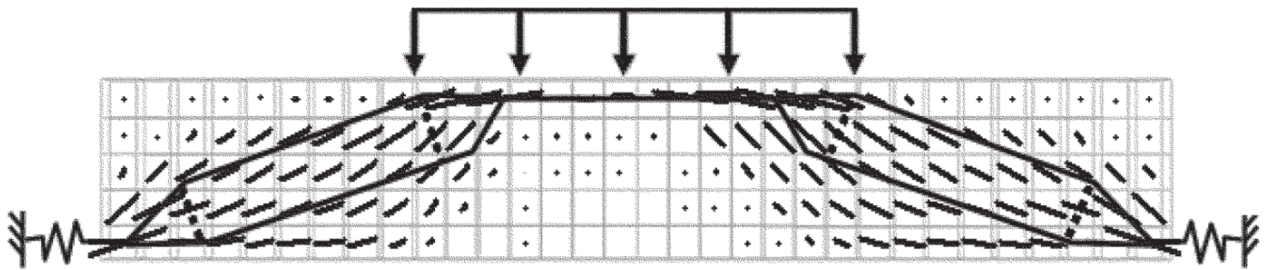


Figure 2.11: STM and compression stress trajectory. [29]

Figure 2.12 shows a top view of the STM and the spring components included in the STM. The proposed model applies lateral springs to account for the lateral stiffness of adjoining girders, flexural stiffness about the minor axis and torsional stiffness. However, parts of the modelling approach depended on FEM analysis to determine displacement, which may be challenging to apply to the scope of this thesis. Furthermore, this analysis neglects the vertical equilibrium. Figure 2.12 shows a plan view of the bridge and the components of the horizontal stiffness. Also illustrating how the exterior girder is subject to failure due to its lower stiffness compared to that combined with the interior girders.

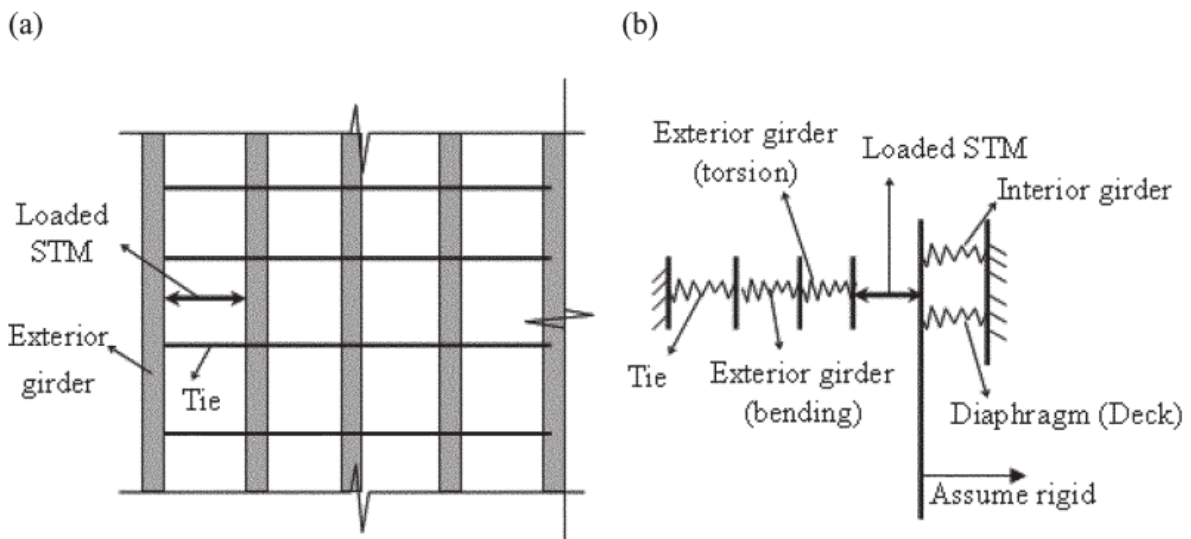


Figure 2.12: a) Plan view of deck and girders. b) Components of lateral stiffness. [29]

This research focuses on failure modes other than punching shear, regardless of the mechanical behaviour of the STM that may be adapted for this research. The historic steel-concrete composite bridges in Amsterdam are similar to those used for this STM, as the geometry is similar, despite the lateral steel ties. Moreover, the Amsterdam bridges have different materials. In addition, the Amsterdam bridges are also reinforcement free, assuming that the relatively low amount of reinforcement can be neglected.

## 2.4.2 Compatibility-based Strut and Tie Method

In the study described in the previous section, the stiffness of the steel ties was accounted for by considering these as spring elements. Another method to directly account for the stiffness of the steel ties and the compression struts is to include compatibility into the model. For instance, this can be done by considering the strut and ties as bars with only axial deformation.

In a study by Park and Kuchma [30], a strain compatibility-based strut and tie method is proposed to determine the bearing capacity of 214 deep beams. This method is proposed to challenge the recommendations from the provisions on STM design from ACI318-5 and the Canadian Code. The strain compatibility was included as an attempt to make a more accurate strength prediction method with the STM. The research proves that the method consistently provides accurate results. Furthermore, the method provided valuable insight into the behaviour of deep beams, as it provided input on the strain behaviour of the different struts and ties. The C-STM is shown in Figure 2.13. As the method considers strain compatibility, a stiffness formulation is required, for this, a secant stiffness formulation is used.

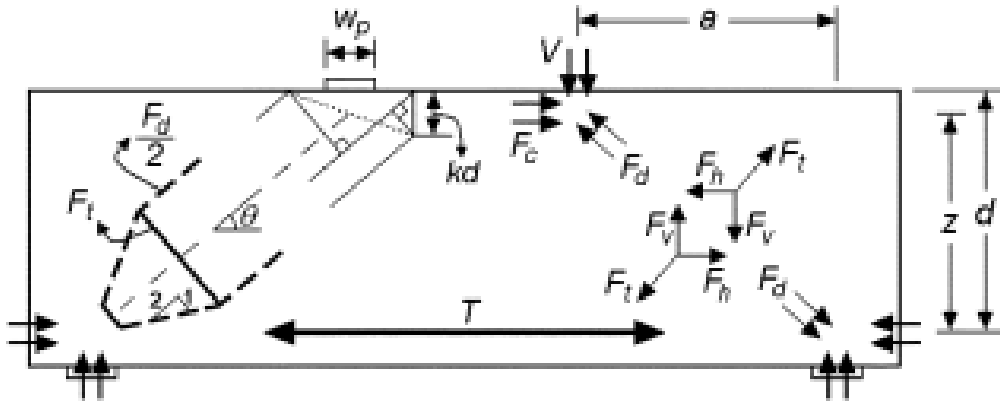


Figure 2.13: C-STM for a deep beam. [30]

In addition, the constitutive laws considered also account for cracked reinforced concrete. This may be difficult to apply for the scope of this research, as the steel-concrete composite bridges in Amsterdam are considered reinforcement-free due to the small amount of reinforcement. Although the computation of the compatibility-based strut and tie method (C-STM) is more sophisticated than for a typical STM, this can, as in the study by Park and Kuchma, give more accurate results and a better insight into the behaviour of the analysed structure.

## 2.4.3 Design Requirements - Eurocode NEN-EN 1992-1-1:2004

The strength of the struts, ties and nodal zones must be determined to ensure sufficient capacity. As the method is applied primarily for ULS design, the stresses in the struts and ties are generally the maximum allowable. EN 1992-1-1:2004 [12] describes how to determine the capacity of the elements in the strut and tie model. However, as tensile ties generally refer to reinforcement and the Amsterdam steel-concrete composite bridges have very little reinforcement, the capacity requirements for tensile ties are neglected. Instead, the capacity of the tensile ties is assumed to equate to the tensile strength of concrete. For compressive struts subject to either transverse compressive stress or no transverse stress, the capacity of the strut is defined as the concrete compression strength according to Eq. 2.19.

$$\sigma_{Rd,max} = f_{cd} \quad (2.19)$$

Otherwise, if the struts are subject to transverse tension, the capacity must be reduced as shown from Eq. 2.20.

$$\sigma_{Rd,max} = 0,6\nu'f_{cd} \quad (2.20)$$

Where:

$$\nu' = 1 - \frac{f_{ck}}{250} \quad (2.21)$$

The capacity for compression nodes without ties is determined from Eq. 2.22.

$$\sigma_{Rd,max} = k_1\nu'f_{cd} \quad (2.22)$$

Where the recommended value for  $k_1$  is 1.0. The capacity for compression-tension nodes without ties is determined from Eq. 2.23.

$$\sigma_{Rd,max} = k_2\nu'f_{cd} \quad (2.23)$$

The recommended value for  $k_2$  is 0.85.

## 2.5 Transverse Load Distribution Models

Namely, two methods to analyse bridges' transverse load distribution (TLD) have been investigated. These methods are **Guyon Massonnet Method** and **Transfer Matrix Method (TMM)**. The TLD methods are different from each other in complexity and use. The Guyon Massonnet Method is widely known within bridge engineering for designing concrete bridges, whereas the TMM has recently been developed to analyse the TLD of articulated bridges. The models mentioned in the following have been deemed feasible, assuming that, with some modifications, these models can be used to determine the bearing capacity of steel-concrete composite bridges. It must be regarded that the methods should be feasible for the analytical design of steel-concrete composite bridges. Hence, high complexity is not necessarily the aim of this study.

### 2.5.1 Guyon Massonnet Method

A commonly used and widely known method to determine the TLD of concrete bridges is the Guyon Massonnet Method, also called Mourice - Little Theory [31]. This method, depending on the stiffness of the bridge, gives a nonlinear load distribution that is assumed to be more accurate than linear load distribution methods such as Courbon's Method. The Guyon Massonnet Method accounts for the torsional and flexural stiffness of the bridge girders, respectively, using the parameters  $\alpha$  and  $\theta$ , given from Eq. 2.24 and 2.25.

$$\alpha = \frac{\gamma_x + \gamma_y}{2\sqrt{\rho_x + \rho_y}} \quad (2.24)$$

$$\theta = \frac{b}{l} \sqrt[4]{\frac{\rho_x}{\rho_y}} \quad (2.25)$$

The Guyon Massonnet Method uses a reference system where each point can represent a bridge girder. For the case of this example, the reference system is divided into 8 segments, as shown in Figure 2.14.

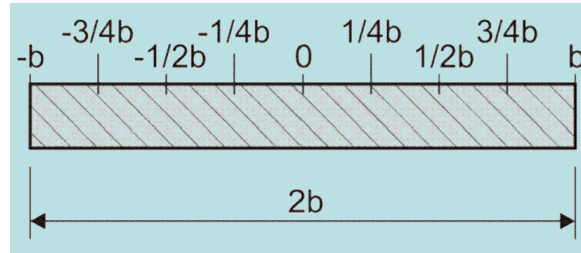


Figure 2.14: Guyon Massonnet Method reference system [31].

The influence line of the TLD is determined using distribution coefficients that depend on the stiffness coefficients. The distribution coefficients are denoted as  $K_0$  and  $K_1$ , where the subscript indicates the torsional stiffness. As the torsional stiffness often is somewhere between 0 and 1, the distribution coefficients are determined assuming that the torsional stiffness either is 0, 1 or the intermediate value of the distribution coefficients are obtained from Eq. 2.26.

$$K_\alpha = K_0 + (K_1 + K_0) \times \sqrt{\alpha} \quad (2.26)$$

The distribution coefficients are determined for each point of the reference system using design aid graphs like the one shown in Figure 2.15. These graphs depend on the reference system location; however, interpolation is used to obtain the distribution coefficients for a reference system with reference points different than the ones in Figure 2.14.

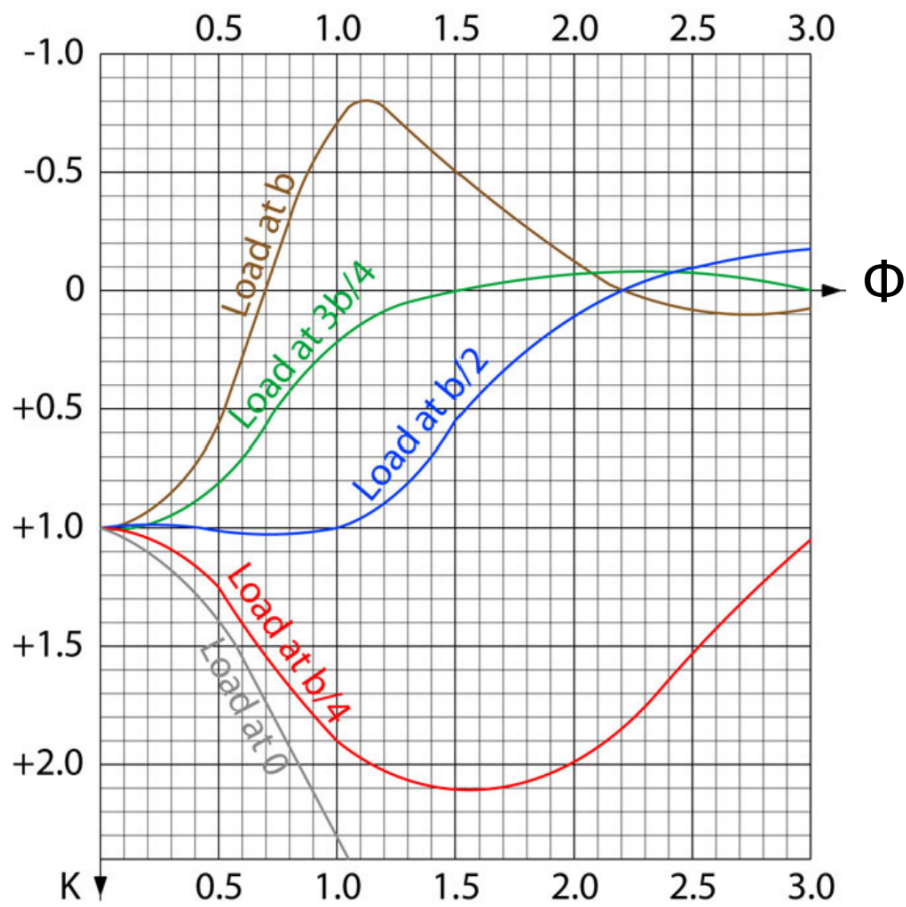


Figure 2.15: Distribution coefficient  $K_0$  at point 0 [31].

Finally, an influence line can be constructed using the design aid graphs by finding the distribution coefficient for each reference point along the system. Figure 2.16 shows the influence lines for the same bridge at different loading points.



Figure 2.16: Influence lines at reference points between 0 and b [31].

An advantage of the Guyon Massonnet Method is that it gives a nonlinear transverse load distribution. Furthermore, it is possible to account for both the torsional and flexural stiffness of the bridge girders. Moreover, it is feasible to determine the transverse moment using the GMM. However, the method is mainly used for concrete bridges. Therefore, stiffness assumptions must be made to apply it to composite bridges.

## 2.5.2 Transfer Matrix Method

An alternative method to analytically determine the TLD is using the Transfer Matrix Method (TMM), which recently was proposed in a study by Guo *et al.* [32]. The study investigated the possibility of using the TMM to determine the TLD of an articulated slab bridge by comparing it to the Force Method (FM) and FEM analysis. The derivation of the TMM is based on the following assumptions:

1. Ends of slabs are simply supported
2. The torsional deformation of the slab is restrained
3. The slab sections have no warping

4. The lateral connection between the slabs is replaced by an articulated point in the loading position

Figure 2.17 shows each slab's TLD influence line peaks across the span. Compared to FM and FEM analysis, the study proved that TMM provided results similar to FEM analysis. Contrary to FM, the TMM also accounts for the distance between the applied load and the supports, as shown in Figure 2.17. Another advantage of TMM is that it provides the vertical displacement, the torque and the rotation of each bridge element.

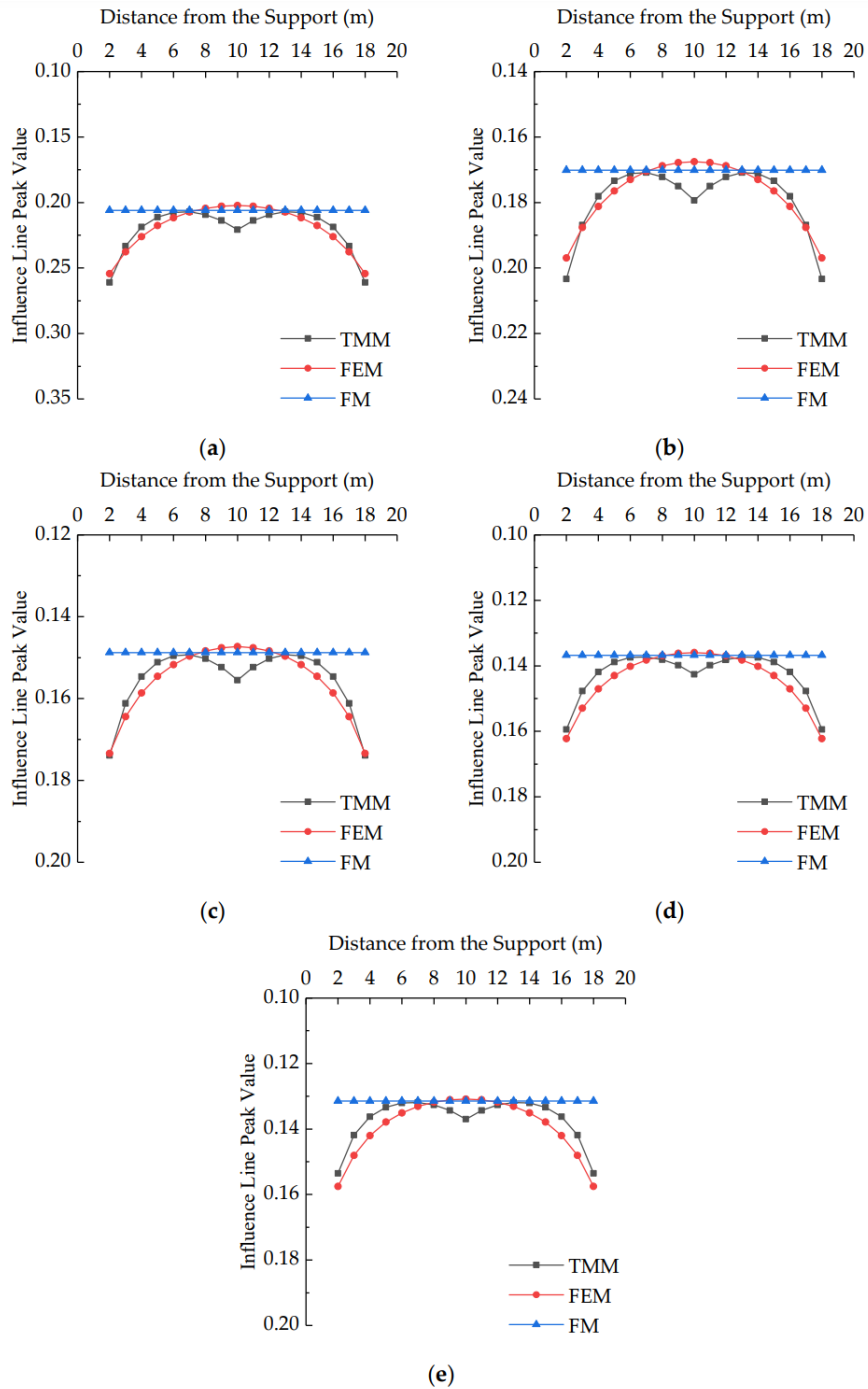


Figure 2.17: TLD influence line peak values for slab 1-5 at L/8. **a)** slab 1. **b)** slab 2. Etc. [32].

The TMM considers flexural bending and torsion using stiffness coefficients, like the Guyon Massonnet Method. These are given from Eq. 2.27 and 2.28.

$$f_b = \frac{d^2(L-d)^2}{3EIL} \quad (2.27)$$

$$f_t = \begin{cases} \frac{a^2d}{2GJ} & (0 \leq d \leq L/2) \\ \frac{a^2(L-d)}{2GJ} & (L/2 \leq d \leq L) \end{cases} \quad (2.28)$$

With relatively few means, the TMM can calculate the TLD, as each bridge has a matrix assembled from vectors describing the displacement and vertical shear force at each node, as shown in Figure 2.18. Assuming that each bridge element is similar, the only matrix that varies is the matrix of the loaded bridge element. Figure 2.18 shows the forces the TMM considers.

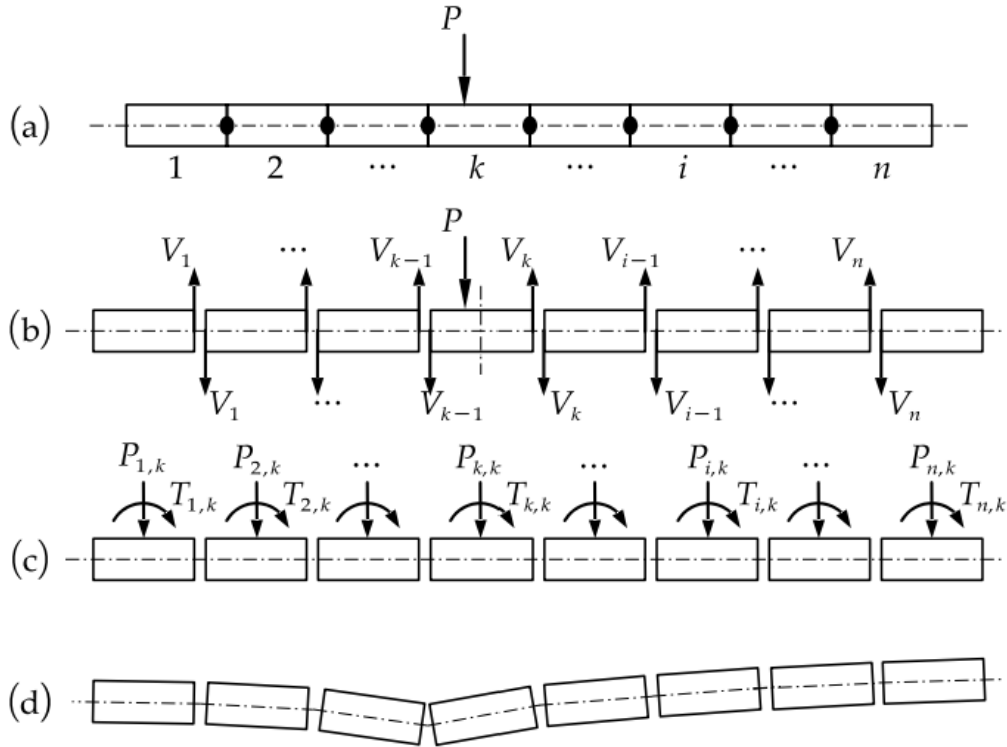


Figure 2.18: The force diagram of articulated slab bridge. (a) external force, (b) vertical shear of joints, (c) distribution load of each slab, (d) deflection of slabs. [32]

As mentioned, the TMM in the study considers articulated slab bridges with shear keys between each box girder. Therefore, it neglects the transfer of the transverse moment. In contrast, the steel-concrete composite bridge slabs in Amsterdam would require the method to account for the transverse moment, as there is concrete between the composite girders. Thus, if TMM is applied to determine the bearing capacity of the steel-concrete composite bridges analytically, an additional degree of freedom must be derived to account for the transfer of transverse moments between the slabs. Alternatively, a rotational spring can be introduced to decrease

the rotation of the slabs. The stiffness of this spring element must also vary depending on cracked or uncracked concrete in the longitudinal direction.

## 2.6 Summary

To summarise, the elements that have been discussed in this literature review:

### **Eurocode Design Recommendations**

Following the review of the European Standards, it must be verified that the steel-concrete composite bridges have sufficient resistance for *bending, vertical- and longitudinal shear*. It can be concluded that the Eurocode does not include any guidelines for the design of existing steel-concrete composite structures. Additionally, the Standards do not allow designing new steel-concrete composite bridges without mechanical connectors, which is reasonable for an efficient design. However, these guidelines can be conservative for the assessment of existing bridges that are constructed without any mechanical connectors. This is a problem despite there being multiple studies that found the natural steel-concrete bond sufficient to provide composite interaction. On the other hand, there is a lack of studies investigating the bond strength of historical structures, as the bond strength may decrease with time.

The recommendations in the standards assume that bending can be determined using Eq. 2.4. For vertical shear resistance, the European Standard generally assumes that the steel girders merely provide vertical shear resistance. but the account of the encasement may be taken. However, there is no recommendation from the European Standards for how the shear connection affects the interaction of steel and concrete for vertical shear resistance. Therefore, additional literature was discovered to determine the vertical shear strength of steel-concrete composite beams. It is assumed that the findings from the study by Vasedravellis and Uy [13] can be applied to this study, as they proposed an analytical method to determine the vertical shear contribution of the concrete and account for the degree of shear connection.

### **Longitudinal Shear Resistance**

The literature review revealed multiple studies investigating the steel-concrete bond of concrete-encased I-profiles. These studies proved that the natural bond due to cohesion contributes to significant resistance and must be accounted for. However, many of these studies were performed with relatively small HEB profiles. Only one study covered the time effects, investigating the natural bond of specimens half a year after they were cast. Nonetheless, the loss of bond strength due to time effects requires further research. Therefore, the bond strength, due to cohesion, is taken as the lowest value from this literature review, e.i. the bond strength is assumed to be 0.54 MPa.

When accounting for the natural-steel concrete bond, it can be difficult to determine the effects of the Mohr-Coulomb mechanism. However, it is considered conservative to neglect the Coulomb mechanism, and the bearing capacity may be unnecessarily reduced. Therefore, the following study uses a value of 0.30 for the coefficient of friction, assuming that a high coefficient of friction can not coexist with cohesion being present, as the coefficient of friction increases with increasing force, but concrete crushing occurs due to the force, which damages the steel-concrete interface.

### **The Strut and Tie Method**

As the literature review covers, the strut and tie method is often used for reinforced or prestressed concrete structures. In addition, this showed that the STM previously had been employed in a study with a bridge slab of similar geometry, although the materials were different. Generally, the STM proved to be applicable for the scope of this thesis, as this method is widely used and can be applied similarly to the research by Ug Bae *et al.* [29].

### **Transverse Load Distribution Models**

For the transverse load distribution (TLD), two methods were considered: **Guyon Massonnet Method** and **Transfer Matrix Method**. The Transfer Matrix Method proved relevant for this research, providing accurate results with relatively little computation. The study applying TMM investigated bridges with shear keys between the box girders. Therefore, applying the TMM for this research would require that an additional degree of freedom is derived or that rotation springs are implemented since the steel-concrete composite bridges in Amsterdam can transfer the transverse moment. In addition, both TMM and GMM would require assumptions to include the composite material parameters, as the methods generally only concern concrete bridges.

## 3 Experimental and Numerical Study

A series of investigations have been initiated to help determine the bearing capacity of the historic steel-concrete Amsterdam bridges, including testing and FEM modelling. The testing was performed over two phases, first in situ testing followed by laboratory testing, both accompanied by numerical models. The findings of these investigations are studied and described in the following. The main purpose of studying these results is to gain insight into the behaviour of the bridges, helping to construct an analytical model based on this understanding. Thus, these results will not be used to derive or calibrate parameters for the analytical model proposed in Chapter 4.

### 3.1 Experimental Setup

The experimental testing includes in situ testing and laboratory testing. First, in situ, testing was performed on Amsterdam Bridge 70, one of the about 30 steel-concrete composite bridges in Amsterdam without mechanical connectors. Following the in situ testing, decks from the same bridge were cut out and transported to Delft for laboratory testing by TNO and TU Delft. The bridge consists of a main span and two side spans.

#### 3.1.1 In Situ Testing

The first phase of the assessment of the historic Amsterdam bridges involved in cyclic in situ testing of Amsterdam Bridge 70, which was accompanied by a numerical model. The construction drawings of Bridge 70 date back to the early 1930s, discovered through an archive study by de Boer *et al.* [1]. Moreover, the lifetime of the bridge has already passed. Regardless the bridge is considered to be in relatively good condition. It was possible to test Bridge 70, as a larger construction of the inner Amsterdam infrastructure was already underway, which involved demolishing a number of bridge decks. The in situ tests were performed over two weeks. Only the side spans were available for testing, as the main span had to remain open for the boat traffic. Before the in situ testing, concrete cores were drilled, and samples of the steel girders were taken to determine the material parameters of the concrete and steel. The material parameters were used to input for a FEM model that accompanied the in situ testing.

The two tested samples of the bridge deck part had a width of 3.95 m and a length of 6.5 m. The bridge deck was disconnected from the remaining part of the bridge by sawing the concrete along the span of the bridge deck. The tested bridge deck consisted of six steel girders, as shown in Figure 3.3, where the steel girders are marked with red rectangles. The cross-section of one of the composite girders in the bridge deck is shown in Figure 3.1.

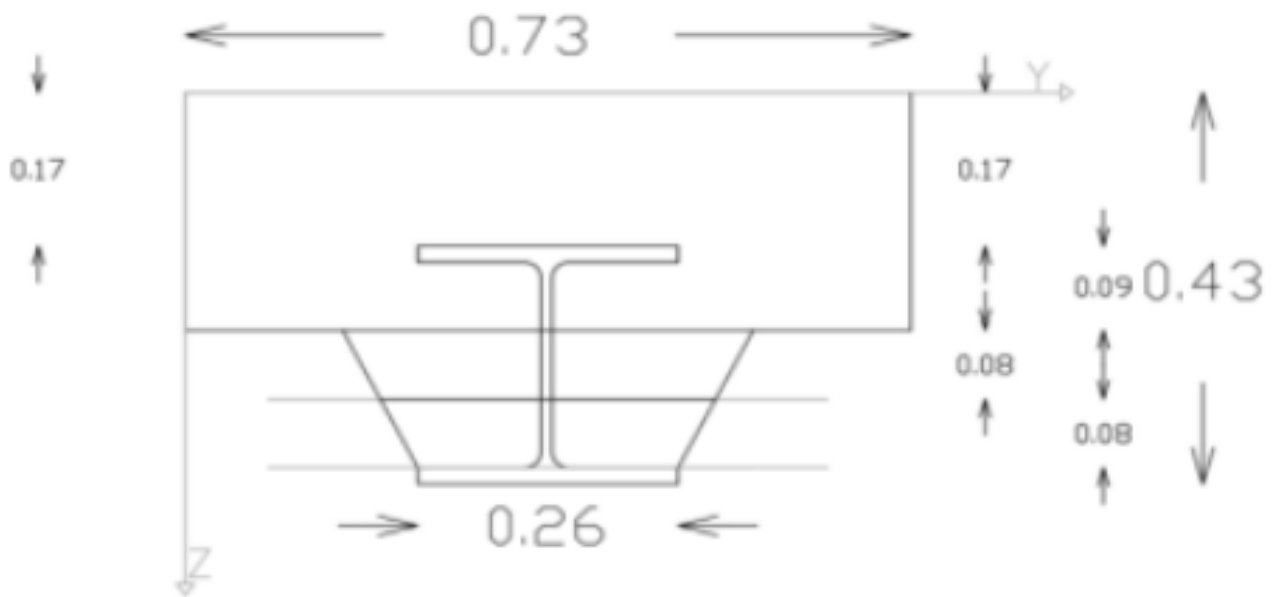


Figure 3.1: Cross section of Amsterdam Bridge 70 side span bridge deck [1].

Before the in situ testing, the hypothesis was that the bridges would be subject to punching shear failure due to the geometry of the cut-out section where the concrete is thinnest. This was also anticipated due to the lack of transverse reinforcement. Thus the bridge was loaded between the steel girders. Figure 3.2 shows the position of the loading that is between the two composite girders.

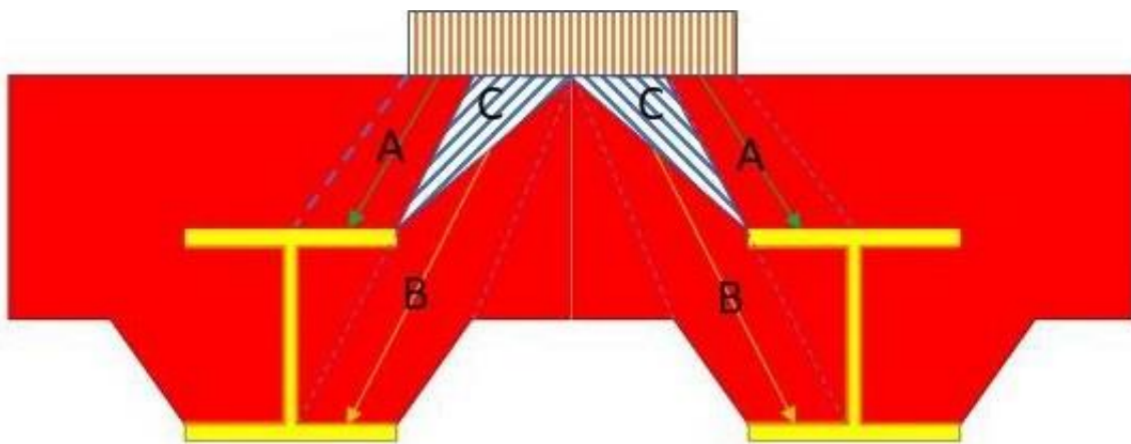


Figure 3.2: Position of the load before the in situ testing. Internal distribution of stresses from the load. [1]

The bridge was loaded by a single wheel-print with increasing load. The wheel-print was positioned between beams 3 and 4, as shown in Figure 3.3. The wheel print was applied at five different locations. One location was at the mid-span, and the remaining were between the supports and the mid-span. The measurements and location of sensors are shown in Figure 3.3. The bridge was tested to a maximum load of 475 kN, which was the limit due to the capacity of the foundation. The testing lasted 14 days as there were several load steps before the maximum load was reached, and between each load level, which was reached three times

before increasing the load, there were additional intermediate load steps of 25 kN. Moreover, the load was applied at five different locations, so this had to be done five times.

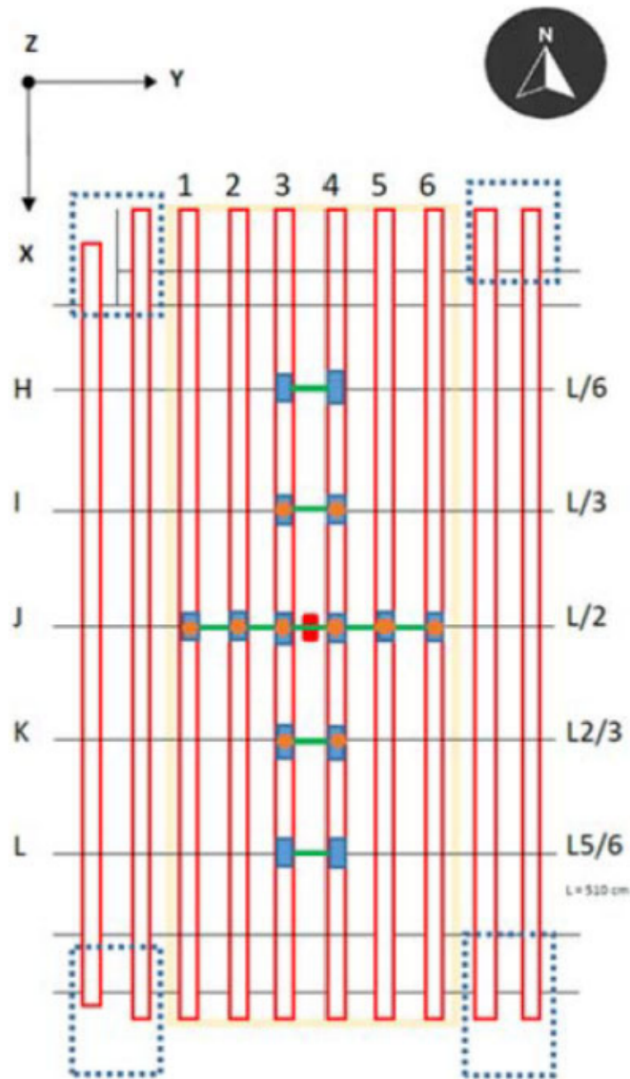


Figure 3.3: Load and sensor location of the testing at midspan. The red rectangle indicates the wheel print load. The blue rectangles indicate strain sensors on the bottom steel flanges. The orange dots are the lasers measuring the vertical displacement. The green lines show the measurement of the transverse displacement between the bottom steel flanges.[1]

During testing, cracking only occurred at a micro level. From the vertical displacement, it was possible to conclude that final the load still was distributed over the four girders adjacent to the wheel print load, e.i. beams 2-5, according to Figure 3.3. It is assumed that the distribution may differ when the load is between the exterior and the adjacent girders. Slip behaviour was measured only at one in situ loading but requires more investigation. Additionally, the expected stiffness of the bridge deck was higher than first expected. Also, the numerical model showed remaining capacity up to 1900 kN. Still, after 675 kN, the cracks started propagating above the top steel flange, which is not desired. Thus, it is assumed that the maximum acceptable wheel print load is expected to be about 675 kN. [1]

### 3.1.2 Laboratory Testing

From Amsterdam Bridge 70, which was tested in situ, three cut-out sections (LB1, LB2 and LB3) were taken following the in situ testing of the same bridge. One specimen was taken from the main span, whereas the other two others were taken from the side spans of the bridge, as illustrated by Figure 3.4.

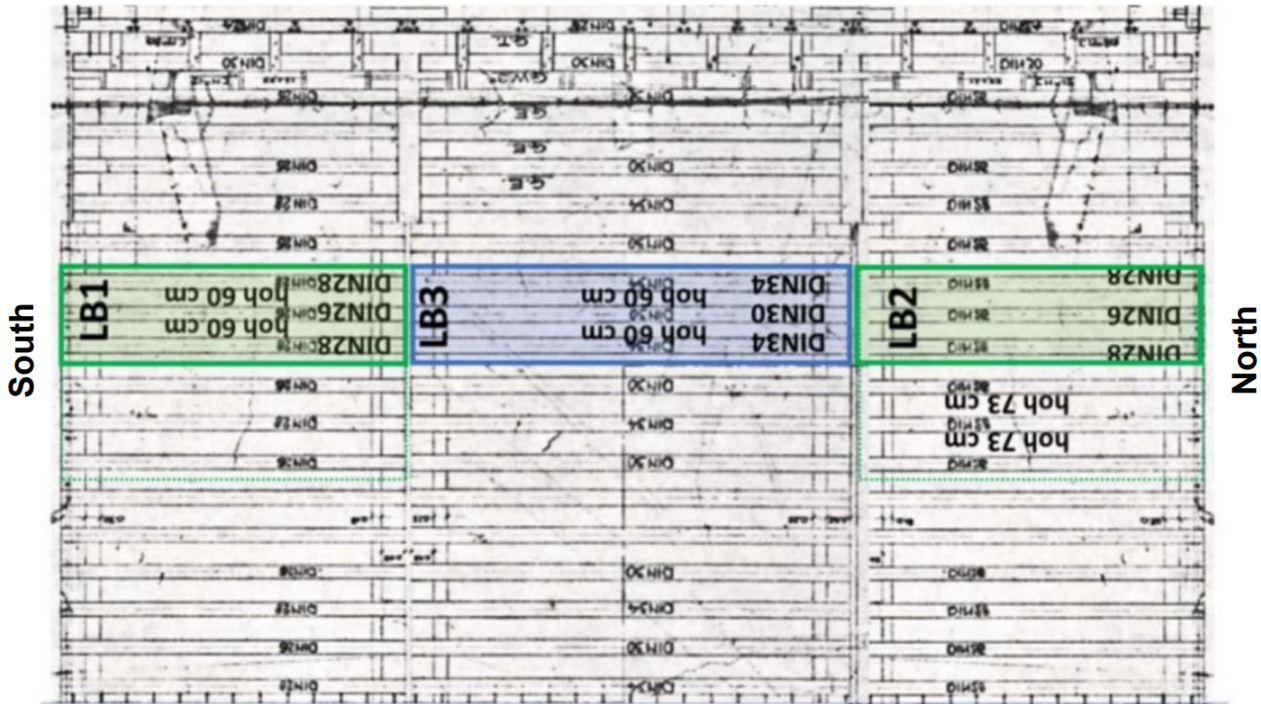


Figure 3.4: Western half of bridge 70. Showing the location of cut-out sections LB1-LB3. [33]

The details of the experiments and the results are further described in the report ”*Experiment report on steel-concrete-composite bridge deck without mechanical connectors (Verbundträger)*” by Jørgensen *et al.*[34]. For this study, only the main conclusions and observations are considered.

All specimens consisted of three encased steel girders without mechanical connectors. These specimens were transported to Delft for laboratory testing. The specimens were tested using a 4-point bending test. TNO tested specimen LB2 but did not achieve failure at first. However, TNO improved the test setup following the testing, and it was possible to achieve failure after the initial testing [35]. The remaining specimens, LB1 and LB3, were tested by TU Delft in the Stevin Lab and achieved failure. Only LB1 and LB3 are considered in the following, as LB2 was tested with cyclic loading, which does not compare to the scope of this research.

The specimens LB1 and LB3 differ in length and cross-section dimensions. LB1 has a span of 5950 mm and consists of three I-girders, two exteriors that are DIN280-profiles and one middle that is a DIN260-profile. The cross-section dimensions of LB1 are shown in Figure 3.5. Additionally, the concrete cover above the steel girders varies greatly between 400 mm and 490 mm along the length of the width of the specimen.

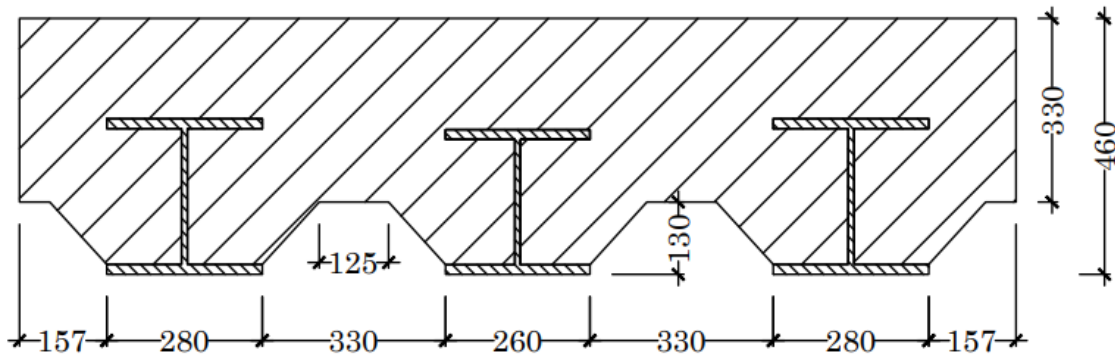


Figure 3.5: Cross-section of LB1 showing the dimensions.

LB3 has a span of 7600 mm and consists of three I-girders, two exterior DIN340-profiles and one middle a DIN300-profile. The dimensions of LB3 are shown in Figure 3.6. The specimens differ as LB3 has larger steel girders but a smaller concrete cover, which is assumed to affect the longitudinal shear resistance. Similar to LB1, the concrete cover above the steel girders also varies. However, the variation is less as it is between 405 mm and 430 mm. The centre-to-centre distance between the girders is similar.

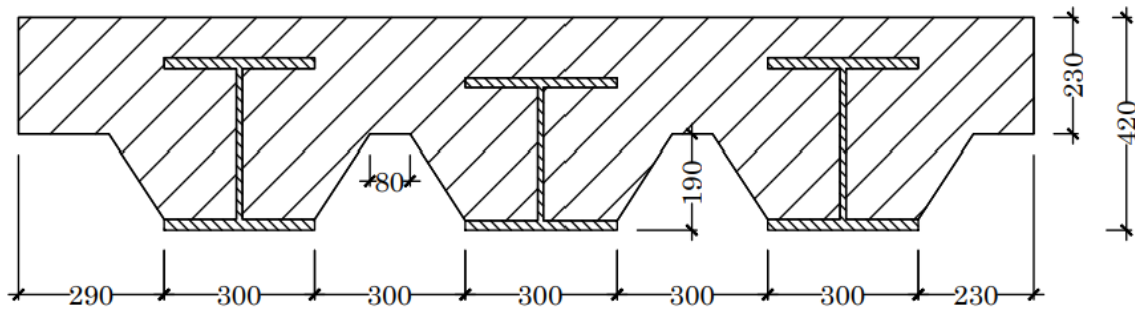


Figure 3.6: Cross-section of LB3 showing the dimensions.

The loading was applied as displacement control using hydraulic jacks. The load from each hydraulic jack was transferred via a transfer beam to two loading plates, as shown in Figures 3.7 and 3.8. The hydraulic jacks were applied, each with a distance of 600 mm from midspan. Furthermore, the loading location was right between the middle girder and the exterior girders, considered the most critical location. The purpose of this loading was to simulate the loading from a vehicle.

Supports were positioned underneath each steel girder, with a corresponding load cell at each support. These were used to measure the reaction forces at each beam to help understand the load distribution between the beams.

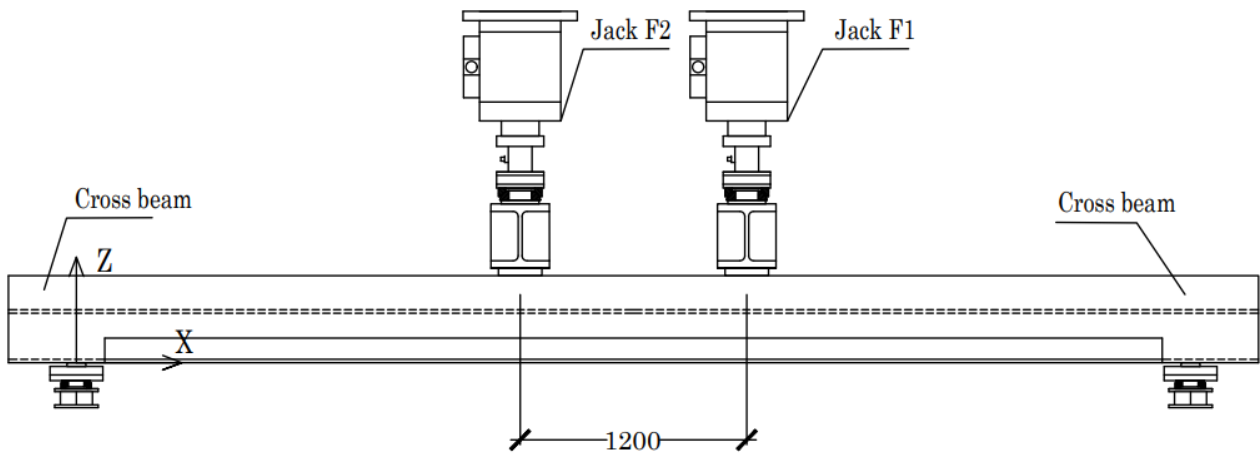


Figure 3.7: Side view of the test setup of LB1. Showing the position of hydraulic jacks.[34]

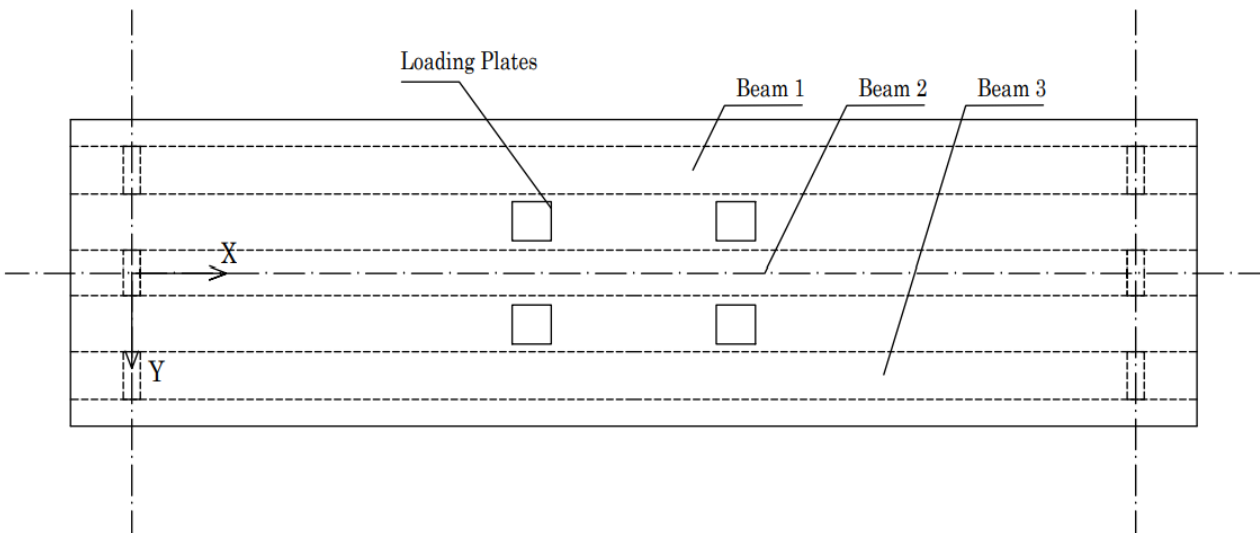


Figure 3.8: Top view of the test setup of LB1. Showing the position of loading plates.[34]

Due to the lack of transverse reinforcement, the transverse behaviour has been investigated using 3D DIC and LVDTs positioned underneath the specimens. The location of the 3D DIC is shown in Figures 3.9 and 3.10. Using this, it is possible to see how cracking propagates with increasing load. Unfortunately, 3D DIC measurements were only taken during load holds. Thus, these do not give a fully accurate presentation of the behaviour. Additionally, only the 3D DIC results from the testing of LB1 are relevant for the following, as the 3D DIC during the testing of LB3 was positioned wrong.

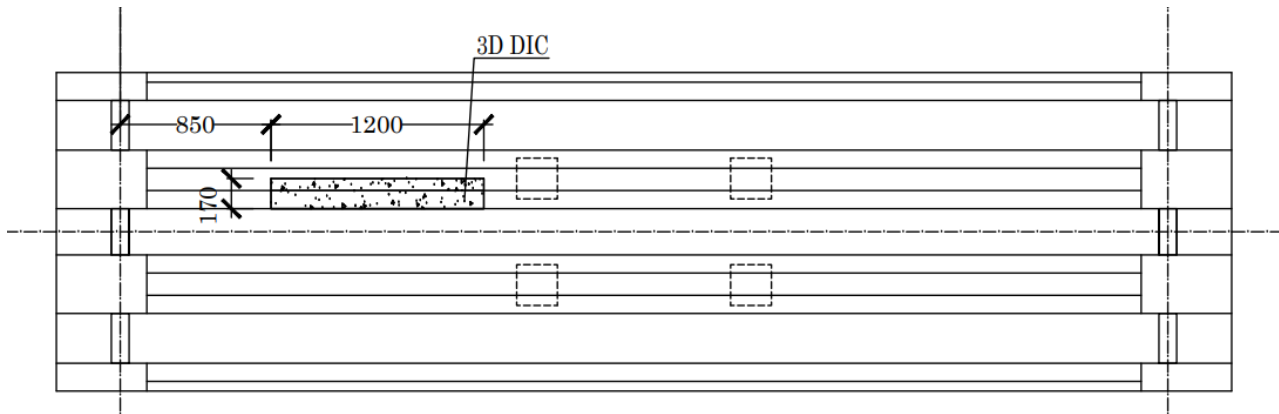


Figure 3.9: Bottom view position of 3D DIC at LB1.

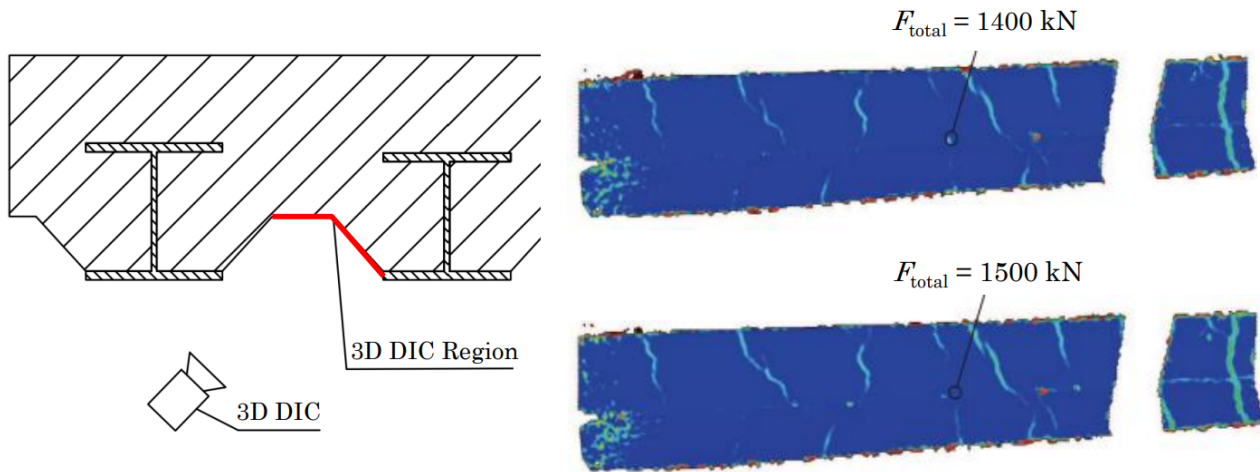


Figure 3.10: Orientation of the 3D DIC positioned underneath LB1. Showing the DIC when the total load is 1400 kN and 1500 kN at LB1.

From the 3D DIC in Figure 3.10, it is possible to see that at a load around 375 kN the longitudinal cracking starts to propagate. However, as the bottom view in Figure 3.9 indicates, it is impossible to see the onset of this longitudinal cracking, as the DIC measures from a distance to the loading plates.

An additional method to further assess the transverse behaviour is using LVDTs that are positioned at the bottom flange of the steel girders, measuring the relative displacement between the exterior girders and the middle girder, as shown in Figures 3.11 and 3.12.

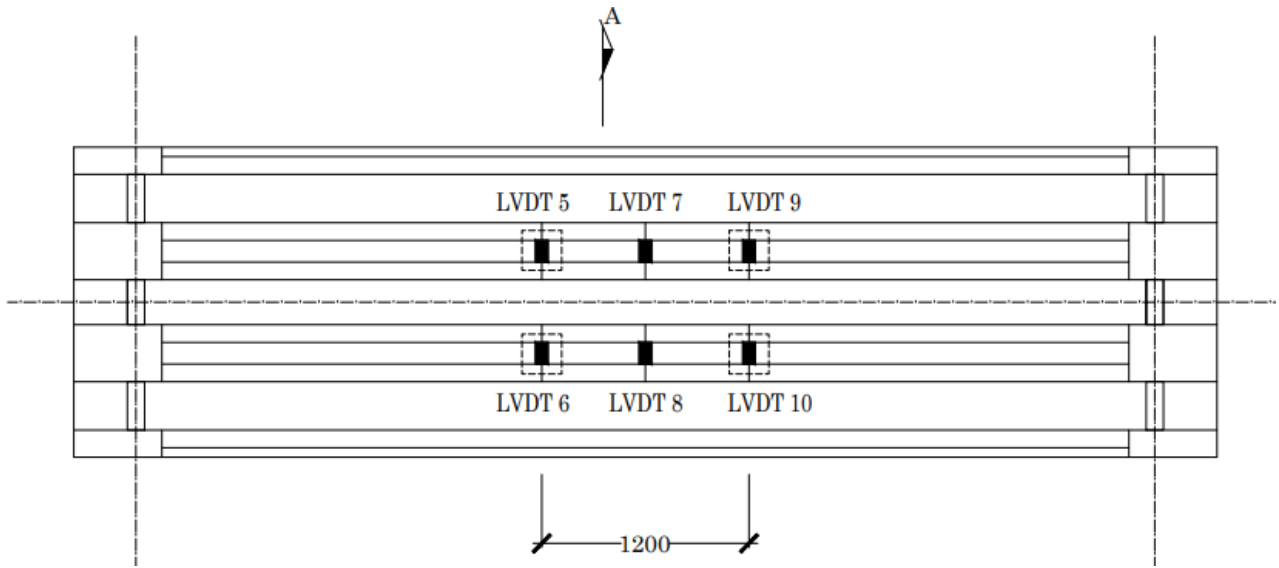


Figure 3.11: Bottom view of the specimen indicating the location of the LVDTs relative to the loading plates.

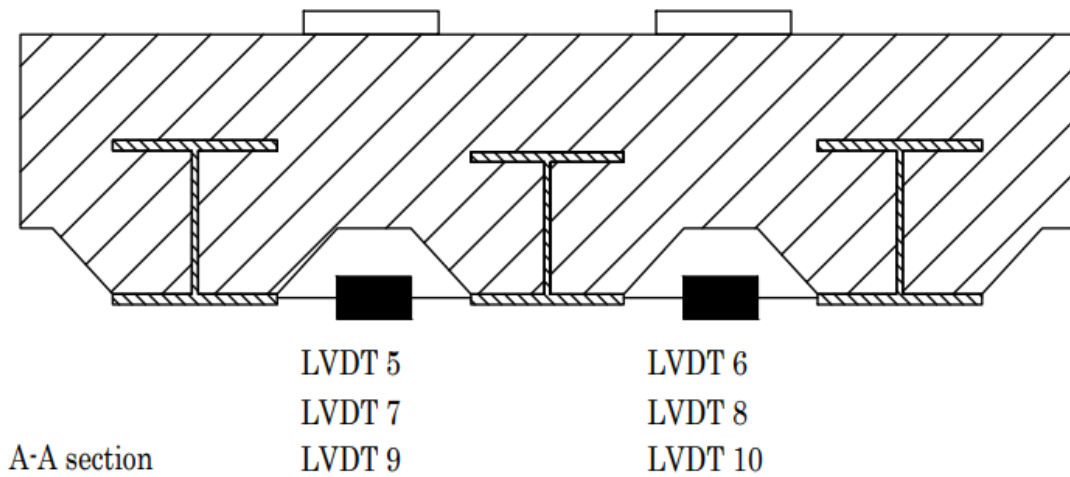


Figure 3.12: A-A section of the specimen in Figure 3.11 a cross-section with the position of LVDTs underneath the specimen of LB1.

The onset of the longitudinal cracking is assumed to occur when the transverse displacement increases nonlinearly. However, this can also be due to yielding of the steel girders, but with the limited ductility of the concrete, it must crack before the displacement can increase nonlinearly. The uncracked concrete is assumed to keep the exterior girder relatively rigid. Figures 3.13 and 3.14 show the transverse displacement.

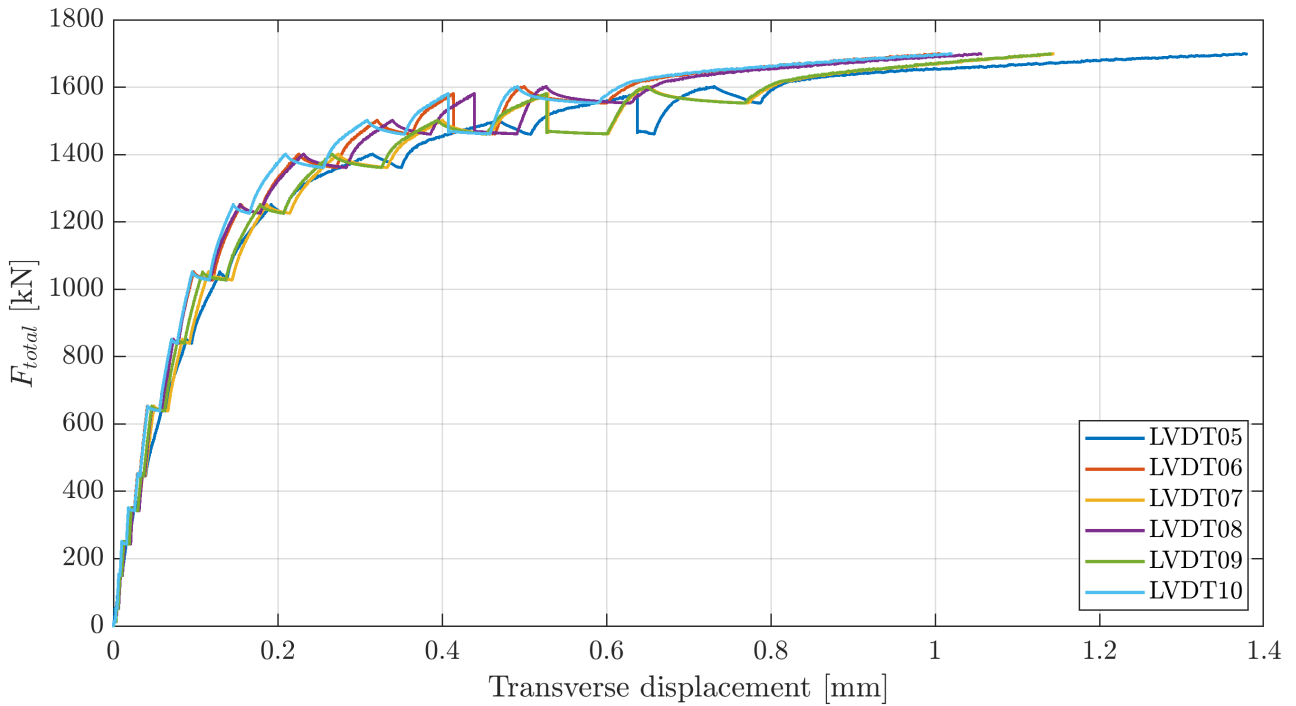


Figure 3.13: LB1 - Transverse displacement versus loading measured from underneath.  $F_{total}$  is the total load.

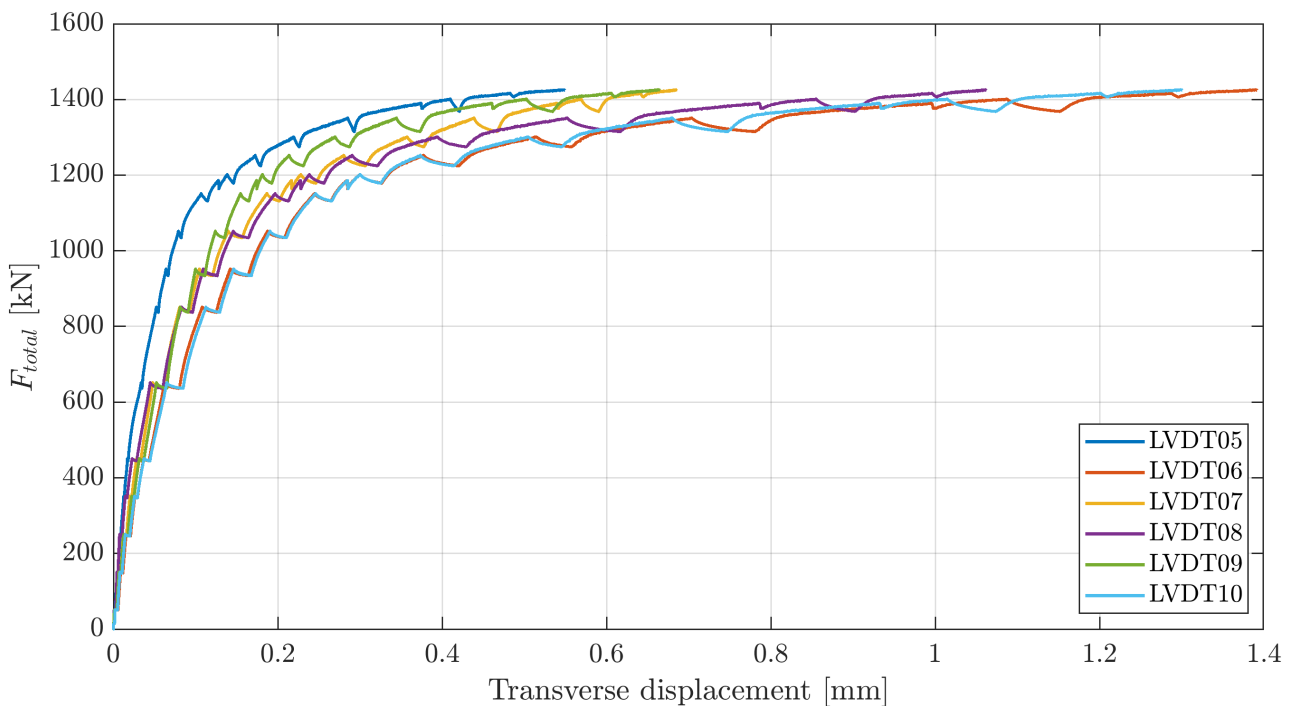


Figure 3.14: LB3 - Transverse displacement versus loading measured from underneath.  $F_{total}$  is the total load.

From Figures 3.13 and 3.14 it is assumed that for LB1 longitudinal cracking occurs at  $F_{total} = 1300$  kN and LB3 at  $F_{total} = 1100$  kN. From the above figures, it is also clear that following what is assumed to be longitudinal cracking, the composite girders still have the remaining capacity.

The specimens LB1 and LB3 were loaded until failure. LB1 failed at a maximum load at 1746 kN due to yielding of the steel beams followed by a slip between the steel and concrete. The maximum resistance of LB1 can be seen in Figure 3.15, which also shows how the specimen yielded before failure. The figure also shows that the specimen was unloaded before loading until failure, which for the other measurements, was removed for simplicity, as the girders already were yielding.

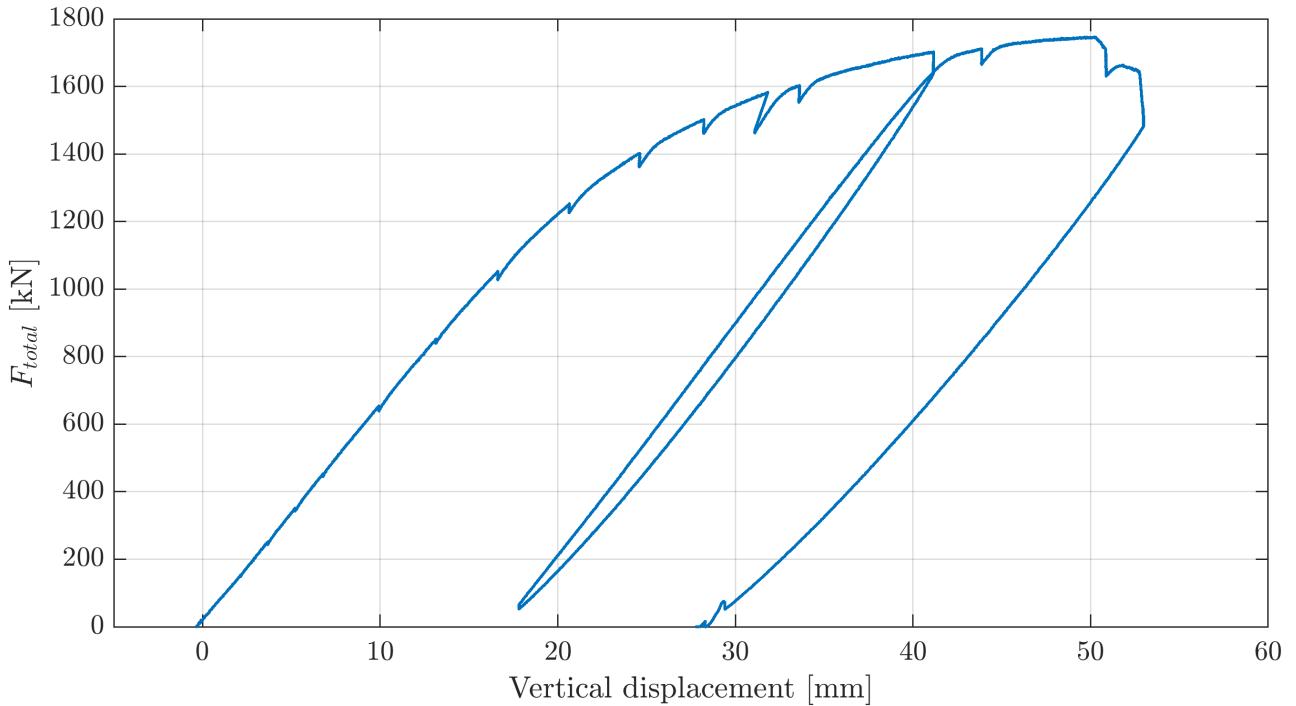


Figure 3.15: LB1 - Vertical displacement versus the total load  $F_{total}$ . Vertical displacement was measured from the hydraulic jack.

Following the failure of LB1, it was observed that there was an opening between the steel and concrete at one of the exterior composite girders. Additionally, longitudinal cracks had propagated as shown in Figure 3.16.



Figure 3.16: At the left: Opening between steel and concrete at one of the exterior girders observed after the failure of LB1. At the right: Longitudinal cracking observed after the failure of LB1.[34]

LB3 failed at a maximum load at 1494 kN to yielding of the steel girders and concrete crushing at the top fibre. The maximum capacity can be seen in Figure 3.17, showing the vertical displacement versus the total load. In addition, the figure shows that the specimen was unloaded before it was loaded till failure.

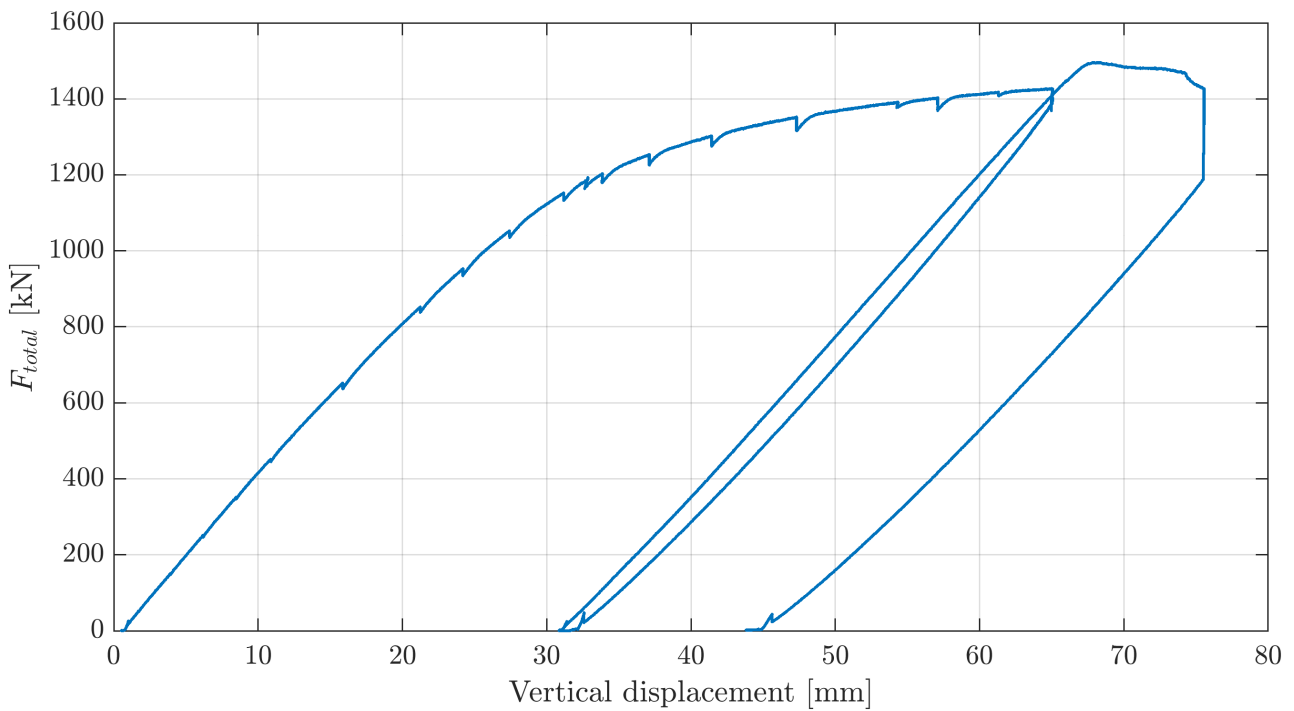


Figure 3.17: LB3 - Vertical displacement versus the total load  $F_{total}$ . Vertical displacement was measured from the hydraulic jack.

The concrete crushing is shown in Figure 3.18. Additionally, longitudinal propagating cracks

appeared between the steel beams from transverse bending due to the missing lateral reinforcement, as was the case for LB1. Moreover, the figure shows flexural cracks at the bottom propagating approximately up to the height of the top steel flange.



Figure 3.18: Sideview of LB3 showing concrete crushing at the top concrete fibre following failure [34].

## 3.2 Numerical Model

To better investigate the correlation between the longitudinal cracking and the loading, two numerical models of LB1 and LB3 have been investigated. These models are from a previous study by Poliotti *et al.* [36] investigating the specimens LB1 and LB3 by replicating their geometry and the loading from the laboratory testing. However, there are variations between the modelled geometry and the actual geometry, which may cause different results. The specimens in the laboratory had a concrete cover that varied along the length of the specimens, which may have caused a different load distribution in the specimens, as also was seen from the reaction forces. These can be seen in Appendix D. The geometry in the FEM assumed a constant concrete height and did not account for any imperfections.

For this study, it is desired to derive a generalised analytical model, so it can easily be modified or adjusted for other loading cases. Therefore, the numerical models of LB1 and LB3 have been adjusted so the loading is 3-point bending instead of 4-point bending. The numerical models help better understand the specimens' behaviour where the test measuring is insufficient, for instance, the transverse displacement at other points than measured during the testing. Thus a more accurate displacement profile can be achieved than the one achieved using LVDT, as was the case for the experimental testing. Numerical modelling has not been used to derive input parameters for the analytical model. The following describes the properties of the model and the boundary and loading conditions, whereas only the loading conditions have been changed from 4-point bending to 3-point bending. Except for the loading conditions, the models are identical to the models constructed by Poliotti *et al.*

The two test specimens from the laboratory are modelled in 3D using DIANA v10.5. Four elements of the bridge specimen are modelled, concrete, steel girders, steel plates for loading and support, and interface elements. The average size of the mesh is 50 mm. Figure 3.19 shows the mesh of LB1. A more detailed overview of the finite element types and the iterative scheme can be found in Appendix E.

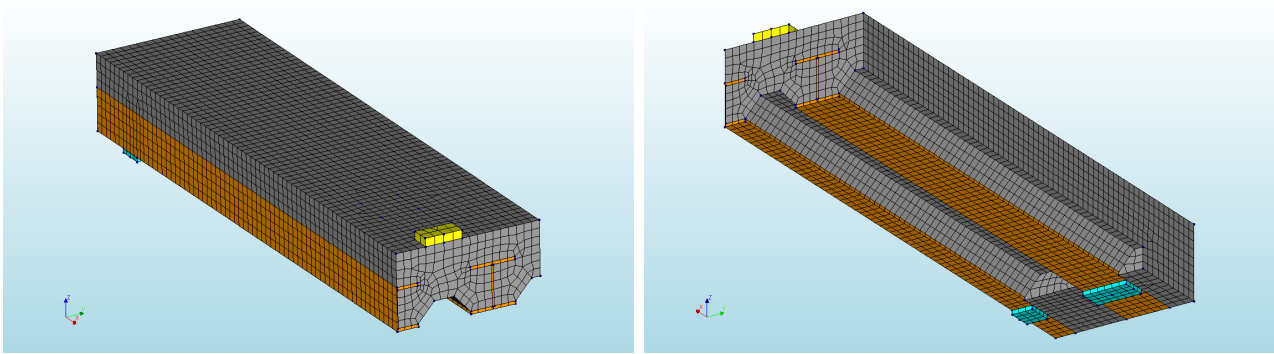


Figure 3.19: 3D view of the mesh of LB1.

### 3.2.1 Material Properties

The material properties of the numerical models are derived from the concrete cores drilled during the in situ testing of Amsterdam Bridge 70 and are given from Table 3.1.

Table 3.1: Material properties of the concrete, steel and interface.

<b>Concrete Properties</b>		
Compressive Strength	$f_{cm} =$	50.9 MPa
Tensile Strength	$f_{tm} =$	3.68 MPa
Poisson's Ratio	$\nu =$	0.2
Young's Modulus	$E =$	37 GPa
Fracture Energy	$G_f =$	148 N/m
Compressive Energy	$G_{fc} =$	37 000 N/m
<b>Steel Properties</b>		
Young's Modulus	$E =$	200 GPa
Poisson's Ratio	$\nu =$	0.3
Yielding Stress	$f_y =$	235 MPa
<b>Interface Properties</b>		
Cohesion	$c =$	0.1 MPa
Friction	$\mu =$	0.5

The applied bond strength is relatively low compared to values found in the Literature Review 2. However, the study by Poliotti *et al.* [36] also stated that further study of these parameters is required.

### 3.2.2 Boundary and Loading Conditions

As the numerical models are similar to the specimens from the laboratory testing. Only three steel girders are considered. The specimens are loaded at midspan, 3-point bending at two locations between the interior and exterior beams. Double symmetry is used, so a quarter of the specimens are modelled. To secure convergence, the model is loaded using displacement control. The boundary- and loading conditions of the two FEM models of LB1 and LB3 are shown as 3D in Figure 3.20. The exact boundary- and loading conditions apply to the FEM model of LB3.

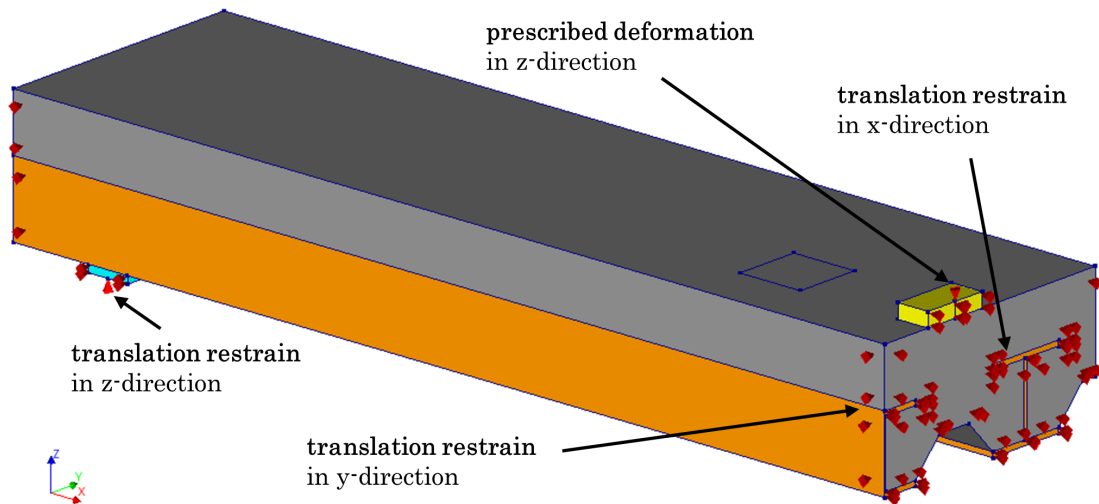


Figure 3.20: 3D view of LB1 showing the boundary- and loading conditions.

The main objective of the FEM models is to determine when the longitudinal cracking starts propagating since the experimental tests only can measure this using LVDTs and 3D DIC. However, the 3D DIC was not positioned correctly during the testing of LB3 to measure when the longitudinal cracking started to propagate. Furthermore, the specimens were subject to 4-point bending, which makes it difficult to compare to a generalized case, where the specimens only are subject to a load at midspan.

### 3.2.3 Results

A finite element analysis has been performed to understand the bridges' behaviour further. The analysis mainly focuses on the transverse behaviour and the occurrence of cracking. The experiments showed that the composite girders' lateral stiffness changes and is affected by longitudinal cracking between the steel girders. From FEM analysis, a more accurate picture of the behaviour along the specimen can be obtained. The transverse displacement is measured at the midheight of the steel flange of the exterior I-girder, as shown in Figure 3.22. The focal point is to determine when longitudinal cracking occurs and what mechanisms take place before the occurrence of longitudinal cracking.

Figure 3.21 shows the transverse displacement versus the total load of the exterior composite girder measured at the location shown in Figure 3.22. The transverse displacement increases linearly until a certain point where a kink occurs. Afterwards, multiple linear parts are interrupted by kinks until the displacement increases nonlinearly.

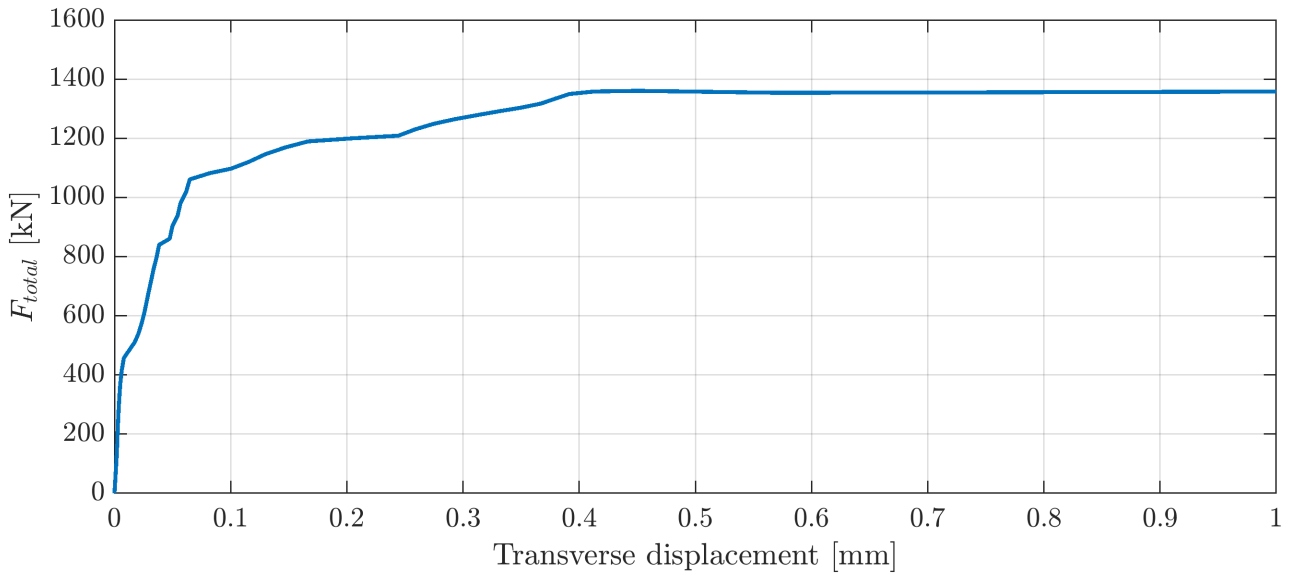


Figure 3.21: Total load versus transverse displacement at midspan of LB1.

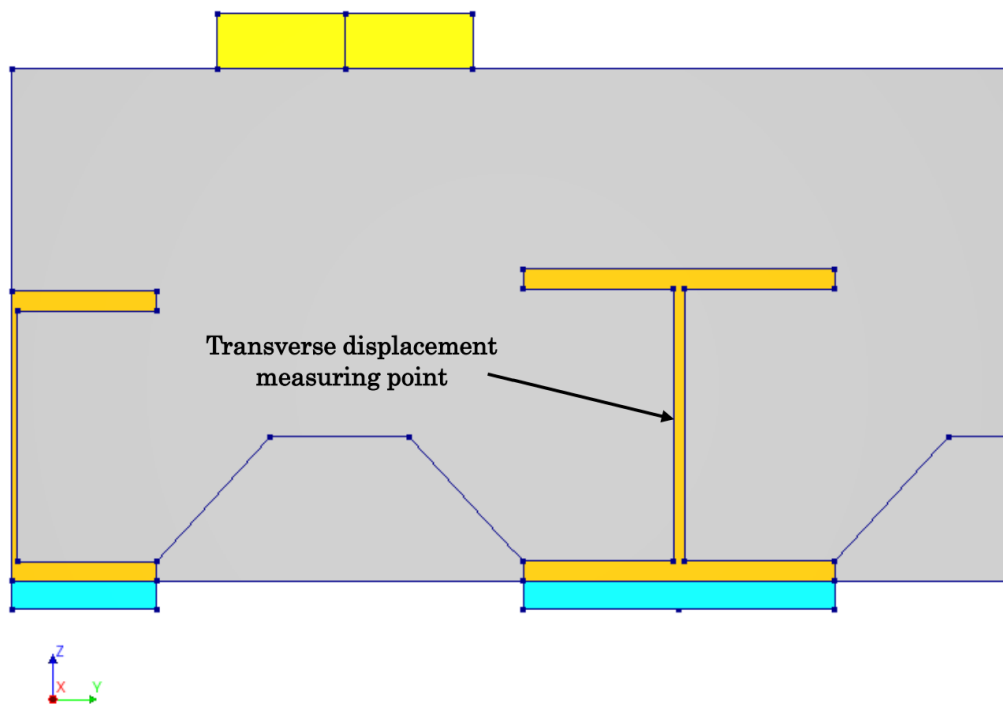


Figure 3.22: Cross-section showing the measuring point for the transverse displacement profiles of LB1 and LB3.

About 450 kN in Figure 3.21 the first kink occurs, which has been examined further to determine if this is due to longitudinal cracking. From the analysis, it was possible to see that no longitudinal cracks had occurred yet. However, flexural cracks had started propagating, as shown in Figure 3.23. Therefore, this jump is assumed to occur because of major axis flexural cracking.

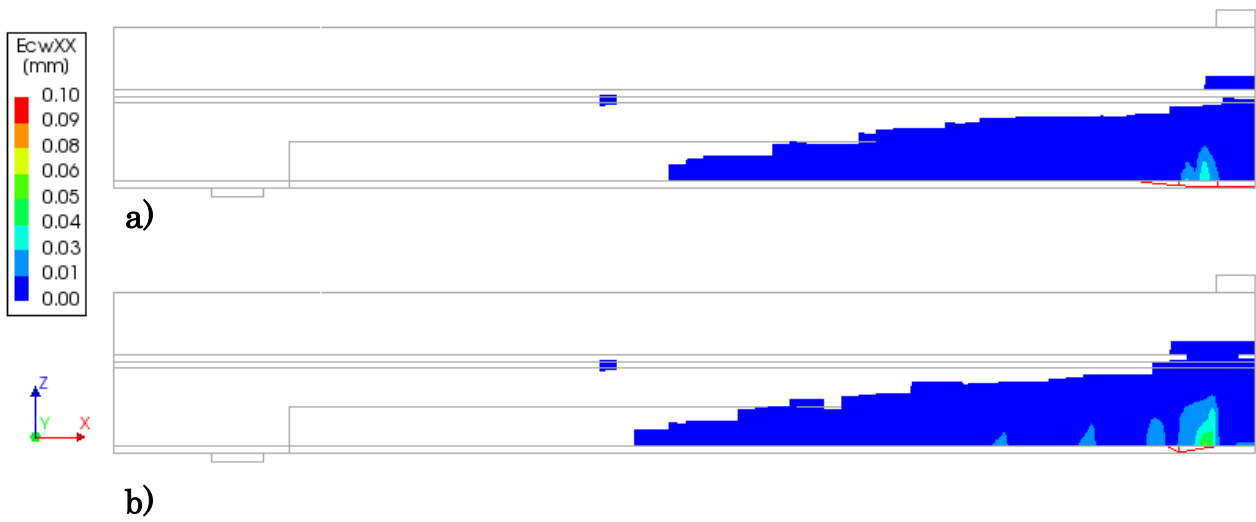


Figure 3.23: Sideview of LB1 at the onset of cracking. a) Crack width at 457 kN. b) Crack width at 488 kN.

Around 900 kN another sudden change in the displacement occurs, which is due to yielding of the steel girders, as shown in Figure 3.24.

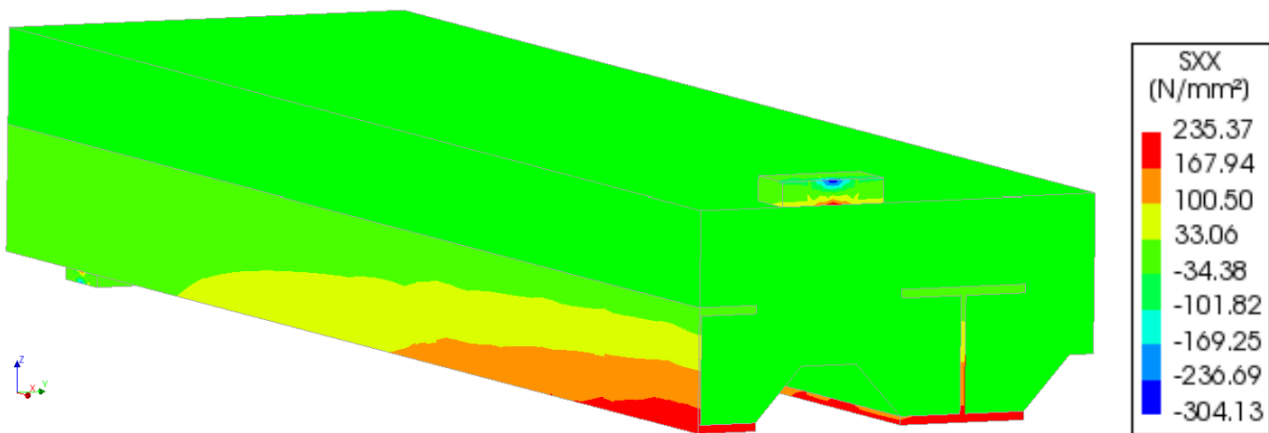
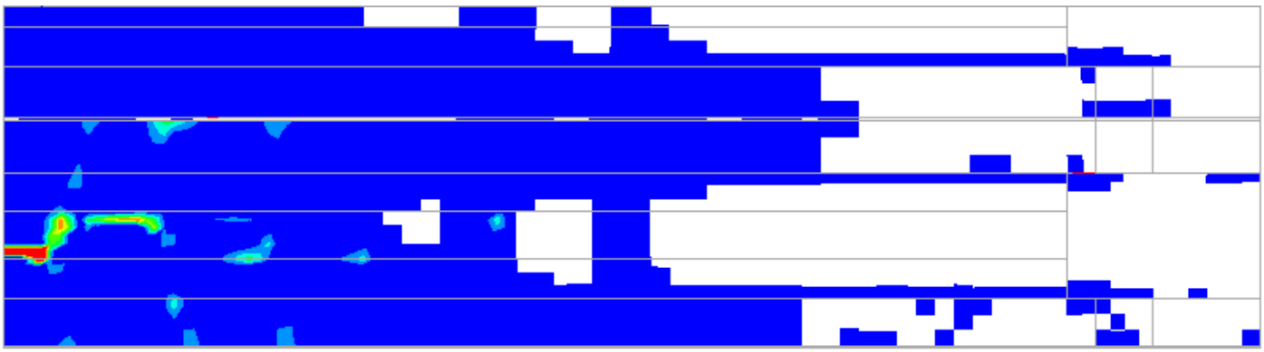
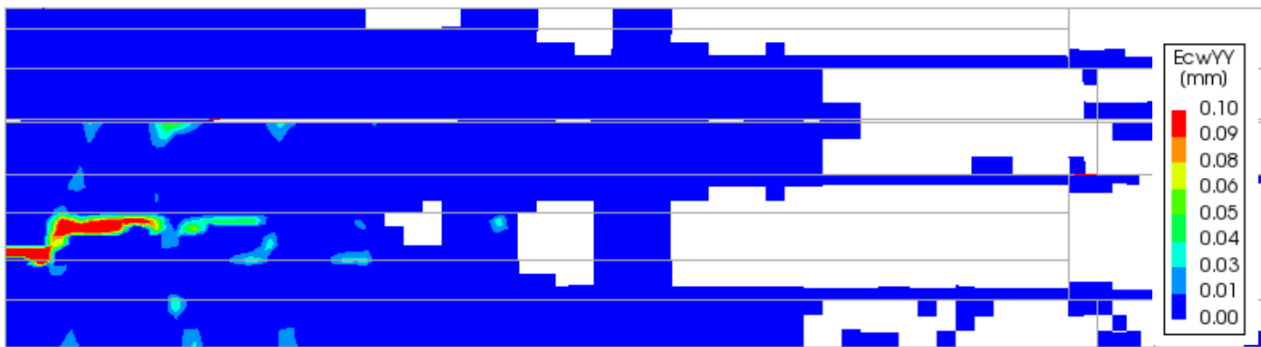


Figure 3.24: 3D view of LB1 showing the start of yielding at 940 kN.

Finally, when the load increases from 1145 to 1169 kN, longitudinal cracking propagates progressively, as shown in Figure 3.25. The onset of cracking occurred around 1169 kN but did not indicate this from Figure 3.21. Following longitudinal cracking at 1169 kN, the load increases further before the maximum capacity of the specimen has been achieved.



a)



b)



Figure 3.25: Bottom view of LB1 showing the longitudinal cracking. a) crack width at 1145 kN. b) crack width at 1169 kN.

The transverse displacement profiles in Figures 3.26 that show the transverse displacement from support to midspan show that the cracks never fully propagate from support to support. Close to the supports, the transverse displacement is about zero, which indicates that the lateral behaviour can be interpreted as a clamped beam due to the higher lateral stiffness of the cross beams at the supports.

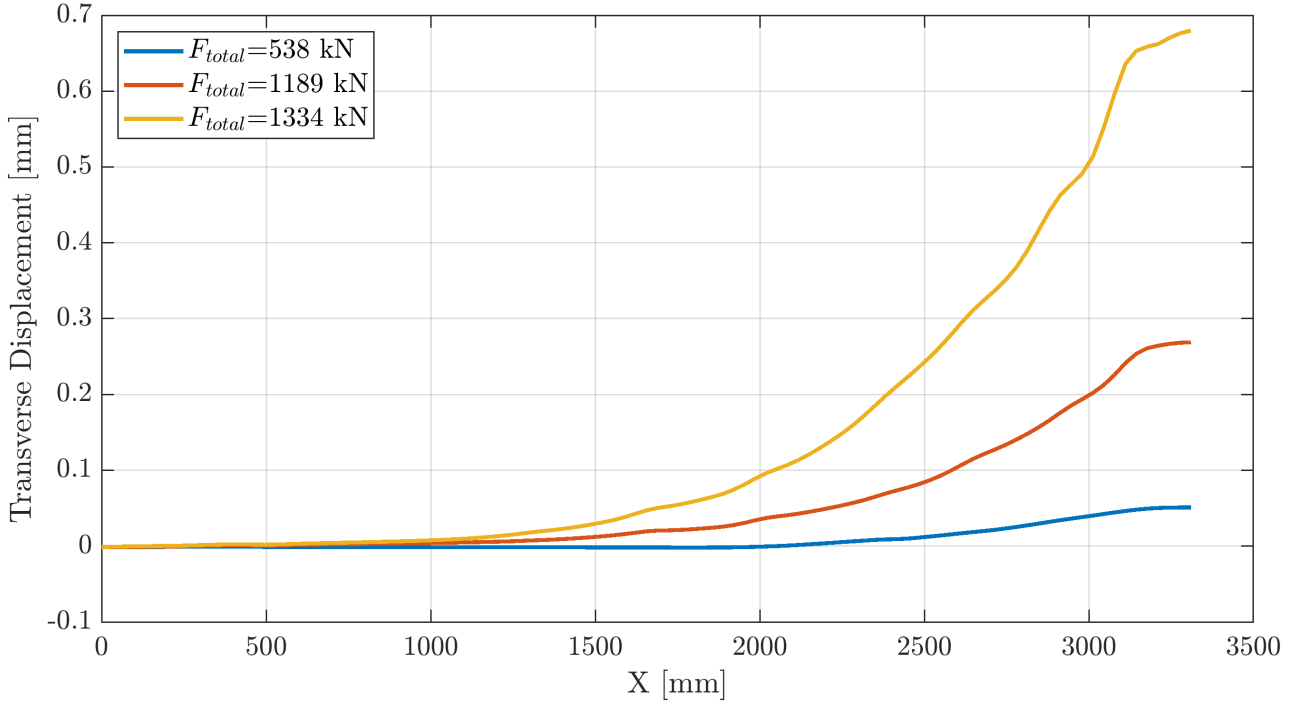


Figure 3.26: X, distance from support to mid-span, including the length of the cross beams, versus the transverse displacement for LB1.

A similar analysis has been performed for LB3. Figure 3.27 shows the transverse displacement versus the total load of LB3. The transverse displacement is measured from midspan, where the load is applied and at midheight of the exterior steel girder as shown in Figure 3.22.

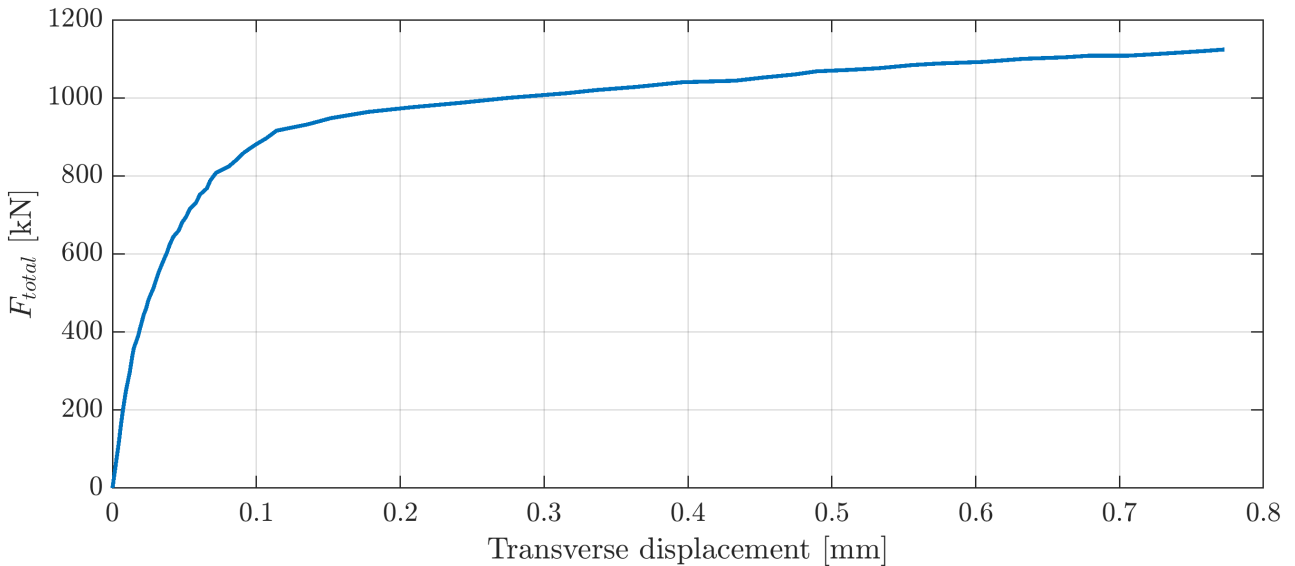


Figure 3.27: Total load versus transverse displacement at midspan of LB3.

There is no sudden kink in the displacement profile in Figure 3.27. However, around 800 kN, a small kink occurs, indicating the start of yielding of the I-girders, as shown in Figure 3.28. This is similar to LB1. However, the displacement profile analysis does not indicate a lateral stiffness decrease following major axis flexural cracking, which would be displayed as a kink on

the linear part of the graph in Figure 3.27. Moreover, the indication of yielding is only shown as a relatively small kink; therefore, the displacement profile of LB3 has a more smooth nonlinear curve than LB1.

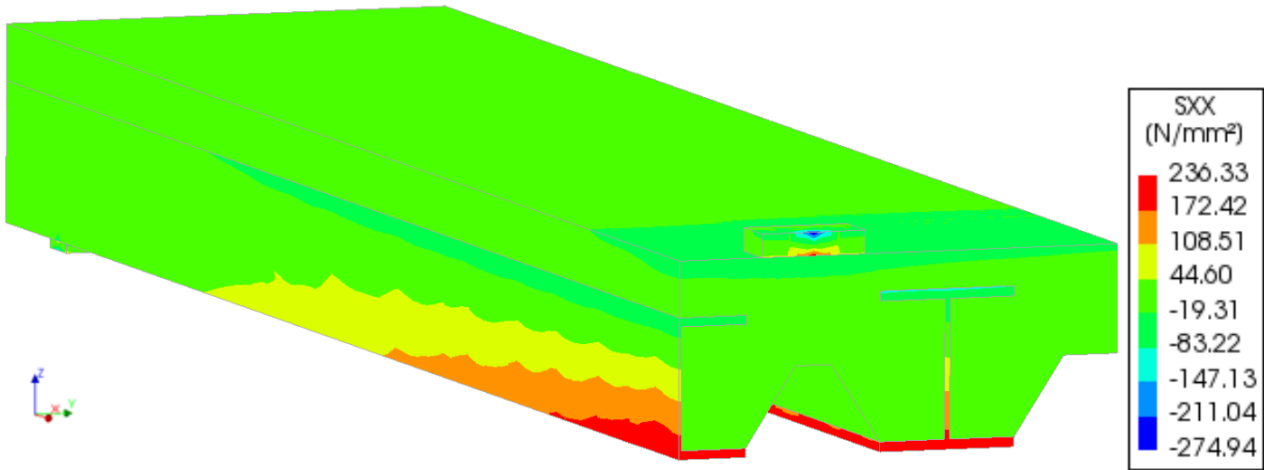


Figure 3.28: 3D view of LB3 showing the start of yielding at 808 kN.

Similarly to LB1, it can be concluded that there is a stiffness reduction following the longitudinal cracking, which occurs around 930 kN, indicating a change of the gradient in Figure 3.27. Moreover, the longitudinal cracking has not fully propagated from support to support when this occurs, as shown in Figure 3.29 when the load increases from 916 kN to 932 kN, which is in the range where the beam starts to displace nonlinearly. However, the longitudinal crack gradually propagates as the loading increases.

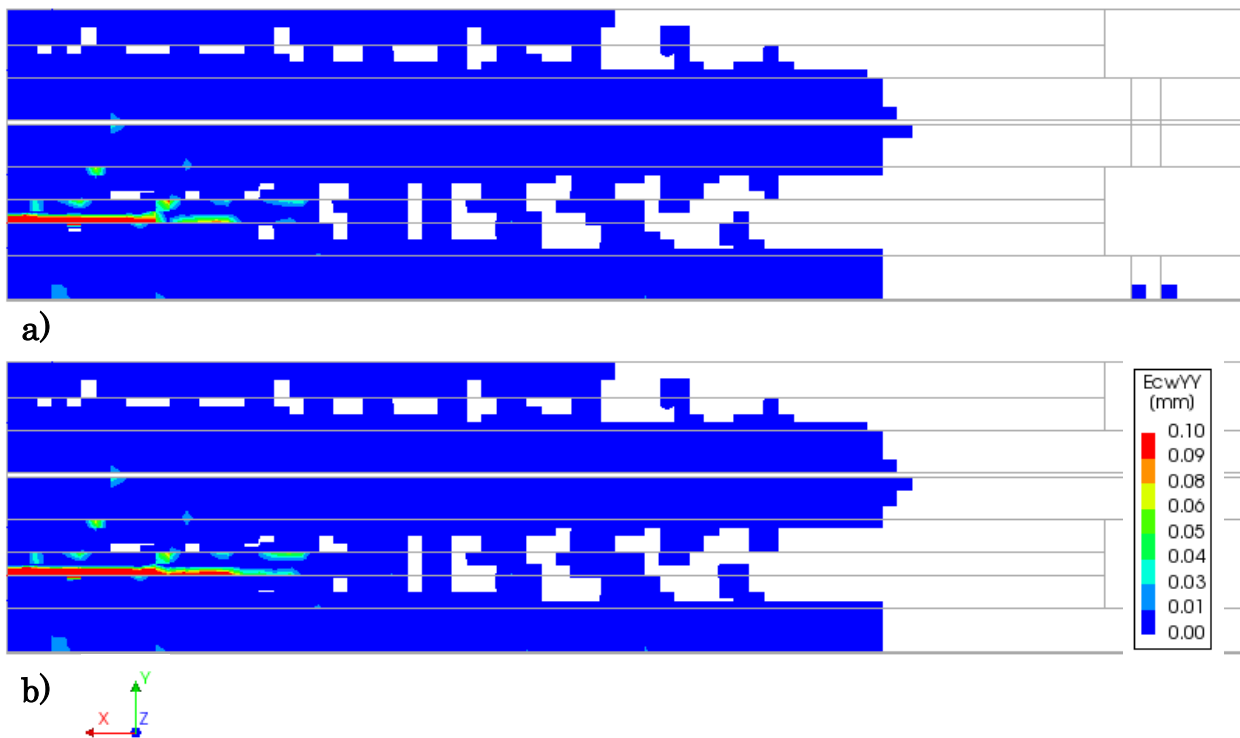


Figure 3.29: Bottom view of LB3 showing the longitudinal cracking. a) crack width at 916 kN. b) crack width at 932 kN.

Similar to LB1, analysing the displacement profile of LB3 from support to midspan at different load stages in Figure 3.30, it can be seen that the transverse displacement is zero close to the supports. This indicates that the composite girders in the lateral direction can be assumed to have clamped supports.

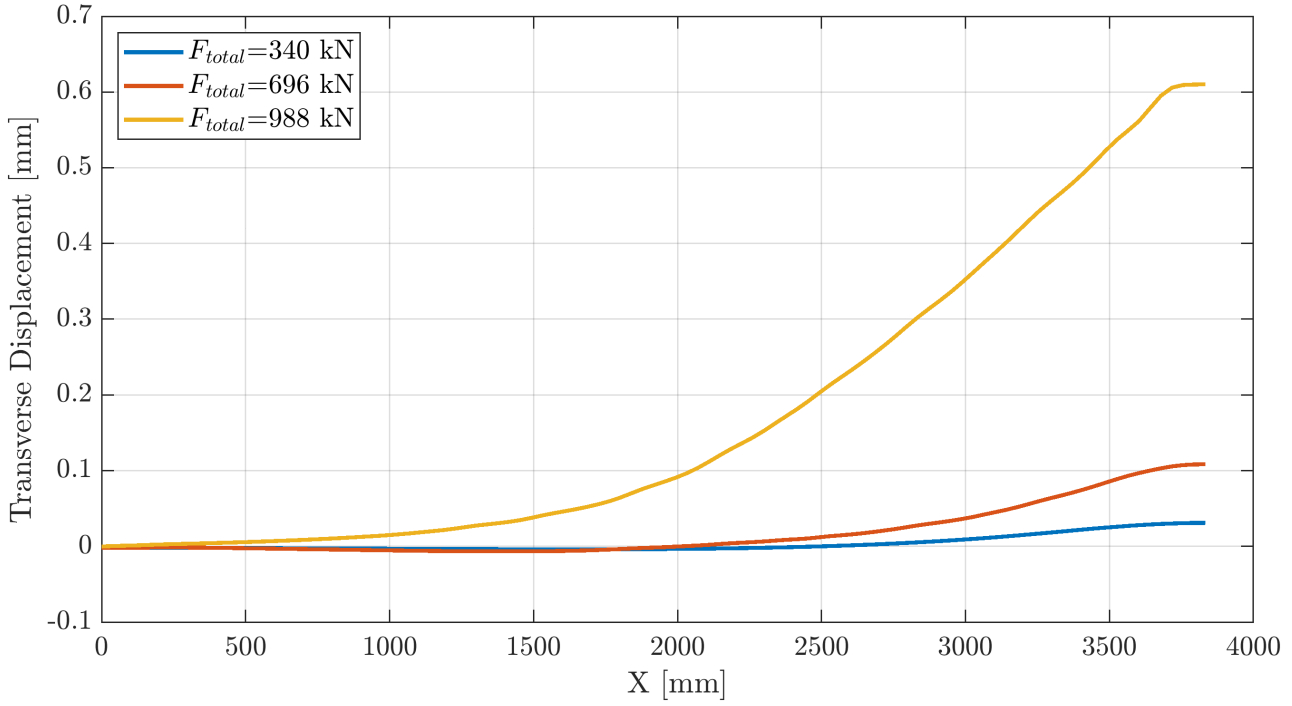


Figure 3.30: X, distance from support to mid-span, including the length of the cross beams, versus the transverse displacement for LB3.

### 3.3 Summary of Experimental and Numerical Study

The following text summarizes the observations and conclusions from the experimental and numerical investigations.

The in situ testing showed that the load was equally distributed between four neighbouring steel girders. However, this was for a case where the load was in the middle of the bridge deck. Following this, it is assumed that a more critical loading situation occurs when the bridge deck is loaded between the exterior and adjacent girder. The in situ testing and numerical model proved that the resistance to punching shear was sufficient and that flexural bending was governing. However, this assessment also suggested investigating the bond-slip behaviour further.

From the study of the experimental and numerical investigations, mainly the specimens LB1 and LB3 were relevant for further study, as these were tested using a similar loading setup. Additionally, these specimens had the same amount of steel girders but a variation in the dimensions of steel and concrete. LB1 failed at a load at 1746 kN due to yielding of the steel, followed by a reduction of ductility due to interface failure. LB3 failed at a load at 1494 kN due to bending with crushing of the top concrete layer, contrary to LB1 without interface failure. Additionally, longitudinal cracks occurred at both specimens during the testing, which decreased the lateral stiffness, but there was still remaining bearing capacity.

The laboratory experiments were conducted as 4-point bending tests due to the recommendations in the European Standards for the examination of asymmetric composite structures. However, for an analytical model, the focal point will be to derive a model that is generalized and, from this generalization, can be further modified for different cases. Therefore, two existing finite element models that were based on the testing of LB1 and LB3 were modified to 3-point bending instead of 4-point bending. These models will be used to verify the proposed analytical model, as the loading situation of these is closer to a generalized case. The numerical models showed how the lateral stiffness reduces gradually when the load is increased due to major axis flexural cracks, yielding and longitudinal cracking. The largest stiffness reduction came from the longitudinal cracking, while the other events only caused a minor reduction. Like the experiments, the numerical models had remaining bearing capacity following the longitudinal cracking. The transverse displacement profiles of the exterior composite girders showed that the girders have zero transverse displacements near the cross beams. The general transverse behaviour of the exterior girders was similar to that of a clamped beam.

Based on the experimental and numerical study, the hypothesis is that longitudinal cracking between the exterior and adjacent girders causes an internal force redistribution. Additionally, as a consequence of the longitudinal cracking, the total lateral stiffness of the exterior composite girder reduces and the lateral displacement increases further.

An analytical model will be modelled based on these observations. Mainly focusing on the exterior composite girder and the adjacent girder since the exterior composite girders have the lowest lateral stiffness. First, considering the load until longitudinal cracking followed by an internal force redistribution that eventually leads to failure is assumed to be governed by longitudinal shear resistance or biaxial bending. Additionally, vertical shear is also included in the verification, as it is required according to European Standards. However, none of the previously studied investigations proved that vertical shear was critical. Thus, vertical shear is considered but can not be directly linked to the proposed analytical model.

# 4 Analytical Design Using the Strut and Tie Method

The following chapter describes the design framework for the existing steel-concrete composite bridges without mechanical connectors. The framework is based on observations from laboratory experiments on bridge specimens and FEM analysis of similar specimens. A further description of these can be found in Chapter 3. The focal point of this framework is to describe the behaviour of the exterior bridge girder and the mechanism that leads to failure. The framework links the analytical model to the cross-section verifications for longitudinal shear, biaxial bending and vertical shear.

## 4.1 Compatibility-based Strut and Tie Method

A nonlinear compatibility-based strut and tie model (C-STM) has been developed to represent the behaviour of steel-concrete composite bridges in Amsterdam. The method aims to describe behaviour helping to determine the bearing capacity of the bridges. The bearing capacity is determined from a cross-section verification of *longitudinal shear*, *vertical shear* and *biaxial bending*. The C-STM first determines when longitudinal cracking between one of the exterior and the adjacent girders occurs. Figure 4.1 indicates cracking between the exterior and adjacent girder from underneath. This cracking occurs due to a combination of transverse bending from the single point load,  $F$ , between the exterior and adjacent steel girder and a lack of transverse reinforcement.

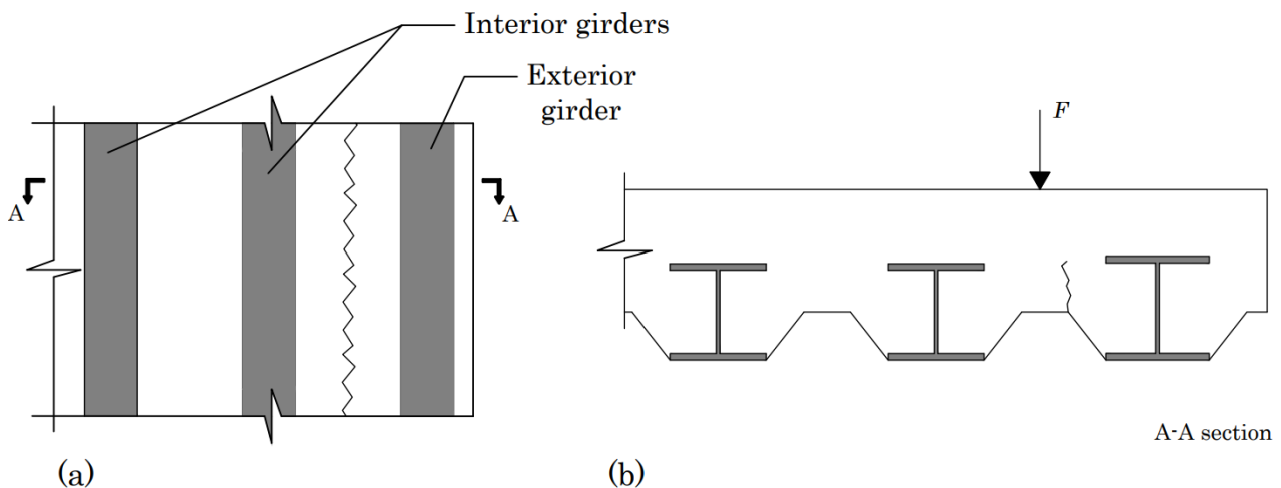


Figure 4.1: The cracks due to lack of transverse reinforcement. (a) bottom view showing the cracks underneath the exterior and adjacent girder. (b) shows the cross-section of the bridge slab.

The exterior girder is investigated as its lateral stiffness is lower than any of the interior girders, which is assumed to decrease its bearing capacity. In contrast, the in situ testing, introduced in Chapter 3, discovered that for loading between interiors girders, the load was distributed to the four adjacent girders. Therefore, the load taken by each girder is lower than for loading

between an exterior composite girder and the adjacent girder. The proposed C-STM is shown in Figure 4.2, showing the geometry of the model and the forces acting on it.

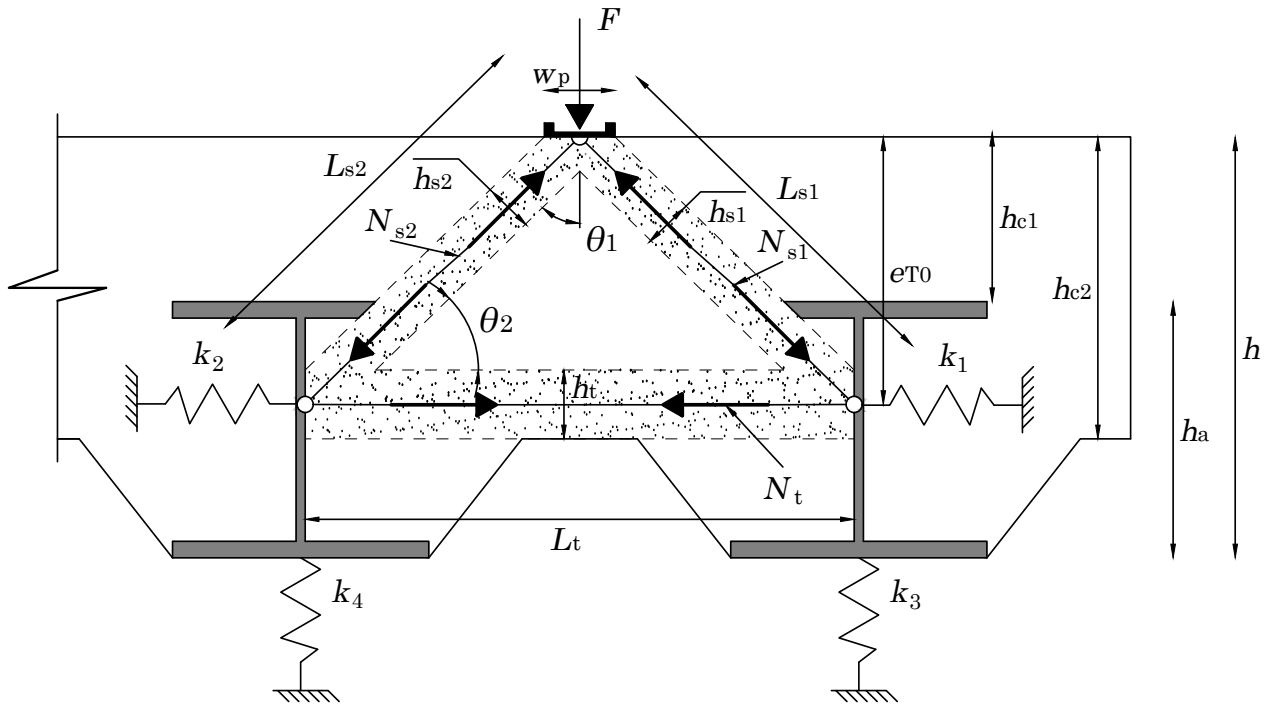


Figure 4.2: Geometry of C-STM and forces acting on the model.

From Figure 4.2 it is assumed that the stresses distribute to the elastic neutral axis of the composite girders. In reality, the stresses will distribute over the height of the steel girders, mainly concentrating at the bottom steel flange, as shown in Figure 3.2. The principle of the C-STM is to simplify nonlinear stress patterns. The C-STM is developed as a generalized model, assuming that the single point load,  $F$ , is applied at the midspan of the composite bridge and located between the exterior and adjacent composite girders. Figure 4.3 illustrates a top view of the C-STM.

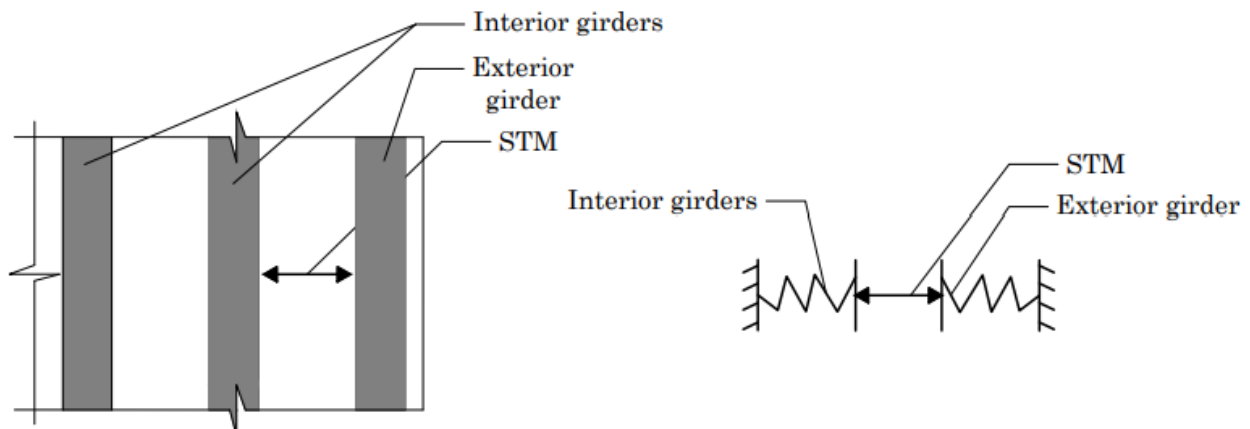


Figure 4.3: Topview of the C-STM, showing the spring components.

The geometry of the C-STM is first defined by determining the position of the spring nodes, which is assumed to equate the elastic neutral axis of the composite section determined from

Eq.4.2, where the modular ratio is obtained from Eq.4.1. The geometrical properties are defined in Figure 4.4.

$$n = \frac{E_a}{E_c} \quad (4.1)$$

$$e_{T0} = \frac{\frac{A_c}{n} z_c + A_a z_a}{A_a + \frac{A_c}{n}} \quad (4.2)$$

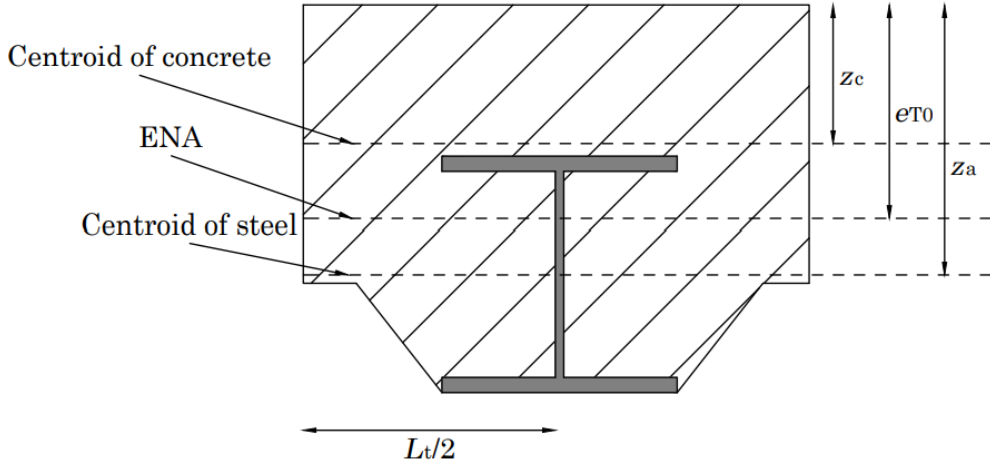


Figure 4.4: Definition of cross-section properties used to determine the geometry of the C-STM and flexural stiffness.

The angles  $\theta_1$  and  $\theta_2$  between the struts and the tie are determined according to Eqs.4.3 and 4.4.

$$\theta_1 = \tan^{-1} \left( \frac{e_{T0}}{0.5L_t} \right) \quad (4.3)$$

$$\theta_2 = 90^\circ - \theta_1 \quad (4.4)$$

The width of the struts and the tie equates to the load dispersal, determined following EN1991-2 [8], at a 1:1 spread-to-depth ratio until the centroid of the bridge, shown in Eq.4.5. Figure 4.5 illustrates the elements included in the load dispersal.

$$L_d = 2e_{T0} + b \quad (4.5)$$

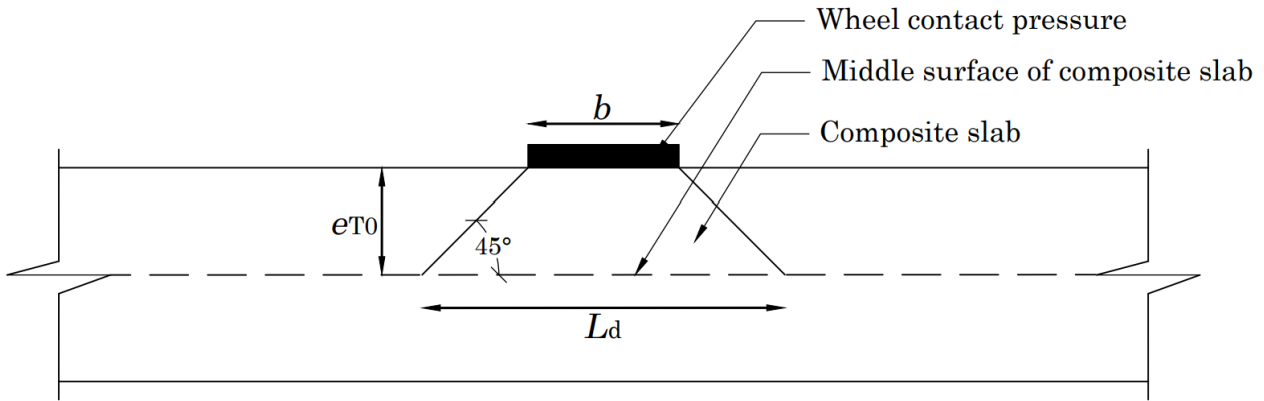


Figure 4.5: Load dispersal according to EN1991-2.

### 4.1.1 Compression Strut

Figure 4.6 shows the constitutive relation for the compression struts in Figure 4.2, which is assumed to be linear elastic. From Figure 4.6, it can be seen that the linear elastic relation only is limited by the ultimate load,  $F_u$ .

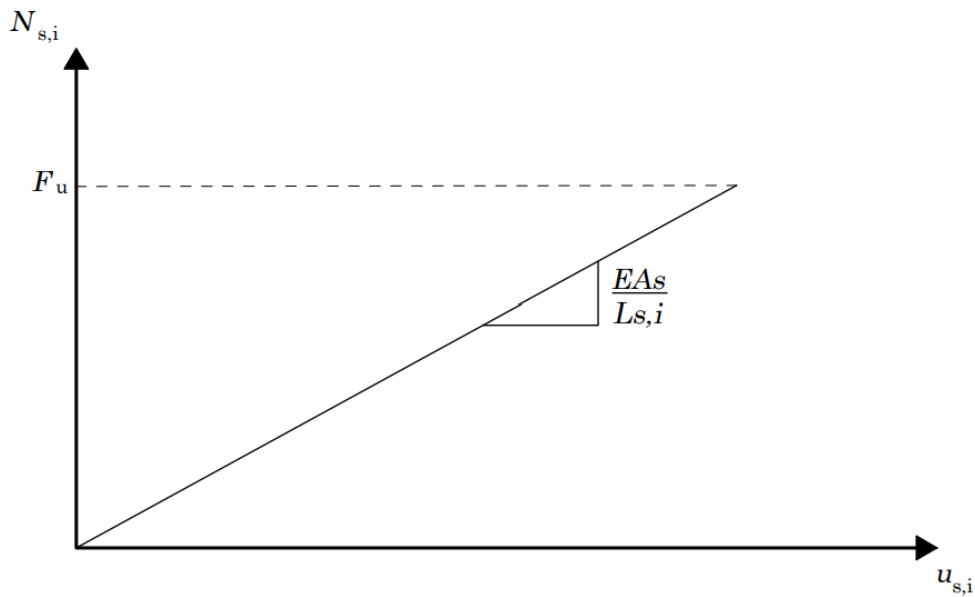


Figure 4.6: Linear constitutive relation of the compression struts.

The height of the compression struts is determined according to Eq.4.6 and depends on the angle between the horizontal plane and the struts and the width of the loading plate as illustrated in Figure 4.2.

$$h_{s,i} = w_p \cos(\theta_1) \quad (4.6)$$

The area of the compression struts is determined according to Eq. 4.7.

$$A_{s,i} = L_d h_{s,i} \quad (4.7)$$

### 4.1.2 Tensile Tie

The constitutive material properties of the tensile tie are nonlinear, as it is assumed to fail when the stresses in the tie reach the tensile strength of concrete. The material properties are shown in Figure 4.7. However, the constitutive relation in Figure 4.7 may be limited by the ultimate load  $F_u$ , although this is not assumed, as none of the test specimens from the laboratory testing failed without longitudinal cracking occurring.

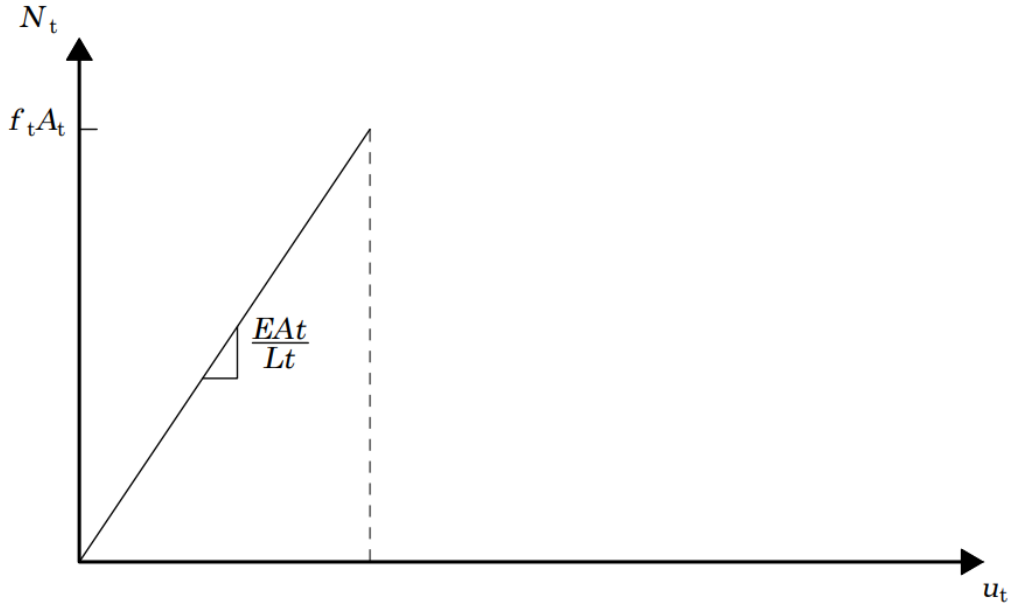


Figure 4.7: Nonlinear constitutive relation of the tensile tie.

The height of the tensile tie,  $h_t$ , is defined, according to Eq.4.8 as half the height of the thinnest concrete section with a limit at the top steel flange.

$$h_t = \frac{h_{c2}}{2} \leq h_{c2} - h_{c1} \quad (4.8)$$

The area of the tensile tie is determined according to Eq.4.9. The area of the tensile tie only considers a limited concrete area, which is a simplification. Ideally, the entire length of the concrete in tension would be accounted for. However, this necessitates dividing the tensile tie into multiple discrete springs over the length of the specimen or including the entire length into the area of the tensile tie by getting a significantly higher stiffness and resistance, which is not assumed to be representative of the onset of cracking.

$$A_t = L_d h_t \quad (4.9)$$

Figure 4.8 shows the C-STM following longitudinal cracking, where the tensile tie is removed.

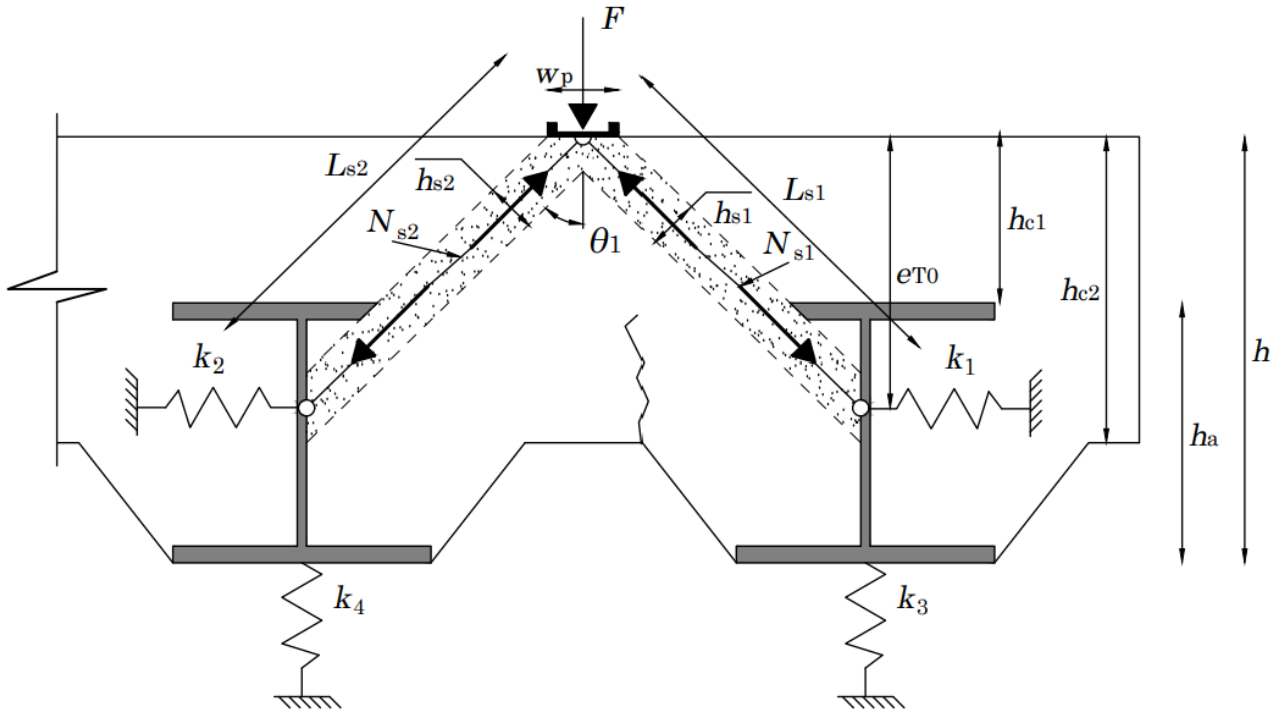


Figure 4.8: Forces acting on the C-STM following the failure of the tensile tie.

### 4.1.3 Vertical Springs

The vertical stiffness of the C-STM is expressed through the position of the single springs,  $k_3$  and  $k_4$ , representing a simply supported beam with a uniform load distributed over a partial length at midspan. The length the load is distributed over equates to the load dispersal. The loading and boundary conditions for the derivation of the vertical springs are shown in Figure 4.9.

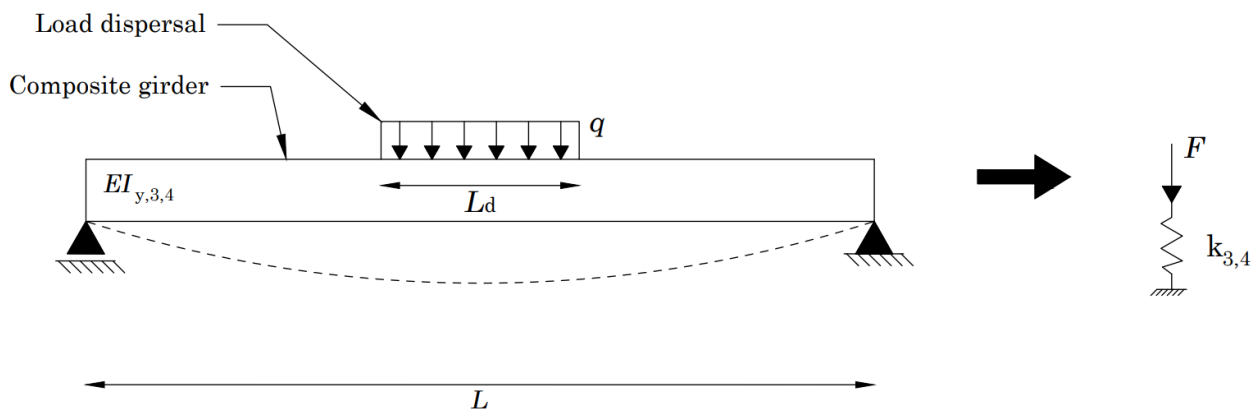


Figure 4.9: Sideview showing the assumption of the vertical spring.

Figure 4.10 shows the constitutive relation for the vertical springs. Hence, assuming linear elastic behaviour, although, in reality, this would be nonlinear, depending on when flexural cracking and yielding occurs. However, the vertical displacement is not the focal point of this research, thus this simplification. From Figure 4.10, it can be seen that the linear elastic relation only is limited by the ultimate load,  $F_u$ .

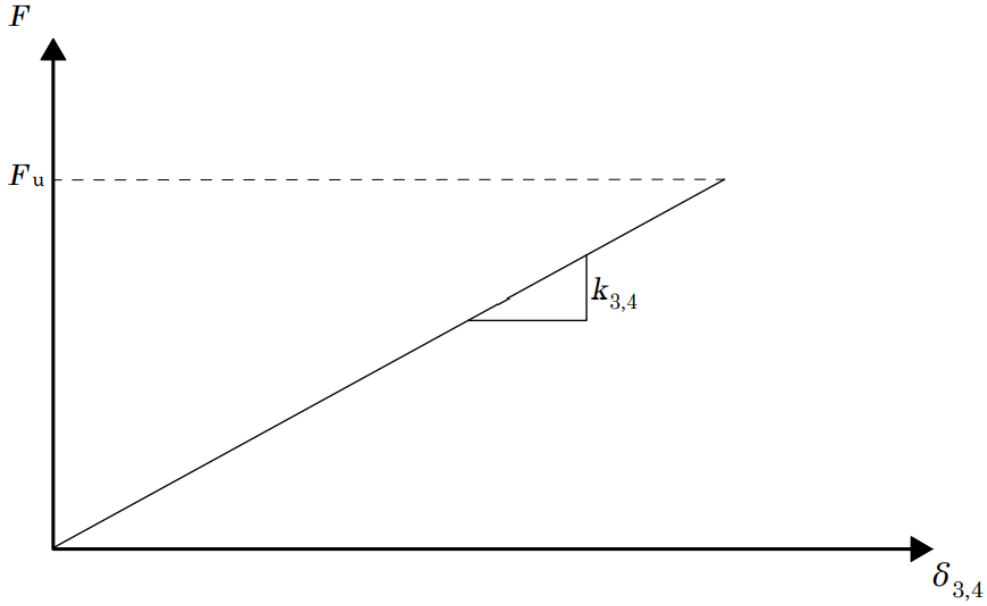


Figure 4.10: Linear constitutive relation for the vertical springs.

The spring constant of the single springs,  $k_3$  and  $k_4$ , requires that the flexural stiffness is obtained. For the following stiffness calculations, the stiffness of the composite slab is determined considering the cross-section of the composite girder, including the steel girder and the concrete encasement. The cross-section of the composite girders is separated at  $L_t/2$ . To fully utilise the concrete area, all the concrete is accounted for and assumed uncracked. The major axis flexural stiffness is determined by transforming the concrete into equivalent steel, using the modular ratio from Eq.4.1. Thus, the vertical flexural stiffness is determined from Eq.4.10.

$$EI_{y,i} = E_a (I_{a,y,i} + I_{c,y,i}n) \quad (4.10)$$

The spring constants,  $k_3$  and  $k_4$ , representing the vertical stiffness of the C-STM, are determined from Eqs.4.11 and 4.12.

$$\delta_{v,i} = \frac{qL_d \left( L^3 - \frac{L_d^2}{2}L + \frac{L_d^3}{8} \right)}{48EI_{y,i}} \quad (4.11)$$

$$k_{3,4} = \frac{qL_d}{\delta_{v,i}} = \frac{48EI_{y,i}}{\left( L^3 - \frac{L_d^2}{2}L + \frac{L_d^3}{8} \right)} \quad (4.12)$$

#### 4.1.4 Lateral Spring Beams

The lateral springs  $k_1$  and  $k_2$  in Figure 4.2 are interpreted as clamped spring beams as shown in Figure 4.11. The beams are assumed to be clamped as shown in the Experimental and Numerical Study in Chapter 3, that the lateral displacement was zero at the location of the cross beams close to the supports. The beams are considered as Euler-Bernoulli beams.

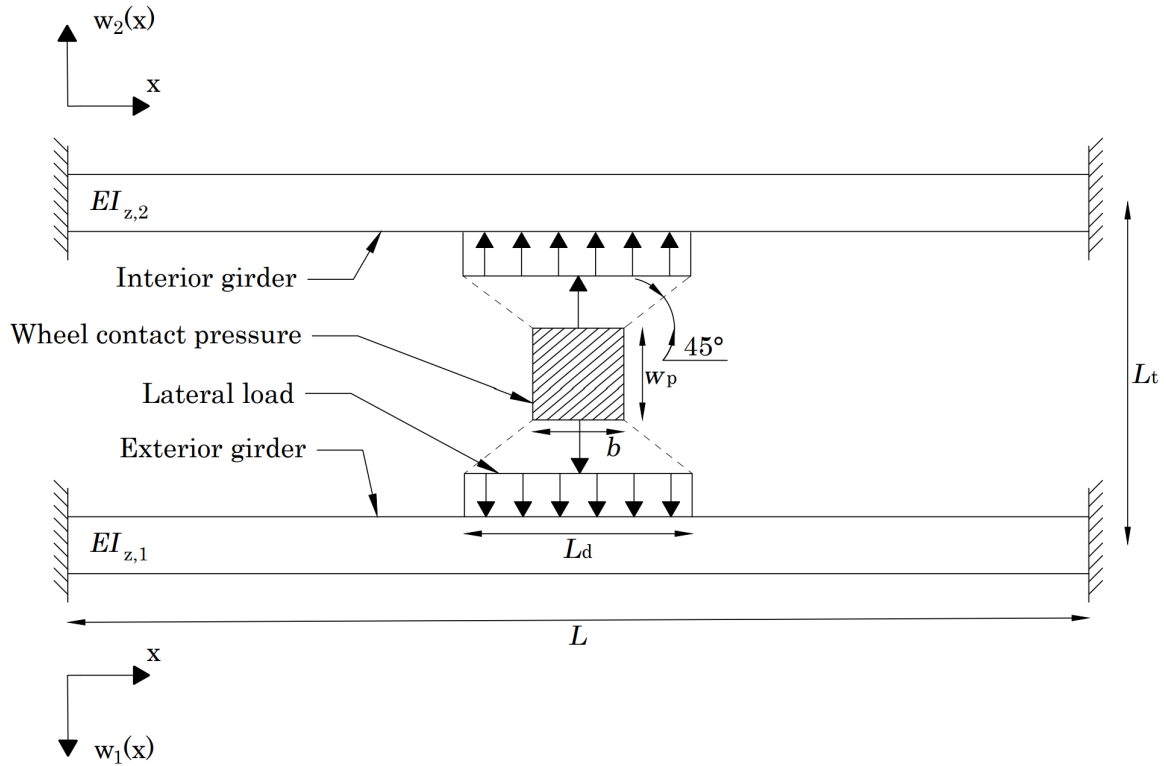


Figure 4.11: Topview of the C-STM in Figure 4.2. Showing configuration of the spring beams, as Euler-Bernoulli beams.

The lateral behaviour is a focal focus point of this model. Therefore, contrary to the vertical springs, described using elastic springs, the lateral stiffness is described using Euler-Bernoulli spring beams. This is done to describe the displacement along the span length of the exterior composite girder.

The interior spring beam is considered linear elastic, as this beam, due to its higher lateral stiffness, is assumed not to crack from minor axis bending. Additionally, the principle of the model is that the interior lateral spring beam always will have a significantly higher stiffness than the exterior lateral spring beam. The constitutive relation for the lateral behaviour of the interior composite girder is shown in Figure 4.12. From the figure, it can be seen that the linear elastic relation only is limited by the ultimate load,  $F_u$ .

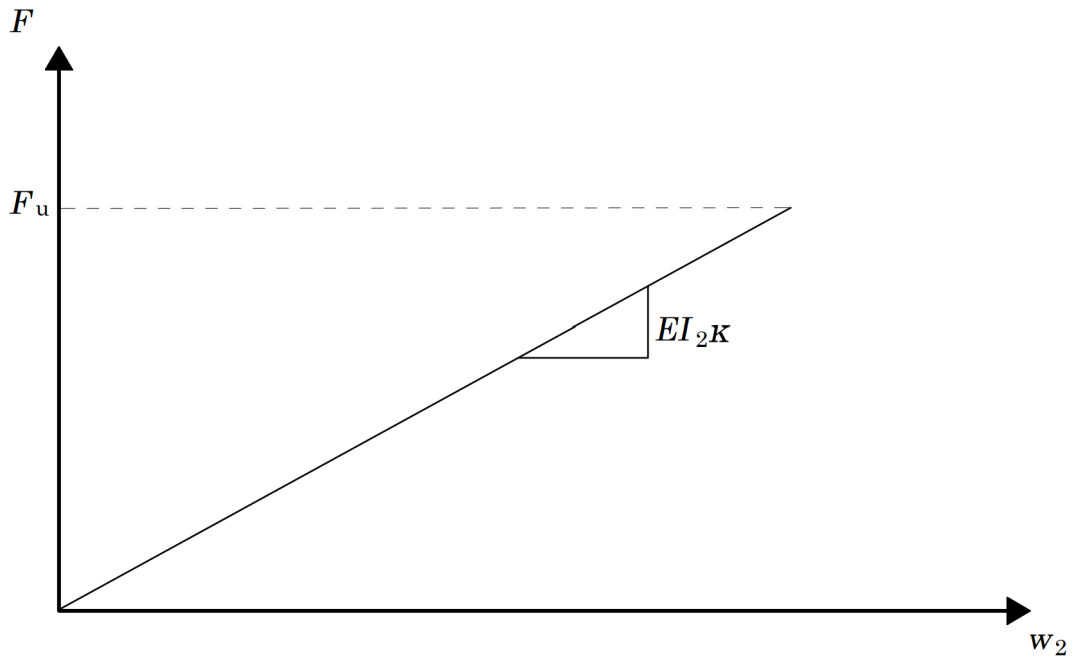


Figure 4.12: Linear elastic constitutive relation for spring 2.

The constitutive relation for the spring 1 is nonlinear, assuming that the stiffness reduces after longitudinal cracking. Spring 1 has the constitutive relation shown in Figure 4.13. However, the ultimate load may occur earlier than shown in Figure 4.13, for instance, before longitudinal cracking.

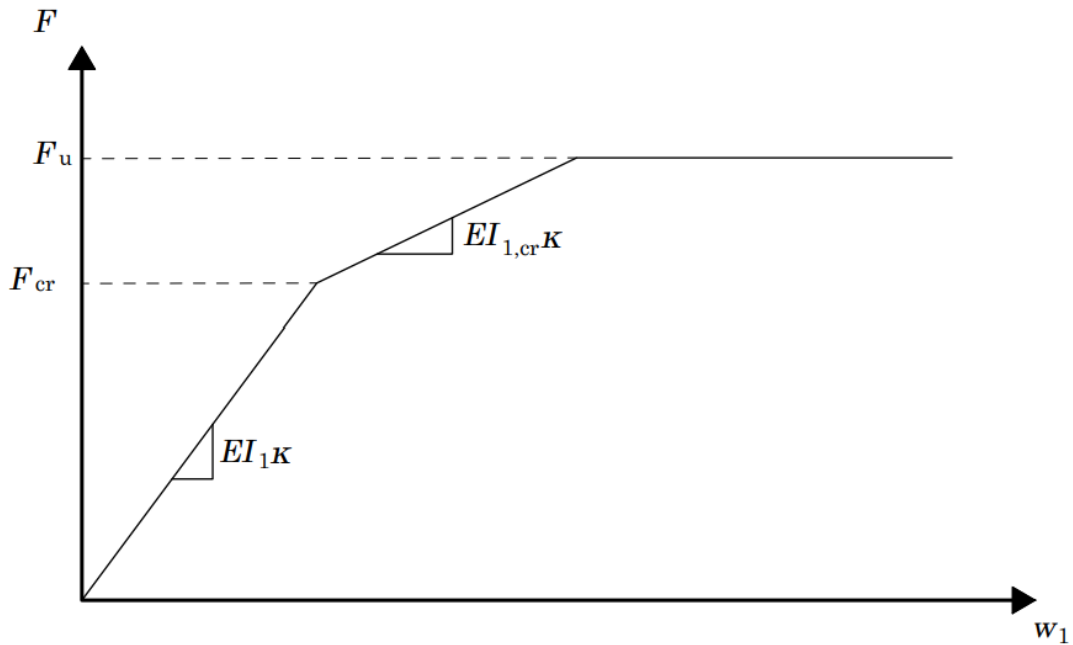


Figure 4.13: Constitutive relation for spring 1.  $F_u$  is the ultimate load assuming full shear connection

As previously mentioned following longitudinal cracking, it is conservatively assumed that the concrete at the tensile tie has failed. Thus for the lateral stiffness, the stiffness of the exterior

girder is determined by neglecting this concrete. Figure 4.14 illustrates the concrete considered when determining the lateral flexural stiffness of the exterior girder (spring 1).

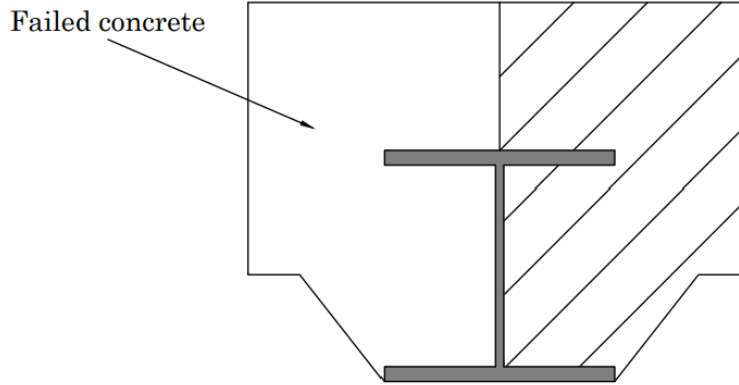


Figure 4.14: Cross section considered for calculating the flexural stiffness of the cross-section,  $EI_{1,cr}$ , following longitudinal cracking.

The beams in Figure 4.11 have the stiffness  $EI_i$ . The previous section demonstrated how to determine the flexural stiffness of the composite girders about the major axis; a similar approach is required to determine the flexural stiffness about the minor axis. However, the stiffness is described through the differential equation of a clamped beam. Therefore, only the flexural stiffness must be obtained as part of the lateral stiffness calculation. The lateral flexural stiffness is determined from Eqs.4.13 and 4.14. The stiffness of the interior girder is assumed to account for the lateral stiffness of the adjacent composite girders. Thus  $p$  is the total number of girders without the exterior girder.

$$EI_{z,1} = E_a (I_{a,z,1} + I_{c,z,1}n) \quad (4.13)$$

$$EI_{z,2} = EI_{z,1}p \quad (4.14)$$

Although the dimensions of the steel girders may vary, meaning the exterior and adjacent steel girder may have slightly different dimensions, it is for simplicity assumed that this difference can be neglected.

Following longitudinal cracking, the lateral stiffness of the exterior composite girder is reduced, so only the area in Figure 4.14 is considered. The lateral flexural stiffness is determined from Eq.4.15.

$$EI_{z,1,cr} = E_a (I_{a,z,1} + I_{c,z,1,cr}n) \quad (4.15)$$

However, the constitutive relation in Figure 4.13 may be limited by failure due to longitudinal shear, biaxial bending, vertical shear or crushing of the concrete struts. Hence, the cross-section verification includes two stages, stages 1 and 2. The first stage checks the bearing capacity at longitudinal cracking and whether the resistance is sufficient to resist the load at longitudinal cracking,  $F_{cr}$ . If this happens, it is expected that brittle failure will occur, as the bearing capacity will reduce following longitudinal cracking. The second stage determines the bearing

capacity following longitudinal cracking, where it is expected that a reduction of the resistances has occurred. From what has been observed during experiments and from the numerical models, it can be expected that this will occur as a ductile failure. Figure 4.15 shows the loading versus displacement depending on the failure type. If the failure occurs when the load reaches the load at longitudinal,  $F_{cr}$ , it is expected to be brittle. However, it is still related to uncertainty, as no case of failure before or at longitudinal cracking has been observed from the testing.

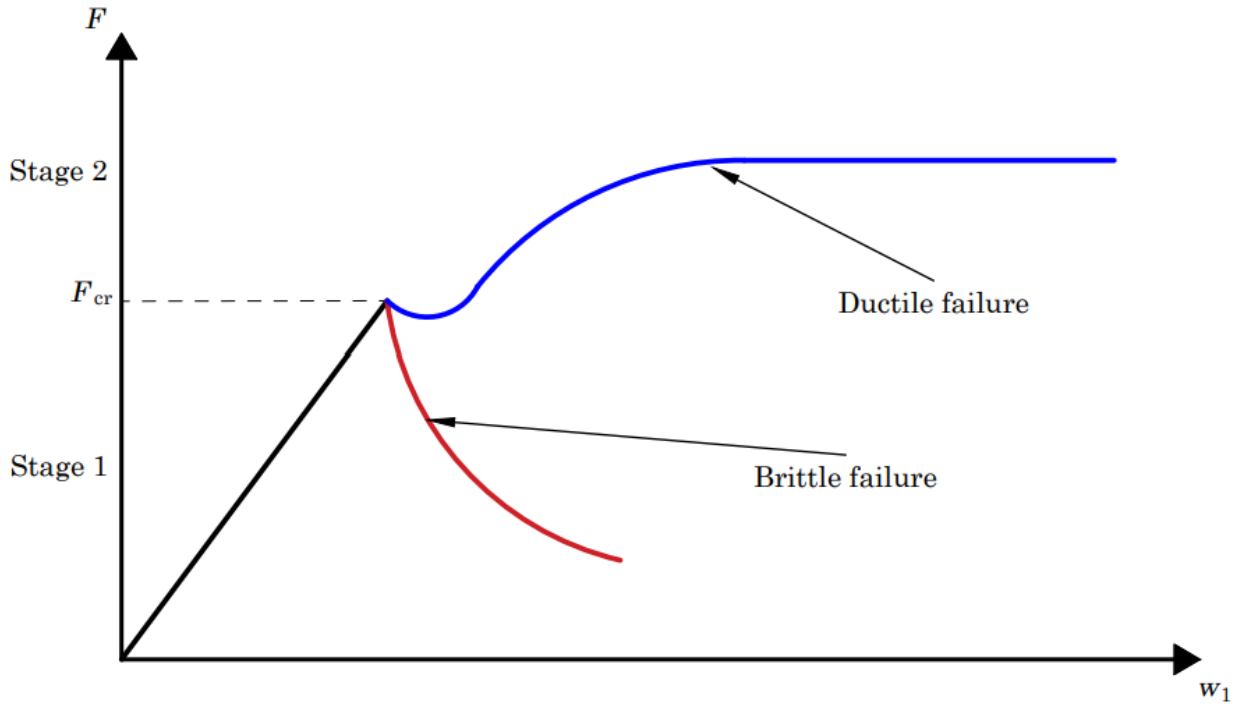


Figure 4.15: Example of the load versus displacement depending on failure type.

Using the constitutive relations, the load at longitudinal cracking,  $F_{cr}$ , can be determined from the criteria in Eq.4.16.

$$\sigma_t(F_{cr}) = f_t \quad (4.16)$$

When this occurs, it must be verified that the bearing capacity is sufficient. If this is not the case, the specimen is expected to fail when longitudinal cracking occurs, as this reduces the bearing capacity. Thus, the expected failure is brittle. Figure 4.16 shows a flowchart to establish the C-STM.

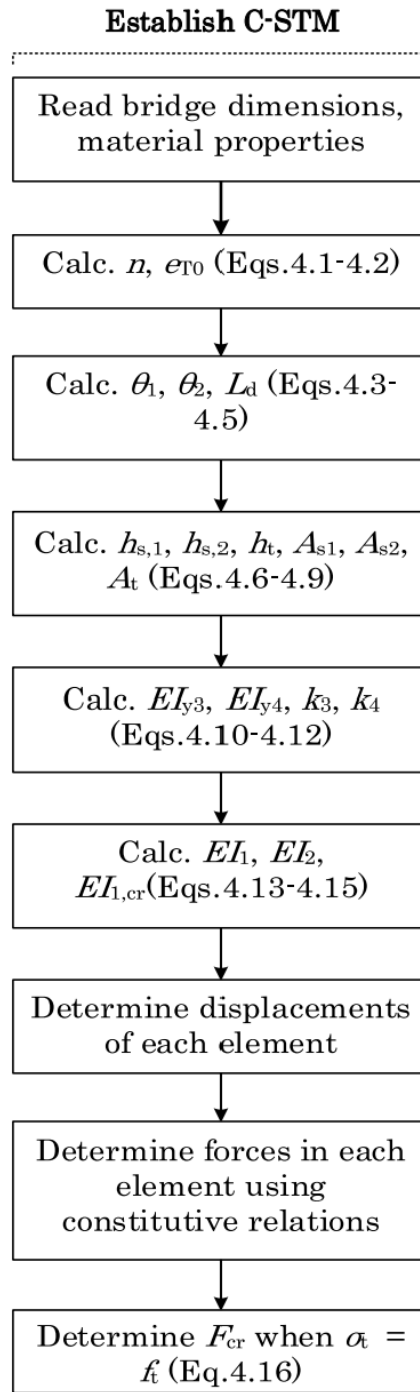


Figure 4.16: Flowchart to establish the C-STM.

#### 4.1.5 Stage 1 - Cross-section Verification

The following goes through the cross-section verification, assuming the specimen will fail before longitudinal cracking, which is expected to be brittle, as following longitudinal cracking, a reduction of the bearing capacity is expected to occur. The load at longitudinal cracking is determined using the proposed C-STM. If the bearing capacity is sufficient, the cross-section verification for the stage following longitudinal cracking must be performed to determine the bearing capacity and the failure mode.

#### 4.1.5.1 Compression Resistance of Struts

The capacity of the compression struts must be sufficient. This can be verified by calculating when the strut reaches its maximum capacity from Eq.4.17 and from the C-STM determining at what load this force is exceeded.

$$\sigma_{s,i,max} = f_c \quad (4.17)$$

#### 4.1.5.2 Longitudinal Shear Resistance

The longitudinal shear resistance is evaluated globally, as the steel-concrete interface must be able to transfer the shear force. Before longitudinal cracking, the concrete is assumed to be in full contact with the steel. Additionally, it is assumed that the longitudinal shear resistance only comes from cohesion, which is a simplification neglecting the Mohr-Coulomb mechanism until longitudinal cracking occurs. It is assumed that the steel-concrete cohesion is 0.54 MPa derived from the literature review in chapter 2. This is the lowest value found from experiments studying the steel-concrete bond strength of encased HEB profiles, similar to DIN profiles. It is assumed that this value distributes around the effective contact perimeter, but only considering 50% of the perimeter of the bottom part of the top steel flange, as this usually has a lower bond due to air bubbles from the casting [19]. The effective perimeter is the steel-concrete contact within the concrete cover requirements. The longitudinal shear resistance is sensitive to the concrete cover, so it is assumed that for any longitudinal shear resistance of the steel-concrete contact surfaces, there must be at least 38 mm concrete cover at the bottom and the sides of the encased girders. At least 51 mm concrete cover must be at the top [19]. The following assumes the concrete cover at the bottom is insufficient due to the concrete-free bottom flanges as illustrated in Figure 4.17. However, to determine the longitudinal shear resistance, it must generally be considered that the concrete cover on the other sides can also be insufficient.

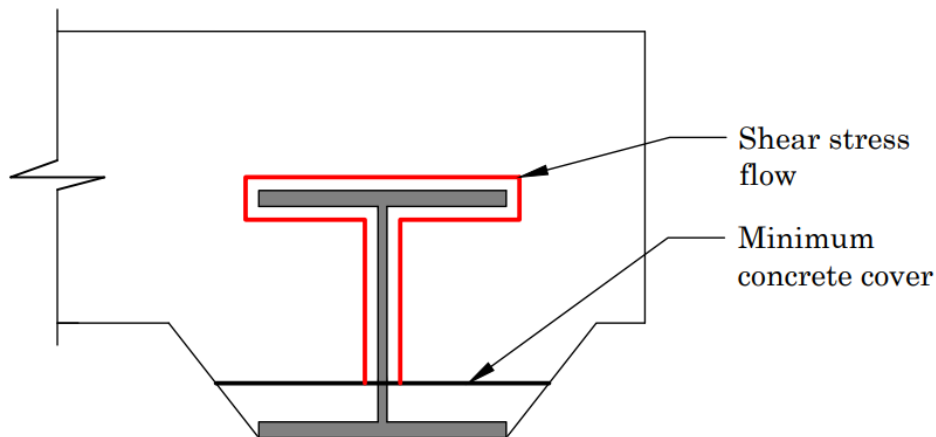


Figure 4.17: Contact perimeter for the longitudinal shear resistance before longitudinal cracking.

The longitudinal shear resistance on a stress level is determined using Eq.4.18. Evaluating the longitudinal shear resistance globally, it is obtained from Eq.4.19.

$$\tau_{Rd} = c \quad (4.18)$$

$$V_{x,Rd} = cLu_{eff} \quad (4.19)$$

Where  $u_{eff}$  is the effective contact perimeter, shown as the red line in Figure 4.17.

#### 4.1.5.3 Biaxial Bending Resistance

The resistance to biaxial bending is determined by satisfying the condition in Eq.4.20.

$$\sqrt{\left(\frac{M_{y,Ed}}{M_{y,Rd}}\right)^2 + \left(\frac{M_{z,Ed}}{M_{z,Rd}}\right)^2} \leq 1, 0 \quad (4.20)$$

The acting bending moments are determined according to Eqs.4.22 and 4.24, as the inclined force from the compression strut can be separated into a vertical and lateral force component, as shown in Figure 4.18.

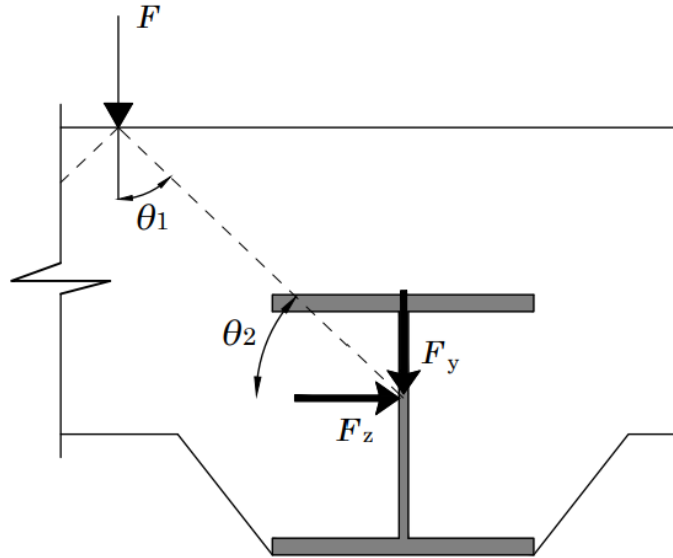


Figure 4.18: Vertical and lateral force components acting on the exterior girder.

The moment from the vertical force component,  $F_y$ , is determined for a simply supported beam subject to a point load at midspan. The moment due to the lateral force component,  $F_z$ , is determined assuming the beam is subject to a single point load at midspan and clamped at both ends, as shown in Figure 4.11. The force components and their moments are determined from Eqs.4.21 and 4.24.

$$F_y = \frac{F}{2 \cos \theta_1} \cos \theta_1 \quad (4.21)$$

$$M_{y,Ed} = \frac{1}{4} F_y L \quad (4.22)$$

$$F_z = \frac{F}{2 \cos \theta_1} \cos \theta_2 \quad (4.23)$$

$$M_{z,Ed} = \frac{1}{8} F_z L \quad (4.24)$$

The moment resistances are determined assuming the concrete is cracked and considering the cross-section in Figure 4.4. First, the plastic bending moment resistance is determined assuming a full shear connection, which must be checked to determine the degree of shear connection. The plastic neutral axis can be either in concrete or steel and concrete. For the following cases, it is assumed that it is in the steel, so a part of the steel is in compression. The steel is in full tension if the plastic neutral axis is in the concrete. The plastic moment resistance about the major axis,  $M_{y,pl,Rd}$ , is determined in accordance with Figure 4.19 and from Eq.4.25.

$$M_{y,pl,Rd} = F_{cc,y} z_1 + F_{ac,y} z_2 \quad (4.25)$$

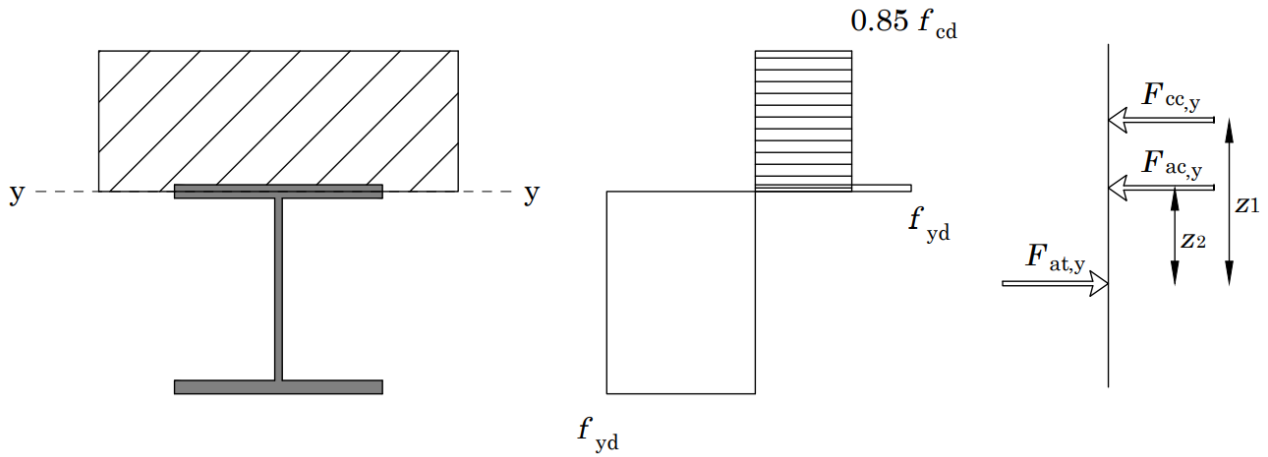


Figure 4.19: Example of plastic bending resistance calculation about the major axis with the plastic neutral axis in the steel flange.

A similar approach is used for the plastic moment resistance,  $M_{z,pl,Rd}$ , about the minor axis and is shown in Figure 4.20 and Eq.4.26.

$$M_{z,pl,Rd} = F_{cc,z} y_1 + F_{ac,z} y_2 \quad (4.26)$$

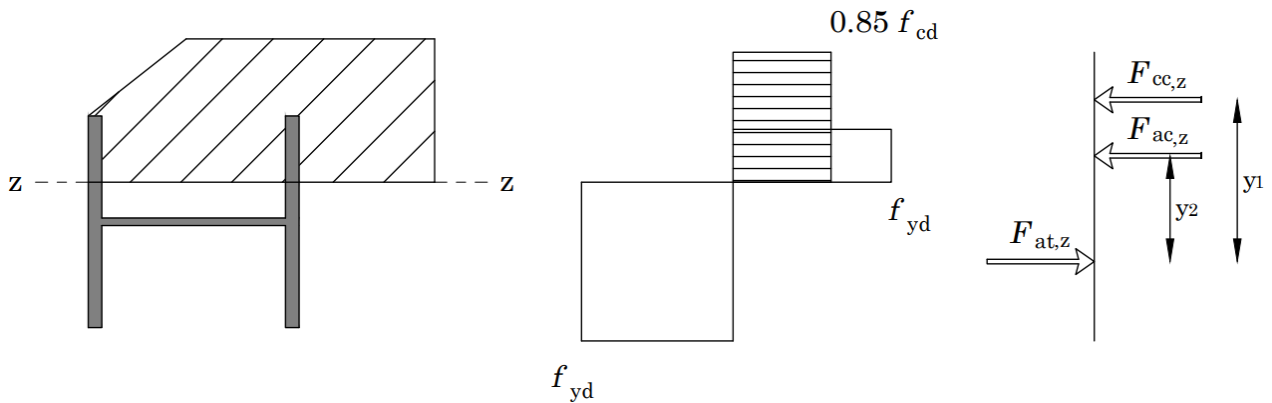


Figure 4.20: Example of plastic bending resistance calculation about the minor axis with the plastic neutral axis in the steel flange.

It must be verified that the longitudinal shear resistance,  $V_{x,Rd}$  is sufficient to transfer the compression force from the concrete. As there is biaxial bending, two compression forces are determined. The degree of shear connection,  $\eta$ , is determined from Eq.4.27. If the degree of shear connection is below 1.0, there is a partial shear connection. Otherwise, there is a full shear connection.

$$\eta = \frac{V_{x,Rd}}{F_{cc,y} + F_{cc,z}} \quad (4.27)$$

If there is a partial shear connection, a reduction of the compression forces is necessary. The compression forces are reduced using Eqs.4.28 and 4.29.

$$F_{cc,y,red} = F_{cc,y}\eta \quad (4.28)$$

$$F_{cc,z,red} = F_{cc,z}\eta \quad (4.29)$$

Figure 4.21 shows an example plastic moment resistance calculation about the major axis in the case of partial shear connection.

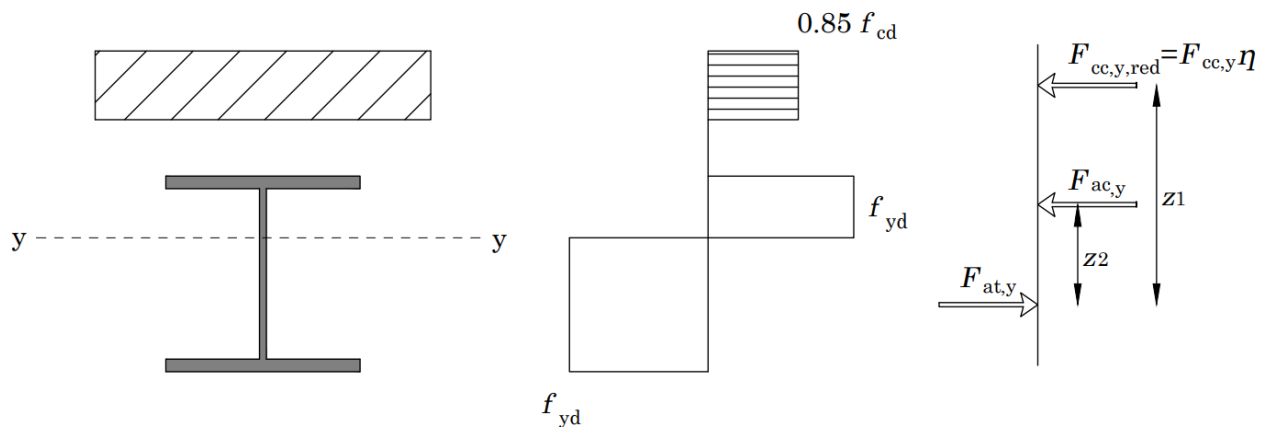


Figure 4.21: Example of plastic moment resistance calculation about the major axis with a reduced concrete compression force due to partial shear connection.

The distances between the compression forces and the tensile force,  $z_1$ ,  $z_2$ ,  $y_1$  and  $y_2$ , are from the centroid of the compressive stress block, which is not necessarily half the height of that block, as the geometry varies across the height. The plastic neutral axis and the centre of each force component are usually solved using an analytical expression, as composite slabs often consist of an I-girder with a concrete slab on top. For this case, where the cross-section has many different geometrical shapes, and the I-girders are encased, iteration is preferred to determine the plastic neutral axis and the centroid of each force component. An example of the iteration procedure using MATLAB is shown in Appendix C, including the remaining calculation steps to determine the plastic bending resistance and how to perform the calculation using this MATLAB code. Additionally, the code also plots the resistances to display an interaction diagram.

The calculation procedure to determine the biaxial bending resistance is shown in the flowchart in Figure 4.22. The calculation of the bending resistance mainly depends on the degree of shear connection, which is determined from the longitudinal shear resistance.

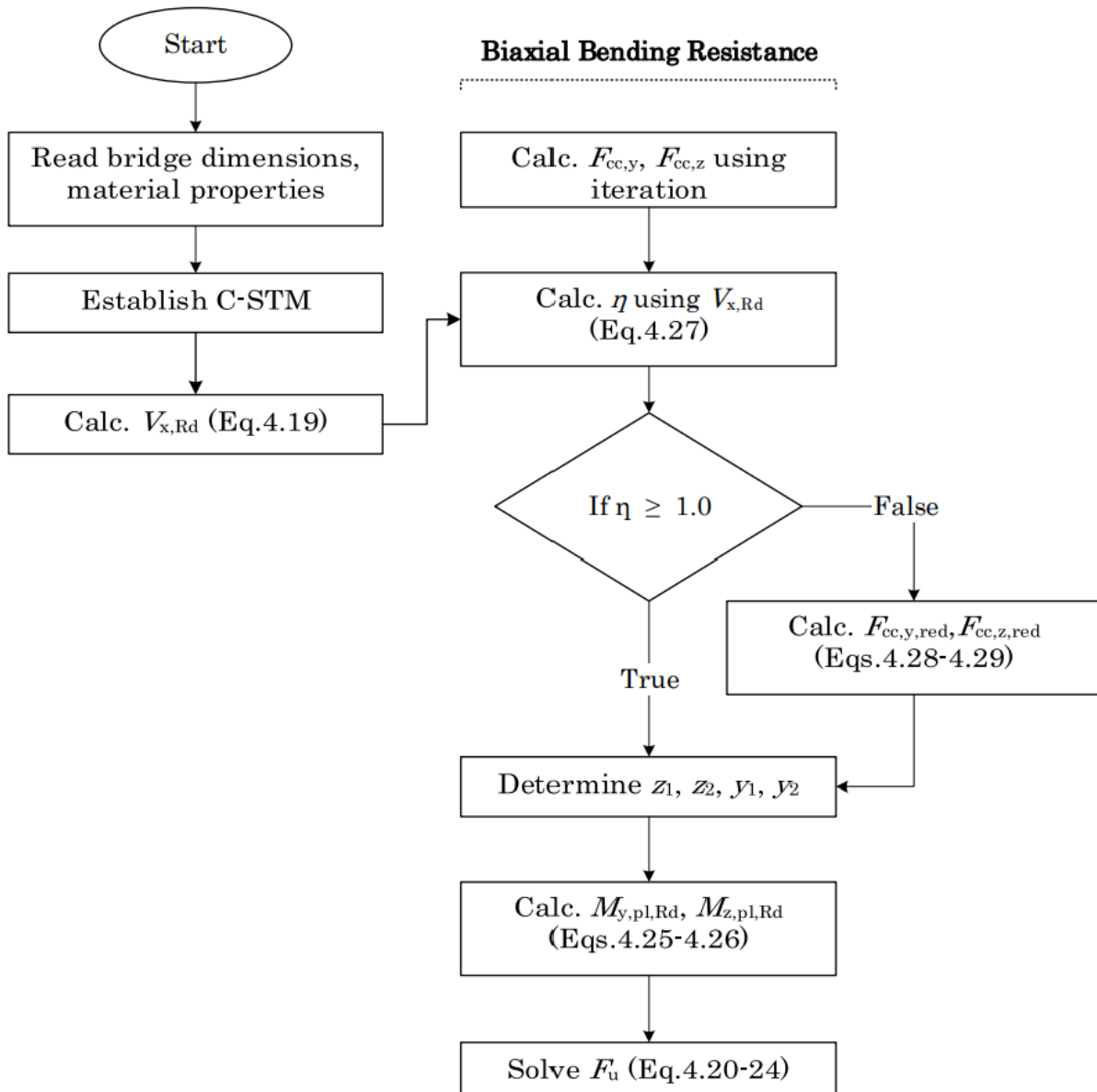


Figure 4.22: Flowchart of the biaxial bending calculation.

#### 4.1.5.4 Vertical Shear Resistance

The vertical shear resistance of the steel-concrete composite bridges without mechanical connectors is calculated, assuming that individual contributions from the steel and the concrete determine the resistance. The equations in the following have been derived based on a study by Vasdravellis and Uy [13], who investigated the shear strength of steel-concrete composite beams. This has been described further in the Literature Review Chapter 2. The concrete encasement below the top steel is conservatively neglected, as its influence on the vertical shear resistance is unknown. Eq.4.30 obtains the composite vertical shear resistance.

$$V_{comp} = V_{pl,Rd} + V_{slab} \quad (4.30)$$

The individual contributions from the steel girder and the concrete are respectively determined from Eqs.4.31 and 4.32, assuming full shear connection. The dimensions from Eq.4.32 are shown in Figure 4.23.

$$V_{pl,Rd} = \frac{A_v f_{yd}}{\sqrt{3}} \quad (4.31)$$

$$V_{slab} = \varphi_s f(\lambda_{sd}) (b_f D_{slab})^{0.7} \sqrt{f_c} \quad (4.32)$$

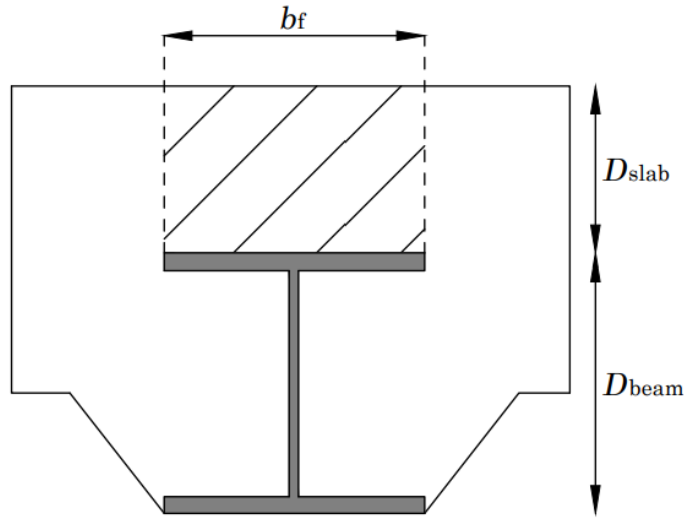


Figure 4.23: Cross-section properties considered for calculation of the vertical shear.

The slenderness ratio,  $\lambda_{sd}$  is determined from Eq.4.33. The function  $f(\lambda_{sd})$  is obtained from Eq.4.34.

$$\lambda_{sd} = D_{slab}/D_{beam} \quad (4.33)$$

$$f(\lambda_{sd}) = 110\lambda_{sd} + 13 \quad (4.34)$$

$\varphi_s$  is a safety factory derived on the mean values and standard deviation from a FEM model used in the study. The above equations are valid for full shear connection. However, for the case of partial shear connection, additional calculation steps are required to account for the degree of shear connection. The first step is to determine the vertical shear resistance assuming full shear connection, as previously. The vertical shear resistance assuming zero interaction,  $V_{comp,0}$ , is determined from Eq.4.35. Thus, the vertical shear resistance for the degree of shear connection,  $V_{comp,\eta}$ , can be determined using linear interpolation between the vertical shear resistance at full and no shear interaction since the relation between the vertical shear resistance and the degree of shear connection is a linear function. The shear resistance for the degree of shear connection,  $V_{comp,\eta}$ , is determined from Eq.4.36.

$$V_{comp} = V_{comp,0}(0.76\lambda_{sd} + 0.92) \quad (4.35)$$

$$V_{comp,\eta} = (V_{comp} - V_{comp,0})\eta + V_{comp,0} \quad (4.36)$$

Figure 4.24 shows the flowchart describing how to calculate the vertical shear resistance, which like the biaxial bending resistance, depends on the longitudinal shear resistance.

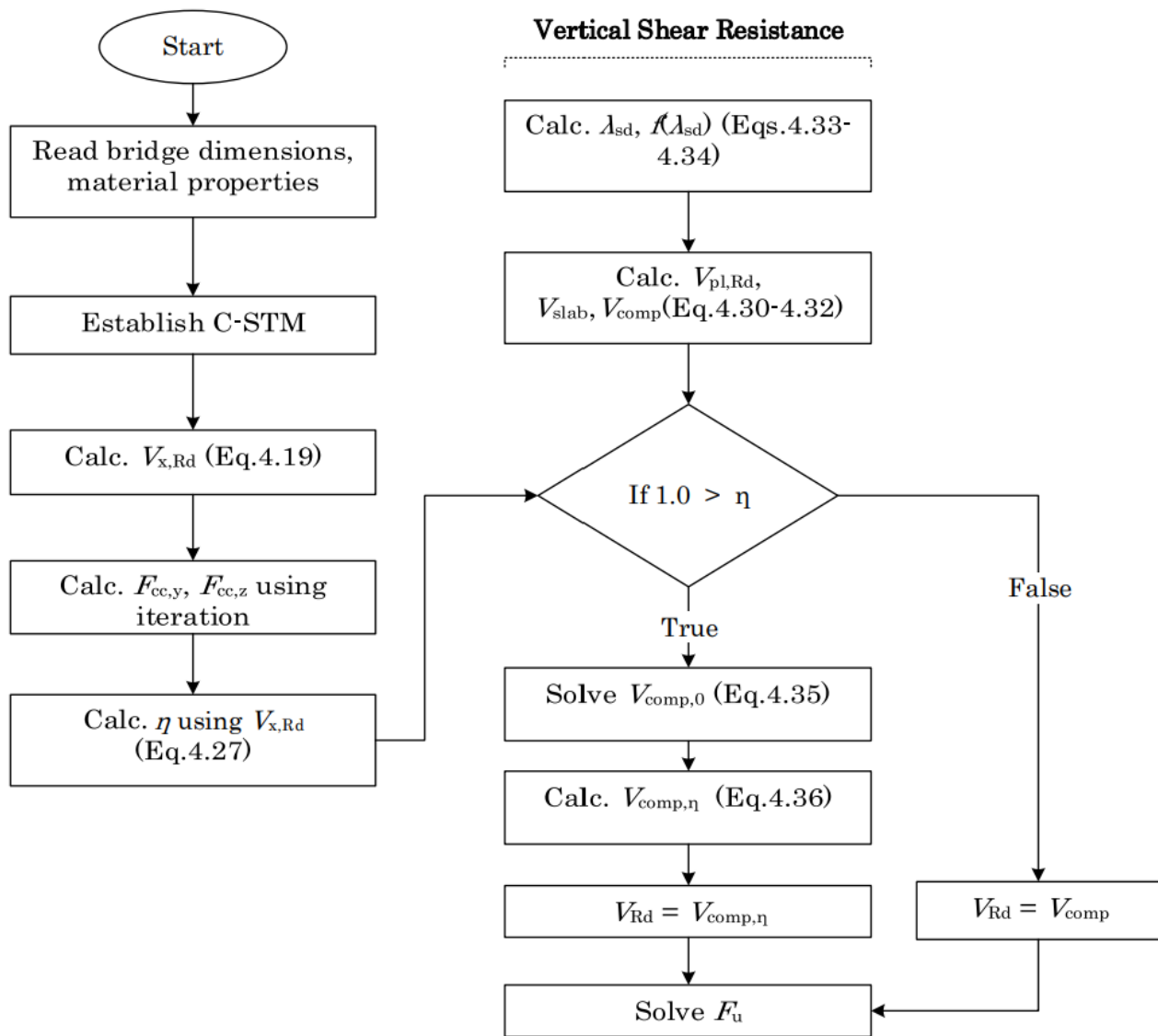


Figure 4.24: Flowchart of the vertical shear resistance calculation.

Figure 4.25 describes the entire procedure of the stage 1 cross-section verification.

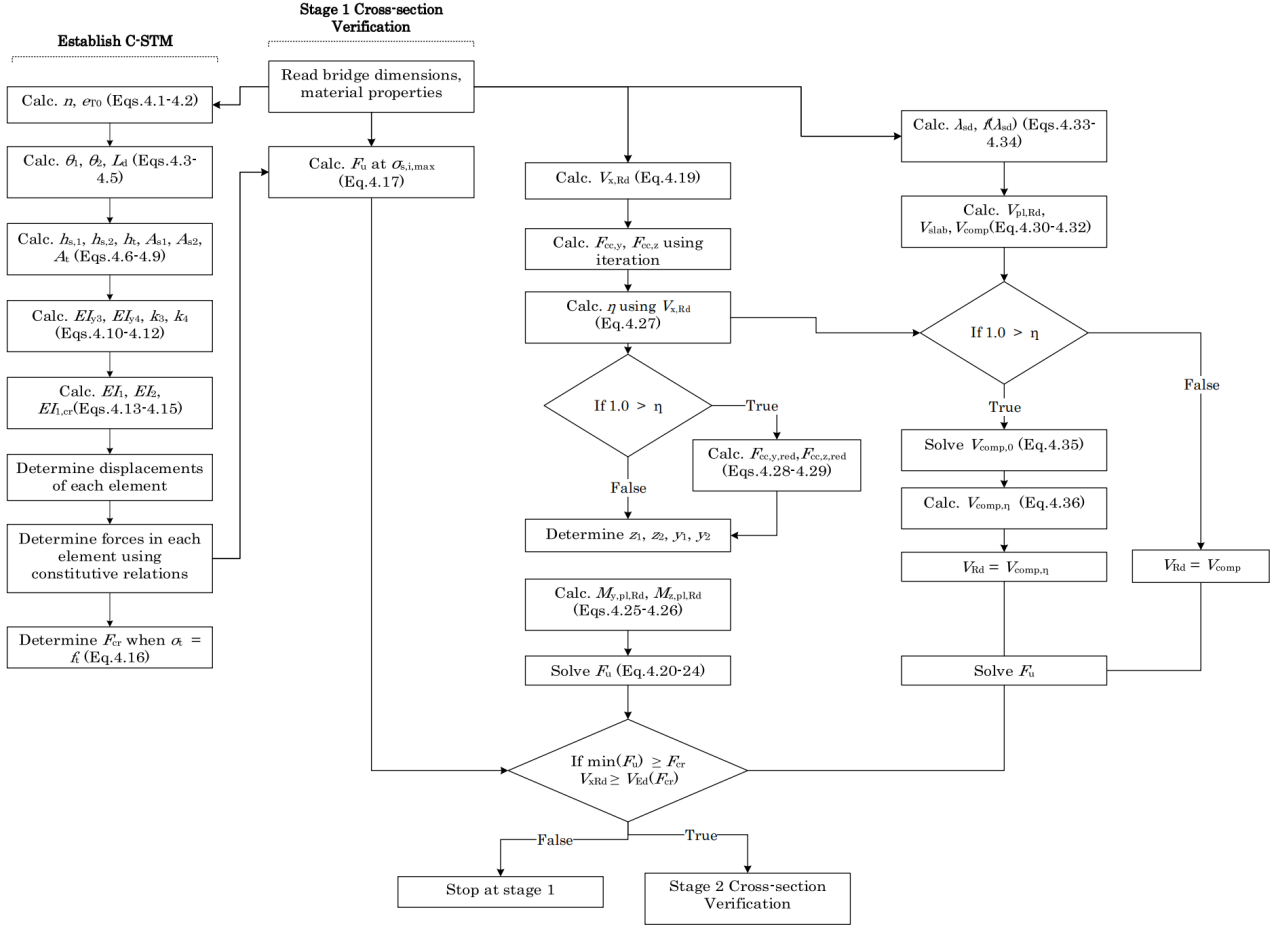


Figure 4.25: Flowchart for the stage 1 cross-section verification.

## 4.1.6 Stage 2 - Cross-section Verification

If the stage 1 cross-sections show that the resistance exceeds the load at longitudinal cracking, ductile failure is expected and the stage 2 cross-section verification must be calculated. This is shown in the following. Only the approach to determine the longitudinal shear resistance changes following longitudinal cracking. However, this must be determined before calculating the biaxial bending and vertical shear resistance, as the degree of shear connection influences both resistances. If, in the following, the longitudinal shear resistance determined provides the same degree of shear connection, the biaxial bending and vertical shear resistances are the same as previously determined.

### 4.1.6.1 Longitudinal Shear Resistance

Following longitudinal cracking, the lateral stiffness reduces as the tensile tie has zero resistance, and the lateral stiffness of the exterior composite girder is reduced as well, as shown in Figure 4.13. This means that the lateral displacement of the exterior composite girder,  $w_1$ , increases further. Thus, due to the limited ductility of the concrete, it will form an opening from the steel, which reduces the effective steel-concrete contact perimeter, as illustrated in Figure 4.26.

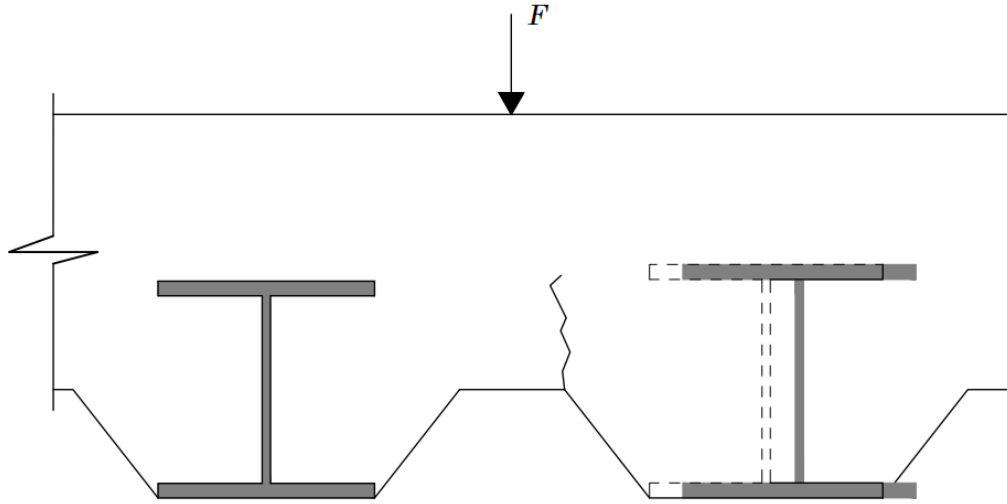


Figure 4.26: An opening is formed between the concrete and steel of the exterior girder facing the other girder.

The steel-concrete opening in Figure 4.26 is evaluated using a strain criterion. This criterion assumes that when the concrete's strain exceeds its tensile strain, it will form an opening between the steel and concrete. The strain criterion is obtained from Eq.4.38. The concrete strain is determined from Eq.4.37, which considers the length of concrete between the steel girders, so a larger concrete length makes the concrete more subject to this opening along the span of the bridge.

$$\epsilon_{w1}(x) = \frac{w_1(x)}{L_t} \quad (4.37)$$

$$\epsilon_{cr} = \frac{f_t}{E_c} \quad (4.38)$$

The contact perimeter is reduced for the section at midspan having a gap between the steel and the concrete. Figure 4.27 illustrates the normal stresses occurring on the outside surface of the exterior girder due to the opening formed by the concrete. The shear resistance due to the Mohr-Coulomb mechanism is shown in Eq.4.39 [20]. It is assumed that the confinement due to the Mohr-Coulomb mechanism only occurs on the vertical surface facing outwards, neglecting the bottom contact perimeter, due to the required concrete cover at 38 mm. Additionally, it is still assumed that there is a reduction of the contact perimeter at the bottom part of the top steel flange due to air bubbles from casting. Closer to the supports, there is full contact between the steel and concrete around the steel perimeter but no confinement. Thus, the shear resistance merely comes from cohesion.

$$\tau_{Rd} = c + \mu\sigma \quad (4.39)$$

As described in the Literature Review Chapter 2, the shear resistance due to adhesion is 0.54 MPa, and the coefficient of friction is 0.30. Figure 4.27 illustrates the shear stress flow along the beam with the assumption that when the concrete forms an opening between the steel, the contact perimeter is reduced.

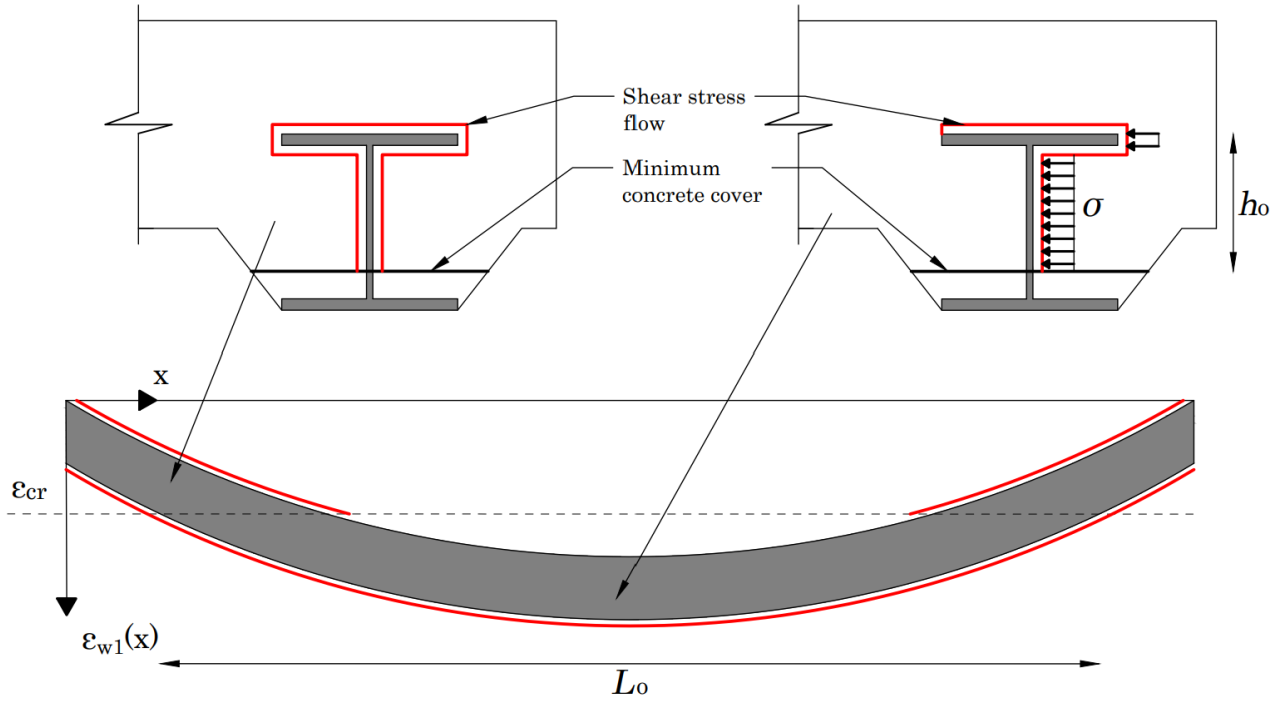


Figure 4.27: Shear stress flow along steel-concrete interface at the exterior composite girder. The red line indicates the contact perimeter accounted for when considering cohesion.

The length over which the concrete has formed an opening from the steel is determined from Eq.4.40.

$$L_o = L_{eff} - 2x_{cr} \quad (4.40)$$

The normal stress,  $\sigma$ , is determined over the confinement area. Thus, the length is the length of the confinement where the steel and concrete have formed a gap. The height of the confinement area is accounted for as the height of the vertical outside surface of the exterior steel girder. Conservatively, no horizontal surfaces are accounted for. The horizontal surfaces in contact with the steel still have resistance due to the adhesion. Therefore, the normal stress on the confinement area is determined using Eq.4.41. The shear force is determined from the lateral exterior beam and is multiplied by 2 as the shear force only is half the total lateral force the composite girder is subject to.

$$\sigma = \frac{2V_1}{h_o L_o} \quad (4.41)$$

The longitudinal shear resistance is a summation of the resistance of the sections close to the supports, where the concrete has not formed an opening, and the section at midspan, where the concrete has formed an opening between the steel, as shown in Figure 4.27. As the longitudinal shear resistance is evaluated globally, the total shear resistance can be determined by multiplying the area at which the Mohr-Coulomb mechanism applies with the confinement area. Therefore, the longitudinal shear resistance due to the Mohr-Coulomb mechanism is obtained from Eq.4.42. The horizontal contact surfaces with a steel-concrete opening only have resistance due to cohesion, as the confinement only affects the vertical outward-facing surface.

$$V_{1,x,Rd} = \mu\sigma h_0 L_0 + cu_{cr} L_0 \quad (4.42)$$

The shear resistance from the area where there still is full steel-concrete contact is determined from Eq.4.43. The effective contact perimeter,  $u_{eff}$ , is determined as the perimeter with steel-concrete contact within the previously described concrete cover. The total longitudinal shear resistance is determined from Eq.4.44.

$$V_{2,x,Rd} = cu_{eff}(L_{eff} + 2L_c - L_o) \quad (4.43)$$

$$V_{x,Rd} = V_{1,x,Rd} + V_{2,x,Rd} \quad (4.44)$$

Figure 4.28 shows how the longitudinal shear resistance decreases following longitudinal cracking as the concrete forms an opening from the steel. Following the idealised behaviour, the longitudinal shear resistance will gradually increase following longitudinal cracking due to the Mohr-Coulomb mechanism from the concrete confinement where the concrete has opened from the steel. This has been simplified, so the longitudinal shear resistance is assumed constant following cracking.

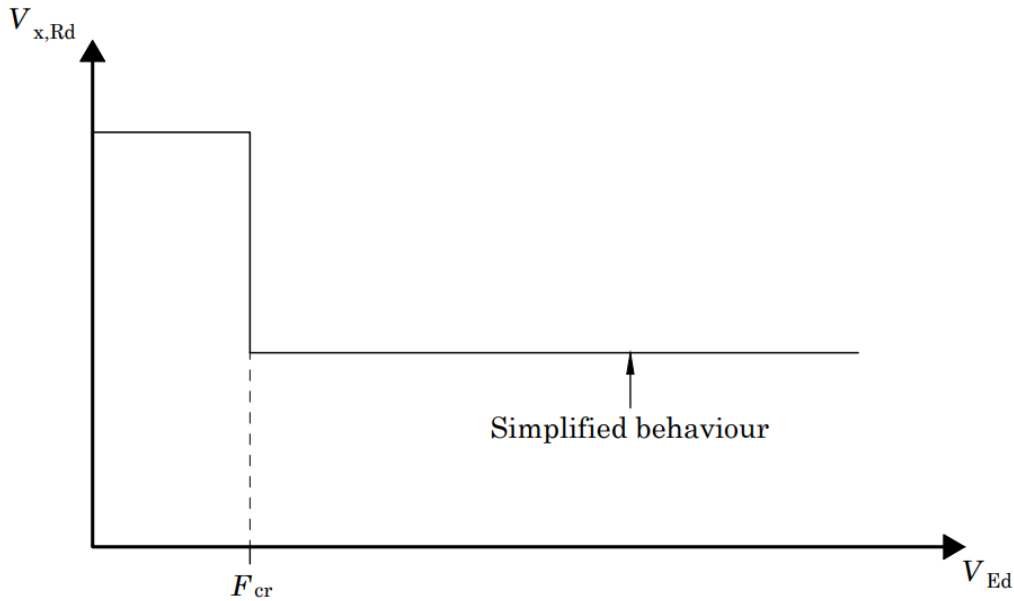


Figure 4.28: Longitudinal shear resistance versus the shear force  $V_{Ed}$ .  $F_{cr}$  is the load at longitudinal cracking.

In the following, the cross-section verifications for biaxial bending and vertical shear must be performed. However, these follow the same method as described for stage 1 cross-section verification. The only difference is that the degree of shear connection may have changed due to reduced longitudinal shear resistance. Therefore, it must be checked if the degree of shear connection has changed. If this is the case, biaxial bending and vertical shear resistance are determined again. If not, the resistances determined from the cross-section verification of stage 1 are also valid.

In Appendix A, a calculation example goes through a solution strategy to determine the displacements and forces of the C-STM and the cross-section verification for stages 1 and 2. This example considers a cross-section similar to LB1 so that the analytical design method can be compared to experimental and numerical results. Additionally, a similar calculation has been performed on the cross-section of LB3, but only the results are shown for this.

Figure 4.29 shows the calculation procedure for determining the stage 2 cross-section resistance, which mainly depends on the longitudinal shear resistance. The following procedures of the cross-section verification are similar if the longitudinal shear resistance for stage 2 cross-section verification is different from the longitudinal shear resistance for stage 1 verification.

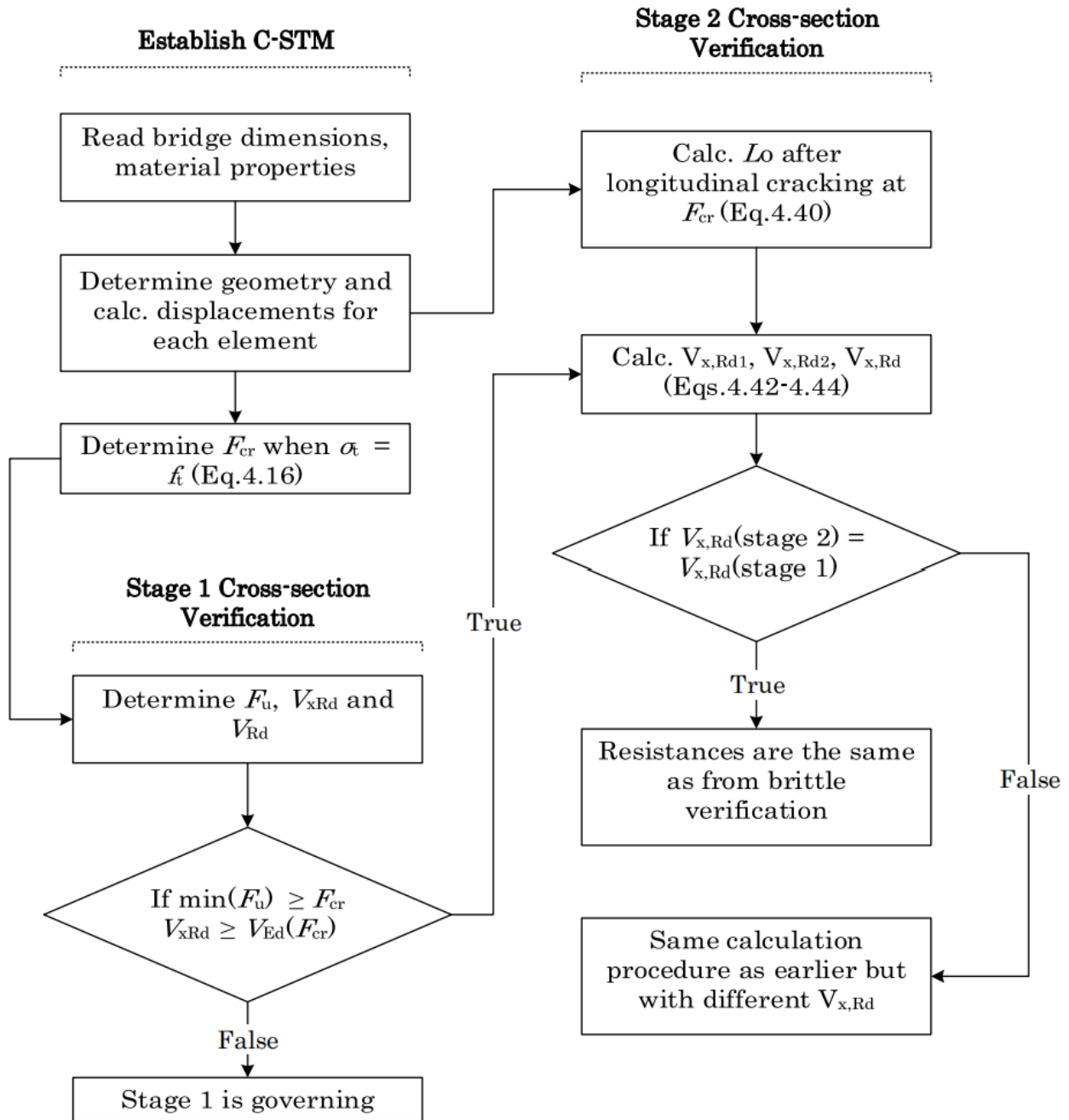


Figure 4.29: Flowchart of the stage 2 cross-section verification.

# 5 Verification of the Analytical Model with Experimental and Numerical Results

The following compares the results of the proposed C-STM and the cross-section verifications to the results of the experiment and numerical models. Therefore, the results of the following calculations are based on the material parameters and geometry of LB1 and LB3, which were introduced in Chapter 3.

## 5.1 Results of Analytical Calculations

The C-STM is established and solved using MATLAB. Ideally, a symbolic expression for the displacement in the lateral direction would be derived. However, the system of differential equations is relatively complex. Therefore only a numeric solution was determined. Appendix A shows the calculation example applying the proposed analytical design method, including establishing the C-STM and the cross-section verifications. This verification is supported by the MATLAB code used to perform mathematical operations in Appendix B and C.

The following shows the key results of the analytical calculations, which mainly focus on LB1. The calculation of LB1 showed that longitudinal cracking between the exterior and adjacent composite girder occurred at 421 kN. Following, it was verified that brittle failure was not governing by verifying the resistance of each failure mode was above the load at longitudinal cracking. This verification included crushing of the compression struts, longitudinal shear, biaxial bending and vertical shear. Additionally, it was proven that the degree of shear connection was 0.56, hence partial shear interaction for the biaxial bending verification. The stage 1 cross-section verification proved none of the failure modes would occur before longitudinal cracking. Thus, a stage 2 cross-section verification is required as well. Table 5.1 gives the resistances determined from the brittle cross-section verification for LB1 and LB3 and the equivalent single-point load for each resistance.

Table 5.1: Resistances of stage 1 cross-section verification and equivalent resistance to the single point load,  $F$ .

<b>Resistances</b>	<b>Unit</b>	<b>LB1</b>	<b>LB3</b>
$N_{s,max}$	[kN]	6164	4983
$V_{x,Rd}$	[kN]	3250	4379
$M_{y,Rd}$	[kNm]	664	772
$M_{z,Rd}$	[kNm]	518	640
$V_{Rd}$	[kN]	1304	1092
<b>Equivalent resistance to <math>F_u</math></b>			
Crushing of struts	[kN]	8726	5666
Longitudinal Shear	[kN]	13000	17516
Biaxial Bending	[kN]	798	666
Vertical Shear	[kN]	5216	4368

As the stage 1 cross-section verification showed that the bearing capacity before longitudinal cracking is sufficient, the stage 2 cross-section verification was required. This calculation shows

that the stage 2 verification has partial shear interaction but is lower than the stage 1 verification. The reason for the reduction is the lower longitudinal shear resistance due to the opening that the concrete formed from the steel. Figure 5.1 shows the actual and simplified longitudinal shear resistance and the shear force versus the load,  $F$ , for LB1. A similar behaviour was noticed for the verification of LB3. From the Figure, it can be seen that following cracking, at 421 kN, a reduction of the longitudinal shear resistance occurs. Afterwards, the resistance keeps increasing with increasing load. Moreover, a gap between the longitudinal shear resistance and the shear force gradually reduces as the loading increases. However, for the cross-section verification, it is assumed that this can be simplified into a constant shear resistance after longitudinal cracking, as seen from Figure 5.1.

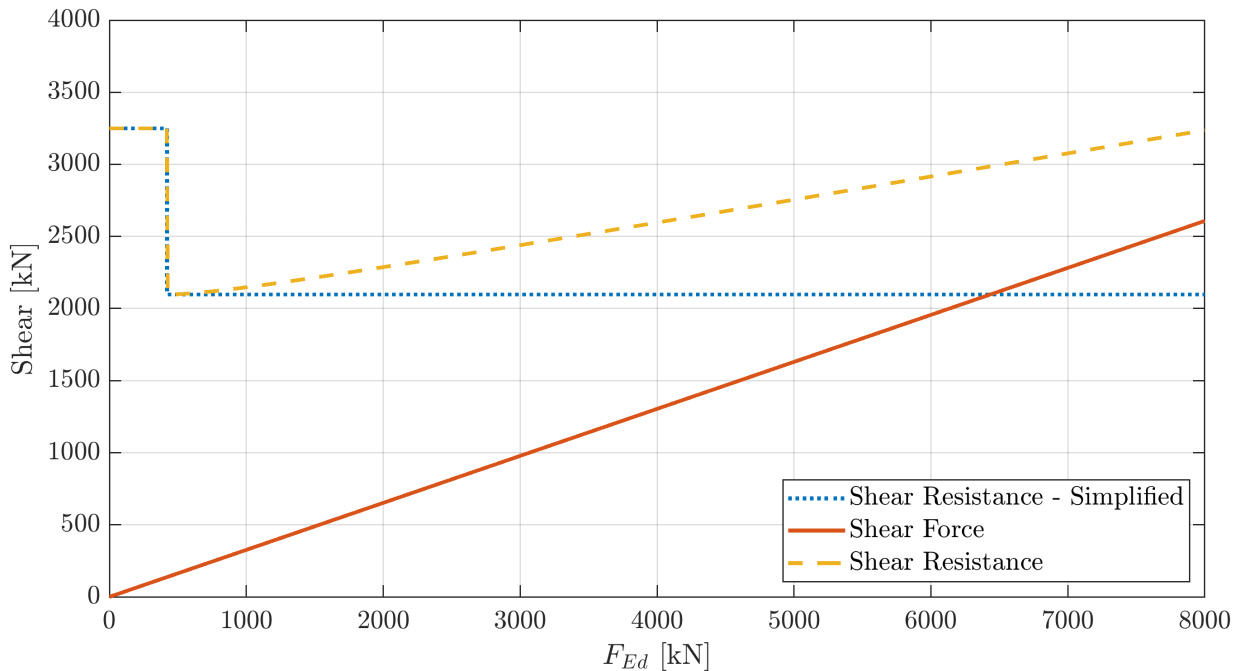


Figure 5.1: LB1 - Actual and simplified longitudinal shear resistance and shear force versus the single point load,  $F$ .

As the longitudinal shear resistance decreases significantly following longitudinal cracking, as shown in Figure 5.1, it can already be concluded that the degree of shear connection is further reduced. Thus, it is necessary to perform the stage 2 cross-section verification, as biaxial bending and vertical shear reduce corresponding with the longitudinal shear resistance reduction. Table 5.2 shows the moment resistance for full shear interaction, partial shear interaction - which applies to this case - and no shear interaction - illustrating how the effects of the longitudinal cracking and the degree of shear connection, in general, impact the bending moment resistance. Figure 5.2 shows the interaction diagram for LB1 at the degree of shear connection before/after longitudinal cracking and the maximum and minimum values. The numeric results of the bending resistances for both LB1 and LB3 are shown in Table 5.2, also showing how increasing the degree of shear interaction will increase the bending moment resistance.

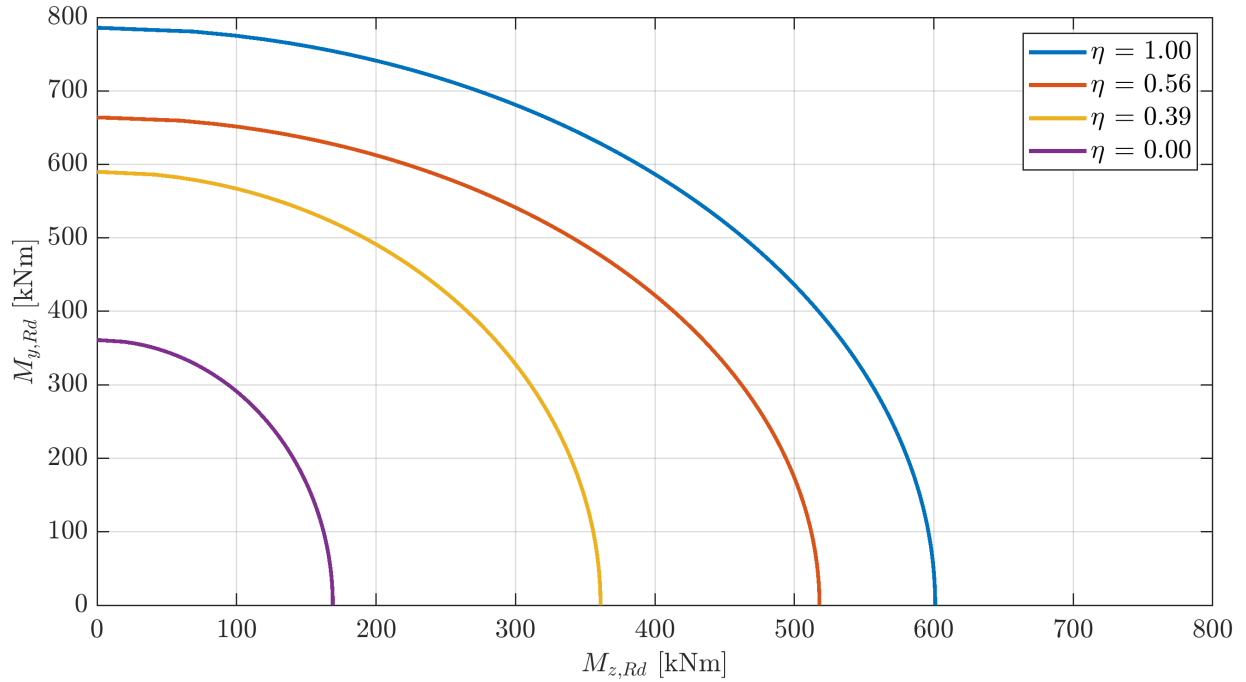


Figure 5.2: Moment interaction diagram for LB1 at different full, partial and zero shear connections.

Table 5.2: (\*) The degree of shear connection before longitudinal cracking. (\*\*) The degree of shear connection after longitudinal cracking. Moment resistance for the full shear connection, partial shear connection and zero shear connection of exterior composite girders with similar geometry to LB1 and LB3.

	$\eta$	$M_{y,Rd}$ [kNm]	$M_{z,Rd}$ [kNm]
LB1	1.00	786	601
LB1	0.56*	664	518
LB1	0.39**	590	361
LB1	0.00	361	169
LB3	1.00	780	660
LB3	0.79*	772	640
LB3	0.46**	726	533
LB3	0.00	565	231

The resistances calculated on the cross-sections are expressed in terms of the load,  $F$ , applied for the generalized case as previously shown in Figure 4.2. Table 5.3 shows the cross-section resistances for each failure mode and the equivalent point load that the failure mode can resist.

Table 5.3: Resistance of stage 2 cross-section verification and the equivalent resistance to the single point load  $F$ .

<b>Resistances</b>	<b>Unit</b>	<b>LB1</b>	<b>LB3</b>
$N_{s,max}$	[kN]	6196	4698
$V_{x,Rd}$	[kN]	2097	2556
$M_{y,Rd}$	[kNm]	590	726
$M_{z,Rd}$	[kNm]	361	533
$V_{Rd}$	[kN]	1217	970
<b>Equivalent resistance to <math>F_u</math></b>			
Crushing of struts	[kN]	11892	6769
Longitudinal Shear	[kN]	8388	10224
Biaxial Bending	[kN]	675	587
Vertical Shear	[kN]	4868	3880

Table 5.3 shows that biaxial bending is the governing failure mode for both specimens but is limited due to the degree of shear connection, as shown in Table 5.3. Therefore, the analytical calculations assume that the cross-section will have ductile behaviour but is limited due to the longitudinal shear resistance.

This means that the concrete's compression forces due to bending eventually exceeds the longitudinal shear resistance, so they can not be transferred to the steel. Moreover, the remaining failure modes are far from governing the bearing capacity.

## 5.2 Verification using Experimental and Numerical Results

The verification focuses on the following three points:

- Failure mode
- Load at longitudinal cracking
- Bearing capacity

To compare the loading from the proposed analytical model, it is assumed that it can be applied to a bridge deck similarly to the numerical model and the experiments. Thus, the middle girder has a load on both sides, as shown in Figure 5.3. It is assumed that the resistance of the middle girder is not critical, as the girder is not subject to biaxial bending due to the loading from both sides that keeps it in horizontal equilibrium. Additionally, it will have higher longitudinal shear resistance, which increases the bending resistance, as the concrete will not form an opening from the steel. Finally, the resistance of the concrete is higher due to biaxial compression from the flexural bending compression force and the horizontal force component from the loads,  $F$ .

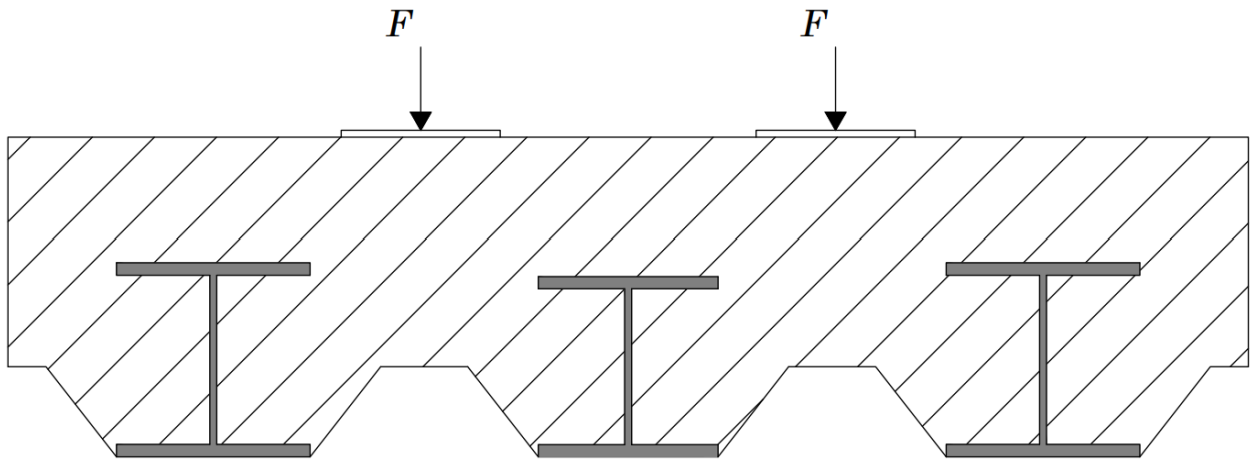


Figure 5.3: Assumed loading of the proposed analytical model for comparison with the experimental and numerical results.

Figure 5.4 shows a bar chart of the results from the experiment, numerical and analytical model. This includes the load at which longitudinal cracking occurs and the load at failure.

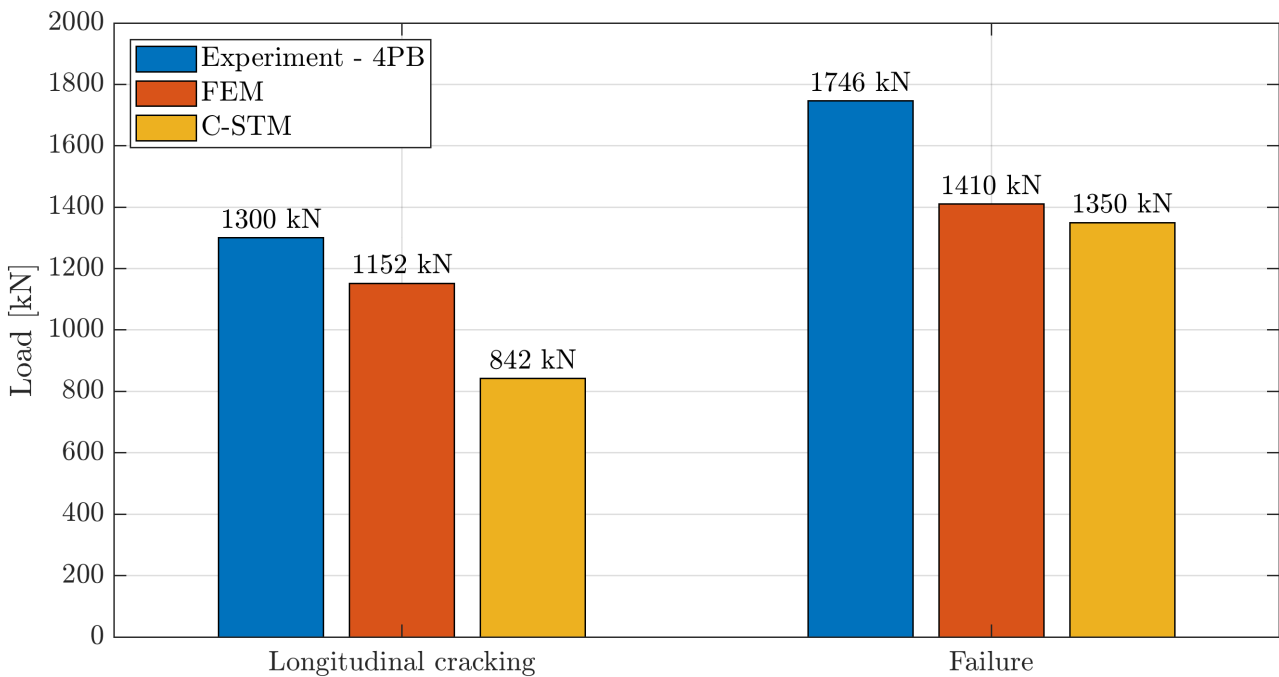


Figure 5.4: LB1 - comparison of the resistance to longitudinal cracking and failure from the experiments, numerical and analytical results.

From Figure 5.4, it can be seen that the analytical model underestimates the load at longitudinal cracking with 27 and 35% compared to the numerical and experimental results. Prior to the laboratory testing of LB1, it was already expected that this specimen had cracked. Therefore, the loads from the experiment may be at the point where the cracks further propagated. The analytical model gets closer to the load at failure but is still below, which is considered safe. Comparing the load at failure, the analytical result comes 4.2% below the numerical result, which is considered relatively accurate. Whereas the result of the analytical calculation comes 23% below the experimental, the loading case is different, which may be why. Additionally, the

analytical calculation showed that biaxial bending governs the resistance of LB1 but is limited by the partial shear connection. This occurs because the interface can not transfer the concrete compression forces from bending despite the high longitudinal shear resistance. The failure of LB1 during the experiment was yielding of the steel girders due to bending with limited ductility due to interface failure. Therefore, the failure mode predicted by the analytical model is the same as during the experiment.

A similar comparison is made to the results of LB3. Figure 5.5 shows the experimental, numerical, and analytical results of LB3, including the load at longitudinal cracking and failure.

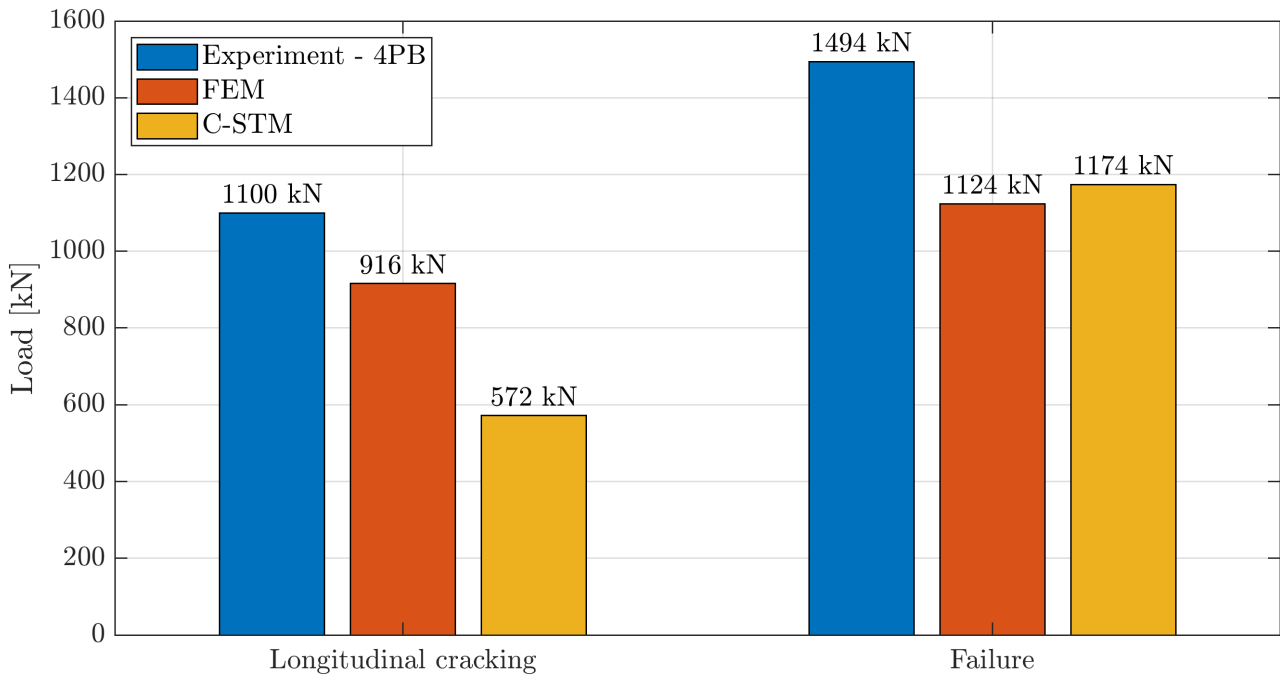


Figure 5.5: LB3 - comparison of the resistance to longitudinal cracking and failure from the experiments, numerical and analytical results.

From Figure 5.5, similar trends are shown from the figure comparing the results of LB1. Thus, the analytical model underestimates the load at longitudinal cracking with 38 to 48% compared to the numerical and experimental results. Likewise, in LB1, the analytical calculation underestimates the result compared to the experimental with 21%, possibly due to the different loading conditions. Contrary to LB1, the analytical model overestimates the bearing capacity compared to the numerical with 4.4%. However, still relatively close to the numerical bearing capacity, which is considered accurate. The analytical calculation of LB3 also showed failure due to biaxial bending but was limited by partial shear interaction, as was the case for LB1. During the testing, LB3 failed due to bending by concrete crushing. The reason why LB3 failed due to the crushing of the concrete during the experiment could be due to the lower concrete cover compared to LB1.

For both the analytical results of LB1 and LB3, longitudinal cracking occurs earlier than expected. The transverse displacement profile of LB1 and LB3 has been investigated further to get an indication of the lateral stiffness. It can be seen that the analytical model with a small margin either underestimates or overestimates the load at failure compared to the numerical model. However, the proposed analytical model still determines the same failure mode shown during the testing. The proposed model also accounts for the longitudinal cracking that

occurred prior to failure. However, the behaviour of the longitudinal cracking may still be optimized further, as this underestimates the load at which longitudinal cracking occurs by a large margin. Additionally, the C-STM and the cross-section verifications prove that the exterior composite girders yield before failure and are limited due to partial shear connection.

Figure 5.7 shows the transverse displacement profile of LB1 from the numerical model and the analytical model at  $F = 380$  kN, right before longitudinal cracking occurs. The displacement is determined using the C-STM. Additionally, the length of the cross beam has been added, at which the transverse displacement is 0. The transverse displacement profile of the numerical model is measured at midheight of the exterior steel girder as shown in Figure 5.6, roughly where the spring node is localized in the C-STM. For the experiments, it was measured from underneath the bottom flange of the steel girders. Thus, the lateral displacement may be larger than at midheight due to torsion.

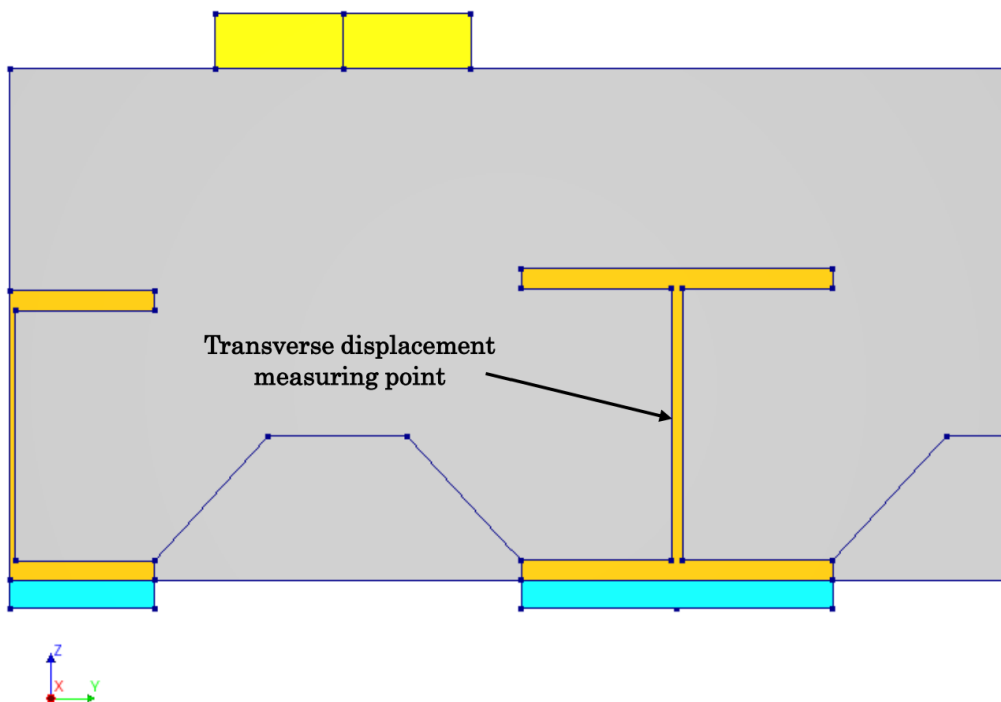


Figure 5.6: Cross-section showing the measuring point for the transverse displacement profiles of LB1 and LB3.

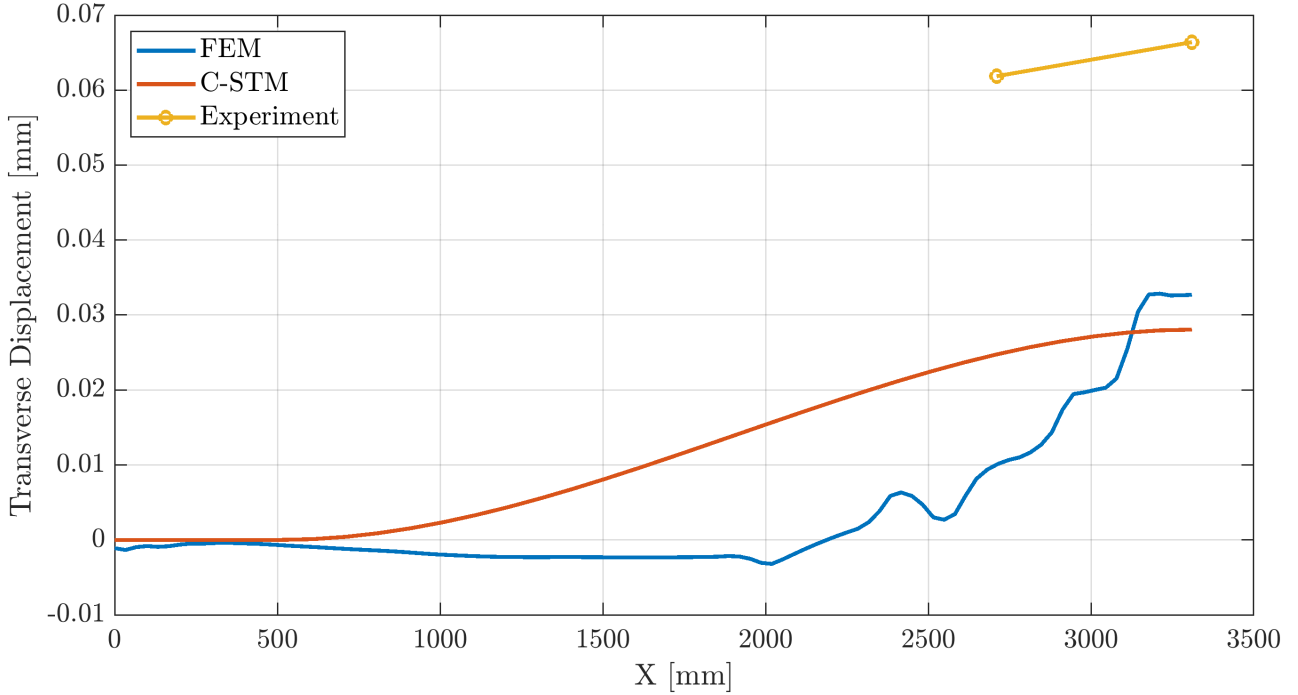


Figure 5.7: LB1 - Transverse displacement profile at  $F = 380$  kN from the experiment, numerical and analytical model.  $X$  is the distance from the support to the midspan.

From Figure 5.7 it can be seen that the analytical model roughly follows the displacement profile of the numerical model, especially at midspan and close to the supports. The gap between the analytical and numerical displacement profiles can be due to the interpretation of the tensile tie, which works as a single spring for the analytical model. In contrast, for the numerical model, this would be similar to a uniformly distributed spring. The lateral stiffness assumptions before longitudinal cracking are assumed to be sufficient, as they are similar to the numerical model but far from the experimental model, which can be due to imperfections in the load distribution and different loading conditions. As previously mentioned, the lateral displacement from the experiment is higher because it was measured from the bottom steel flange, where the lateral displacement due to torsion is higher. Hence, the lateral displacement would have been lower if it was closer to the midheight of the steel girder. Additionally, prior to the testing of LB1, it was already assumed that some of the concrete had cracked, which would have reduced the lateral stiffness.

Figure 5.8 shows a similar transverse displacement profile for LB3 from the experiment and numerical and analytical models, which also was measured at midheight of the exterior steel girder as shown in Figure 5.6. Moreover, the lateral displacement from the experiment of LB3 comes closer to the analytical model than was the case for LB1. Thus, indicating that LB1 already had longitudinal cracks prior to the experiment, which increased the lateral stiffness.

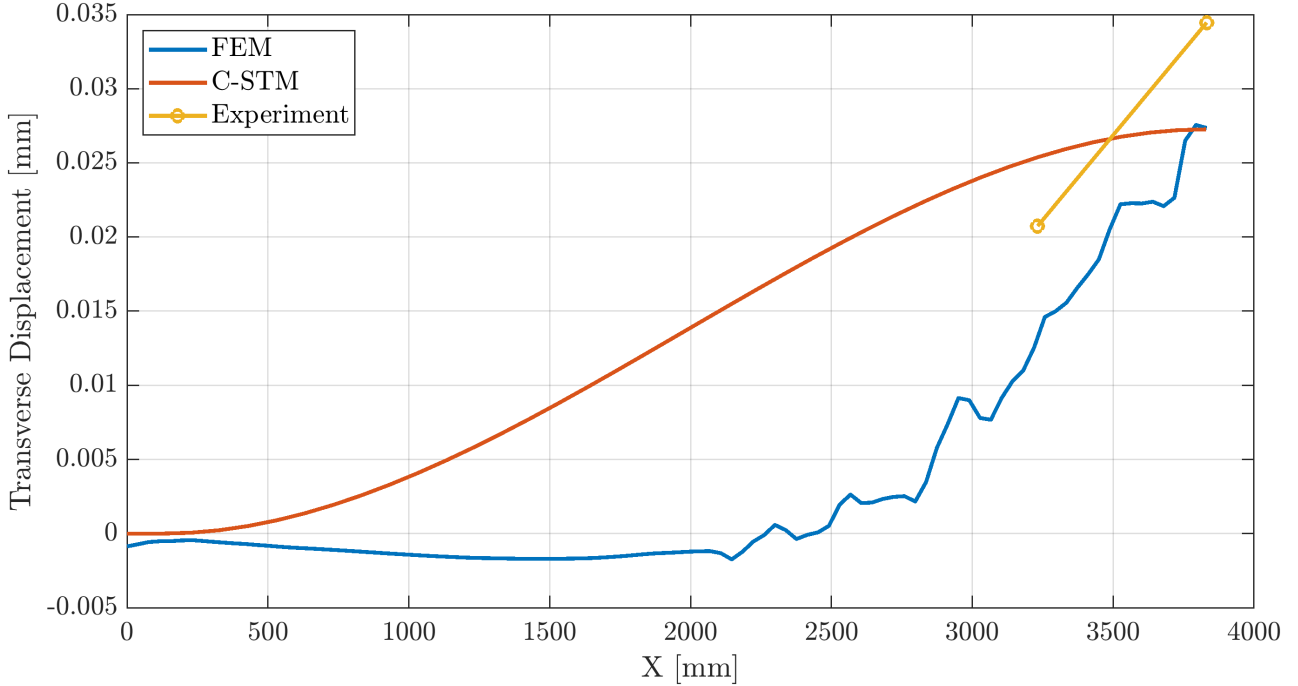


Figure 5.8: LB3- Transverse displacement profile at  $F = 250$  kN from the experiment, numerical and analytical model. X is the distance from the support to the midspan.

Following cracking, the experiment and numerical results showed that the steel girders were already yielding. Therefore, it can be difficult to compare these results accurately. Based on the stiffness used before cracking, it is assumed that similar assumptions but with reduced stiffness due to failure of the tensile tie are an accurate interpretation of the lateral stiffness in the analytical model.

There is a number of reasons why the analytical model underestimates the bearing capacity compared to the experiment and the numerical model. First, the reaction forces at the supports during the testing showed that the middle girder took more than half the load from each loading plate, possibly due to eccentricities of the supports or the loading. The reaction forces at each beam are shown in Appendix D. If the loading from each plate is distributed half-half to each adjacent girder, a more critical case may have been present, where the loading at the exterior girder is larger. Thus, the composite bridge would have failed at a lower loading. As previously argued, it is assumed that the middle composite girder has a higher capacity. Thus if the middle girder takes more of the load due to eccentricities etc., the capacity may be higher. Another reason the bearing capacity during the experiments was higher was the height of the concrete cover, which changed over the length. For the calculations, the lowest concrete cover was assumed. The concrete cover influences the bond strength and the biaxial bending moment resistance.

### 5.3 Extended Comparison of Results

During the experiments, the specimens were loaded using 4-point bending. Therefore, the load gives a different moment distribution than the 3-point bending. The experiments and the analytical model showed that the specimens failed due to bending. Hence, it is assumed that the failure load from 4-point bending can be transformed into an equivalent load at 3-point

bending, which gives the same bending moment, for a more accurate comparison of the results. The assumption of the equivalent 3-point bending is shown in Figure 5.9. This equivalent load is determined using Eq.5.1.

$$\frac{1}{4}F_{Eq}L = FL_1 \quad (5.1)$$

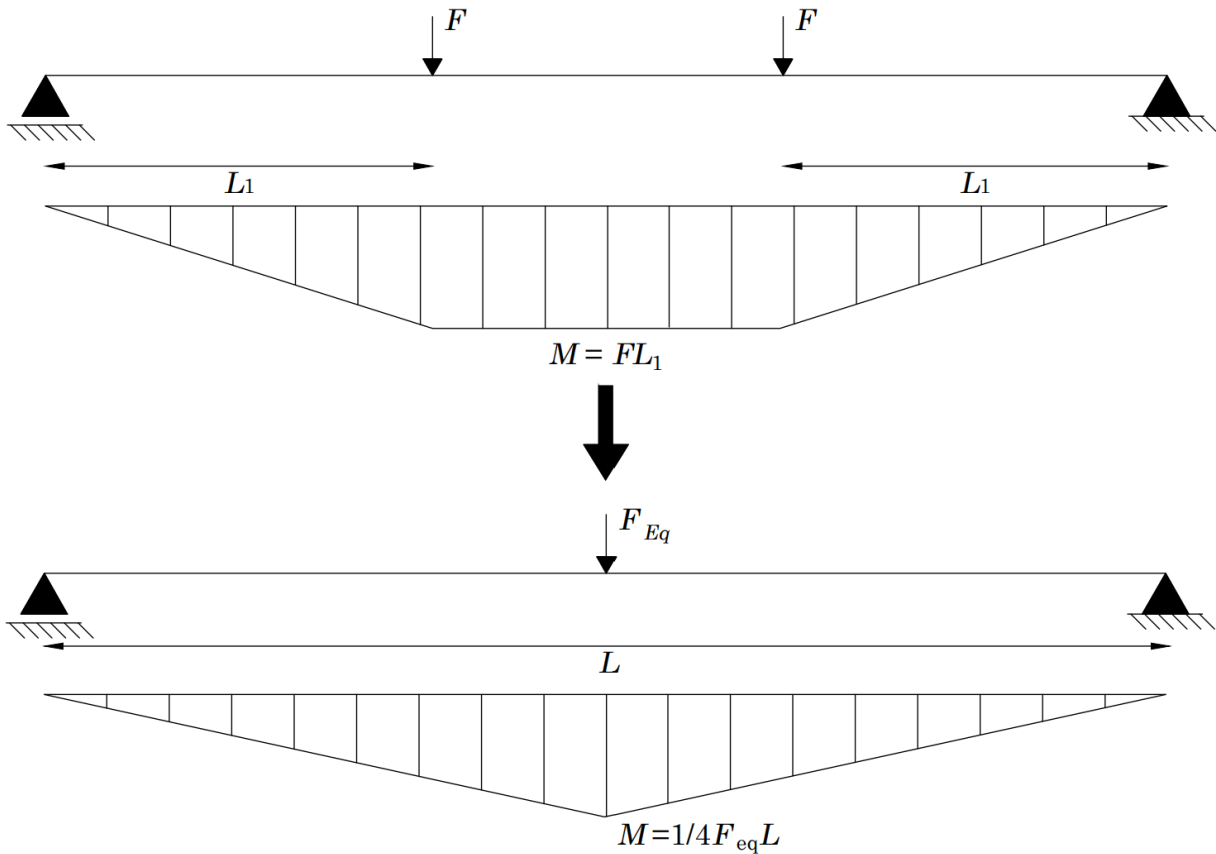


Figure 5.9: Location and notation of loads for calculating the point load at midspan, giving a maximum bending moment equivalent to 4-point bending.

LB1 gives an equivalent 3-point bending load at 1394 kN. The equivalent load for LB3 is 1258 kN. Therefore, the load is slightly lower than it was for 4-point bending. However, the analytical model still underestimates the bearing capacity. The equivalent force is determined assuming uniaxial bending, which is assumed to be adequate as an estimate. The equivalent single point loads are compared to the other results in Figure 5.10.

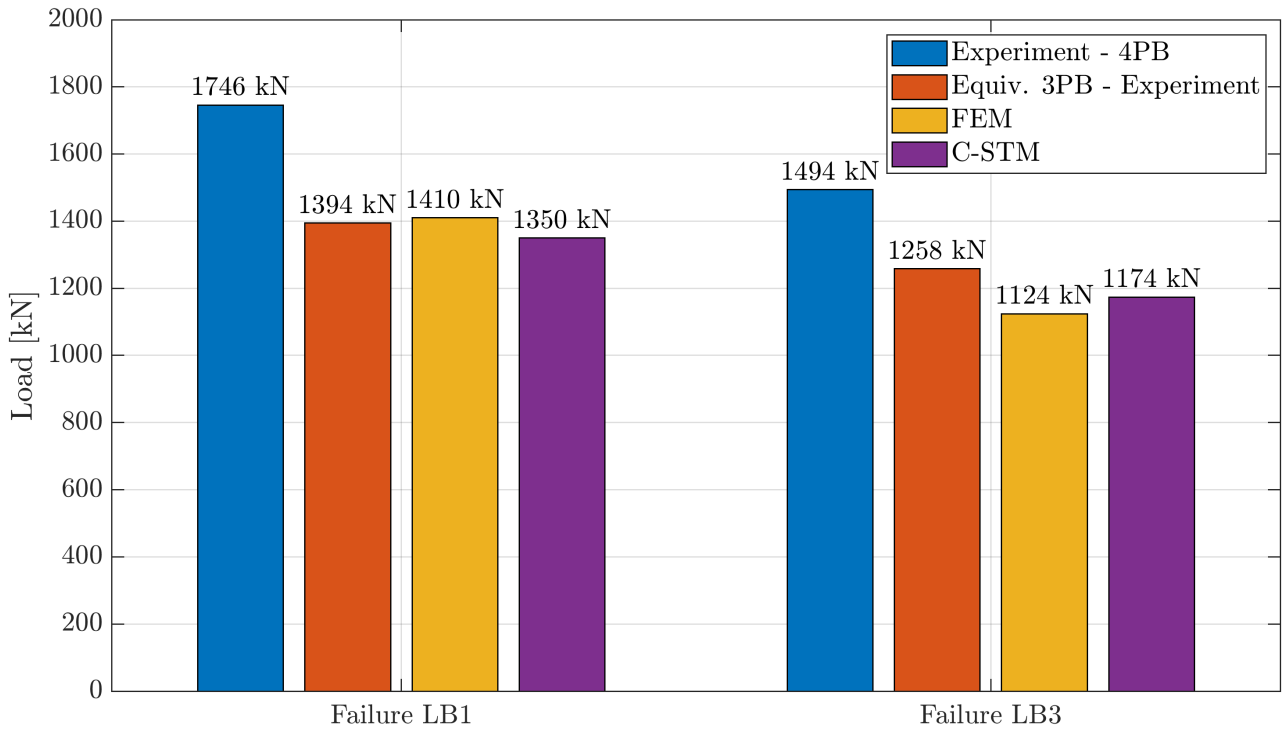


Figure 5.10: Comparison of the resistances for LB1 and LB3 from experiments, numerical and analytical results.

From Figure 5.10 it can be seen that the analytical model comes close to both the experimental and numerical results. The analytical model for LB1 underestimates the load at failure compared to the other results, which is considered safe. Additionally, the margin between the results is relatively small. The same is valid for LB3, although the model overestimates the load at failure compared to the numerical model. Although this comparison is a relatively simplified method to determine the resistance for different loading cases, it is possible that the current model can be used to verify the loads from 4-point bending using the transformation. For instance, reversing this process so the 3-point bending resistance is transformed into an equivalent 4-point bending resistance. For loading cases that are less critical but still have to be verified, for instance, loading between interior girders, the model may be modified. The in situ testing in Amsterdam showed that the load distributes equally to the four adjacent girders for loading between interior girders. Therefore, the loading on each beam can be reduced compared to the C-STM. Additionally, it may be assumed that the concrete does not form an opening from the steel, which will increase the longitudinal shear resistance.

To summarize the verification, it can be concluded that the analytical model predicts the same failure modes observed during testing, which for LB1 is bending with limited ductility due to interface failure. For LB3, this is bending with concrete crushing. Additionally, the analytical results get close to the experimental and numerical results, especially regarding the load at failure, when considering the equivalent 3-point bending load from the experiments. However, the model underestimates the load at longitudinal cracking with a relatively large margin, which the verification showed was not due to the lateral stiffness, as this gave similar displacement profiles to the experimental and numerical results. This can be due to the tensile area or the height of the spring node, as these are parameters that influence the stresses and the force components in the C-STM. Nonetheless, it is considered more important that the load at failure is closer to the experimental and numerical results.

## 6 Discussion

A compatibility-based strut and tie model (C-STM) has been proposed. The model simplifies the distribution of forces into struts and ties. The absence of transverse reinforcement means that the C-STM interprets the concrete in tension as ties, which typically would be the assumption for the reinforcement. The vertical stiffness of the composite girders is accounted for as elastic single-point springs, whereas the lateral stiffness is computed as lateral spring beams. The C-STM considers the struts and ties as axial bars and the spring beams as clamped Euler-Bernoulli beams. The lateral displacement of the exterior composite girder determines if the concrete has formed an opening from the steel, which reduces the effective contact perimeter and the longitudinal shear resistance. The longitudinal shear resistance is linked to the remaining cross-section verifications, as they depend on the degree of shear connection. The contributions to the longitudinal shear resistance mainly come from the cohesion determined through a literature review and taken as the lowest value. Additionally, the model considers the Mohr-Coulomb mechanism, which has a relatively low influence on the bearing capacity.

### 6.1 Differences Between the FEM and the Analytical Model

One of the differences between the numerical and analytical model are the assumptions regarding lateral behaviour. The numerical model considers the concrete in tension as multiple discrete elements so that it will fail gradually. In contrast, the analytical model considers the tensile tie as a single spring, when this fails, the entire concrete in transverse tension has failed. Figure 6.1 shows the assumption from the numerical and analytical model.

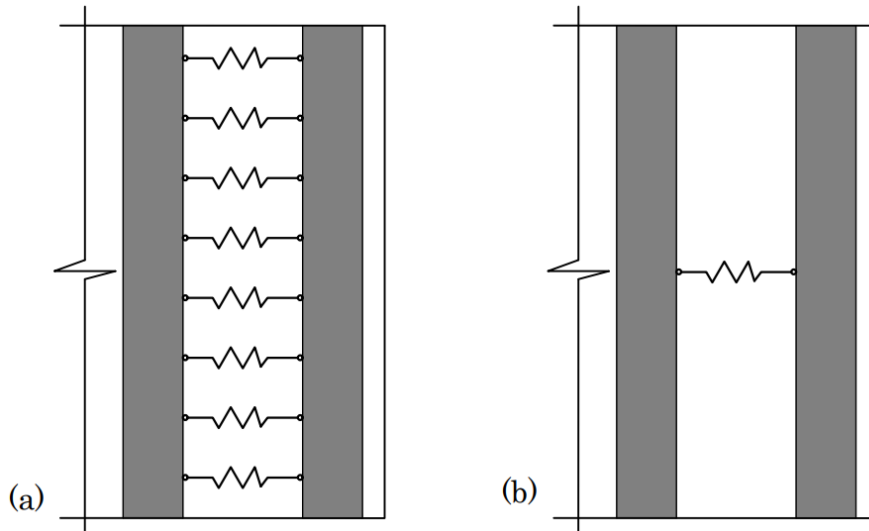


Figure 6.1: Bottom view exterior and adjacent composite girder. (a) numerical model concrete tensile tie as uniformly distributed spring. (b) analytical model concrete tensile tie as single spring.

As a consequence of the configuration of the analytical model, the numerical model gives a better

representation of the transverse displacement profile along the length of the specimen. Whereas the analytical model only gives an accurate representation of the supports and midspan, as shown in Figure 6.2.

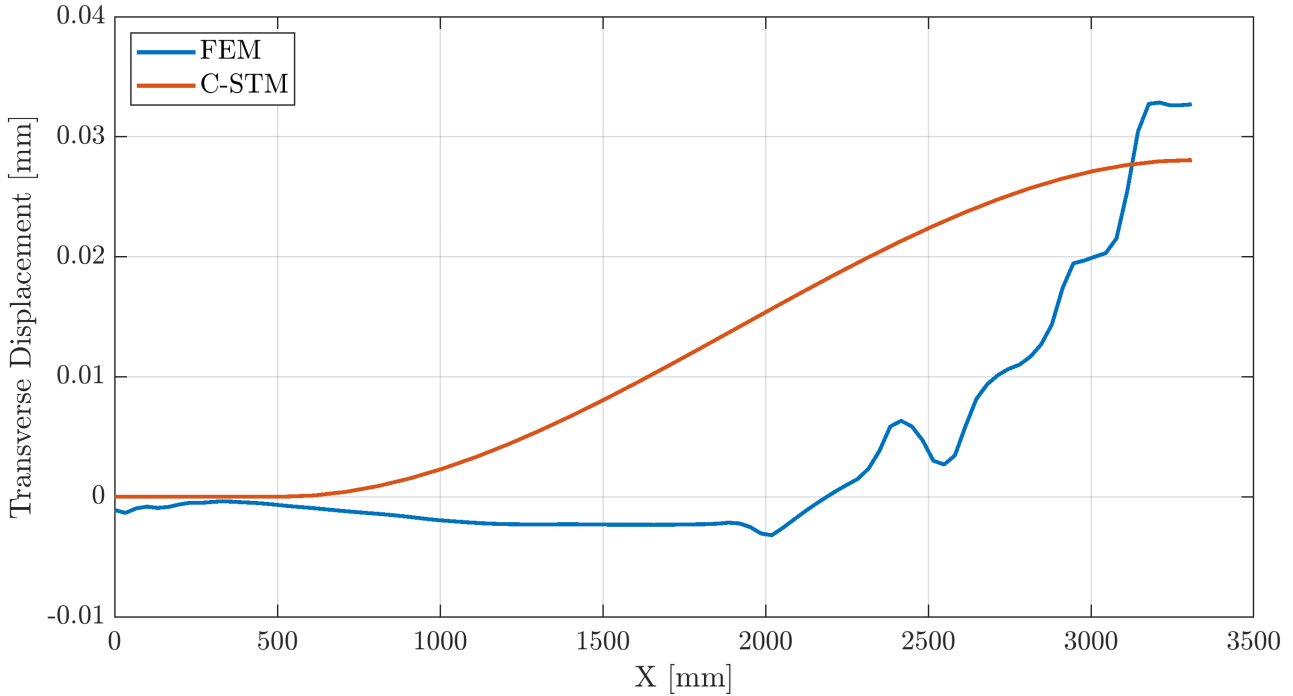


Figure 6.2: The lateral displacement profile of LB1 before cracking the C-STM and the numerical model. X is the distance from the support to the midspan.

Another consequence of using the analytical model is that it assumes a constant shear resistance along the contact perimeter, as shown in Figure 6.3. The shear resistance around the contact perimeter is variable due to the confinement, which will vary depending on the location around the steel girder. Additionally, it can be assumed that there is stronger cohesion between the top part of the top steel flange compared to other areas. This is something the analytical model does not account for. However, it is assumed that the simplification, assuming constant values for cohesion and the coulomb mechanism, reduces the calculation time and still provides accurate results.

The numerical model uses a coefficient of friction at 0.5, which is significantly higher than the coefficient of friction at 0.3 used for the analytical model. The analytical model assumes that cohesion is 0.54 MPa, whereas the numerical model uses 0.1 MPa. However, the analytical model simplifies the Mohr-Coulomb mechanism to a limited area. In contrast, the ideal behaviour would be that the mechanism gives higher resistance closer to the top steel flange. Then the value reduces along the height of the steel girder, combined with confinement due to torsion of the steel girder. Therefore, these parameters can not necessarily be directly compared. Figure 6.3 shows the idealised shear resistance around the perimeter of the steel girders compared to the simplified shear resistance, which is assumed for the analytical model when the concrete has formed an opening from the steel. The principal idea about simplifying the shear resistance is to average it along the effective contact perimeter using the lowest cohesion value found in the literature review.

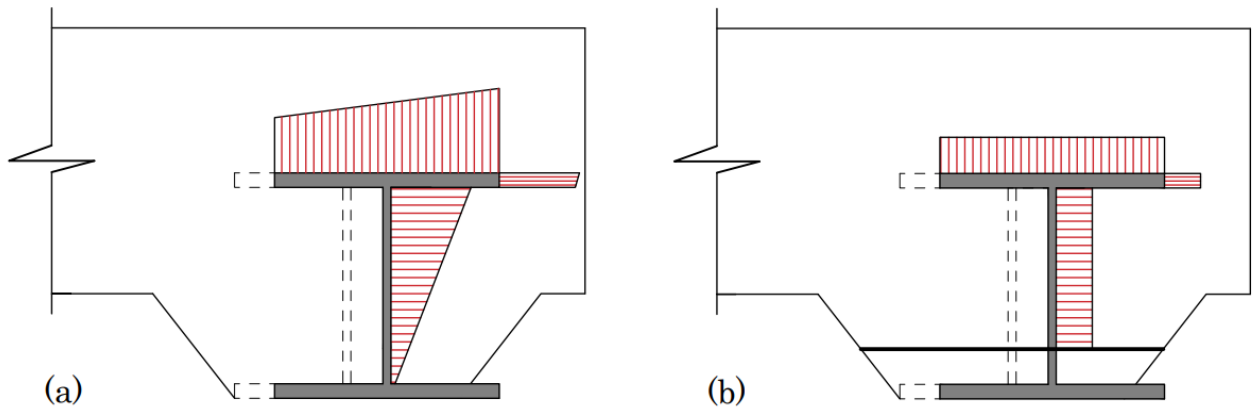


Figure 6.3: Longitudinal shear resistance of the exterior composite girder. (a) idealised distribution of the longitudinal shear resistance. (b) Simplification of the distribution of the longitudinal shear resistance in the analytical model.

The analytical model is highly dependent on the bond strength values, as these directly influence the longitudinal shear resistance and, therefore, the degree of shear connection linked to the biaxial bending - and vertical shear resistance. The cohesion especially impacts the degree of shear connection before and after longitudinal cracking. This is shown in Figure 6.4 showing the longitudinal shear resistance of LB1 assuming the cohesion is 0.01 MPa and the coefficient of friction at 0.3 as previously. When decreasing the cohesion close to 0, the longitudinal shear resistance governs the failure before longitudinal cracking occurs. Therefore, changing these parameters highly influence the longitudinal shear resistance, thus, the failure mode and the bearing capacity. The numerical model is less dependent on the cohesion value as this is significantly lower than the analytical model.

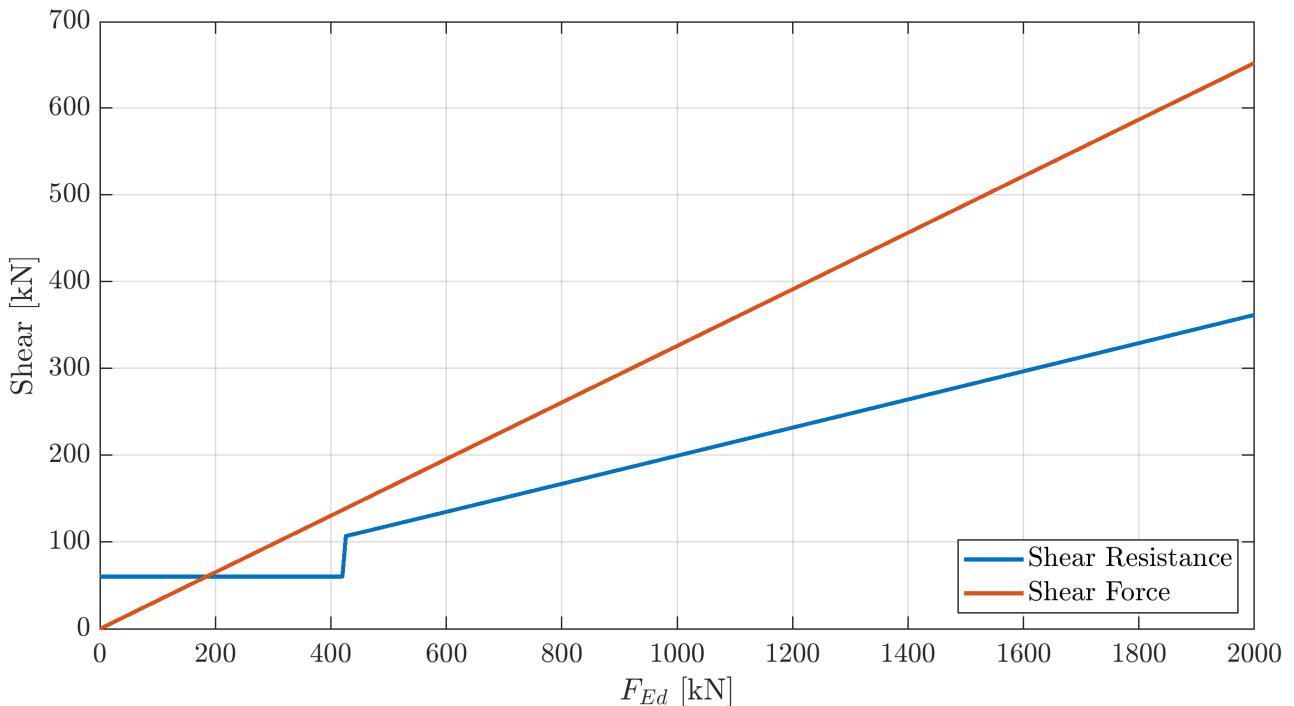


Figure 6.4: Longitudinal shear resistance and shear force versus the single point load,  $F_{Ed}$ .

For future work, it may be considered that the strain criteria used to determine when the concrete opens from the steel is relatively conservative, as following longitudinal cracking, most of the steel opens from the concrete, which is shown in Figure 6.5 showing the strain from lateral displacements of LB1 right after longitudinal cracking. For LB1, the cross beams have a length of 510 mm, and almost all of the concrete that can displace in the lateral direction already has formed an opening from the steel.

For instance, the configuration of the Mohr-Coulomb mechanism is considered for the analytical model. This assumes that confinement occurs where the concrete has formed an opening from the steel, which is determined using the strain criteria. However, the current calculations show that most of the concrete has formed an opening following longitudinal cracking, as shown in Figure 6.5. Therefore, the longitudinal shear resistance is not reduced when increasing the loading further. When increasing the loading, the longitudinal shear resistance increases as the confinement area remains while the normal stress increases.

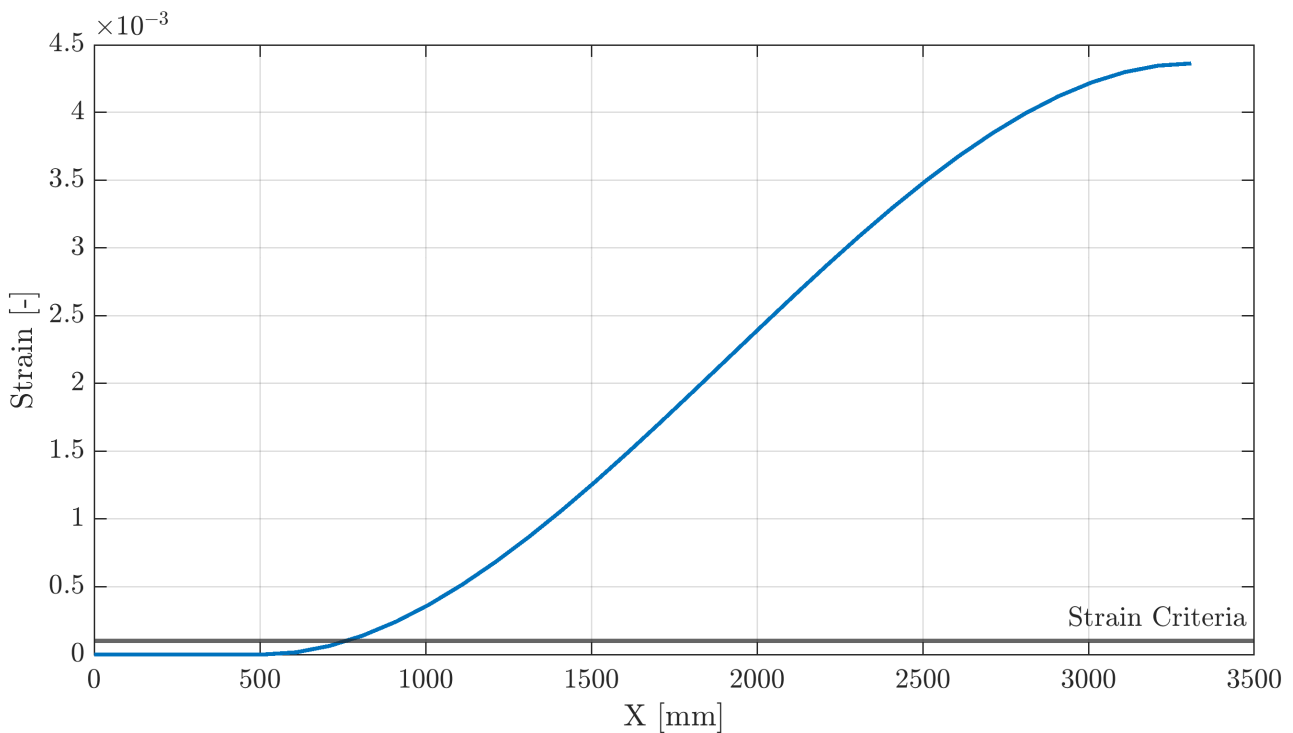


Figure 6.5: The lateral strain along the exterior composite girder of LB1 right after longitudinal cracking. X is the distance from the cross beam to the midspan.

## 6.2 Other Loading Cases

The proposed C-STM is configured to analyse 3-point bending at the midspan between the exterior composite girder and the adjacent girder. However, changing the loading case to 4-point bending or applying a uniformly distributed load necessitates adjustments in the configuration of the C-STM. This is especially important as certain elements within the C-STM depend on the specific loading conditions, such as the height of the compression struts that depends on the width of the loading plate.

Modifications must be made for 3-point bending at different locations in longitudinal direction other than midspan. The vertical springs and the lateral spring beams are derived based on this

load location. Therefore this must be modified. Similarly, for 4-point bending, as used in the experiments, the stiffness of the vertical springs must be adjusted accordingly. Moreover, it is crucial to determine if the loads impact the same area, as illustrated in Figure 6.6. The current C-STM configuration only accounts for 3-point bending and does not consider this aspect. If the loads affect the same area, the C-STM can be retained by potentially increasing the area of the struts and ties. However, an alternative configuration with two tensile ties should be examined if the loads do not impact the same area.

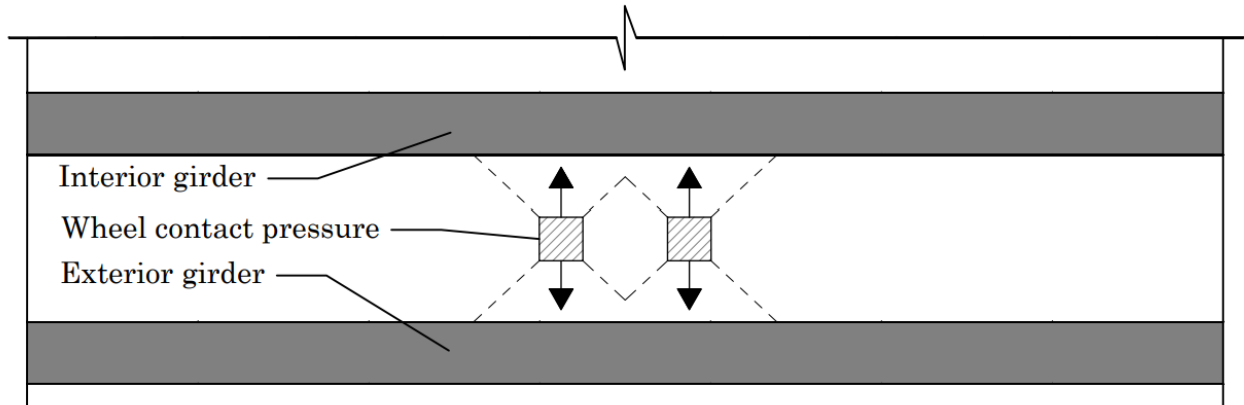


Figure 6.6: Example of load dispersal in the transverse direction from the two wheel print loads influencing the same area.

The proposed C-STM considers the loading following longitudinal cracking in a simplified way, where almost all the concrete has formed an opening from the steel following longitudinal cracking. Therefore, it is assumed that this will also occur for other loading cases, meaning that the longitudinal shear resistance is the same. Assuming the specimen will fail due to biaxial bending with limited ductility due to interface failure, a quick scan can be performed for 4-point bending without any modification. As shown in the extended verification in chapter 5, the 4-point bending load is transferred into an equivalent 3-point bending load, giving the same bending moment. By reversing this, it is possible to determine the equivalent 4-point bending load from the 3-point bending resistance, as shown in Figure 6.7.

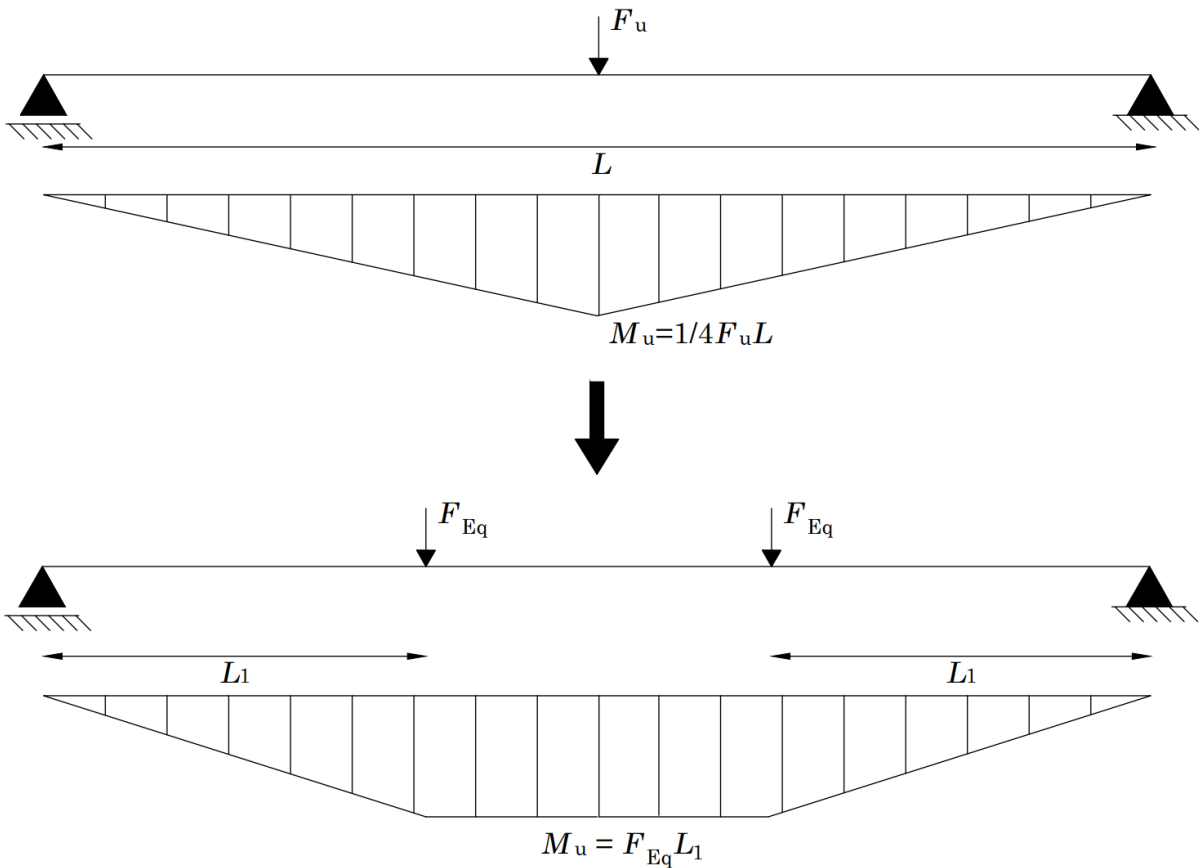


Figure 6.7: Location and notation of loads for calculating the point load equivalent 4-point bending resistance from the 3-point bending ultimate load.

When changing the position of the load in the transverse direction so the load is between two interior girders, the lateral stiffness model and assumptions may be redefined. Similarly, as shown in Figure 6.8 during the in situ testing, the load will distribute to the 4 adjacent girders. Therefore, the load distribution may be redefined as well.

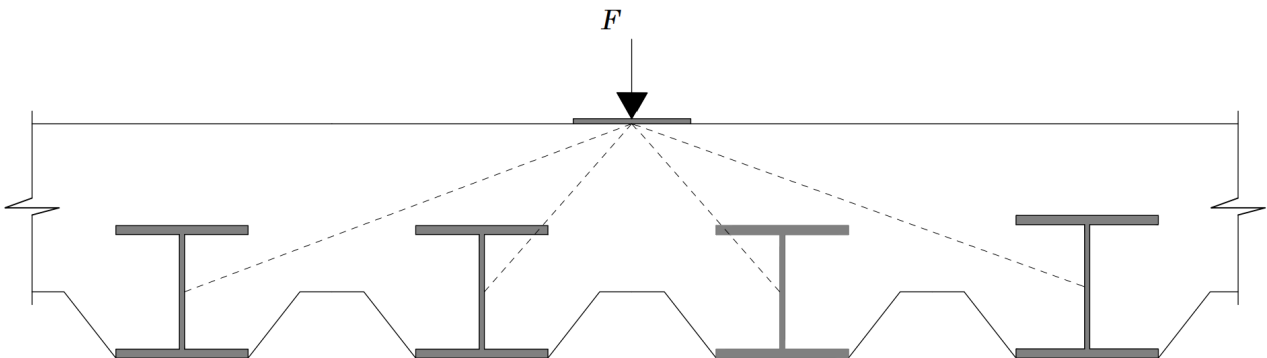


Figure 6.8: Example showing the load distribution at loading between interior composite girders.

Since the model mainly focuses on the lateral displacement of the exterior girder, which has a significantly lower stiffness than the adjacent girder. For the case of a uniform distributed

load, especially the load dispersal and the loading of the C-STM must be changed. However, the general principles of the model should remain, as the loading of the exterior girder merely changes from a single-point load to a uniform distributed load. One thing that remains when changing any of the above loading conditions is the cross-section verifications, as it is assumed that these can be performed following the same procedure as has been proposed. However, when loading between two interior girders, the concrete may not form an opening from the steel, and there will be full steel-concrete contact.

The loading case considered for the laboratory testing was between an exterior and interior girder. Therefore, this gave very little indication of the load distribution between the girders in the case of a load between interior girders. However, the in situ testing showed that the load was distributed equally between the four adjacent girders. On the other hand, this testing did not lead to failure, and therefore, the full picture for this loading case is still missing. It is assumed that another configuration of the proposed analytical model will have to be used, as it mainly focuses on the lateral behaviour of the exterior composite girder. The lateral stiffness will be significantly higher for loading between two interior composite girders. Despite this, the general principles and material parameters may still be applicable, such as bond strength properties and the rules for concrete cover around the encasement. Additionally, the cross-section verifications will still rely on the same principles but with different lateral behaviour due to the higher lateral stiffness.

The engineers of Gemeente Amsterdam can apply the proposed analytical to determine the bearing capacity for the critical case where the load is present between the exterior composite girder and an adjacent girder. Additionally, this method can predict the onset of longitudinal cracking, and as a quick scan, the method can be used to determine the resistance for 4-point bending as previously described. However, adjustments must be made to the proposed method for other loading cases. These adjustments would involve modifying the geometry of the elements of the C-STM, as they largely depend on the specific loading conditions. Nonetheless, the main principles of the C-STM are expected to remain. Similarly, the proposed cross-section verifications will still be applicable, although there may be instances where there is full steel-concrete contact based on the loading case. Consequently, the degree of shear connection will be higher when the lateral strain exceeds the strain criteria and the concrete forms an opening from the steel.

## 6.3 Sensitivity Analysis of Stiffness Parameters

The stiffness of some elements from the C-STM has been studied in a minor sensitivity analysis aiming to understand the elements further. This may as well contribute to recommendations for further research.

### 6.3.1 Compression Struts

It is interesting to investigate the influence of the strut's stiffness as the height of these is determined from the width of the wheel print load. Therefore, a relatively small amount of concrete may be utilized, whereas, in reality, the stresses distribute over a larger area. Figure 6.9 shows that increasing the axial stiffness by multiple factors barely changes the load at longitudinal cracking. However, when decreasing it from its original value, the load at longitudinal cracking is slightly reduced, indicating that when increasing the axial stiffness, it at some point reaches a plateau.

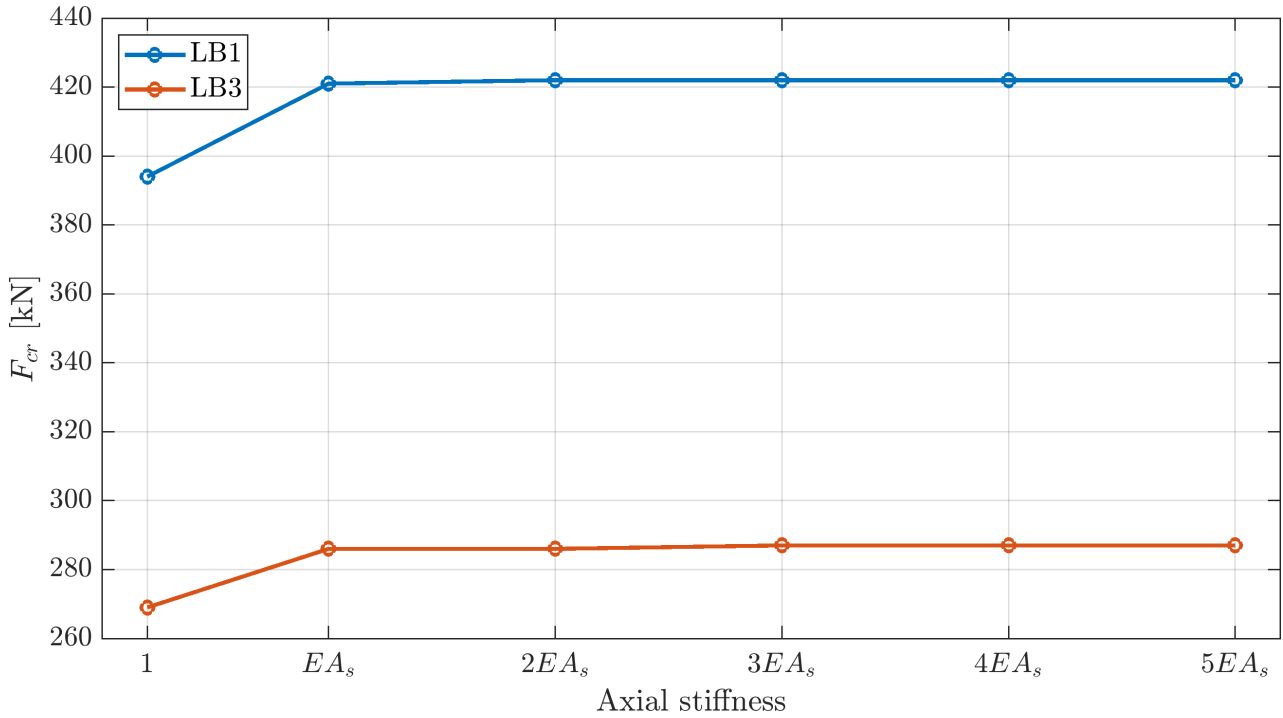


Figure 6.9: The sensitivity to longitudinal cracking to changes of the axial stiffness of the compression struts relative to the original axial stiffness.

From the analysis of Figure 6.9, it is determined that it is not necessary to increase the stiffness of the struts, as this has a low impact on the load at longitudinal cracking. Another reason increasing the stiffness does not influence the load at longitudinal cracking is that the stiffness of the struts is relatively small compared to the stiffness of the vertical springs and the lateral spring beams. Therefore, no further modification is done to the stiffness of the struts to increase the accuracy of the proposed analytical model.

### 6.3.2 Tensile Tie

It is reasonable to analyse the effects of changing the stiffness of the tensile tie, as this is the element that fails when longitudinal cracking occurs. Figure 6.10 shows the sensitivity of the load at longitudinal cracking to changes in the axial stiffness of the tensile tie. The axial stiffness has been changed by increasing the cross-section area of the tensile tie, which shows that by doing this, the load at longitudinal cracking increases linearly because the area is directly related to the resistance of the tensile tie.

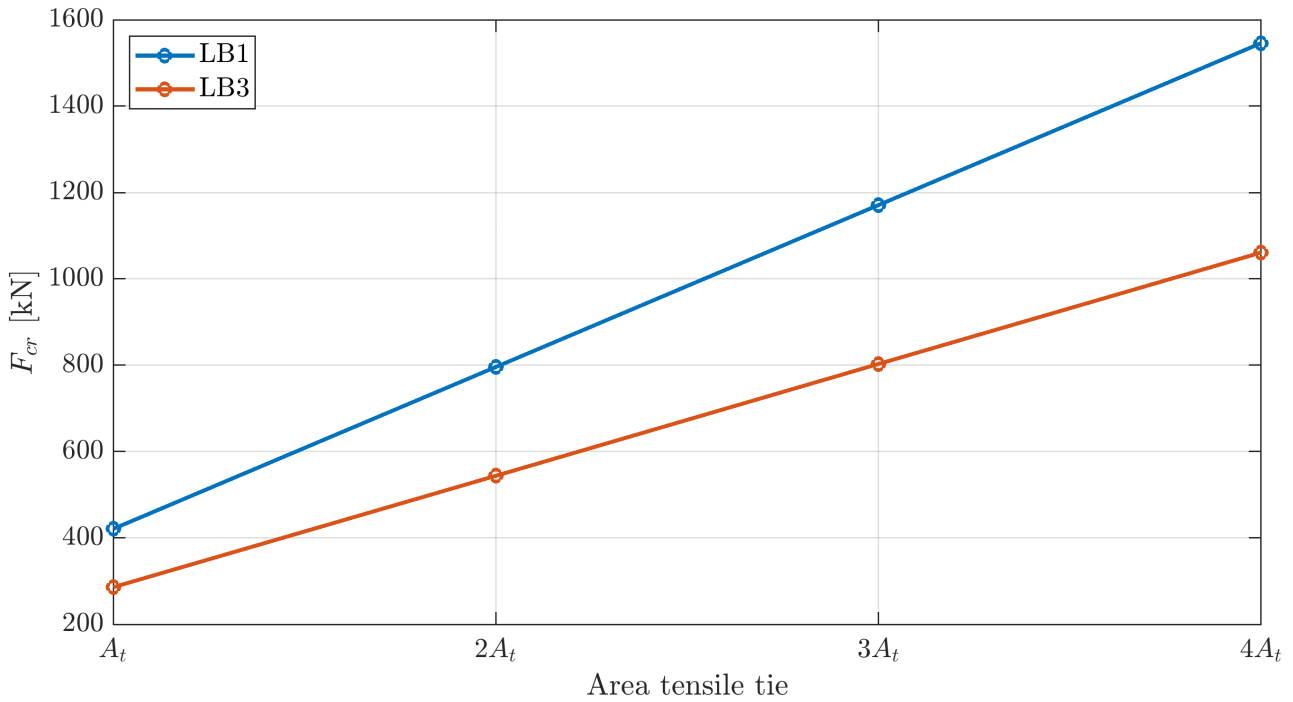


Figure 6.10: The sensitivity to longitudinal cracking to changes of the cross-section area of the tensile tie relative to the original axial stiffness.

Figure 6.11 shows how the lateral displacement decreases when increasing the cross-section area of the tensile tie.

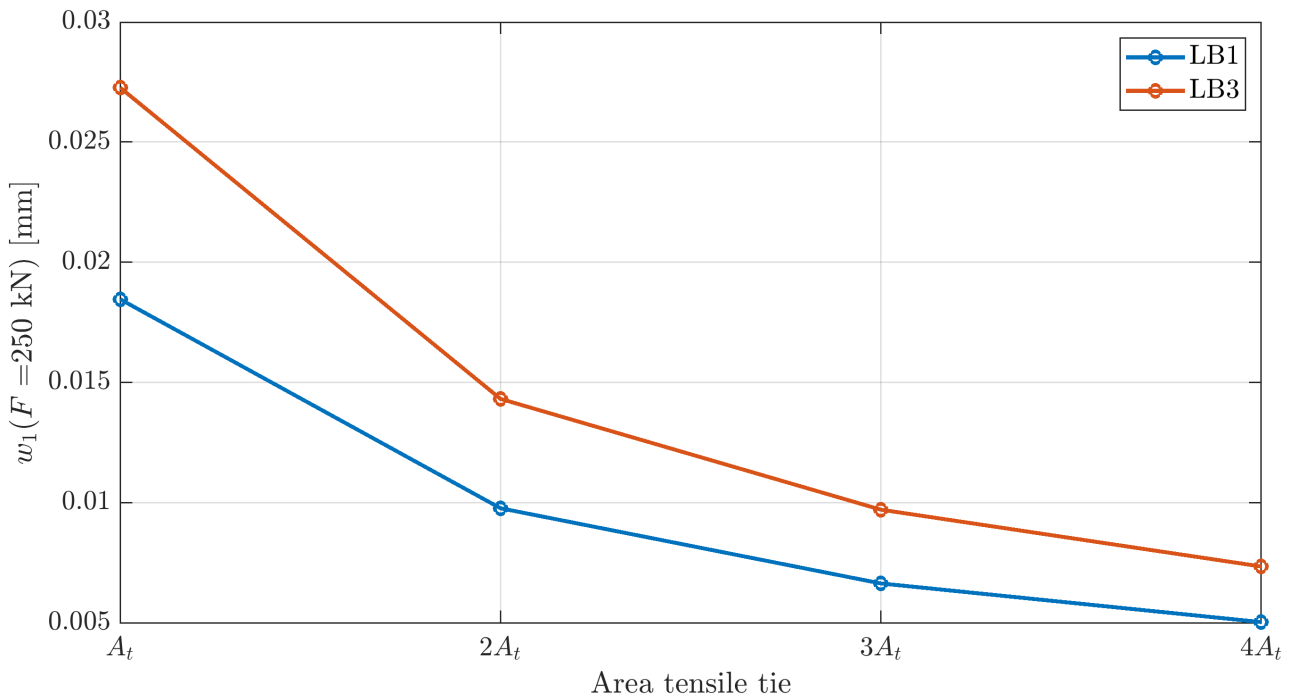


Figure 6.11: The sensitivity of the exterior lateral displacement at 250 kN to changes of the cross-section area of the tensile tie relative to its original value.

Thus, it can be concluded that increasing the axial stiffness of the tensile ties increases the load at longitudinal cracking, which was significantly lower than the load measured from the

experiments and numerical models. However, this also decreases the lateral displacement, which was similar to the displacement profile of the numerical models. Therefore, it is relevant to see if, by adjusting the stiffness of the interior spring beam, the load at longitudinal cracking of the analytical model can be increased while keeping the displacement profile similar to the numerical models.

### 6.3.3 Interior Spring Beam

A similar study has been conducted on the interior springs to understand the stiffness parameters' influence further. The elements related to the exterior composite girder are especially essential as the lateral behaviour of this girder is a focal point of the proposed analytical design method. However, if the elements related to the interior composite girder can be reduced or removed, this may help simplify the solution of the C-STM.

When the spring beams' lateral stiffness increases, the load at longitudinal cracking increases as well. This can be seen in Figure 6.12. Therefore, results closer to the numerical and experimental studies can be achieved by increasing the stiffness of the interior spring beam. However, the load distribution between the struts also changes when the stiffness increases. Therefore, it must be ensured that adequate load distribution is still ensured, which is currently related to many uncertainties. As seen in Appendix D the reaction forces of the supports vary greatly between the support ends and each experiment.

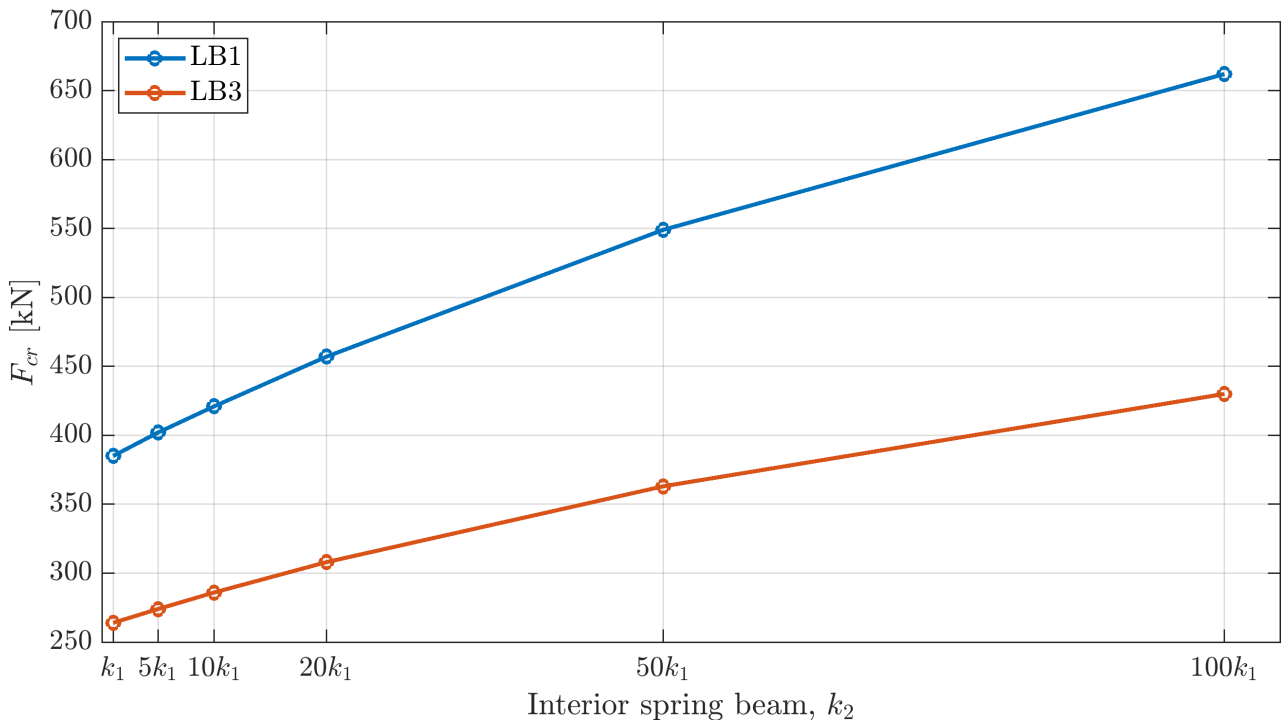


Figure 6.12: The sensitivity to longitudinal cracking to changes of spring  $k_2$  relative to spring  $k_1$ .

Figure 6.13 shows the effects of increasing the lateral stiffness on the lateral displacement of the exterior composite girder. When the stiffness increases, the lateral displacement decreases. However, as shown in the verification, the displacement of the C-STM with the assumed spring

stiffness  $k_2$  comes relatively close to the numerical values. Therefore, it is not desired to increase the stiffness if it significantly impacts the behaviour of the exterior composite girder.

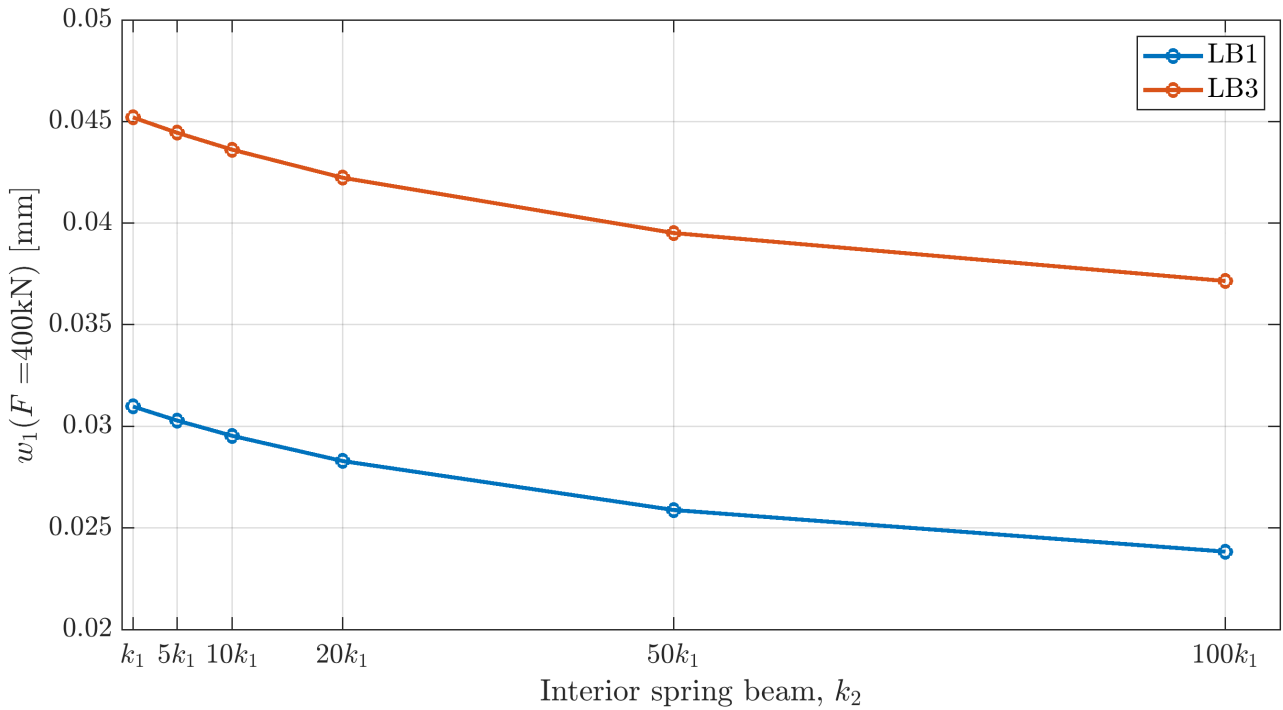


Figure 6.13: The sensitivity of the exterior lateral displacement to changes of spring  $k_2$  relative to spring  $k_1$  at a load at 400 kN.

Thus it can be seen from Figures 6.12 and 6.13 that increasing the stiffness of spring  $k_2$  impacts the displacement and load significantly compared to increasing the stiffness of the struts. A reason for this can be that any changes in the stiffness of spring  $k_2$  relative to spring  $k_1$  decreases the symmetry, e.i. the distribution of the force  $F$  to each of the struts. This is also shown in Figure 6.14, showing how increasing the stiffness of  $k_2$  changes the load distribution.

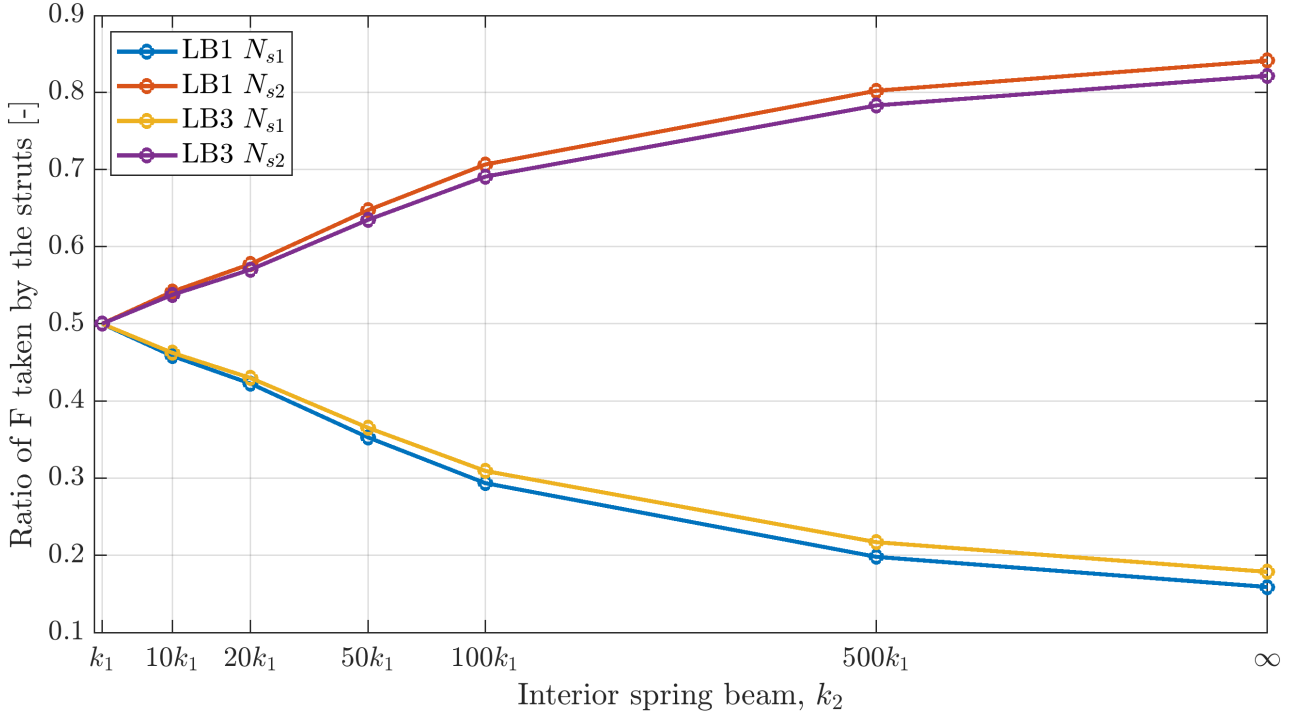


Figure 6.14: The sensitivity of the load distribution to changes of spring  $k_2$  relative to spring  $k_1$ .

Figure 6.14 shows that increasing the stiffness greatly impacts the load distribution, especially when increasing the stiffness close to infinite, which may be equivalent to a horizontal support at spring  $k_2$ . As the load distribution is related to a lot of uncertainty, it is assumed that some general limits on the load distribution can be established based on the results from Figure 6.14. For a loading where the middle girder has an infinite stiffness compared to the exterior composite girder, it can be assumed that the exterior girder takes about 0.2 of  $F$  between the two girders. Whereas, for a system where the interior girder has a stiffness closer to the exterior, it is recommended to use a load at the exterior girder of 0.5 of  $F$ .

## 6.4 Limitations

The proposed analytical model has limitations as it is only verified using two test specimens and two numerical models based on the same test specimens. These specimens are relatively short, about 6 to 7.5 m considering the span range of the Amsterdam bridges with a maximum span of about 14 m. To enhance the reliability of the model, it is recommended to include a larger number of specimens for verification. To address the limitation of the proposed model, further research should involve the verification of the model using longer-spanning bridge decks, which can be achieved by using the same modelling approach as was currently used. Further research should consider the effects on the bearing capacity when increasing the span length.

Another limitation of the analytical model is its configuration to analyse the most critical loading case between the exterior composite girder and an adjacent girder. However, loading between the interior girders, where the load distributes to multiple adjacent girders, needs to be considered as well, which is considered less critical. The proposed analytical model should be adjusted to account for this scenario, focusing on the composite girders' load distribution

and vertical behaviour. Nonetheless, there is currently no available data for verifying this configuration. Therefore, additional testing or numerical modelling is necessary.

Finally, a limitation of the proposed model is that it only girders 3-point bending. As previously discussed by a few means, the model can, in a simplified way, account for 4-point bending, assuming that failure occurs from flexural bending. However, the model has shortcomings considering other loading cases, such as a uniformly distributed load or loading between interior girders. To overcome this limitation, modifications to the load dispersal and adjustments in the model geometry is necessary as the current model assumes a single-point load.

# 7 Conclusions and Recommendations

## 7.1 Conclusions

This research project has been conducted with the aim of providing an analytical model to determine the bearing capacity of historic steel-concrete composite bridges in Amsterdam. Such a model is critical to avoid oversimplified analytical calculations and time-consuming FEM calculations. To address this problem, it has strived to answer the following research question:

**How can the bearing capacity of existing steel-concrete-composite bridges without mechanical connectors be determined using an analytical model?**

The main assumptions of the analytical model are described in the following:

- The distribution of stresses is represented through a compatibility-based strut and tie model (C-STM).
- The model considers loading between the exterior composite girder and the adjacent girder. Determined from an experimental and numerical study.
- When the tensile tie exceeds its resistance, it fails, and longitudinal cracking occurs.
- The lateral behaviour of the girders is interpreted as lateral spring beams with clamped supports, which is derived from displacement profiles from FEM.
- The lateral behaviour of the exterior girder is linked to the cross-section verifications.
- When the lateral displacement increases sufficiently, the concrete will form an opening from the steel, and the effective contact perimeter between the steel and concrete reduces.
- The effective contact perimeter is linked to the longitudinal shear resistance, which impacts the biaxial bending and the vertical shear resistances through the degree of shear connection.

The analytical model has been compared to numerical and experimental results by calculating cross-sections similar to the ones modelled and tested in the laboratory. In the following, the main results and observations from the model are shown:

- The load at longitudinal cracking is underestimated with a significant leeway compared to the experiments and numerical models.
- Analytical calculations show that test specimens LB1 and LB3 fail due to biaxial bending with limited ductility due to partial shear connection.
- The load at failure from the analytical calculation is close to that of the numerical models.
- The load at failure is close to the analytical when transferring the 4-point bending load from the experiments into an equivalent 3-point bending load.

The proposed model predicts a similar failure as was observed during the experiments. The method can replace oversimplified analytical calculations and time-consuming NLFEM calculations. However, this model is only valid for 3-point bending between the exterior composite and adjacent girder. Nonetheless, contributing to the research and assessment of these Amsterdam

bridges. Other bridges around the Netherlands or Europe may be constructed after similar design methods as the steel-concrete composite bridges in Amsterdam. Thus, the application of the method may be broader than for the current amount of bridges under assessment.

## 7.2 Recommendations

This research proposes an analytical model based on observations from experiments and numerical models. However, the sample size of the Amsterdam bridge decks tested was relatively small. Therefore, a further investigation of the bridges would require increasing the sample size. Alternatively, implementing NLFEM would be sufficient, as numerical models of the two specimens have already been created and verified. The same modelling approach could be implemented on other Amsterdam bridges, avoiding more laboratory tests that are time-demanding and expensive. This would especially be relevant for bridges with larger dimensions than the bridge decks already tested, as the ones tested are some of the shortest-spanning bridges of this type, which is about 5 m. In contrast, the maximum span is 14 m. However, looking at the results from the current calculations, it can be expected that the failure mode will be the same as for LB1 and LB3. When increasing the span, generally, bending becomes more critical. Additionally, the current specimens, which had a relatively short span, already proved that a large margin governed biaxial bending compared to vertical shear.

A general limitation of this research is the absence of literature or experiments on similar topics. One reason for this is the composite bridges' complexity, as they are missing shear connectors and transverse reinforcement. Very few composite structures in bending are designed without shear connectors. Therefore, no or little research has been done in this field. The same applies to unreinforced concrete structures, which rarely appear. Moreover, this construction method was used almost a century ago and is not as relevant for research as current design methods. Experiments or an extended literature review should further investigate the bond strength parameters, as previously shown how dependent the bearing capacity is on the bond strength parameters, especially the cohesion. This should consider the time effects on cohesion as the literature review currently regarded the bond strength from experiments conducted relatively short from the casting. This could also be done by using push-out tests and further examining the bridges' steel-concrete interface. On the other hand, push-out tests may not be suitable for the bridges due to their asymmetric encasement, which is not desired for this type of test. The influence of the concrete cover, which also affects bond strength parameters, would be relevant to the study, as this varies a lot for the specimens. Similar to investigating the influence of the span length, this can also be studied using numerical modelling.

Following the verification of this method to bridges with larger dimensions, it is recommended to expand the method to other loading cases, as was mentioned in the discussion. The next step will mainly be loading between interior girders. This will have to focus more on the vertical behaviour of the composite girders and the load distribution between adjacent girders, which can be done by modifying the proposed C-STM. The following, the bearing capacity to 3-point bending can be determined regardless of the loading position. This theory can then be elevated to consider multiple loading cases, such as 4-point bending and a uniformly distributed load.

# References

- [1] Ane de Boer, Long Ha, and Andrew Quansah. “Assessment by in situ load tests of historical steel-concrete bridge decks”. In: *Computational Modelling of Concrete and Concrete Structures*. CRC Press, May 2022, pp. 712–719. DOI: 10.1201/9781003316404-85.
- [2] European Committee for Standardization. “EN 1994-1-1. Eurocode 4: Design of composite steel and concrete structures - Part 1-1: General rules and rules for buildings”. In: (2004).
- [3] European Committee for Standardization. *EUROPEAN STANDARD English Version Eurocode 4-Design of composite steel and concrete structures-Part 2: General rules and rules for bridges*. Tech. rep. 2005.
- [4] Directie van Waterstaat. *Voorschriften voor het ontwerpen van stalen bruggen (VOSB1933)*. Tech. rep. Ministerie van Waterstaat., 1933.
- [5] Peter Dawe. *Research Perspectives: Traffic loading on highway bridges*. Thomas Telford Publishing, 2003, pp. 1–31.
- [6] Holger Eggemann and Karl Eugen Kurrer. “Zur internationalen Verbreitung des Systems Melan seit 1892: Konstruktion und Brückenbau”. In: *Beton- und Stahlbetonbau* 101.11 (Nov. 2006), pp. 911–922. ISSN: 00059900. DOI: 10.1002/best.200690163.
- [7] Markus Schäfer. “European design code for composite structures in steel and concrete: Historical development and investigation in the second generation of Eurocode 4”. In: *Steel Construction* 12.2 (May 2019), pp. 70–81. ISSN: 18670539. DOI: 10.1002/stco.201800031.
- [8] European Committee for Standardization. *Eurocode 1: Belastingen op constructies-Deel 2: Verkeersbelasting op bruggen Eurocode 1: Actions on structures-Part 2: Traffic loads on bridges*. Tech. rep. 2003.
- [9] European Committee for Standardization. *EN 1993-1-1: Eurocode 3: Design of steel structures - Part 1-1: General rules and rules for buildings*. Tech. rep. 2005.
- [10] Shun Ichi Nakamura and Naoya Narita. “Bending and shear strengths of partially encased composite I-girders”. In: *Journal of Constructional Steel Research* 59.12 (2003), pp. 1435–1453. ISSN: 0143974X. DOI: 10.1016/S0143-974X(03)00104-4.
- [11] R Narayanan, R I M Ai-Amery, and T M Roberts. *Shear Strength of Composite Plate Girders with Rectangular Web Cut-Outs*. Tech. rep. 1989, pp. 151–166.
- [12] European Committee for Standardization. “EN 1992-1-1”. In: (2004).
- [13] George Vasdravellis and Brian Uy. “Shear Strength and Moment-Shear Interaction in Steel-Concrete Composite Beams”. In: *Journal of Structural Engineering* 140.11 (Nov. 2014). ISSN: 0733-9445. DOI: 10.1061/(asce)st.1943-541x.0001008.
- [14] Federation internationale du beton., Comite euro-international du beton., and Federation internationale de la precontrainte. *Model code 2010 : first complete draft*. Federation internationale du beton, 2010. ISBN: 9782883940956.
- [15] Maciej Chrzanowski et al. *Transfer of shear stresses at steel-concrete interface: Experimental tests and literature review*. Feb. 2019. DOI: 10.1002/stco.201800024.
- [16] K. Roik. *Untersuchung der Verbundwirkung zwischen Stahlprofil und Beton bei Stützenkonstruktionen*. Düsseldorf: Studiengesellschaft für Anwendungstechnik von Eisen und Stahl e.V, 1984.

- [17] J. A. Wium. “Composite Columns: Force Transfer from Steel Section to Concrete Encasement”. PhD thesis. Lausanne: Ecole Polytechnique Federale de Lausanne, 1992.
- [18] H. Degée et al. *Smart Composite Components – Concrete Structures Reinforced by Steel Profiles*. Tech. rep. European Commission, 2016.
- [19] American Institute of Steel Construction. “Manual of Steel Construction”. In: 7 (1970).
- [20] Grawira Ganjur Giwangkara et al. “Analysis of Internal Friction Angle and Cohesion Value for Road Base Materials in a Specified Gradation”. In: *Journal of Advanced Civil and Environmental Engineering* 3.2 (Oct. 2020), p. 58. DOI: 10.30659/jacee.3.2.58-65.
- [21] B. G. Rabbat and H. G. Russell. *Friction Coefficient of Steel on Concrete or Grout*. Tech. rep. 1985.
- [22] By Peter Baltay and Atle Gjelsvik. *COEFFICIENT OF FRICTION FOR STEEL ON CONCRETE AT HIGH NORMAL STRESS*. Tech. rep.
- [23] J Schlaich and K Schiifer. *Design and detailing of structural concrete using strut-and-tie models*. Tech. rep. 1991.
- [24] Kannan C. Bhanu, N. Ganesan, and P. V. Indira. “A Review on Strut and Tie Methods”. In: *IOP Conference Series: Materials Science and Engineering*. Vol. 936. 1. IOP Publishing Ltd, Oct. 2020. DOI: 10.1088/1757-899X/936/1/012051.
- [25] ACI (American Concrete Institute). “Building code requirements for structural concrete and commentary. ACI 318-19”. In: (2019).
- [26] CSA (Canadian Standards Association). “Design of concrete structures. CAN/CSA A23.3-19”. In: (2019).
- [27] J.C. Walraven and C.R. Braam. *CIE3150/4160 - Prestressed concrete*. Tech. rep. Delft: Faculty of Civil Engineering and Geosciences, 2019.
- [28] Imad Shakir Abbood. “Strut-and-tie model applications on reinforced concrete deep beam: A comprehensive review”. In: *Case Studies in Construction Materials* (Dec. 2022), e01767. ISSN: 22145095. DOI: 10.1016/j.cscm.2022.e01767. URL: <https://linkinghub.elsevier.com/retrieve/pii/S2214509522008993>.
- [29] Han Ug Bae, Michael G Oliva, and Lawrence C Bank. *Reinforcement-Free Decks Using Modified Strut-and-Tie Model*. Tech. rep. 5. 2011.
- [30] J.w. Park and D. Kuchma. *Strut-and-tie model analysis for strength prediction of deep beams*. Tech. rep. 2007. URL: <https://www.researchgate.net/publication/285744070>.
- [31] Yuguang Yang. *Lecture Notes: Guyon Massonnet*. 2021.
- [32] Kaiqiang Guo, Zhao Liu, and Jesús Miguel Bairán. “Transfer Matrix Method for Calculating the Transverse Load Distribution of Articulated Slab Bridges”. In: *Buildings* 12.10 (Oct. 2022). ISSN: 20755309. DOI: 10.3390/buildings12101610.
- [33] G. G. A. Ir. Dieteren et al. “TNO 2021 R11449 Meetplan LB2 Gemeente Amsterdam”. In: (2021).
- [34] Anders Jørgensen, Mauro Poliotti, and Yuguang Yang. *Experiment report on steel-concrete-composite bridge deck without mechanical connectors (Verbundträger)*. Tech. rep. 2022.
- [35] From B Ir Brongers GGA Dieteren. *Memorandum Municipality of Amsterdam in the laboratory of Structural Dynamics of TNO in*. Tech. rep. 2021. URL: [www.tno.nl](http://www.tno.nl).

- [36] Mauro Poliotti, Yuguang Yang, and Ane De Boer. *Experimental and numerical assessment of historical steel-concrete composite bridge decks without mechanical connectors*. Tech. rep.

# A Calculation Example

In the following is a calculation example shown of the analytical C-STM design with the corresponding cross-section verifications. However, some of these calculations are performed using MATLAB functions and iterations. Thus, the MATLAB code is shown in Appendix B and C and will frequently be referred to where the MATLAB code has been used.

## A.1 Example - Establish the C-STM

The following example considers the cross-section of the middle and exterior girder of LB1 shown in Figure A.1 with a load applied between these two girders. In the longitudinal direction, the load is applied at midspan. The total height of the bridge deck is assumed to be 460 mm; however, the height of specimen LB1 varied between 400 mm and 490 mm. 460 mm is used as this is the height of the numerical model of LB1. Moreover, the profiles are DIN profiles, but for simplicity they are considered as HEB profiles.

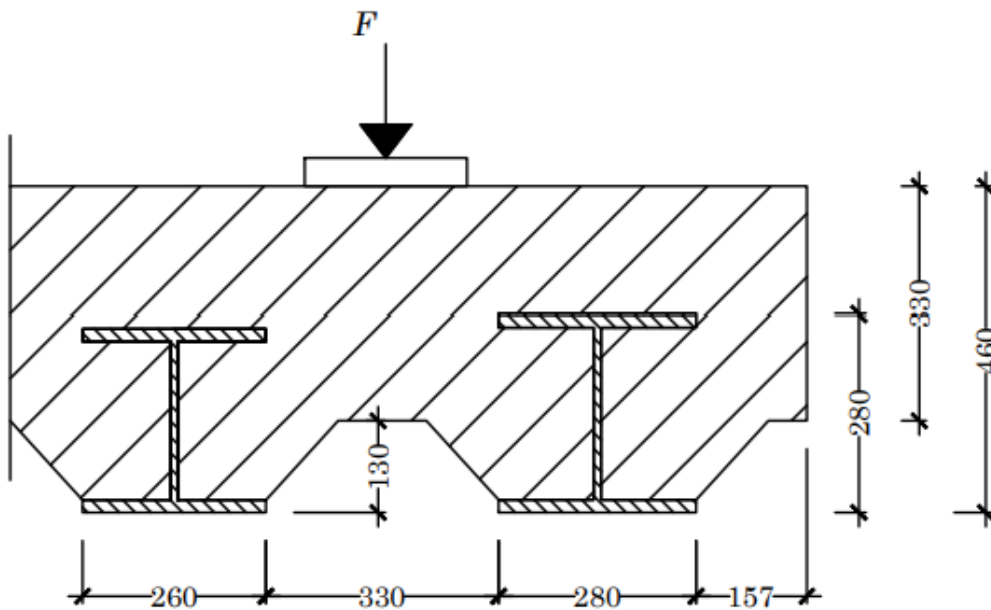


Figure A.1: Cross-section of LB1 of the exterior and middle girder.

Table A.1 gives the input parameters for the following calculation example.

Table A.1: Material properties of the concrete, steel and interface for LB1. \* Calculated from the reference system in Figure A.2.

<b>Concrete Properties</b>		
Compressive Strength	$f_c =$	50.9 MPa
Tensile Strength	$f_t =$	3.68 MPa
Young 's Modulus	$E_c =$	37 GPa
<b>Steel Properties</b>		
Young 's Modulus	$E_a =$	200 GPa
Yielding Stress	$f_y =$	235 MPa
<b>Geometry</b>		
Wheel print width	$w_p =$	230 mm
Wheel print length	$b =$	230 mm
Length tie	$L_t =$	600 mm
Total height bridge deck	$h =$	460 mm
Concrete cover above the exterior steel girder	$h_{c1} =$	180 mm
Height cut-out section	$h_{c2} =$	330 mm
Height exterior steel girder	$h_a =$	280 mm
Span length between supports	$L =$	5950 mm
Span length between cross beams	$L_{eff} =$	5600 mm
Length cross beams	$L_c =$	510 mm
<b>Interface Properties</b>		
Cohesion	$c =$	0.54 MPa
Friction	$\mu =$	0.3
<b>Cross-section properties - exterior composite girder</b>		
Moment of inertia concrete major axis	$I_{c,y,1} =$	* $1.33 \cdot 10^{10} \text{mm}^4$
Moment of inertia concrete minor axis	$I_{c,z,1} =$	* $2.79 \cdot 10^{10} \text{mm}^4$
Moment of inertia cracked concrete minor axis	$I_{c,z,1,cr} =$	* $2.44 \cdot 10^{10} \text{mm}^4$
Moment of inertia steel major axis	$I_{a,y,1} =$	* $1.48 \cdot 10^9 \text{mm}^4$
Moment of inertia steel minor axis	$I_{a,z,1} =$	* $1.18 \cdot 10^9 \text{mm}^4$
Centroid of concrete to the top of the concrete	$z_c =$	204 mm
Centroid of steel to the top of the concrete	$z_a =$	320 mm
Shear area of the steel girder	$A_v =$	4109 mm <sup>2</sup>

### 1. Calc. $\eta, e_{T0}$

$$n = \frac{200 \text{ GPa}}{37 \text{ GPa}} = 5.4$$

$$e_{T0} = \frac{\frac{235743 \text{ mm}^2}{5.4} \cdot 204 \text{ mm} + 12642 \text{ mm}^2 \cdot 320 \text{ mm}}{12642 \text{ mm}^2 + \frac{235743 \text{ mm}^2}{5.4}} = 230 \text{ mm}$$

### 2. Calc. $\theta_1, \theta_2, L_d$

$$L_d = \frac{2 \cdot 230 \text{ mm}}{\tan 45^\circ} = 690 \text{ mm}$$

$$\theta_1 = \tan^{-1} \left( \frac{230 \text{ mm}}{0.5 \cdot 600 \text{ mm}} \right) = 39.9^\circ$$

$$\theta_2 = 90^\circ - 39.9^\circ = 50.1^\circ$$

3. Calc.  $h_{s,1}$ ,  $h_{s,2}$ ,  $h_t$ ,  $A_{s,1}$ ,  $A_{s,2}$ ,  $A_t$

$$h_{s1} = \cos(39.9^\circ) \cdot 230 \text{ mm} = 176 \text{ mm}$$

$$h_{s2} = h_{s1} = 176 \text{ mm}$$

$$h_t = \frac{330 \text{ mm}}{2} = 150 \text{ mm} \leq 330 \text{ mm} - 180 \text{ mm} = 150 \text{ mm}$$

$$A_{s1} = 176 \text{ mm} \cdot 690 \text{ mm} = 121\,720 \text{ mm}^2$$

$$A_{s2} = 176 \text{ mm} \cdot 690 \text{ mm} = 121\,720 \text{ mm}^2$$

$$A_t = 150 \text{ mm} \cdot 690 \text{ mm} = 103\,520 \text{ mm}^2$$

4. Calc.  $EI_{y3}$ ,  $EI_{y4}$ ,  $k_3$ ,  $k_4$

The moments of inertia for the specimens are calculated using a MATLAB function. This function calculates the moment of inertia around the x- and y-axis as shown in Figure A.2.

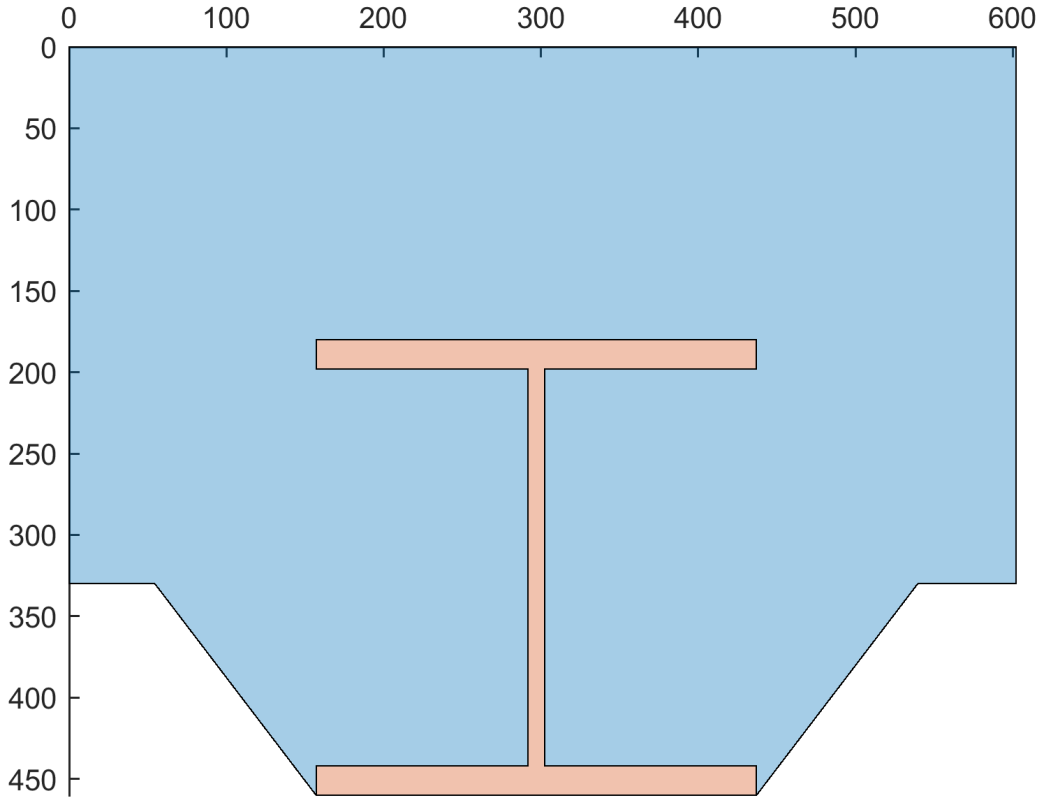


Figure A.2: Reference axis for cross-section properties of LB1 and LB3.

However, as it is desired to determine the total bending stiffness for the composite girder around its neutral axis, Steiner's Theorem is applied to shift the axis from the x- and y-axis. This is shown from Eq. A.1.

$$I_{y1} = (I_{a,y,1} + I_{c,y,1}n) - e_{T0,y}^2(A_a + A_c n) \quad (\text{A.1})$$

$$\begin{aligned} EI_{y1} &= 200 \text{ GPa} \left( [1.48 \cdot 10^9 \text{ mm}^4 + 1.33 \cdot 10^{10} \text{ mm}^4] \right. \\ &\quad \left. - (230 \text{ mm})^2 \cdot (12\,642 \text{ mm}^2 + 235\,743 \text{ mm}^2 \cdot 5.4) \right) \\ &= 1.94 \cdot 10^{14} \text{ Nmm}^2 \end{aligned}$$

$$k_3 = \frac{48 \cdot 1.94 \cdot 10^{14} \text{ Nmm}^2 \cdot 690 \text{ mm}}{690 \text{ mm} \left( (5950 \text{ mm})^3 - \frac{(690 \text{ mm})^2}{2} \cdot 5950 \text{ mm} + \frac{(690 \text{ mm})^3}{8} \right)} = 5.34 \cdot 10^4 \text{ N/mm}$$

$$EI_{y2} = 1.94 \cdot 10^{14} \text{ Nmm}^2$$

$$k_4 = 5.34 \cdot 10^4 \text{ N/mm}$$

### 5. Calc. $EI_1$ , $EI_2$ , $EI_{1,cr}$

The same principles as in the previous are applied to calculate the moment of inertia for the minor axis.

$$\begin{aligned} EI_{z_1} &= 200 \text{ GPa} \left( [1.18 \cdot 10^9 \text{ mm}^4 + 2.79 \cdot 10^{10} \text{ mm}^4 \cdot 5.4] \right. \\ &\quad \left. - (299.6 \text{ mm})^2 \cdot (12\,642 \text{ mm}^2 + 235\,743 \text{ mm}^2 \cdot 5.4) \right) \\ &= 2.57 \cdot 10^{14} \text{ Nmm}^2 \end{aligned}$$

For the case of this calculation, it is assumed that  $p$ , which is the number of interior composite girders, is relatively high, giving a high stiffness of the composite girder. This is due to the loading of the specimens during the laboratory testing, as they were loaded at both sides of the middle girder. This loading keeps the middle composite girder in horizontal equilibrium, equating to high lateral stiffness.

$$EI_{z_2} = 2.57 \cdot 10^{14} \text{ Nmm}^2 \cdot 10 = 2.57 \cdot 10^{15} \text{ Nmm}^2$$

The flexural stiffness of the failed concrete is shown in Figure A.3 using a similar calculation to uncracked concrete; the only difference is the reduction of the concrete area considered.

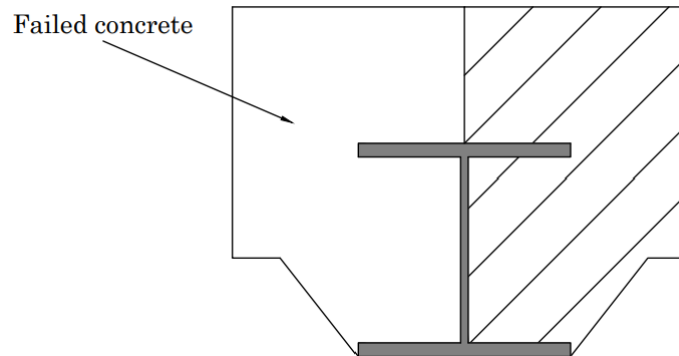


Figure A.3: Concrete considered following longitudinal cracking.

For this calculation, the elastic neutral axis must be calculated again. This is calculated to the following.

$$e_{T0,x,cr} = 389.4 \text{ mm}$$

$$\begin{aligned} EI_{1,cr} &= 200 \text{ GPa} \left( [1.18 \cdot 10^9 \text{ mm}^4 + 2.44 \cdot 10^{10} \text{ mm}^4 \cdot 5.4] \right. \\ &\quad \left. - (389 \text{ mm})^2 \cdot (12\,642 \text{ mm}^2 + 120\,140 \text{ mm}^2 \cdot 5.4) \right) \\ &= 7.98 \cdot 10^{13} \text{ Nmm}^2 \end{aligned}$$

## 6. Determine displacements of each element

Now the parameters used to describe the C-STM have been determined. Following the displacement of each element can be determined. For this example, the solution strategy of the C-STM

relies on ordinary differential equations that can be solved from equilibrium and compatibility conditions. However, a more direct solution strategy may be found, for instance, using the matrix method. The displacements of the system are solved numerically using MATLAB. The MATLAB code is also shown in Appendix B. The displacements are determined as the following.

$$u_{s1}(x_{s1}, F) = -1.33 \cdot 10^{-10} Fx + 1.65 \cdot 10^{-7} F \quad [\text{N,mm}]$$

$$u_{s2}(x_{s2}, F) = -1.57 \cdot 10^{-10} Fx + 1.65 \cdot 10^{-7} F \quad [\text{N,mm}]$$

$$u_t(x_t, F) = 2.36 \cdot 10^{-10} Fx - 6.80 \cdot 10^{-8} F \quad [\text{N,mm}]$$

$$w_1(x, F) = -6.70 \cdot 10^{-18} Fx^3 + 2.83 \cdot 10^{-14} Fx^2 \quad [\text{N,mm}]$$

$$w_2(x, F) = -6.20 \cdot 10^{-18} Fx^3 + 2.60 \cdot 10^{-14} Fx^2 \quad [\text{N,mm}]$$

The stresses and strains can be determined using the constitutive relation for each element.

### 7. Determine $F_{cr}$ when $\sigma_t = f_t$

The stresses in the tensile tie can be determined by using the constitutive relation for the tensile tie as given from Eq.A.2, where the strain is determined as the derivative of the displacement of the tensile tie.

$$\sigma_t = \varepsilon_t E_c = \frac{du_t}{dx} E_c \quad (\text{A.2})$$

Therefore, the stresses in the tensile tie can be described using the following equation.

$$\sigma_t = 2.36 \cdot 10^{-10} F \cdot 37 \text{ GPa} = 8.7320 \cdot 10^{-6} F \quad \text{MPa}$$

Thus, with a tensile resistance of concrete at 3.68 MPa, the load at cracking can be determined as the following.

$$3.68 \text{ MPa} = 8.7320 \cdot 10^{-6} F_{cr} \Rightarrow F_{cr} = 421 \text{ kN}$$

Therefore, the load at longitudinal cracking is 421 kN.

### A.1.1 Stage 1 Cross-section Verification

Following longitudinal cracking, it must be determined if the specimen fails before the load at longitudinal cracking occurs. This is checked using the load at longitudinal cracking  $F_{cr}$  to verify each resistance. The following resistances are checked:

- Resistance of the compression struts

- Longitudinal shear resistance
- Biaxial bending resistance
- Vertical shear resistance

#### A.1.1.1 Resistance Compression Struts

The forces in the compression struts at  $F_{cr} = 421$  kN is determined using the constitutive relation for the struts from Eq.A.3.

$$\sigma_{s,i} = \varepsilon_{s,i} E_c = \frac{du_{s,i}}{dx} E_c \quad (\text{A.3})$$

$$\sigma_{s,1}(F) = 1.33 \cdot 10^{-10} F \cdot 37 \text{ GPa} = 4.92 \cdot 10^{-6} F$$

$$\sigma_{s,1}(F_u) = 4.92 \cdot 10^{-6} F_u = 50.9 \text{ MPa} \Rightarrow F_u = 1.03 \cdot 10^4 \text{ kN}$$

$$\sigma_{s,2}(F) = 1.57 \cdot 10^{-10} F \cdot 37 \text{ GPa} = 5.81 \cdot 10^{-6} F$$

$$\sigma_{s,2}(F_u) = 5.81 \cdot 10^{-6} F_u = 50.9 \text{ MPa} \Rightarrow F_u = 8760 \text{ kN}$$

Thus, the compression struts fail when the single point load exceeds 8760 kN, far from the load at longitudinal cracking.

#### A.1.1.2 Longitudinal Shear Resistance

##### 1. Determine the longitudinal shear resistance $V_{x,Rd}$ .

The total length of LB1 with cross beams is:

$$L_{total} = 5600 \text{ mm} + 2 \cdot 510 \text{ mm} = 6620 \text{ mm}$$

The effective contact perimeter is 909 mm with the 50% reduction of the bottom part of the top steel flange. Thus, the longitudinal shear resistance of the exterior composite girder is determined by the following:

$$V_{x,Rd} = 6620 \text{ mm} \cdot 909 \text{ mm} \cdot 0.54 \text{ MPa} = 3250 \text{ kN}$$

The force, that the exterior composite girder is subject to can be calculated as half the force of the compression force in the strut. The force in the compression strut is determined from the constitutive relation in Eq.A.4.

$$N_{s,1}(F) = \frac{du_{s1}}{dx} E A_{s,1} \quad (\text{A.4})$$

$$N_{s,1}(F = F_{cr}) = 1.33 \cdot 10^{-10} \cdot 421 \text{ kN} \cdot 37 \text{ GPa} \cdot 121\,720 \text{ mm}^2 = 252 \text{ kN}$$

$$V_{Ed} = \frac{N_{s,1}}{2} = 126 \text{ kN}$$

Therefore, the longitudinal shear resistance is larger than the vertical shear force at longitudinal cracking.

### A.1.1.3 Biaxial Bending Resistance

The following shows a calculation example of how to determine the biaxial bending resistance of LB1. As previously mentioned, some of these calculations involved iteration and other mathematical operations where software such as MATLAB is preferable. Thus, where software has been used, references to the corresponding appendix with the MATLAB code are provided.

#### 1. Calc. $F_{cc,y}$ , $F_{cc,z}$ using iteration

For biaxial bending, the concrete compression forces are first determined, assuming a full shear connection. These are determined using iteration with the MATLAB code in Appendix C. The compression force from major axis bending and minor axis bending has been determined to  $F_{cc,y} = 2995 \text{ kN}$  and  $F_{cc,z} = 2768 \text{ kN}$ .

#### 2. Calc. $\eta$ using $V_{x,Rd}$

The minimum value of the longitudinal shear resistance occurs following the longitudinal cracking. This value is 3250 kN. Hence the degree of shear connection can be determined as the following.

$$\eta = \frac{3250 \text{ kN}}{2995 \text{ kN} + 2768 \text{ kN}} = 0.56$$

As the degree of shear connection is below, there is a partial shear connection. Thus, the concrete compression forces must be reduced.

#### 3. Calc. $F_{cc,y,red}$ , $F_{cc,z,red}$

$$F_{cc,y,red} = 0.56 \cdot 2995 \text{ kN} = 1677 \text{ kN}$$

$$F_{cc,z,red} = 0.56 \cdot 2768 \text{ kN} = 1550 \text{ kN}$$

#### 4. Determine $z_1$ , $z_2$ , $y_1$ , $y_2$

The distance between the respective compression forces and the tension forces are similarly determined using iteration that also is included in the MATLAB code in Appendix C. The values are determined to  $z_1 = 326 \text{ mm}$ ,  $z_2 = 173 \text{ mm}$ ,  $y_1 = 274 \text{ mm}$  and  $y_2 = 129 \text{ mm}$ . Figure A.4 shows the compression and tension components of the steel and concrete for major axis bending. Figure A.5 shows the same for minor axis bending.

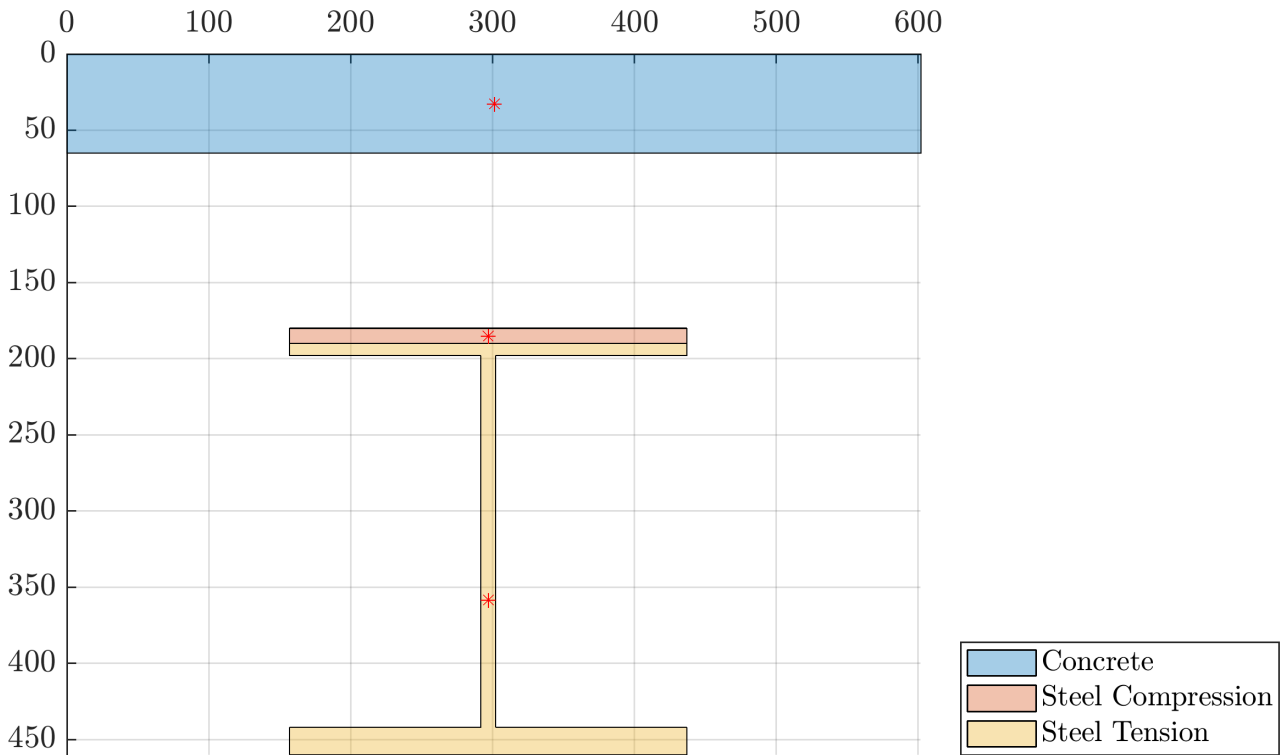


Figure A.4: Internal force components from major axis bending of the exterior composite girder. The red dots indicate the centroid of each force component.

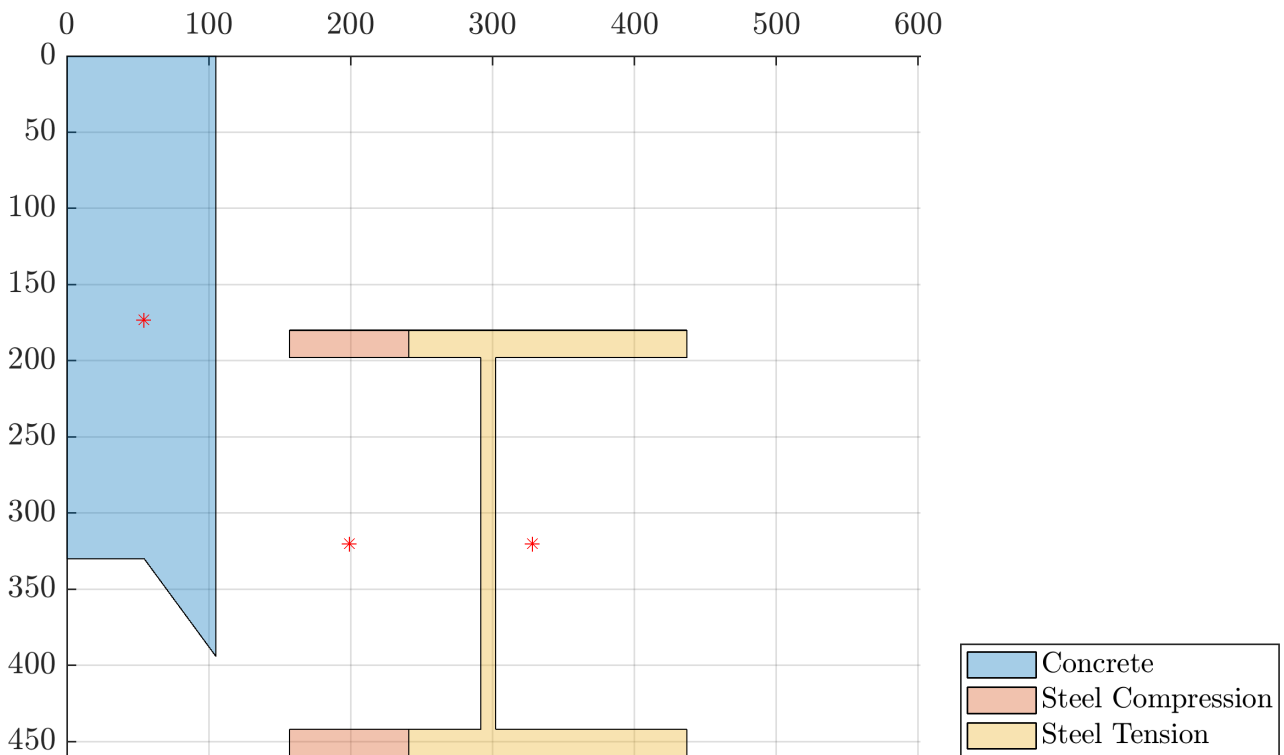


Figure A.5: Internal force components from minor axis bending of the exterior composite girder. The red dots indicate the centroid of each force component.

### 5. Calc. $M_{y,pl,Rd}$ , $M_{z,pl,Rd}$

$$M_{y,pl,Rd} = 1677 \text{ kN} \cdot 326 \text{ mm} + 658 \text{ kN} \cdot 173 \text{ mm} = 664 \text{ kNm}$$

$$M_{z,pl,Rd} = 1550 \text{ kN} \cdot 274 \text{ mm} + 710 \text{ kN} \cdot 129 \text{ mm} = 518 \text{ kNm}$$

## 6. Solve $F_u$

Knowing the bending resistance, the bearing capacity can be found as the maximum value of  $F$ . The horizontal force components,  $F_y$  and  $F_z$ , are defined below.

$$F_y = \frac{F_u}{2 \cos \theta_1} \cos \theta_1$$

$$F_z = \frac{F_u}{2 \cos \theta_1} \cos \theta_2$$

For the major axis bending, the span length between the supports,  $L$ , is used as this is considered a simply supported beam. Whereas, for the minor axis bending, accounted for as a clamped beam, the length is the span between the cross beams  $L_{eff}$ . Thus, the maximum force the biaxial bending resistance can resist is determined as follows:

$$\sqrt{\left(\frac{\frac{1}{4}F_y \cdot 5950 \text{ mm}}{664 \text{ kNm}}\right)^2 + \left(\frac{\frac{1}{8}F_z \cdot 5600 \text{ mm}}{518 \text{ kNm}}\right)^2} \leq 1.0 \Rightarrow F_u = 798 \text{ kN}$$

### A.1.1.4 Vertical Shear Resistance

#### 1. Calc. $\lambda_{sd}$ , $f(\lambda_{sd})$ .

$$\lambda_{sd} = \frac{180 \text{ mm}}{280 \text{ mm}} = 0.64$$

$$f(\lambda_{sd}) = 110 \cdot 0.64 + 13 = 83.7$$

#### 2. Calc. $V_{pl,Rd}$ , $V_{slab}$ .

$$V_{pl,Rd} = \frac{4109 \text{ mm}^2 \cdot 235 \text{ MPa}}{\sqrt{3}} = 557 \text{ kN}$$

$$V_{slab} = 0.8 \cdot 83.7 \cdot (280 \text{ mm} \cdot 180 \text{ mm})^{0.7} \sqrt{50.9 \text{ MPa}} = 935 \text{ kN}$$

#### 3. Calc. $V_{comp}$

$$V_{comp} = 935 \text{ kN} + 557 \text{ kN} = 1493 \text{ kN}$$

#### 4. Solve $V_{comp,0}$

As the degree of shear connection, previously shown, is below 1.0, there is partial shear connection. Therefore, the vertical shear resistance to the degree of shear connection is calculated as a linear relation between  $V_{comp}$  and  $V_{comp,0}$ .

$$1493 \text{ kN} = V_{comp,0}(0.76 \cdot 0.64 + 0.92) \Rightarrow V_{comp,0} = 1060 \text{ kN}$$

### 5. Calc. $V_{comp,\eta}$

The vertical shear resistance can be determined according to the degree of shear connection, which is 0.56.

$$V_{comp,\eta} = 1060 \text{ kN} + 0.56 \cdot (1493 \text{ kN} - 1060 \text{ kN}) = 1304 \text{ kN}$$

## A.1.2 Stage 2 Cross-section Verification

Following longitudinal cracking, the struts and spring beams' displacements and forces have changed. It is assumed that the computation can be simplified by using the same load distribution as was determined with the previous configuration. This load distribution means that the exterior strut takes 45% of the load  $F$ . Therefore, the displacements are described using a new set of equations. However, as the system following cracking mainly focuses on the exterior composite girder, merely the displacement of one strut and the exterior spring beam are considered.

$$u_{s,1}(x, F) = -7.72 \cdot 10^{-72} F (1.69 \cdot 10^{61} x - 1.13 \cdot 10^{66}) \quad [\text{N}, \text{mm}]$$

$$w_1(x, F) = -5.10 \cdot 10^{-16} F x^2 (x - 4200) \quad [\text{N}, \text{mm}]$$

The expression for the lateral displacement of the exterior composite girder only considers the effective length of the specimen, e.i. for LB1. This is 5600 mm. The full length, including the cross beams, is 6620 mm.

### A.1.2.1 Resistance of Compression Struts

The maximum resistance of the compression strut is determined using the same constitutive relation from Eq.A.3 as was used for the cross-section verification to brittle failure. The only difference for the ductile verification is that the equation describing the struts has changed due to the failure of the tensile tie.

$$\sigma_{s,1}(F) = 1.30 \cdot 10^{-10} F \cdot 37 \text{ GPa} = 4.82 \cdot 10^{-6} F$$

$$\sigma_{s,1}(F_u) = 4.82 \cdot 10^{-6} F_u = 50.9 \text{ MPa} \Rightarrow F_u = 11\,892 \text{ kN}$$

$$N_{s,max} = 50.9 \text{ MPa} \cdot 121\,720 \text{ mm}^2 = 6196 \text{ kN}$$

Therefore, the compression strut can resist a load of 9487 kN.

### A.1.2.2 Longitudinal Shear Resistance

In the following, the longitudinal shear resistance is determined for stage 2 after longitudinal cracking.

#### 1. Calc. $L_o$ after longitudinal cracking

As it is assumed that the longitudinal shear resistance is constant following longitudinal cracking, only the values right after longitudinal cracking must be determined. From the expression for the lateral displacement of the exterior composite girder, it can be determined when the strain criteria is exceeded.

$$\varepsilon_{w1}(x, F_{cr}) = \frac{w_1(x)}{L_t} = -3.97 \cdot 10^{-13} x^2 (x - 4200)$$

Thus, the length of the crack opening can be determined by determining when the strain of exterior composite beam equates to the strain criteria.

$$9.9502 \cdot 10^{-5} = -3.97 \cdot 10^{-13} x_{cr}^2 (x_{cr} - 4200) \Rightarrow x_{cr} = 251 \text{ mm}$$

Therefore, the length of the steel-concrete opening can be determined as:

$$L_o = L_{eff} - 2x_{cr} = 5600 \text{ mm} - 2 \cdot 251 \text{ mm} = 5098 \text{ mm}$$

Thus most of the concrete has formed an opening from the steel over the span. The strain along the exterior girders right after longitudinal cracking is shown in Figure A.6. Only half the beam is considered as symmetry is used.

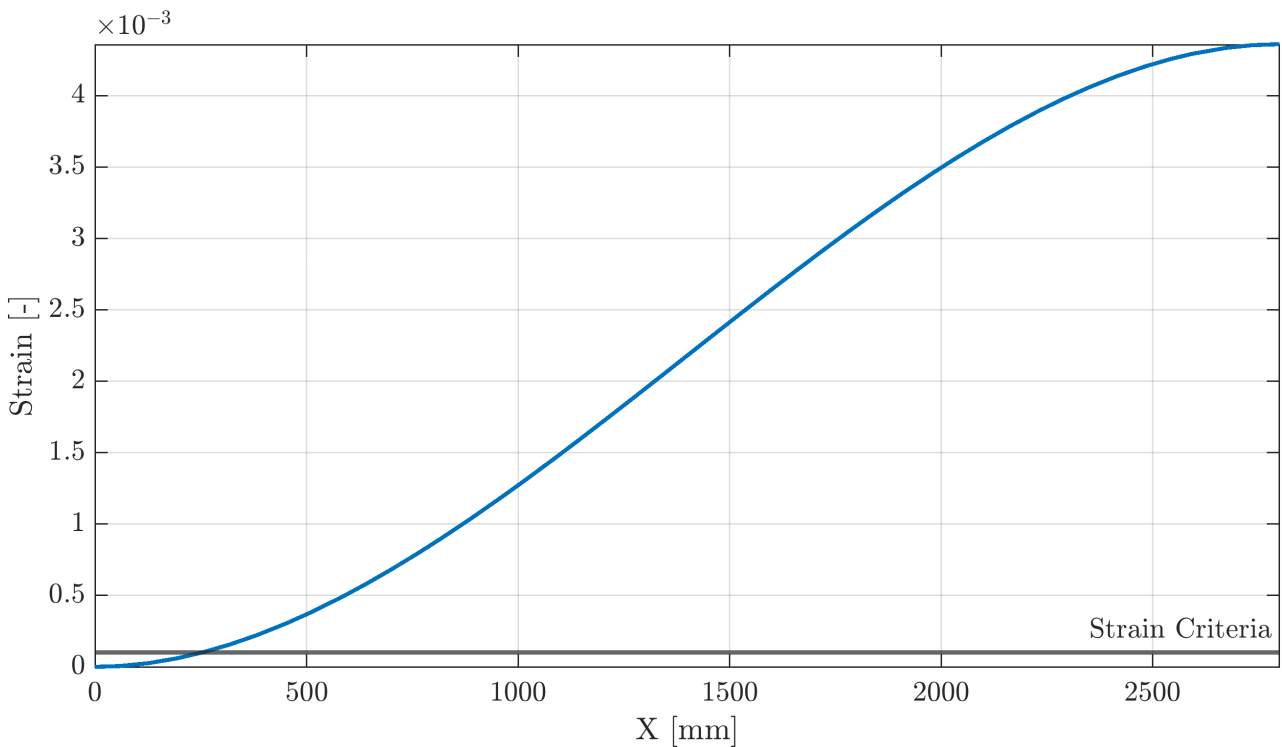


Figure A.6: Concrete strain and strain criteria along the length of LB1 at  $F_{cr} = 421 \text{ kN}$ .

## 2. Calc. $V_{1,x,Rd}$ .

The first part of the longitudinal shear resistance is determined where the confinement occurs, due to the concrete that opens from the steel. For his calculation, the normal stress at the confinement must be determined. This is done from the constitutive relation for an Euler-Bernoulli beam. Using the constitutive relation, the shear force that the beam is subject to is determined.

$$V_1 = -EI_{1,cr} \frac{d^3 w_1}{dx^3} = 0.27F$$

$$V_1(F_{cr}) = 0.27 \cdot 421 \text{ kN} = 113.7 \text{ kN}$$

The stress due to the confinement is calculated as the following.

$$\sigma = \frac{2V_1(F_{cr})}{h_o L_o}$$

Where  $h_o$  is the height of the steel girder excluding the minimum concrete cover at the bottom of 38 mm.

$$\sigma = \frac{2 \cdot 113.7 \text{ kN}}{242 \text{ mm} \cdot 5098 \text{ mm}} = 0.19 \text{ MPa}$$

Thus, the longitudinal shear resistance  $V_{1,x,Rd}$  be calculated assuming a coefficient of friction at 0.3 and cohesion at 0.54 MPa according to the literature review chapter 2.

$$V_{1,x,Rd} = 0.3 \cdot 0.19 \text{ MPa} \cdot 242 \text{ mm} \cdot 5098 \text{ mm} + 0.54 \text{ MPa} \cdot 5098 \text{ mm} \cdot 465 \text{ mm} = 1342 \text{ kN}$$

## 3. Calc. $V_{2,x,Rd}$ .

The longitudinal shear resistance of the part of concrete and steel that steel has full contact is determined in the following using the same effective contact perimeter as was used in the first verification. Besides the part of the span that is in full contact, the length of the cross beams must also be added, assuming that these also are in full contact. For LB1, the length of the cross beams at each side is 510 mm. For LB1, the effective contact perimeter is 909 mm, considering the concrete cover requirements not fulfilled at the bottom and the 50% reduction of the bottom part of the top steel flange due to air bubbles from casting. The same reduction is applied for the part following the steel-concrete opening. However, this only regards one side, as the side facing the interior girder does not have contact anymore.

$$V_{2,x,Rd} = 0.54 \text{ MPa} \cdot 909 \text{ mm} \cdot (5600 \text{ mm} + 2 \cdot 510 \text{ mm} - 5084 \text{ mm}) = 754 \text{ kN}$$

## 4. Calc. $V_{x,Rd}$ .

$$V_{x,Rd} = 1342 \text{ kN} + 754 \text{ kN} = 2096 \text{ kN}$$

It is assumed that the longitudinal shear resistance remains constant after cracking, which is considering safe as the resistance will keep increasing. Additionally, this simplifies the calculation procedure, as when the longitudinal shear resistance changes depending on the loading, the degree of shear connection will simultaneously change, which makes the calculation an iterative process.

### A.1.2.3 Biaxial Bending Resistance

For the ductile calculation of the biaxial bending resistance the same calculation principles are applied. However, on the safe side the concrete from the cut out section is neglected as this may have cracked, which reduces the moment resistance by a small margin. the cross-section considered for the cross-section verification of LB1 is shown in Figure A.7.

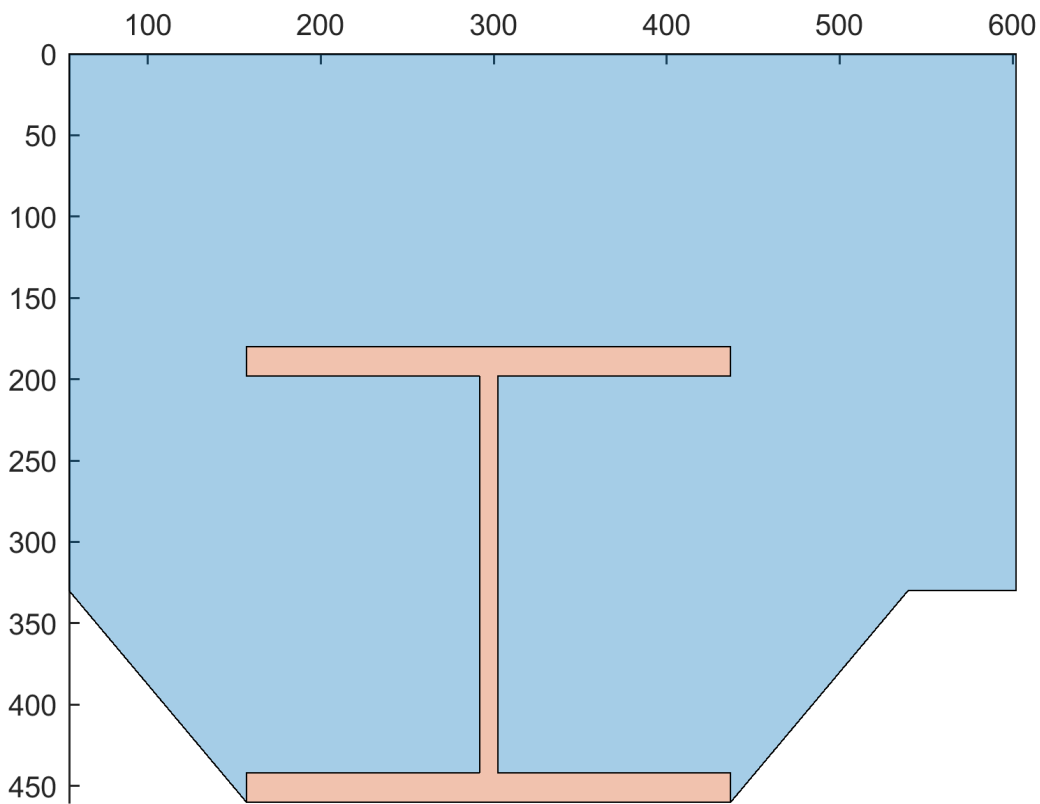


Figure A.7: Reduced cross-section considered following longitudinal cracking

#### 1. Calc. $F_{cc,y}$ , $F_{cc,z}$ using iteration

For biaxial bending, the concrete compression forces are first determined, assuming a full shear connection. These are determined using iteration with the MATLAB code in Appendix C. The compression force from major axis bending and minor axis bending has been determined to  $F_{cc,y} = 2985$  kN and  $F_{cc,z} = 2403$  kN.

#### 2. Calc. $\eta$ using $\min(V_{x,Rd})$

The minimum value of the longitudinal shear resistance occurs following the longitudinal cracking. This value is 2096 kN. Hence the degree of shear connection can be determined as the following.

$$\eta = \frac{2096 \text{ kN}}{2985 \text{ kN} + 2403 \text{ kN}} = 0.39$$

As the degree of shear connection is below 1.0, there is a partial shear connection. Thus, the concrete compression forces must be reduced.

**3. Calc.  $F_{cc,y,red}$ ,  $F_{cc,z,red}$**

$$F_{cc,y,red} = 0.39 \cdot 2985 \text{ kN} = 1164 \text{ kN}$$

$$F_{cc,z,red} = 0.39 \cdot 2403 \text{ kN} = 937 \text{ kN}$$

**4. Determine  $z_1$ ,  $z_2$ ,  $y_1$ ,  $y_2$**

The distance between the respective compression forces and the tension forces are similarly determined using iteration that also is included in the MATLAB code in Appendix C. The values are determined to  $z_1 = 355 \text{ mm}$ ,  $z_2 = 193 \text{ mm}$ ,  $y_1 = 254 \text{ mm}$  and  $y_2 = 121 \text{ mm}$ .

Figure A.8 shows the compression and tension components of the steel and concrete for major axis bending. Figure A.9 shows the same for minor axis bending.

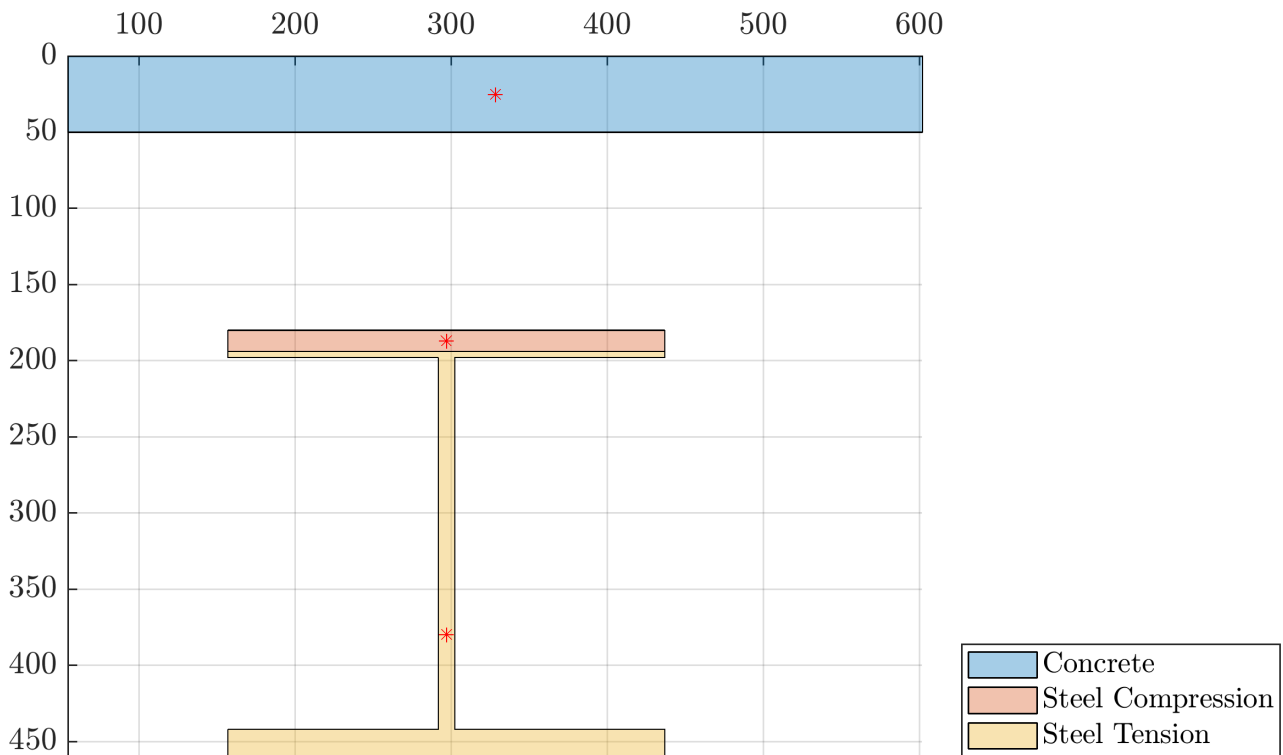


Figure A.8: Internal force components from major axis bending of the exterior composite girder. The red dots indicate the centroid of each force component.

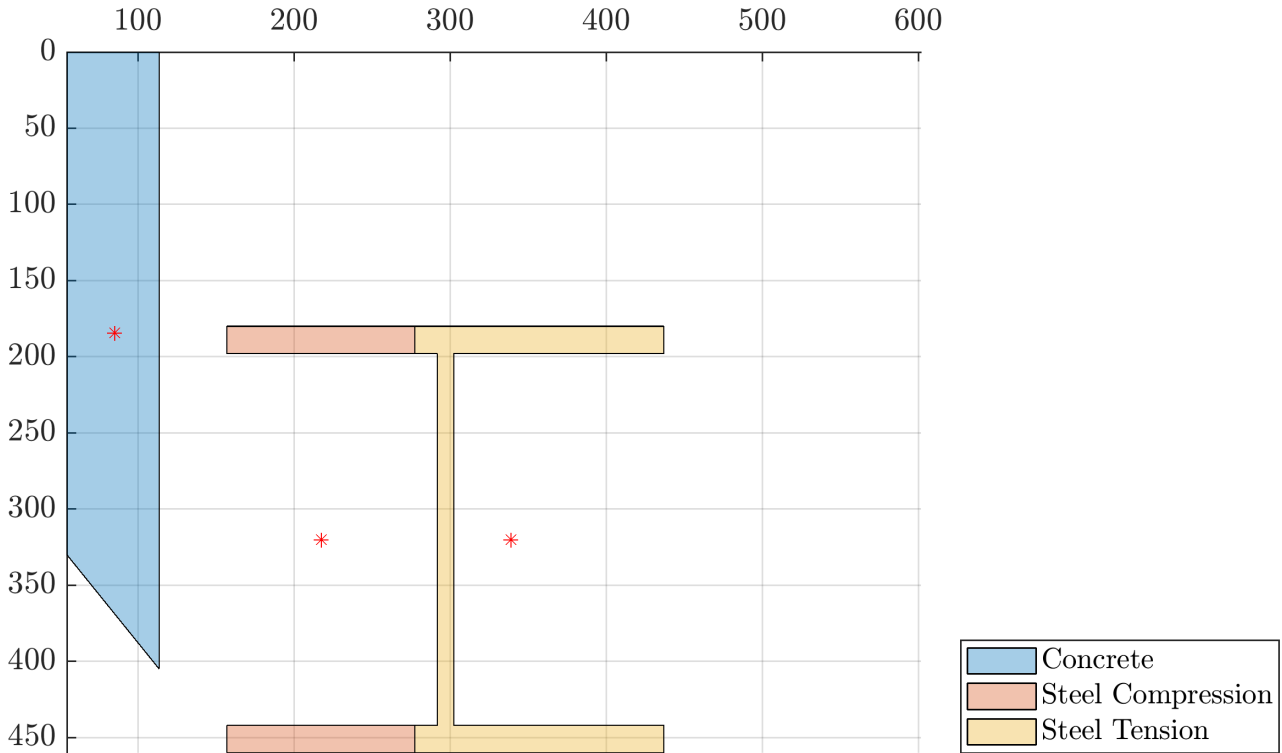


Figure A.9: Internal force components from minor axis bending of the exterior composite girder. The red dots indicate the centroid of each force component.

### 5. Calc. $M_{y,pl,Rd}$ , $M_{z,pl,Rd}$

$$M_{y,pl,Rd} = 1164 \text{ kN} \cdot 355 \text{ mm} + 921 \text{ kN} \cdot 193 \text{ mm} = 590 \text{ kNm}$$

$$M_{z,pl,Rd} = 937 \text{ kN} \cdot 254 \text{ mm} + 1019 \text{ kN} \cdot 121 \text{ mm} = 361 \text{ kNm}$$

### 6. Solve $F_u$

Knowing the bending resistance, the bearing capacity can be found as the maximum value of  $F$ . The horizontal force components,  $F_y$  and  $F_z$  are defined below.

$$F_y = \frac{F_u}{2 \cos \theta_1} \cos \theta_1$$

$$F_z = \frac{F_u}{2 \cos \theta_1} \cos \theta_2$$

For the major axis bending, the span length between the supports,  $L$ , is used as this is considered a simply supported beam. Whereas, for the minor axis bending, accounted for as a clamped beam, the length is the span between the cross beams  $L_{eff}$ . Thus, the maximum force the biaxial bending resistance can resist is determined as follows:

$$\sqrt{\left(\frac{\frac{1}{4}F_y \cdot 5950 \text{ mm}}{590 \text{ kNm}}\right)^2 + \left(\frac{\frac{1}{8}F_z \cdot 5600 \text{ mm}}{361 \text{ kNm}}\right)^2} \leq 1.0 \Rightarrow F_u = 675 \text{ kN}$$

#### A.1.2.4 Vertical Shear Resistance

Most values for calculating the vertical shear resistance have already been determined in the previous section determining the vertical shear resistance for brittle failure. The only thing that has changed is the degree of shear connection.

##### 1. Calc. $V_{comp,\eta}$

$$V_{pl,Rd} = 557 \text{ kN}$$

$$V_{slab} = 935 \text{ kN}$$

$$V_{comp} = 1493 \text{ kN}$$

As previously shown, the degree of shear connection is below 1.0 and, therefore, is a partial shear connection. Therefore, the vertical shear resistance to the degree of shear connection is calculated as a linear relation between  $V_{comp}$  and  $V_{comp,0}$ .

$$1493 \text{ kN} = V_{comp,0}(0.76 \cdot 0.64 + 0.92) \Rightarrow V_{comp,0} = 1060 \text{ kN}$$

The vertical shear resistance can be determined according to the degree of shear connection, which is 0.36.

$$V_{comp,\eta} = 1060 \text{ kN} + 0.39 \cdot (1493 \text{ kN} - 1060 \text{ kN}) = 1228 \text{ kN}$$

# B Solution Strategy to Determine Displacements of the C-STM

## B.1 Equilibrium Conditions

The compatibility-based strut and tie model is defined using the coordinate system in Figures B.1 and 4.11. The struts and ties are considered trusses. Thus, only axial forces and deformations are accounted for. The lateral beams are Euler-Bernoulli beams.

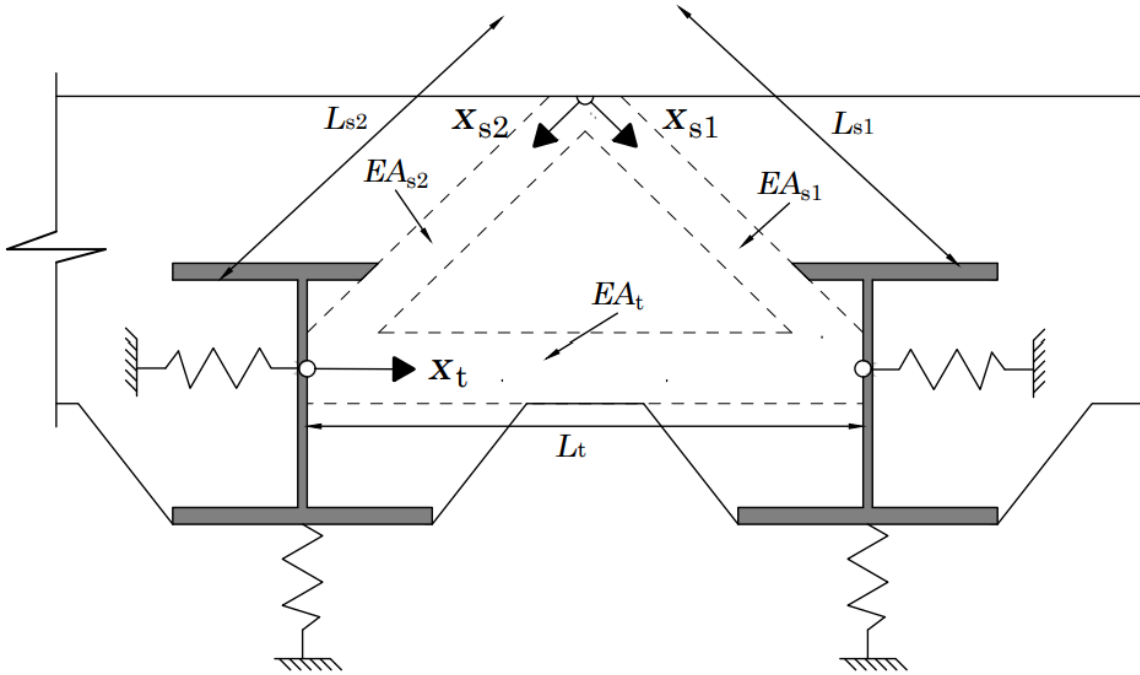


Figure B.1: Coordinate system for the ordinary differential equations.

The system's equilibrium is first determined by considering the top compression node, where the point load,  $F$ , is applied. The equilibrium at the top node where the point load is applied is determined based on Figure B.2 and stated as Eqs. B.1 and B.2.

$$u_{s1} = u_{s2} \quad (\text{B.1})$$

$$-F = (N_{s1} + N_{s2}) \cos \theta_1 \quad (\text{B.2})$$

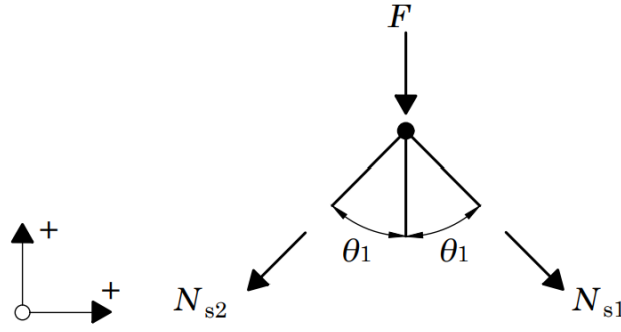


Figure B.2: Forces at the top compression node.

Symmetry is applied for the lateral Euler-Bernoulli beams, so the beams are described through equilibrium and compatibility conditions at one of the supports and midspan. Since the lateral beams are described using 4th-order differential equations, two equilibrium and two compatibility conditions are required. For a clamped Euler Bernoulli beam, the equilibrium conditions are given from Eqs.B.3 and B.4.

$$\varphi_1 = 0 \tag{B.3}$$

$$w_1 = 0 \tag{B.4}$$

Similar principles apply to the interior lateral Euler-Bernoulli beam. The equilibrium conditions are given from Eqs.B.5 and B.6.

$$\varphi_2 = 0 \tag{B.5}$$

$$w_2 = 0 \tag{B.6}$$

## B.2 Compatibility Conditions

The remainder of the system is described through compatibility conditions. The compatibility conditions for the spring node of the exterior composite girder are determined mainly by considering displacement equilibrium, as three different elements are connected in this node. Figure B.3 shows the forces acting on the node. The compatibility conditions are given from Eqs.B.7 to B.10. The force equilibrium in Eq.B.9 has been determined using the method of joints. Similarly, displacement compatibility is considered as the displacement of the tensile tie, the compression strut and the exterior lateral beam must be equal in the horizontal direction, as shown in Eqs.B.7 and B.8.

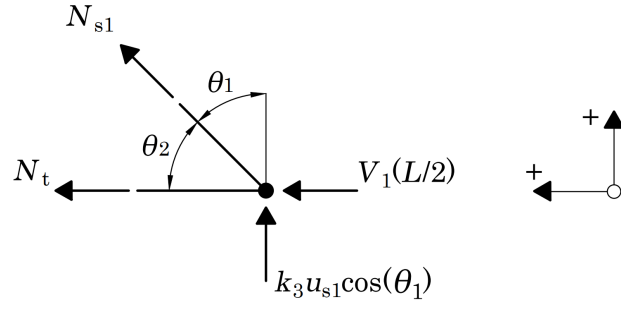


Figure B.3: Forces considered for at the bottom right joint of the C-STM.

$$u_t = u_{s1} \cos \theta_2 \quad (\text{B.7})$$

$$u_t = w_1(L/2) \quad (\text{B.8})$$

$$-V_1(L/2) \cos \theta_2 = \frac{N_{s1} \cos \theta_2 + N_t \cos \theta_2 + u_{s1} k_3 \cos \theta_1^2}{2} \quad (\text{B.9})$$

$$\varphi_1(L/2) = 0 \quad (\text{B.10})$$

The compatibility conditions for the node of the interior composite girder are determined similarly. Figure B.4 shows the forces acting on this node. The compatibility conditions are given from Eqs.B.11 to B.14.

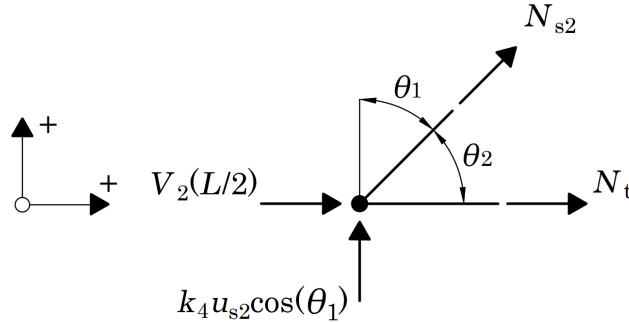


Figure B.4: Forces considered for at the bottom left joint of the C-STM.

$$-u_t = u_{s2} \cos \theta_2 \quad (\text{B.11})$$

$$-u_t = w_2(L/2) \quad (\text{B.12})$$

$$-V_2(L/2) \cos \theta_2 = \frac{N_{s2} + N_t \cos \theta_2 + u_{s2} k_4 \cos \theta_1^2}{2} \quad (\text{B.13})$$

$$\varphi_2(L/2) = 0 \quad (\text{B.14})$$

### B.3 Kinematic and Constitutive Relations

The kinematic and constitutive relations for the C-STM are derived in the following based on the coordinate system shown in Figures 4.11 and B.1. The struts and ties are considered extension bars, as previously mentioned. Thus, only axial deformations are accounted for. The axial deformations of the struts and the tie can be determined using the ordinary differential equations from Eqs.B.15 and B.16, where the index  $i$  is for strut 1 and 2.

$$EA_{s,i} \frac{d^2 u_{s,i}}{dx^2} = 0 \quad \text{for} \quad 0 \leq x_{si} \leq L_{si} \quad (\text{B.15})$$

$$EA_t \frac{d^2 u_t}{dx^2} = 0 \quad \text{for} \quad 0 \leq x_t \leq L_t \quad (\text{B.16})$$

The kinematic and constitutive relations for extension bars are obtained from Eqs.B.17 and B.18.

$$\epsilon = \frac{du}{dx} \quad (\text{B.17})$$

$$N = EA\epsilon \quad (\text{B.18})$$

As previously mentioned, the lateral spring beams in Figure 4.11 are considered Euler-Bernoulli beams, with the ordinary differential equation from Eq.B.19.

$$EI_{z,i} \frac{d^4 w_i}{dx^4} = 0 \quad \text{for} \quad 0 \leq x \leq L \quad (\text{B.19})$$

The kinematic and constitutive relations for the Euler-Bernoulli beams are obtained from Eqs.B.20 to B.22.

$$\varphi = -\frac{dw}{dx} \quad (\text{B.20})$$

$$M = EI \frac{d\varphi}{dx} \quad (\text{B.21})$$

$$V = \frac{dM}{dx} \quad (\text{B.22})$$

The kinematic and constitutive relations are solved using the 14 equilibrium and compatibility conditions in the previous sections.

## B.4 MATLAB Compatibility-based Strut and Tie Method

The cross-section is graphically analysed using a *polyshape* function that creates the shape based on coordinates. These coordinates are defined following the system in Figure B.5. The shape is defined by the MATLAB code shown below. The plots in the below code are created to illustrate the geometry that is constructed for the user to understand if there are any mistakes or errors.

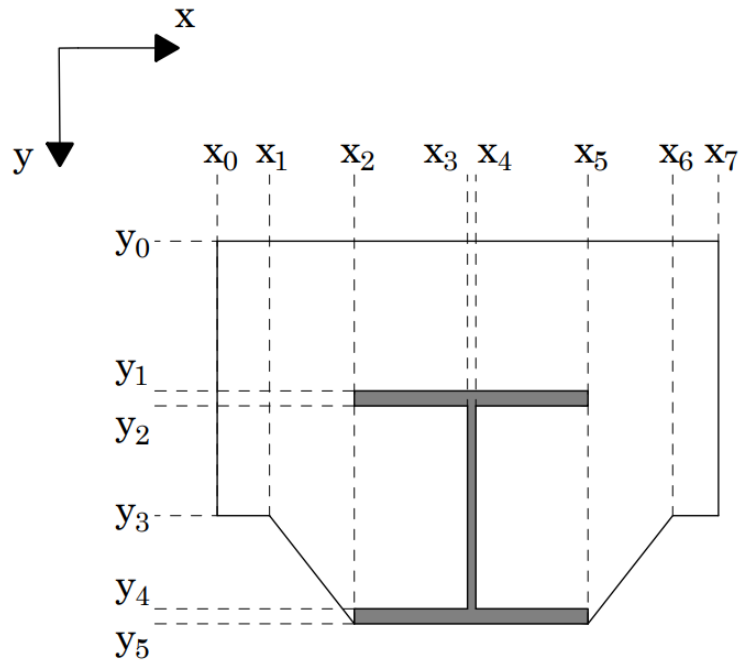


Figure B.5: Coordinates used to create the MATLAB *polyshape*.

```
xlim=[x0 x7];
x_steel = [x2 x2 x3 x3 x2 x2 x5 x5 x4 x4 x5 x5];
y_steel = [y1 y2 y2 y4 y4 y5 y5 y4 y4 y2 y2 y1];
x_boundary = [x0 x0 x1 x2 x5 x6 x7 x7 x6];
y_boundary = [y0 y3 y3 y5 y5 y3 y3 y0 y0];
steel = polyshape(x_steel,y_steel);
edges = polyshape(x_boundary,y_boundary);
concrete = subtract(edges,steel);
figure(1)
plot(concrete)
hold on
plot(steel)
yticklabels();
set ( gca, 'ydir', 'reverse','xlim',[x0 x7],'ylim',[y0 y5
])
figure(2)
plot(steel)
yticklabels();
set ( gca, 'ydir', 'reverse','xlim',[x0 x7],'ylim',[y0 y5
])
```

The above code also plots the steel and the concrete of the exterior girder, so it is possible to see if the correct dimensions have been applied. Using the above code the C-STM has been defined as the following.

```

%% STM: Geometry and stiffness
wp = 230; Ld = 2*eT01/(tand(45))+wp; Ls1 = sqrt((Lt/2)^2+eT01^2)
; Ls2 = Ls1;
theta1 = acosd(eT01/(Lt/2)); theta2 = 90 -theta1;
k3 = (48*EIy3)/(L^3-(Ld^2)/2*L+(Ld^3)/8); %Vertical springs -
with the composite stiffness considered.
k4 = (48*EIy4)/(L^3-Ld^2/2*L+(Ld^3)/8); %Vertical springs - with
the composite stiffness considered.
p = 10; %number of girders without the exterior one
EIz2 = p*EIz1;
if y3/2 <= y3-y1
ht = y3/2;
At = Ld * ht;
"Tensile height below top flange"
else
ht = y3-y1;
At = Ld * ht;
"Tensile height limited"
end
%% ODE
syms w1(x) w2(x) us1(x) us2(x) ut(x) F
hs1 = cosd(theta1)*wp;
As1 = Ld*hs1;
As2 = As1;
ODE1 = Ec*As1*diff(us1,x,2) == 0;
ODE2 = Ec*As2*diff(us2,x,2) == 0;
ODE3 = Ec*At*diff(ut,x,2) == 0;
ODE4 = EIz1*diff(w1,x,4) == 0;
ODE5 = EIz2*diff(w2,x,4) == 0;
ODES = [ODE1; ODE2; ODE3; ODE4; ODE5];
%% Kinematic and constitutive relations
epsilon_s1 = diff(us1); Ns1 = epsilon_s1*Ec*As1;
epsilon_s2 = diff(us2); Ns2 = epsilon_s2*Ec*As2;
epsilon_t = diff(ut); Nt = epsilon_t*Ec*At;
phi1 = -diff(w1); M1 = EIz1*diff(phi1) ; V1 = diff(M1);
phi2 = -diff(w2); M2 = EIz2*diff(phi2) ; V2 = diff(M2);
%% STM: BC before cracking
% Node 1 - top node
cond1 = us1(0) == us2(0);
cond2 = -F -(Ns1(0)+Ns2(0))*cosd(theta1) == 0;
% Node 2 - bottom right node
cond3 = ut(Lt) == us1(Ls1)*cosd(theta2);
cond4 = w1(L/2) == ut(Lt);
cond5 = phi1(L/2) == 0;
cond6 = -V1(L/2)*cosd(theta2) == (Nt(Lt)*cosd(theta2)+k3*us1(Ls1)

```

```

    *cosd(theta1)^2+Ns1(Ls1))/2;
% Boundary at spring beam k1
cond7 = phi1(0) == 0;
cond8 = w1(0) == 0;
% Node 3 - bottom left node
cond9 = ut(0) == -us2(Ls2)*cosd(theta2);
cond10 = w2(L/2) == -ut(0);
cond11 = phi2(L/2) == 0;
cond12 = -V2(L/2)*cosd(theta2) == (Nt(0)*cosd(theta2)+k4*us2(Ls2)
    *cosd(theta1)^2+Ns2(Ls2))/2;
% Boundary at spring beam k1
cond13 = phi2(0) == 0;
cond14 = w2(0) == 0;
conds = [cond1 cond2 cond3 cond4 cond5 cond6 cond7 cond8 cond9
    cond10 cond11 cond12 cond13 cond14];
[u1(x,F),u2(x,F),ut(x,F),w1(x,F),w2(x,F)] = dsolve(ODES,conds);
eq1 = diff(ut(x,F),x)*Ec == 3.68;
F_cracking = vpa(solve(eq1,F))
%% STM: BC after cracking
x_cr = [x3 x3 x5 x6 x7 x7 x6];
y_cr = [y0 y5 y5 y3 y3 y0 y0];
edges2 = polyshape(x_cr,y_cr);
concrete_cr = subtract(edges2,steel); %Concrete with a reduced
    size due to the failure of the tensile tie.
Ac_cr = area(concrete_cr);
Cxc_cr = MOMENT(concrete_cr,1,0)/Ac_cr;
eT0_cr = (Ac_cr*Cxc_cr*n+As*Cxs)/(As+Ac_cr*n);
Ixx_concrete_cr =MOMENT(concrete_cr,2,0);
Ixx_total_cr = (Ixx_steel+Ixx_concrete_cr*n)-eT0_cr^2*(As+Ac_cr*n
    );
EIz1_cr = Es*Ixx_total_cr; % Lateral stiffness cracked concrete
syms w1_c(x) us1_c(x) F
ODE1 = Ec*As1*diff(us1_c,x,2) == 0;
ODE2 = EIxx_Ext_cr*diff(w1_c,x,4) == 0;
ODES_s2 = [ODE1; ODE2];
% Kinematic and constitutive relations
epsilon_s1 = diff(us1_c); Ns1 = epsilon_s1*Ec*As1;
phi1 = -diff(w1_c); M1 = EIz1_cr*diff(phi1) ; V1 = diff(M1);
% Node 1 - top node
cond1 = -F*0.45 == Ns1(0)*cosd(theta1);
% Node 2 - bottom right node
cond2 = w1_c(L/2) == us1_c(Ls1)*cosd(theta2);
cond3 = -V1(L/2)*cosd(theta2) == (k3*us1_c(Ls1)*cosd(theta1)^2+
    Ns1(Ls1))/2;
cond4 = phi1(L/2) == 0;
% Boundary at spring beam k1
cond5 = phi1(0) == 0;
cond6 = w1_c(0) == 0;

```

```
conds = [cond1 cond2 cond3 cond4 cond5 cond6];  
S = dsolve(ODES_s2,conds);  
u1_cracked(x,F) = simplify(S.us1_c);  
w1_cracked(x,F) = simplify(S.w1_c);
```

## C MATLAB Iteration for Biaxial Bending

Using the geometry defined in Appendix B and the longitudinal shear resistance, the bending moment resistance can be determined by the below function. The code is created in such a way that it can determine the position of the plastic neutral axis  $z$  for any angle of the axis between 0 and 90 degrees. However, for this case, only the angles 0 and 90 degrees are used. The area of the force components is determined using the *polyshape* function. Furthermore, using the *centroid* function, the centroid of each force component is determined. Finally, the bending moment resistance for the corresponding angle is determined using these values and the steel and concrete resistance. In the calculation, it is assumed that the concrete is cracked.

```
angle = [0 90];
z = ones(size(angle));
t = ones(size(angle));
x_centroid=zeros(length(angle),3);
y_centroid=zeros(length(angle),3);
h_tension_steel = zeros(size(angle));
h_compression_concrete = zeros(size(angle));
h_compression_steel = zeros(size(angle));
M_Rd = zeros(size(angle));
x_tension=zeros(length(angle),4);
y_tension=zeros(length(angle),4);
x_compression=zeros(length(angle),4);
y_compression=zeros(length(angle),4);
Aca = zeros(size(angle));
Acc = zeros(size(angle));
At = zeros(size(angle));
Fc = zeros(size(angle));
Ft = ones(size(angle));
Fconcrete = zeros(size(angle));
x_concrete = zeros(length(angle),4);
y_concrete = zeros(length(angle),4);
x_ca = zeros(length(angle),4);
y_ca = zeros(length(angle),4);

for i = 1:length(angle) %i == 1 denotes the major axis whereas i
    == 2 denotes the minor axis
    while Fc(i) < Ft(i)
        if i == 1;
            x_tension(i,:) = [x0 x0 x7 x7];
            y_tension(i,:) = [y5 y0+z(i) y0+z(i) y5];
            x_compression(i,:) = [x0 x0 x7 x7];
            y_compression(i,:) = [y0 y0+z(i) y0+z(i) y0];
        else
            x_tension(i,:) = [x0+z(i) x0+z(i) x7 x7];
            y_tension(i,:) = [y5 y0 y0 y5];
            x_compression(i,:) = [x0 x0 x0+z(i) x0+z(i)];
```

```

        y_compression(i,:) = [y0 y5 y5 y0];
    end
    z(i) = z(i) +1;
    compression_zone(i) = polyshape(x_compression(i,:),
        y_compression(i,:));
    tension_zone(i) = polyshape(x_tension(i,:),y_tension(
        i,:));
    compression_concrete(i) = subtract(concrete,
        tension_zone(i));
    compression_steel(i) = subtract(steel,tension_zone(i)
        );
    tension_steel(i) = subtract(steel,compression_zone(i)
        );
    Acc(i) = area(compression_concrete(i));
    Aca(i) = area(compression_steel(i));
    At(i) = area(tension_steel(i));
    Fcc(i) = Acc(i)*fc*0.85;
    Fca(i) = Aca(i)*fy;
    Fc(i) = Fcc(i)+Fca(i);
    Ft(i) = At(i)*fy;
end
end
Fccy = Fcc(1); Fccz = Fcc(2); %Concrete compression forces
    respectively for the major and minor axis
Fc = zeros(size(angle));
Ft = ones(size(angle));
if Fcc(1)/VxRd_min+Fcc(2)/VxRd_min <= 1.0
    "Full shear connection"
    for i = 1:length(angle)
        [x_centroid(i,1),y_centroid(i,1)] = centroid(tension_steel(i)
            ); %CA in coordinates
        [x_centroid(i,2),y_centroid(i,2)] = centroid (concrete_block(
            i)); %CA in coordinates
        [x_centroid(i,3),y_centroid(i,3)] = centroid (
            compression_steel(i)); %CA in coordinate
        if i == 1;
            h_tension_steel(i) = y_centroid(i,1)-z(i);
            h_compression_concrete(i) = z(i)-y_centroid(i,2);
            h_compression_steel(i) = z(i)-y_centroid(i,3);
        else
            h_tension_steel(i) = x_centroid(i,1)-z(i);
            h_compression_concrete(i) = z(i)-x_centroid(i,2);
            h_compression_steel(i) = z(i)-x_centroid(i,3);
        end
        h_compression_steel(isnan(h_compression_steel))=0;
        M_Rd(i) = (h_compression_concrete(i)+h_tension_steel(i))*
            Fcc(i)+(h_compression_steel(i)+h_tension_steel(i))*Fca
            (i);
    end
end

```

```

end
else
"Partial shear connection"
Fcc(1) = Fccy/(Fccy+Fccz)*VxRd_min; %Reduction of the
    concrete compression from major axis bending
Fcc(2) = Fccz/(Fccy+Fccz)*VxRd_min; %Reduction of the
    concrete compression from minor axis bending
for i = 1:2
    while Fcc(i) > Fconcrete(i) %To determine the reduced
        concrete area
        if i == 1;
            x_concrete(i,:) = [x0 x0 x7 x7];
            y_concrete(i,:) = [y5 y0+t(i) y0+t(i) y5];
        else
            x_concrete(i,:) = [x0+t(i) x0+t(i) x7 x7];
            y_concrete(i,:) = [y5 y0 y0 y5];
        end
        t(i) = t(i) + 1;
        concrete_subtract(i) = polyshape(x_concrete(i,:),
            y_concrete(i,:));
        concrete_block(i) = subtract(concrete,concrete_subtract(i
            ));
        Fconcrete(i) = area(concrete_block(i))*fc*0.85;
    end
    while Fc(i) < Ft(i) %To determine the new steel
        compression and tension areas
        if i == 1;
            x_tension(i,:) = [x0 x0 x7 x7];
            y_tension(i,:) = [y5 y0+z(i) y0+z(i) y5];
            x_ca(i,:) = [x0 x0 x7 x7];
            y_ca(i,:) = [y0 y0+z(i) y0+z(i) y0];
        else
            x_tension(i,:) = [x0+z(i) x0+z(i) x7 x7];
            y_tension(i,:) = [y5 y0 y0 y5];
            x_ca(i,:) = [x0 x0 x0+z(i) x0+z(i)];
            y_ca(i,:) = [y0 y5 y5 y0];
        end
        z(i) = z(i) +1;
        ca_zone(i) = polyshape(x_ca(i,:),y_ca(i,:));
        tension_zone(i) = polyshape(x_tension(i,:),
            y_tension(i,:));
        compression_steel(i) = subtract(steel,
            tension_zone(i));
        tension_steel(i) = subtract(steel,ca_zone(i));
        Aca(i) = area(compression_steel(i));
        At(i) = area(tension_steel(i));
        Fca(i) = Aca(i)*fy;
        Fc(i) = Fcc(i)+Fca(i);
    end
end

```

```

        Ft(i) = At(i)*fy;
    end
[x_centroid(i,1),y_centroid(i,1)] = centroid(tension_steel(i)
); %CA in coordinates
[x_centroid(i,2),y_centroid(i,2)] = centroid (concrete_block(
i)); %CA in coordinates
[x_centroid(i,3),y_centroid(i,3)] = centroid (
compression_steel(i)); %CA in coordinate
    if i == 1;
        h_tension_steel(i) = y_centroid(i,1)-z(i);
        h_compression_concrete(i) = z(i)-y_centroid(i,2);
        h_compression_steel(i) = z(i)-y_centroid(i,3);
    else
        h_tension_steel(i) = x_centroid(i,1)-z(i);
        h_compression_concrete(i) = z(i)-x_centroid(i,2);
        h_compression_steel(i) = z(i)-x_centroid(i,3);
    end
h_compression_steel(isnan(h_compression_steel))=0;
M_Rd(i) = (h_compression_concrete(i)+h_tension_steel(i))*Fcc(
i)+(h_compression_steel(i)+h_tension_steel(i))*Fca(i);
figure(i)
hold on
    grid on
    plot(concrete_block(i))
    plot(compression_steel(i))
    plot(tension_steel(i))
    plot(x_centroid(i,:),y_centroid(i,:), 'r*')
    yticklabels();
    set ( gca, 'ydir', 'reverse', 'xlim', [x0 x7], 'ylim', [y0 y5
])
hold off
end
end
eta = VxRd_min/(Fccy+Fccz) %Degree of shear connection
MyRd = M_Rd(1)
MzRd = M_Rd(2)

```

# D Experimental Results - LB1 and LB3

Figure D.1 shows the location and notation of the six supports used during testing.

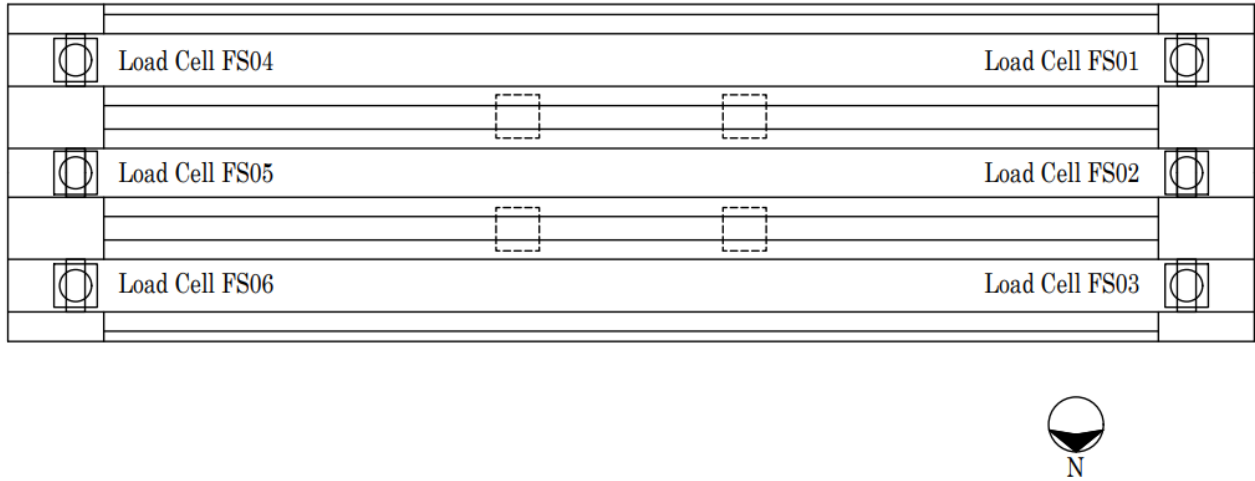


Figure D.1: Location and notation of the supports used during experimental testing.

## D.1 LB1 Reaction Forces

Figures D.2 and D.3 show the support reaction forces at each support for LB1.

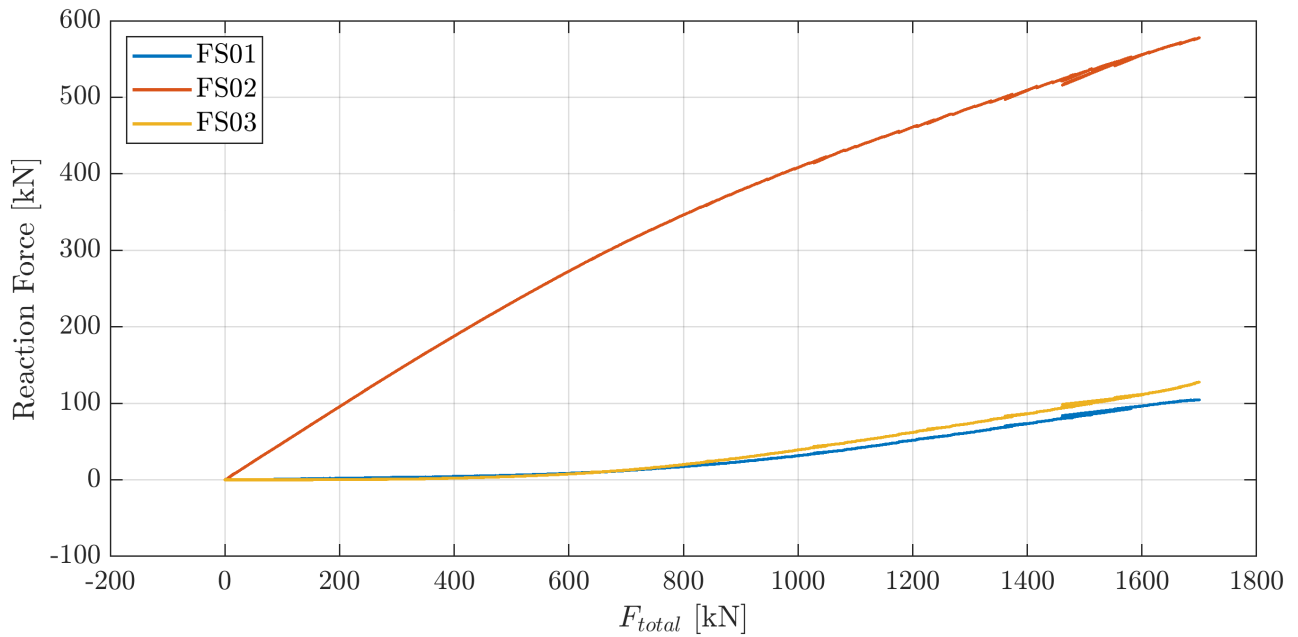


Figure D.2: LB1 - Support reaction forces of support FS01-FS03 positioned at the west end of the specimen

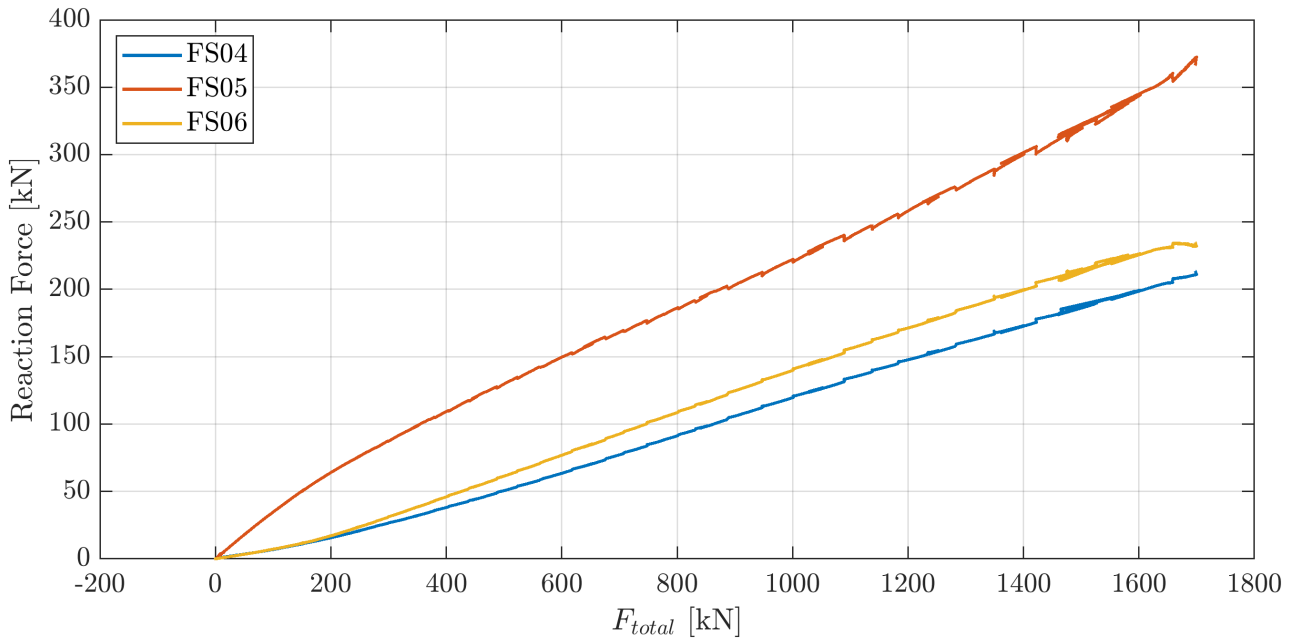


Figure D.3: LB1 - Support reaction forces of support FS04-FS06 positioned at the east end of the specimen.

## D.2 LB3 Reaction Forces

Figures D.4 and D.5 show the support reaction forces at each support for LB3.

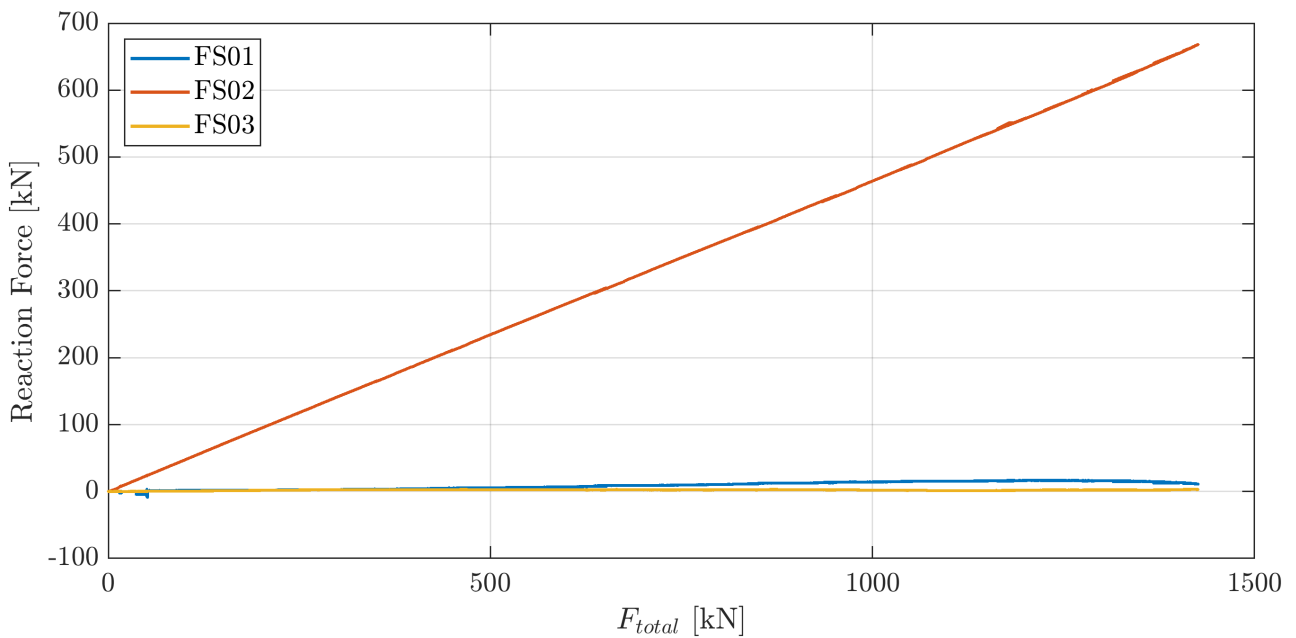


Figure D.4: LB3 - Support reaction forces of support FS01-FS03 positioned at the west end of the specimen.

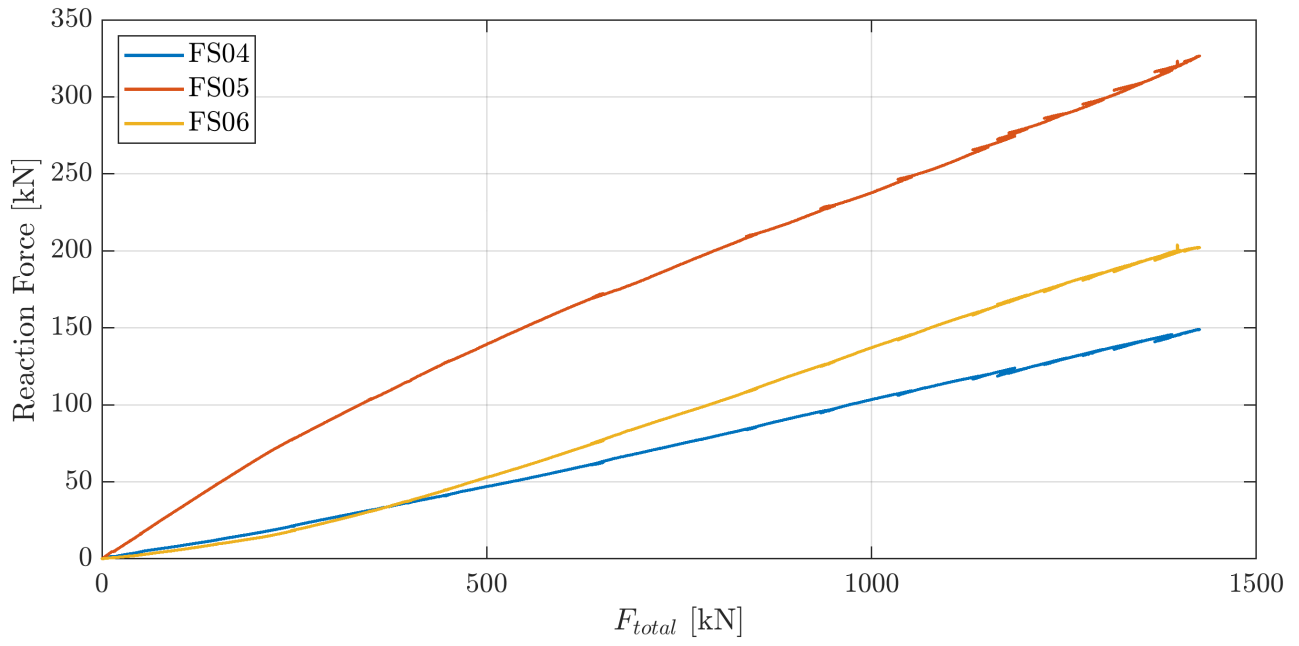


Figure D.5: LB3 - Support reaction forces of support FS04-FS06 positioned at the east end of the specimen.

# E Numerical Model Input

## Finite Element Types

Table E.1: Finite elements types in the model

Element	Element Type
Concrete	Solid brick, 20 nodes, quadratic (CHX60)
Steel girders	Solid brick, 20 nodes, quadratic (CHX60)
Steel plates	Solid brick, 20 nodes, quadratic (CHX60)
Interface	Quadrilateral interface, 16 nodes, quadratic (CQ48I)

## Iterative Scheme

The iterative scheme is shown in Table E.2. The prescribed deformation is 0.5 mm.

Table E.2: Iterative scheme for LB1 and LB3.

	LB1	LB3
Iteration method	Regular Newton-Raphson	Regular Newton-Raphson
Convergence norm	Energy	Energy
Convergence tolerance	0.0001	0.0001
Step size	0.5(100)	0.5(140)
Maximum number of iterations	150	150

## Material Properties

The material properties of the numerical models are shown in Table E.3.

Table E.3: Material properties of the concrete, steel and interface.

Concrete Properties		
Compressive Strength	$f_{cm} =$	50.9 MPa
Tensile Strength	$f_{tm} =$	3.68 MPa
Poisson's Ratio	$\nu =$	0.2
Young's Modulus	$E =$	37 GPa
Fracture Energy	$G_f =$	148 N/m
Compressive Energy	$G_{fc} =$	37 000 N/m
Steel Properties		
Young's Modulus	$E =$	200 GPa
Poisson's Ratio	$\nu =$	0.3
Yielding Stress	$f_y =$	235 MPa
Interface Properties		
Cohesion	$c =$	0.1 MPa
Friction	$\mu =$	0.5